Université catholique de Louvain
Institute of Condensed Matter and Nanosciences
Nanoscopic Physics

Photon- and electron-induced ionization of metastable helium and light anions

Matthieu Génévriez

Thesis presented for the Ph.D. degree
in Physics

Thesis jury :
Prof. **Xavier Urbain** (Université catholique de Louvain), Advisor
Prof. **Dag Hanstorp** (University of Gothenburg)
Prof. **Michel Godefroid** (Université Libre de Bruxelles)
Prof. **Mariko Dunseath-Terao** (Université de Rennes 1)
Prof **Pierre Defrance** (Université catholique de Louvain)
Prof. **Clément Lauzin** (Université catholique de Louvain)
Prof. **Bernard Piraux** (Université catholique de Louvain), Chairman

22nd of September 2017

'À ce non-sens qui le captivait
justement parce qu'il n'avait aucun sens'

Milan Kundera

Remerciements

Le doctorat est une aventure aussi bien personnelle que collective. Ce manuscrit est ainsi le fruit d'un long travail de 5 ans qui doit beaucoup aux personnes avec lesquelles j'ai travaillé, qui m'ont entouré et soutenu. Puissent les mots maladroits qui suivent exprimer au mieux mes remerciements les plus chaleureux.

Je souhaite tout d'abord remercier Xavier Urbain, mon promoteur, pour son aide précieuse et continue, son soutien, et d'avoir guidé et inspiré mon cheminement scientifique. Il a su créer au sein du laboratoire une ambiance humaine, rigoureuse, pleine d'émulation et foisonnante d'idées. J'ai conscience que sous sa supervision j'ai pu progresser bien plus loin que je ne l'imaginais... et ainsi de théoricien devenir expérimentateur !

J'aimerais également remercier Mariko Terao Dunseath et Kevin Dunseath. C'est sous leur supervision que j'ai débuté dans le domaine de la physique atomique, pour laquelle ils ont su me donner goût et curiosité. C'est aussi grâce à eux que je me suis "expatrié" en Belgique. Nos nombreuses discussions, leurs précieux conseils théoriques et leur enthousiasme constants ont grandement contribué au travail présenté ici.

Je remercie également les membres du jury, les professeurs Dag Hanstorp, Michel Godefroid, Mariko Terao Dunseath, Clément Lauzin, Bernard Piraux et Pierre Defrance, pour le temps qu'ils ont consacré à la lecture et à la correction de ce manuscrit ainsi que pour leurs conseils avisés.

Jozo Jureta a grandement contribué, lors de mon séjour en "chine", aux expériences sur l'hélium métastable. Nos longues soirées de mesures ont porté leur fruit et je souhaite ici le remercier pour son aide et sa pugnacité. Je remercie également Pierre Defrance, qui a joué un rôle important dans ces expériences; ses nombreux conseils m'ont bien aidé.

Les 5 années de thèse n'auraient sans doute pas été les mêmes sans la "colocation" avec Arnaud Dochain – ma porte de bureau non plus, d'ailleurs. Des discussions physiques jusqu'aux "moins qui manquent", sa présence et ses nombreux coups de mains ont été précieux. Je remercie également Raphaël Marion et lui souhaite bon vent pour son doctorat.

La physique expérimentale est bien plus qu'une affaire de science, c'est aussi une histoire de plomberie, visserie, soudure, électronique, etc. Des pompes à vide jusqu'aux nombreuses ouvertures de la chambre du VMI, la plupart des expériences présentées dans ce manuscrit n'auraient pas eu lieu sans l'appui technique de Luca Azzola. Qu'il en soit remercié. L'expertise et soutien technique de Daniel Dedouaire se sont également révélés précieux, et je l'en remercie. Je remercie Hervé Laurent et l'atelier de mécanique qui ont, presque littéralement, forgé quelques uns de nos succès expérimentaux. Aux nombreuses exigences du physicien, celles des "pièces à réaliser le plus vite possible" en particulier, Hervé a su répondre avec calme et grand savoir-faire technique. Enfin, bien que nos sciences des électrons soient de nature fort différente, le support électronique de Jean Pierre Van Roy et Feliz Kapita s'est révélé crucial. Du four à césium jusqu'au port série, ils savent (presque) tout faire. Merci à eux.

Il y a les papiers que l'on publie, et les papiers à remplir. Dans le deuxième cas, la formation de physicien étant inopérante, l'aide de Laurence Lenoir et Nicole Coismans a été importante, et je les en remercie.

J'aimerais remercier toute l'équipe du bâtiment Marc de Hemptinne, Abdouraman, Alexander, Thibault, les nouveaux venus, Alexis et Raghed et les anciens, Amin, Hamido et Kamel, pour l'ambiance amicale qui a régné tout au long de ces 5 ans. Je remercie également mes collègues assistants, et en particulier Adrien Poncelet, avec qui j'ai partagé joies et découragements du métier d'enseignant et (re)découvert que l'éducation est une histoire sans fin.

Merci à Mathieu Soetens pour, suivant un peu une liste à la Prévert, la colocation, la cornemuse et le sodium. Merci aux amis d'ici ou de plus loin, aux amis musiciens, aux amis scientifiques, aux amis historiens, aux amis tout court, à tout ceux qui ont partagé mes joies et frustrations de doctorant.

Merci à mes parents Michel et Catherine et ma sœur, Anne Laure pour bien des choses, leur soutien inconditionnel, leur confiance – inconditionnelle elle aussi – et leur présence.

Enfin, merci à Anna, "because all the rest is detail".

Contents

List of Figures

List of Tables

List of Publications

Published

M. Génévriez, J. J. Jureta, P. Defrance, X. Urbain, *Absolute cross section for electron impact ionization of He(1s2s ^3S)*, Phys. Rev. A **96**, 010701(R) (2017)

M. Génévriez, X. Urbain, A. Dochain, A. Cyr, K. M. Dunseath, and M. Terao-Dunseath, *One- and two-photon detachment of O^-*, Phys. Rev. A **94**, 023407 (2016)

M. Génévriez and X. Urbain, *Animated-beam measurement of the photodetachment cross section of H^-*, Phys. Rev. A **91**, 033403 (2015)

M. Génévriez, X. Urbain, M. Brouri, A. P. O'Connor, K. M. Dunseath, and M. Terao–Dunseath, *Experimental and theoretical study of three-photon ionization of He(1s2p $^3P^o$)*, Phys. Rev. A **89**, 053430 (2014)

To be submitted

M. Génévriez, A. Dochain, X. Urbain, *Photodetachment of O^-: the complete picture*

M. Génévriez, K. M. Dunseath, M. Terao-Dunseath, X. Urbain, *Resonances in the sequential, double detachment of He^-*

M. Génévriez, , J. J. Jureta, P. Defrance, X. Urbain, *Absolute cross sections for electron impact double ionization of He(1s2s ^3S) and He^-*

Chapter 1

Introduction

1.1 Astrophysical, atmospheric & technical plasmas

Light atomic anions are typically encountered in the gaseous ionized media that form dilute plasmas. Their existence is governed by the subtle balance between formation and destruction mechanisms. The former require electron-rich environments in order for, *e.g.* , electron attachment to an atom to be probable. The latter authorize their survival only in dilute, relatively cold conditions since anions are relatively fragile. Such conditions are typical of the outer layers of stars, and it is no surprise that interest in the physics of negative ions first arose from studies of the absorption spectrum of the Sun photosphere[1]. The observed continuous absorption in the near-infrared (NIR) and visible (VIS) ranges was indeed a puzzle for astronomers in the first decades of the twentieth century, and the allegation that it might be due to metal atoms led to unphysical consequences. In 1939, Wildt proposed that the NIR-VIS opacity was due to the photodetachment of H^- [1]. This proposal later proved correct for the Sun and Sun-like stars and led to a rich history of the study of H^- photophysical properties [2]. Since hydrogen is ubiquitous in our universe, the role of H^- in space goes of course well beyond stellar opacities, one paramount example of that being the importance of H^- in the formation of hydrogen molecules in the early universe [3]. Since they possess no bright absorption or emission line, the direct detection of atomic anions in space is very difficult, if not impossible for most species. This is nonetheless possible for molecular anions, but due to the lack of spectroscopic data, it was not before 2006 that the first

[1]The photosphere is a star's outer shell from which the light is radiated

negative ion (CH_6^-) was detected in the molecular shell of an evolved carbon star and in an interstellar molecular cloud [4].

The outer, ionized layers of planetary atmospheres (ionospheres) are another class of dilute plasmas that contain negative ions. Since elements heavier than hydrogen are abundant, not only H^- but also ions such as O^-, C^- and molecular anions take part in the intricate chemistry of these environments. Detachment of an electron from the O^- and O_2^- anions has for example a major influence on the density of free electrons in the ionosphere, which affects in turn radio communication [5, 6]. On a more exotic perspective, large densities (~ 200 cm^{-3}) of molecular negative ions have recently been detected in Titan's atmosphere by instruments aboard the Cassini probe [7], some of which reach mass-to-charge ratios as high as 10,000 amu/q. The subtle molecular anion chemistry in this nitrogen-rich atmosphere was subsequently modeled [8] and, interestingly, the presence of large fluxes of O^- was suggested and attributed to double charge exchange between nitrogen molecules and fast O^+ ions arriving from Saturn's magnetosphere [9], although laboratory-based measurements are required to confirm this.

While negative ions take part in the dynamics of astrophysical and atmospheric plasmas, the role of metastable helium (1s2s ^{3}S) is vastly unexplored. Since helium is rare on Earth, its role in the atmosphere is limited. Nonetheless, it was detected in the Earth upper ionosphere by looking at the resonant scattering of solar light by He(1s2s ^{3}S) atoms, the so-called twilight 1083 nm airglow[2], and its possible application to remote sensing of photoelectron fluxes and neutral helium densities in the upper atmosphere was considered [10, 11]. Since transfer of the large internal energy of metastable helium (19.8 eV) through binary collisions leads to Penning ionization of atoms or molecules in a very efficient way, it was recently proposed that this process is important in the chemistry of atmospheres and interstellar medium [12].

Plasmas containing helium possess important fractions of He(1s2s ^{3}S) atoms, which further play a predominant role in their dynamics. While radiative, de-excitation cascades from singlet excited states populate the 1s^2 ^{1}S ground state or the 1s2s ^{1}S metastable state, all cascades from triplet states populate the 1s2s ^{3}S state. Although He(1s2s ^{3}S) is metastable, its radiative lifetime (7870 s [13]) is orders of magnitude larger than its lifetime in plasma environments and it thus acts as an effective ground state for the triplet manifold. Moreover, conversion of 1s2s ^{1}S to 1s2s ^{3}S by superelastic collision of thermal electrons is a very efficient process and, since the inverse process is less likely, this results

[2] A wavelength of 1083 nm corresponds to the 1s2s ^{3}S- 1s2p ^{3}P^o transition in helium

in the presence of large fractions of metastable, triplet helium in the plasma [14]. In addition, the high electron impact ionization cross section of He(1s2s ^{3}S) and its capability to efficiently ionize all atoms and molecules through Penning ionization play an important role in ionization processes.

Metastable helium is encountered in a wide range of technical plasmas and other technological applications. For example, it plays an important role in the dynamics of cold atmospheric pressure helium plasmas since: (i) it helps sustain the plasma and (ii) it creates molecular radicals in the plasma plume which later interact with, *e.g.* , biological samples for skin treatment and disinfection [15–17]. Note that some negative ions are also involved in the chemistry of these plasmas [15]. Furthermore, the high reactivity of metastable helium confers it very low penetration depth and thus makes it an ideal candidate for surface treatment and analysis, which has spurred the field of metastable de-excitation microscopy [18, 19]. Helium nanolithography makes use of these "nano-grenades", borrowing the word of Baldwin [20], to prepare silicon wafers for chemical etching [21, 22]. This technique relies on Penning ionization by metastable atoms to alter specific regions of a self-assembled molecular layer, sitting on top of the wafer, so that chemical etching occurs only in these areas. It reaches results on pair with, if not better than, standard optical lithography in terms of edge resolutions. Etching is also a domain of application for anion-rich electronegative plasmas [23].

Another broad range of applications for the production and study of negative ions relies on the fact that they are loosely bound and ejection an electron is relatively easy. This property is used for example in tandem accelerators to increase the kinetic energy of the particles. To do so, a beam of anions is extracted from an ion source and accelerated by a high positive voltage (HV). Anions are then converted into positive ions by stripping on a gas target or a thin foil and, as the latter travel from the HV region back to a grounded region, their energy is multiplied by two or more depending on their charge.

A fast, intense beam of hydrogen or deuterium atoms obtained by neutralization of a fast beam of negative ions will be a primary source of plasma heating for thermonuclear fusion devices, with powers up to 50 MW being envisioned for ITER [24]. The current neutralization scheme is based on stripping in a gas target, which cannot reach efficiencies higher than $\sim 60\%$. Although their implementation is rather simple, limitations associated with such schemes yield quite low (30%) wall-plug efficiencies. Alternative neutralization techniques have thus been proposed since higher efficiencies must be reached in the future to

allow electricity production at tolerable costs. One of these proposals is based on photodetachment of H^- and is expected to bring better neutralization efficiency ($\sim 95\%$) and wall-plug efficiency of 50% [25]. However, photodetachment is not very efficient for fast beams since the cross section is relatively low and the interaction time between anions and light is short. Techniques combining high-power laser, on the mega-watt scale, and optical cavities have thus been proposed for DEMO, ITER's planned successor [25]. The formation of neutral beams by photodetachment of fast anion beams has already been proved possible [26], however the technical challenges for fusion applications are daunting, owing to the tremendous laser powers required, the need for stable, long-term operation and the necessary resistance to large fluxes of fast neutrons, amongst other issues [25, 27, 28]. In the perspective of photoneutralization developments, the present work on the photodetachment cross section of H^- certainly bears interest. The development of a neutral helium beamline based on photodetachment, which reaches high neutralization efficiencies for comparably low laser powers, is also interesting, although not directly in line with the requirements for fusion devices.

Besides their use for large-scale heating, neutral beams can also be used for diagnosing thermonuclear fusion plasmas (see, *e.g.* , [29] for ITER). Fast helium beams have been used at ASDEX Upgrade and JET to measure plasma density and temperature by monitoring visible emission lines of neutral helium atoms penetrating the plasma [30]. The contamination of the beam by metastable helium was also taken into account in the modeling. The scrape off plasma layer, *i.e.* the region just after the last closed flux surface in confined fusion devices, is another target for diagnostics with helium through line ratio (LR) measurements. It relies on the injection of an helium "puff" at the plasma edge and on the time-dependent monitoring of the visible emission lines of excited singlet and triplet helium atoms. The absolute line intensities are then compared to the results from collisional radiative models and the electron temperature and density profile of the scrape off layer can be determined. As stressed by several authors, the successful application of such techniques depends on the availability of *accurate* data on elementary reactions, amongst which electron impact excitation and ionization play a major role [31]. In particular, the long relaxation time of He(1s2s ^{3}S) is governed in parts by electron impact ionization, and the present difference of about a factor of 2 between theoretical and experimental data is certainly the cause of much uncertainty. In this respect, the work described below dedicated to measuring the absolute cross section of this process is assuredly significant. LR schemes have been implemented and successfully tested during a test run of the Wendelstein 7-X

fusion device [32] and on the TEXTOR-94 device [33].

1.2 Structure of negative ions

Let us now consider how, in a negative ion, electrons are bound to the nucleus and how this binding differs from atoms and positive ions. In atoms, the nucleus and electronic cloud bear charges that are opposite in sign but identical in magnitude. Therefore, all electrons evolve in the Coulomb potential of the nucleus, proportional to $1/r$ at large distance. Anions are atoms with an extra electron and their electronic cloud bears an excess negative charge compared to the nucleus. Due to the effective screening of the nuclear charge, binding is mediated, at large distance, by weaker, polarization forces which depend on the extent to which the electrons are able to "share" the Coulomb field of the nucleus. As a result, the attractive potential is only of short range and typically behaves asymptotically as $1/r^4$ [34]. The case of hydrogen is particular in this respect since, because the H atom possesses a permanent dipole due to ℓ-degeneracy, the binding potential of H^- behaves asymptotically as $1/r^2$. Another consequence of the screening of the nuclear charge is the increased influence of electron-electron correlations on the structure and dynamics of anions, since the relative weight of electron-nucleus attraction is lowered with respect to inter-electronic interactions. The importance of these many-electron correlation effects has attracted a number of theoretical studies and experimental works in the past decades [34].

Despite Coulomb repulsion, the binding of an extra electron is energetically favorable for most atoms and the energy gained in the process is called the *electron affinity*. The absence of Coulomb interaction between the extra electron and the nucleus results in binding energies lower than for atoms or cations. For example, while the binding energy of oxygen is 13.6 eV, its electron affinity is 1.46 eV, about an order of magnitude lower. About 80% of the naturally occurring atoms can attach an extra electron, however for some atoms like nitrogen or rare gases, this process is not energetically permitted and they do not form stable anions [35].

Consequences of the short range binding potential are also dramatic concerning the electronic structure of negative ions. It is well-known that atoms and positive ions can host, in theory, an infinite number of states whose energies converge to the ionization threshold. In stark contrast, anions possess only one or few bound states. These are in general fine structure states belonging to the same term, *e.g.* , the $J = 1/2$ and $3/2$ levels of $O^-(^2P^o)$, or terms belonging to the same configuration, as for example the $(1s^2 2s^2 2p^3\ ^2D^o)$ state of C^-, lying some 1.23 eV above the

($1s^2 2s^2 2p^3\ ^4S^o$) ground state [36]. A noticeable consequence of this bare structure is that, as we shall see later, negative ions do *fragment* as soon as they absorb energy.

Contrarily to their modest bound states spectrum, negative ions possess in general a rich spectrum of quasi-bound states embedded in the detachment continuum, *i.e.* with energies greater than the electron affinity (see Fig. 1.1). When populated, these states spontaneously and rapidly decay, or autodetach, by ejection of an electron mediated by Coulomb repulsion. Their presence manifests itself as resonances in, *e.g.* , the photodetachment cross section. Autodetaching states are in general associated with: (i) the excitation of a core electron, an example of that being the $2s2p^3\ ^3D$ state of B^- in which a 2s electron from the $2s^2 2p^2\ ^1D$ ground state is promoted to a 2p orbital; (ii) the excitation of more than one electron, as for example the $1s^2 2s^2 2p^3 3s^2$ state of O^- [36]. These states frequently lie energetically close to a bound state of the neutral atom, the aforementioned excited state of B^- being for example close to the the first excited state of boron ($2s2p^2\ ^4S$). The study of such autodetaching states, and the wealth of resonance behaviors and interference effects associated with them, is an important field of investigations that has been reviewed by, *e.g.* , Buckman and Clark [37].

Some autodetaching states are *metastable* against spontaneous detachment and can lead to the formation metastable anions, *i.e.* anions with energies above the atom ground state and possessing relatively long lifetimes. A well-known example is $He^-(1s2s2p\ ^4P^o)$, whose energy lies 19.7 eV above helium's ground state but 77 meV below its first, excited $1s2s\ ^3S$ state [38]. Since selection rules for Coulomb autodetachment are not fulfilled, its spontaneous decay to the neutral's ground state occurs *via* weak, relativistic interactions and the lifetimes of its various fine structure components, ranging from 7.8 to 359 μs, are consequently long by anion standards [39]. Although short on our timescale, these lifetimes are in most cases sufficient for experimental investigation of this metastable anion.

Most negative ions possess either a single bound state or a limited set of bound states that are not coupled by dipole transitions. The Os^-, Ce^- and La^- ions are noticeable exceptions to this rule and present dipole transitions which, for example, may be used for laser cooling [40–42]. Due to the absence, for all other anions, of bright absorption and emission lines, they cannot be studied with standard, state-of-the-art spectroscopic techniques, making their detection in astrophysical environment more difficult. Instead of bound-bound transitions, one has to turn instead to bound-free transitions, *i.e.* photodetachment.

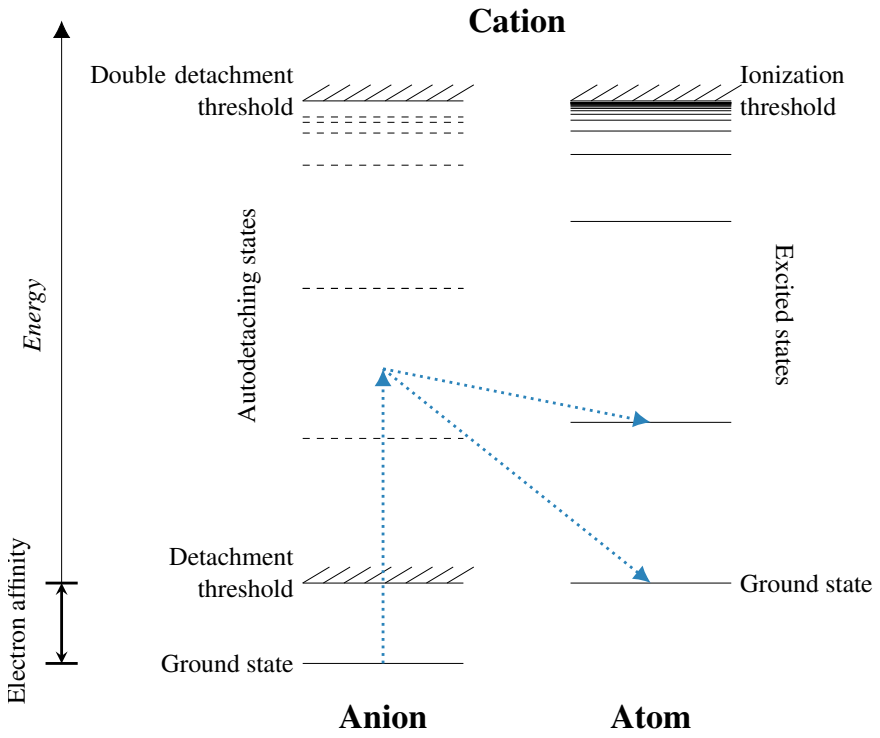

Figure 1.1: *Typical energy level scheme of an anion and an atom. The dotted lines indicate photodetachment into the ground and first excited states of the atom.*

1.3 Photodetachment

The photoelectric effect is the emission of electrons from a material when light is shone onto it. Discovered by, amongst others, Heinrich Hertz and Philipp Lenard in the late 19th century and studied ever since, this effect is significant in the history of modern physics. Indeed, its explanation by Einstein in terms of light quanta, which led to his 1921 Nobel prize, and the parallel he made with Planck's energy quantization is at the origin of the revival of the corpuscular theory of light and did lay foundations for the development of quantum theory [43]. The process of photodetachment is nothing but the photoelectric effect as observed for anions, written as

$$\mathrm{A}^- + \gamma \longrightarrow \mathrm{A}^{(*)} + \mathrm{e}^-, \tag{1.1}$$

where γ represents a photon, e^- an electron and $A^{(*)}$ denotes an atom that is possibly in an excited state. The most fundamental equation for the photoelectric effect is the one relating the kinetic energy E of the emitted electron, termed photoelectron, to the frequency ν of light,

$$E = h\nu - W, \tag{1.2}$$

where W is the work function of the material, *i.e.* the electron affinity in the present case, and h is the Planck constant, underlining the quantum nature of this effect.

While the absorption of a photon of sufficient energy by an atom or positive ion leads to the emission of a photoelectron and leaves an *ion* behind, hence the term photo-ionization, the same process starting from a negative ion and leaving a *neutral atom* behind is coined photo-detachment. Although distinguishing these two processes may seem anecdotal, the structural differences between each of the initial and final systems yield largely different behaviors.

One of the most obvious differences is the region of the electromagnetic spectrum where the photoelectric effect becomes energetically allowed. For atoms and ions, it lies in the ultraviolet range and beyond since the photon energy $h\nu$ required to overcome the ionization potential W is large. Negative ions exhibit much weaker binding energies and photodetachment is already allowed in the near infrared and visible ranges. This explains, in particular, why H^- is responsible for the continuous absorption of the Sun photosphere in these ranges despite H atoms being much more abundant.

The behavior of photodetachment in regions not so far above threshold, *i.e.* for photon energies close to W, is also much different from that of photoionization. Because anions support a single bound state, or a limited set of them, the density of states just below the detachment threshold is essentially zero and so is the excitation cross section. The necessity of continuity across the threshold thus implies that the photodetachment cross section starts from zero and raises along with the photon energy. Because atoms and positive ions possess an infinite number of bound states whose energies converge to the ionization threshold, the density of states is non-zero below threshold and, consequently, the photoionization cross section is non-zero and in general maximum right above it, as shown in Fig. 1.2. The behavior of photodetachment at threshold is well understood and governed by the Wigner law [44],

$$\sigma(E) \propto E^{\ell+1/2} = (h\nu - EA)^{\ell+1/2}, \tag{1.3}$$

where ℓ is the orbital angular momentum quantum number of the ejected

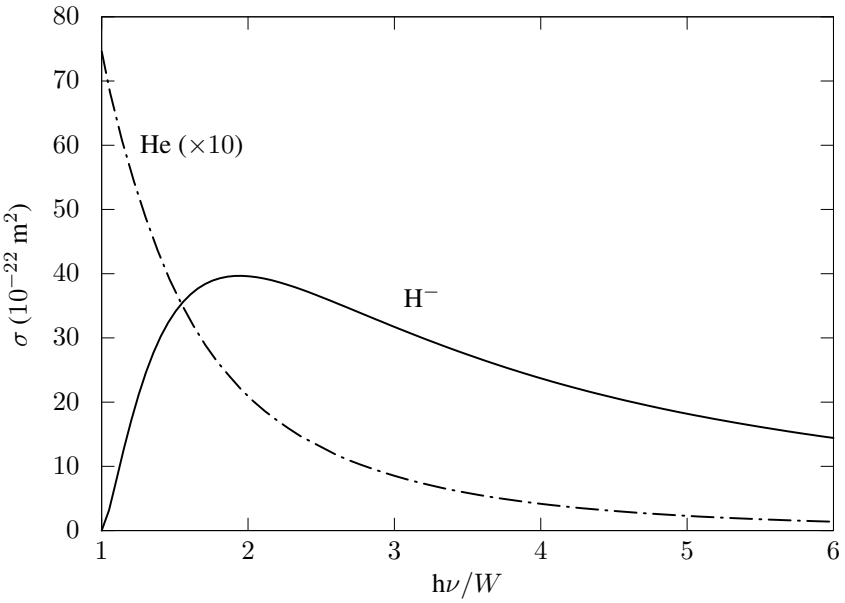

Figure 1.2: *Photodetachment cross section of H^- (full curve) and photoionization cross section of He (chained curve) as a function of the ratio between the photon energy $h\nu$ and the work function W, standing for the electron affinity or ionization potential respectively. Data is from Venuti and Decleva for H^- [47] and from Yan et al. for He [48].*

electron, associated to a given partial wave, and EA is the electron affinity. This type of behavior arises from the asymptotic behavior of the bound and free single-electron wave functions as obtained analytically for short-range potentials. A number of different partial waves, that is a number of different ℓ values, contribute in general to photodetachment but Eq. (1.3) shows that, close to threshold, the one with lowest ℓ predominates. We finally note that while the Wigner threshold law neglects any interaction between the outgoing photoelectron and the atom, some authors have developed extensions that account for multipole forces and polarization effects, with the aim of extending its range of validity [45, 46].

This brings us to the last important property of photodetachment. Since the outgoing photoelectron sees a neutral core, there is virtually no interaction between the two at sufficiently large distances. The photoelectron is thus essentially described as a spherical outgoing wave. Conversely, the outgoing photoelectron produced by photoionization is interacting with the ionic core even as it recedes to infinity, a conse-

quence of the long-range behavior of Coulomb potentials. The photoelectron must be described in this case by a Coulomb wave.

As a final remark, let us note that the study of photodetachment is also interesting from a radiative electron attachment perspective, since the latter process can be viewed as the time-reversed version of the former. Determining photodetachment cross sections allows one to determine radiative electron attachment cross sections [49]. Electron attachment is a major production channel for anions in space [50] and, since it is harder to study experimentally, it is a motivation for photodetachment cross section measurements.

1.4 Cross sections

Photodetachment and photoionization are quantum-mechanical effects, described by non-relativistic quantum theory in the present case since the electrons' velocity in light anions and atoms is small compared to the speed of light. A complete theoretical treatment requires determining the wave function of the anion $|\Psi_i\rangle$, the wave function of the final "photoelectron + atom" system $|\Psi_{jE}\rangle$ and solving the Schrödinger equation including the Hamiltonian of the radiation. We shall assume, in the following and for the rest of the manuscript, that the light-field Hamiltonian can be expressed classically and within the dipole approximation since the number of photons involved is high and the size of the anion is by far smaller than the wavelength of infrared, visible and ultraviolet light. From this treatment, a set of quantities describing photodetachment in its full dimensionality can be derived and bears physical significance. These are the differential, partial and total cross sections, which we shall briefly explain in the following. Cross sections can also be derived in a similar manner for electron impact ionization but will not be considered below. They are described, *e.g.* , in the book of Burke [51].

Considering a negative ion in a well defined quantum state i and an incoming flux ϕ of photons with angular frequency ω, these cross sections essentially try to answer to the following question,

What is the probability, per unit time, that an electron will be ejected with a kinetic energy E and along a direction $\hat{\boldsymbol{k}}$, leaving an atom in a well defined state j?

The most direct answer is given by the fully differential cross section [51],

$$\frac{\mathrm{d}\sigma_{ij}}{\mathrm{d}\Omega} = 4\pi^2\alpha \mathrm{a}_0^2\omega |\left\langle \Psi_{jE}|\hat{\boldsymbol{\epsilon}}\cdot\boldsymbol{D}|\Psi_i\right\rangle|^2, \tag{1.4}$$

where α is the fine structure constant and a_0 the Bohr radius. The quantity $\boldsymbol{D}$ is the dipole operator and $\hat{\boldsymbol{\epsilon}}$ is the polarization of the radiation. If expressed in its length form (L), the operator $\boldsymbol{D}$ reads

$$\boldsymbol{D}_L = -e \sum_{n=1}^{N} \boldsymbol{r}_n, \tag{1.5}$$

where e is the elementary charge, $\boldsymbol{r}_n$ are the coordinates of the n-th electron and the summation runs over all N electrons of the system. Both wave functions in Eq. (1.4) must be appropriately normalized and normalization factors are, for brevity, assumed to be already included within $|\Psi_i\rangle$ and $|\Psi_{jE}\rangle$. The wave function describing a photoelectron of energy $E = k^2/2$ must behave asymptotically as

$$\Psi_{\boldsymbol{k}}(\boldsymbol{r}) \xrightarrow[r\to\infty]{} \frac{1}{(2\pi)^{3/2}} \left[\mathrm{e}^{\mathrm{i}\boldsymbol{k}\cdot\boldsymbol{r}} + f^{-}(\theta) \frac{\mathrm{e}^{-\mathrm{i}\boldsymbol{k}\cdot\boldsymbol{r}}}{r} \right] \tag{1.6}$$

for large distances r [52]. The vector $\boldsymbol{r}$ represents the position of the photoelectron with respect to the nucleus and the vector $\boldsymbol{k}$ is the electron's (linear) momentum. The quantity f^- is the so-called scattering amplitude for an angle θ between $\boldsymbol{k}$ and $\boldsymbol{r}$, and also depends on the magnitude of $\boldsymbol{k}$. The photoelectron wave function is thus asymptotically the superposition of a plane wave and an ingoing spherical wave.

When multiplied by the photon flux ϕ, the differential cross section readily gives the emission rate W_{ij} of a photoelectron with energy E into an infinitesimal solid angle $\mathrm{d}\Omega$,

$$W_{ij} = \phi \frac{\mathrm{d}\sigma_{ij}}{\mathrm{d}\Omega} \mathrm{d}\Omega. \tag{1.7}$$

If one needs not to know the direction of emission of the photoelectron, *e.g.* , because this quantity cannot measured in one's experiment, the differential cross section is integrated over all solid angles Ω and we obtain the partial cross section σ_{ij},

$$\sigma_{ij} = \iint \mathrm{d}\Omega \frac{\mathrm{d}\sigma_{ij}}{\mathrm{d}\Omega}, \tag{1.8}$$

which is related to the probability to leave, upon photodetachment, the atom in a specific quantum state j. Finally, the final state of the atom may not be accessible, or interesting for that matter, and we may just want to know what is the probability, per unit time, to photodetach a negative ion initially in a well defined quantum state i with orbital

angular momentum L_i. Summation of the partial cross sections over all final states j readily gives the total cross section σ_i,

$$\sigma_i = \sum_j \iint \mathrm{d}\Omega \frac{\mathrm{d}\sigma_{ij}}{\mathrm{d}\Omega} = \frac{4\pi^2 \alpha a_0^2 \omega}{3(2L_i+1)} \sum_j \left| (\Psi_{jE} || \hat{\boldsymbol{\epsilon}} \cdot \boldsymbol{D}_L || \Psi_i) \right|^2, \tag{1.9}$$

where the rightmost expression is valid for an unpolarized anion and the term $(a|\hat{\boldsymbol{\epsilon}} \cdot \boldsymbol{D}_L|b)$ represents the *reduced* dipole matrix element [53].

From the above expressions, we see that the (theoretical) knowledge of the initial and final wave functions allows cross sections to be calculated, following what we could call a "bottom-up" approach. Their experimental determination follows instead a "bottom-down" approach, where the photodetachment rate W_{ij} is used to infer the cross section and obtain information on the wave functions. We may further note that, although the formulas given above are for a given initial state of the anion, in some case a number of initial states can be altogether populated and the total cross section, as measured in the experiment, may depend on the initial population distribution. For meaningful comparison between theory and experiment, the cross sections for all initial states must be calculated and summed with weights given by the ion temperature that must be determined experimentally.

It is also important to note that all the above definitions are for absorption of a *single* photon. Generalized cross sections can be derived for n-photon absorption by means of perturbation theory and, when multiplied by ϕ^n, give the detachment or ionization rates. However, they hold only if the process is *non*-resonant. In the case of resonant multiphoton ionization, a process that will be investigated in Sec. 3, the cross section picture breaks down since the dynamics of a given system at a time t does *depend* on its state at a former time $t - \mathrm{d}t$. In that case, one has to resort to resolving the full time-dependent Schrödinger equation.

While the partial and total cross sections are scalar variables, the differential cross section is a 3-dimensional quantity which is somewhat tedious to manipulate. Fortunately, if the system is initially unpolarized, its behavior can be reduced to that of two scalar parameters: the asymmetry parameter β and the partial cross section σ_{ij} [54, 55],

$$\frac{\mathrm{d}\sigma_{ij}}{\mathrm{d}\Omega} = \frac{\sigma_{ij}}{4\pi} \left[1 + \beta_{ij} P_2 \left(\cos\theta_k \right) \right]. \tag{1.10}$$

$P_2(\cos\theta_k) = (3\cos^2\theta_k - 1)/2$ is the Legendre polynomial of 2nd order and θ_k is the angle between the direction of emission of the photoelectron and the quantization axis, chosen as the laser polarization axis. This

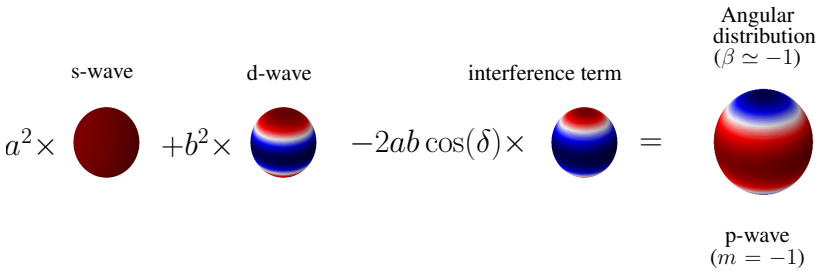

Figure 1.3: *Schematic partial waves contributions to the total photoelectron angular distribution for detachment of a p-electron. The light polarization is linear and along the vertical axis. Red regions correspond to higher differential cross section values and blue regions to lower ones. We assumed that* $\cos(\delta_{\ell-1} - \delta_{\ell+1}) \simeq 1$*, as is typical for negative ions, and* $a = 2b$*. Distributions on the left hand side are computed using Eq.* (1.13) *and that on the right hand side is computed using Eq.* (1.10)*.*

equation is valid for one-photon transitions under linear polarization only, although similar formulas can be derived for multiphoton transitions and circular polarization and include higher-order and odd-order Legendre polynomial terms [51, 54].

A more intuitive take on the photoelectron angular distribution, as given by Eq. (1.10), can be obtained by looking at its connection with the widely used partial wave expansion of the photoelectron wave function[3],

$$\Psi_E = \sum_{\ell' m'} \mathrm{i}^{\ell'} \mathrm{e}^{-i\delta_{\ell'}} \frac{1}{r} u_{E\ell'}(r) Y_{\ell' m'}(\theta, \varphi) Y^*_{\ell' m'}(\theta_k, \varphi_k). \tag{1.11}$$

The photoelectron is represented here as a coherent superposition of waves of different angular momenta, each defined by the quantum numbers ℓ' and m'. They are written as the product of a radial function $u_{E\ell'}(r)$, two spherical harmonics $Y_{\ell' m'}$ and a phase shift term $\mathrm{e}^{-\mathrm{i}\delta_{\ell'}}$. The direction of emission of the photoelectron is determined by the spherical harmonic $Y^*_{\ell' m'}(\theta_k, \varphi_k)$, where the coordinates (θ_k, φ_k) are the angles between the emission direction and the quantization axis.

Since the differential cross section is proportional to the squared norm of the dipole matrix element, the photoelectron angular distribution is of the form

$$a^2 |Y_{\ell-1m}|^2 + b^2 |Y_{\ell+1m}|^2 - ab\,\Re\left(Y^*_{\ell-1m} Y_{\ell+1m} \mathrm{e}^{-i(\delta_{\ell-1} - \delta_{\ell+1})}\right), \tag{1.12}$$

[3]Expansion in terms of Legendre polynomials $P_\ell \cos(\theta)$ is also widely used and is equivalent to the above formula.

where ℓ and m are quantum numbers of the initial electron wave function and we made use of the dipole selection rules $\ell' = \ell \pm 1$ and $m' = m$. The symbol $\Re$ stands for the real part. Of course, a complete calculation must include the wave functions of the initial ion, of the photoelectron and of the residual atom. However, since we are interested in the angular distribution only, terms appearing in the calculation that are not relevant for the present purpose are "hidden" in the parameters a and b. Their dependence on quantum numbers and other variables of the problem is further omitted for the sake of clarity. The interested reader is referred to the work of Bethe [56] or Blatt and Biedenharn [54] for insight on the mathematical details.

Considering an initially unpolarized ion and summing over all possible m values further reduces the angular distribution to

$$\sum_m \Big[a^2 |Y_{\ell-1m}(\theta_k, \varphi_k)|^2 + b^2 |Y_{\ell+1m}(\theta_k, \varphi_k)|^2 \\ -2\,ab\cos(\delta_{\ell-1} - \delta_{\ell+1}) Y^*_{\ell-1m}(\theta_k, \varphi_k) Y_{\ell+1m}(\theta_k, \varphi_k) \Big], \quad (1.13)$$

which, after some involved spherical harmonics algebra, is shown to be proportional to the angular distribution given by Eq. (1.10), *i.e.* , $1 + \beta P_2(\cos\theta_k)$.

Hence, the angular distribution is governed by the squared norm of the coherent superposition of partial photoelectronic waves. It bears terms belonging to each of these waves, summed over all possible values of m, and also includes a cross-product, interference term. This interference term can lead to unexpected consequences, an example of which is shown in Fig 1.3. In this example, the superposition of an s-wave and a d-wave following detachment of a p-electron gives rise to an angular distribution which is identical to that of a p-wave with $m = -1$. This behavior, possible because the difference in phase shift between s- and d-waves is close to 0, was first studied by Cooper and Zare, who established an expression for β in terms of radial dipole matrix elements only [57].

1.5 Experimental overview

The experimental investigation of the structure and dynamics of negative ions has given rise to a variety of experimental techniques [6, 36], some of which are described in more details in the state-of-the art sections in the main body of the manuscript. In most cases, experimental study is made difficult by the low particle densities that can be attained when

compared to neutral atoms and molecules, and which finds its origin in the low production efficiencies and space-charge effects.

The present work, as most others, uses ion sources and small particle accelerator setups to produce a beam of relatively fast (keV) anions. Advantages of the use of fast beams are manifold: the high velocity of the particles counteracts space-charge effects and allows the extraction of relatively high anion fluxes, straightforward mass-selection techniques can be used to purify the beam, appropriate collimation ensures that all particles share essentially the same velocity vector and detection of anions or neutral atoms by single-particle detectors is greatly facilitated. While a variety of ion sources can be used to produce negative ions, such as sputtering or electrospray sources [36, 58], we have used duoplasmatron sources due to their availability in the laboratory.

Negative ions and atoms can be probed by impact of a variety of projectiles including photons, electrons or heavier particles. In the work presented in this thesis, experiments are always performed in a crossed-beams geometry, where a fast anion or atom beam is intersected at right angle by either a laser beam or an electron beam. The following discussion will consider the case of anion and laser beams, however similar considerations apply to atom and electron beams. The crossed-beams geometry facilitates the detection of neutral atoms and the collection of the laser beam. However the experiment is single-pass, in the sense that a given anion will interact only once with the laser, and the interaction volume is relatively small. This is not a problem as long as the yields of the reaction are high enough, but it can be troublesome if the anion flux is low or the cross section small. Experimental schemes with inclined-beams geometries, where the laser intersects the ion beam at a small incidence angle, or collinear geometries, where the incidence angle is zero, are also widely used [26, 59]. In such configurations, the interaction volume and thus the sensitivity are significantly larger. It however comes at the expense of a few, additional complications since, for example, the Doppler effect due to the high velocity of the anions must be taken into account. Multi-pass experiments can be performed with storage rings, in which anions can be stored for as long as thousands of seconds [60–63]. Multi-pass schemes can also be achieved with ion traps such as electrostatic traps or RF multipole traps [64, 65]. In these setups, anions are repeatedly exposed to the laser light and their rate of depletion is measured through lifetime measurements. Trapping thus significantly enhances the sensitivity of the experiment and allows one to study anions that can be produced only in small quantities. Moreover, the long storage times attained with storage rings have proved particularly useful for measuring the lifetimes of metastable anions, such as

He^- [66]. The ability to cool trapped molecular anions, either by spontaneous emission or buffer gas cooling, is also a major advantage.

The two first parts of this thesis are dedicated to detachment and ionization by absorption of photons. Branscomb and others [67] were the first to pioneer photodetachment studies, using arc lamps and optical filters to produce quasi-monochromatic light that intersected a beam of anions in a crossed-beams configuration. The rapid development of laser sources has since given rise to a variety of photodetachment experiments, aiming at studying different properties of anions. Electron affinities E_A can be determined with high accuracy using laser photodetachment threshold spectroscopy [68], in which the photodetachment yield across the detachment threshold is measured and fitted with a Wigner law. The photodetachment microscopy technique takes advantage of the interference between the two paths of a slow photoelectron, emitted upon photodetachment in the presence of a weak electric field, that lead to the same position on the detector. It allows to determine E_A with exquisite accuracy [69]. Electron affinities can also be measured using the slow electron velocity-map imaging technique, which relies on measuring directly the kinetic energy of slow photoelectrons with a velocity map imaging spectrometer [70]. The measurement of photodetachment cross sections has given rise to another ensemble of experimental techniques. Total cross sections are determined, in general, from the yield of neutral atoms produced by photodetachment of a fast anion beam in crossed-beams or collinear-beams geometries. However, the absolute fluxes of anions and photons, the detection efficiency and the overlap between the laser and ion beams must be carefully determined. Measuring such quantities is cumbersome and difficult, explaining the scarcity of absolute cross section measurements. Methods based on the saturation of neutral atom production for increasing laser intensities have been developed to overcome the need for detection efficiency measurement [71, 72]. By measuring the negative ion depletion inside a RF multipole trap and scanning the laser across the trap volume, Hlavenka *et al.* were able to determine absolute photodetachment cross sections without measuring the interaction volume [73]. Resonant ionization spectroscopy has been developed for state-selective experiments, *i.e.* to measure relative partial photodetachment cross sections to a specific final state of the atom [74]. After photodetachment, the atomic state of interest is optically excited to a Rydberg state *via* a resonant transition, the Rydberg state is field-ionized and the positive ions are detected. This technique has been used, for example, to determine the electron affinity of some anions [38, 74] or study the autodetaching spectrum of He^- [75]. Finally, relative differential cross sections, related to photoelectron angular distributions,

can been measured using photoelectron detection systems with low solid angle acceptance and by rotating the angle between the laser polarization and the detection axis [59, 76]. If the detection system comprises an energy analyzer, the photoelectron velocity distribution can also be measured [77]. More recently, velocity map imaging spectrometers have been used to determine photoelectron velocity and angular distributions [78].

The present work contributes to the field of cross section measurements by implementing another method for the determination of absolute, total photodetachment cross section: the animated-crossed-beam technique. This technique was originally developed for electron impact ionization measurements [79], and does not rely on determining the interaction volume. Partial and differential cross sections were measured, as for most other recent works, using a velocity map imaging photoelectron spectrometer. This spectrometer, built in-house, was designed to allow the use of a fast anion beam and the detection of photoelectrons perpendicular to the anion beam axis.

After photodetachment, the atom is left either in its ground state or in an excited state and, since the final state is a fragmented one, a wider ensemble of excited states can be populated compared to optical pumping of ground state atoms. Indeed, dipole selection rules apply to the total, atom plus photoelectron system and restrictions on the symmetry of the final atomic state are relaxed since the photoelectron also carries some angular momentum and spin. For example, while dipole selection rules prevent optical excitation of, *e.g.* , $O(1s^2 2s^2 2p^4\ ^3P^e)$ to $O(1s^2 2s^2 2p^4\ ^1D^e)$ or $O(1s^2 2s^2 2p^4\ ^1S^e)$, these states can be populated by photodetachment of $O^-(1s^2 2s^2 2p^5\ ^2P^o)$. One may thus envision to use photodetachment as a source of excited atoms, backed by the fact that photodetachment cross sections are maximum for near-infrared and visible light, where high-power lasers are commercially available. This idea has already been mentioned in a number of works, starting from Branscomb *et al.* in the 1960's [80]. Moreover, production of fast beams of ground state atoms by photodetachment in an inclined-beams geometry has already been implemented elsewhere [26]. The contribution of the present work to the field of fast neutral beams resides the implementation of a source of metastable helium atoms produced by photodetachment of He^-, presented in the last chapter of the manuscript. It is, to our knowledge, the first metastable atom source based on photodetachment.

The last chapter of the present manuscript is also dedicated to probing atomic systems by electron impact. In such experiments, an impinging electron brings sufficient energy to the atom or negative ion so that it ejects one or two electrons. To do so, one must use an electron gun that produces a beam of electrons which crosses an atom or ion beam,

in general at right angle. Again, a variety of experimental methods exist and, to name only a few, include the animated-crossed-beam technique to determine total cross sections [81] and the reaction microscope technique to investigate fully differential cross sections [82]. The present study is based on the animated-crossed-beam technique following which the final atom or ion is detected irrespective of its particular electronic state. From this, the total electron impact ionization cross section is determined.

Electron impact allows to probe a different range of energies deposited in the system compared to photon impact, albeit with, in general, a lower energy resolution. Electron kinetic energies typically range from a few electron-volts to a few thousand electron-volts, and energy resolutions usually range from a few tens of meV to about 0.5 eV. In contrast, the energy of photons produced by commercial lasers is smaller and hardly reaches more than 5 eV, albeit with resolutions better than a few μeV. One further, major difference between photon and electron impact is that while the photon is absorbed and the deposited energy is strictly equal to its energy hν, the impinging electron is scattered by the target and the deposited energy is *a priori* unknown and at most equal to the projectile's kinetic energy. The negative charge of the electron, of course, also plays an important role.

1.6 Outline

The main body of the present manuscript is subdivided in three chapters. The first and second chapters are dedicated to the photodetachment and photoionization of anions and metastable atoms. The third chapter investigates the electron impact ionization of anions and of metastable atoms produced by photodetachment.

Chapter 2 is dedicated to the measurement of the photodetachment cross sections of H^- and O^-. The adaptation of the animated-crossed-beam technique (ACBT) to the measurement of absolute total photodetachment cross sections is first presented. All types of crossed-beam configurations, including combinations of continuous or pulsed beams, are considered and explicitly treated. Since standard ACBT is limited to the measurement of one-photon cross sections, we also develop an extension of the technique which allows to measure multiphoton generalized cross sections, borrowing ideas from inverse problem theory. The development of a velocity map imaging photoelectron spectrometer is further detailed and its use to measure partial and differential cross sections explained. The values of the absolute total photodetachment cross

section of H^-, measured for photon energies in the range from 1.165 eV to 1.771 eV, are presented and compared against available data. Results on the absolute total cross section of O^-, measured for photon energies ranging from 1.46 eV to 5.5 eV, are also detailed. The partial and differential cross sections obtained from photoelectron distributions are discussed and analyzed. Finally, results obtained with the multiphoton extension of the ACBT for the two-photon detachment of O^- are presented and the influence of photon statistics is discussed.

Chapter 3 considers the 4-photon double detachment of He^- by intense laser pulses with wavelengths in the visible part of the spectrum. After outlining the experimental setup, the theoretical tools used to model this highly non-linear process are presented, based on a sequential picture of double detachment. The first, one-photon detachment step is treated within *R*-Matrix theory while the second, resonance-enhanced multiphoton ionization step is investigated by means of a time-dependent effective Hamiltonian model further checked against *ab initio* *R*-Matrix Floquet calculations. The influence of the laser wavelength, polarization and pulse energy are explicitly treated. The theoretical results concerning the one-photon detachment of He^- are then presented, followed by experimental and theoretical results concerning the double detachment of He^- *via* the He(1s2s ^{3}S) transient state. The underlying, resonant dynamics are discussed in details. Results on the double detachment *via* the He(1s2p ^{3}P^o) transient state are finally presented and analyzed in the light of the various resonance series at play. The cases of linear, circular and elliptical polarizations are studied and their important influence on the above results is made clear.

The last chapter of the present manuscript (4) investigates the single and double ionization of metastable helium (1s2s ^{3}S) by electron impact, along with the double ionization of He^-. The first objective was to develop an intense source of fast metastable atoms with high purity. This source is based on the photodetachment of He^- and, after presenting it, its performances are analyzed in details. The apparatus for measuring electron impact ionization cross sections is also briefly explained. Results on the electron impact single ionization cross section of metastable helium are presented and compared against available experimental and theoretical data. The two last sections are dedicated to the cross sections measured for double ionization of metastable helium and He^- and, since no other data is available for comparison, tentative explanations on the mechanisms at play are given.

Contributions and contributors

The work presented in this thesis has benefited from the contributions of several people. The list below details these contributions.

- The experiments presented in chapter 2 were developed and run by myself and X. Urbain. R. Marion helped setting up the VMI spectrometer. I performed the data analysis. K. M. Dunseath, M. Terao Dunseath and A. Cyr are responsible for the R-matrix and R-Matrix Floquet calculations for O^-. I wrote the corresponding papers

- The experimental work detailed in chapter 3 was performed by myself and X. Urbain, based on earlier work by M. Brouri and X. Urbain. A. P. O'Connor designed the data acquisition system. K. M. Dunseath and M. Terao Dunseath ran the R-matrix and DVR calculations. I performed the R-Matrix Floquet calculation, developed and ran codes for effective Hamiltonian and Quantum Defect theory calculations. I wrote the corresponding articles.

- The metastable helium source presented in chapter 4 was assembled by myself and X. Urbain. Electron impact ionization experiments were performed by myself, X. Urbain and J. J. Jureta. The work also benefited from the contribution of P. Defrance. I wrote the corresponding article.

Chapter 2

Photodetachment of H^- and O^-

2.1 State of the art

Past achievements concerning the photodetachment of the hydrogen and oxygen anions are presented in this chapter. Results on the total photodetachment cross section of H^- by infrared and visible light are first presented. The second section is dedicated to literature on the total, partial and differential photodetachment cross sections of O^-, for photon energies ranging from the infrared to the ultraviolet.

2.1.1 Hydrogen anion

The negative hydrogen ion H^- is one of the simplest quantum-mechanical three-body systems found in the study of atoms and ions. Its prototypical character has attracted numerous studies since the early days of quantum mechanics [2], further motivated by its abundance in the planetary and stellar atmospheres and its wide use in accelerators. Of particular interest is its photodetachment, where electron correlations in that weakly bound system play an important role and yield a behavior differing from that of neutral atoms.

Since the early studies of, *e.g.* , Bates and Massey [83] and Chandrasekar [84], theory has made significant progresses. Over the years, a number of calculations of the photodetachment cross section have been performed reaching, overall, good agreement, *e.g.* , $3.5 - 3.6 \times 10^{-21}$ m^2 at 1064 nm [47, 85–93], except for a few studies [94–96].

On the experimental side, however, fewer studies have been performed, owing to the challenges such an experiment raises. The absolute integrated cross section was first measured by Branscomb and Smith [97] in the mid-fifties, shortly followed by the measurement of the

relative cross section by Smith and Burch [98]. Popp and Kruse [99] later performed an absolute measurement with a low current hydrogen arc. The first laser studies arose with the need to diagnose controlled fusion plasmas, and confirmed the order of magnitude of the cross section [100, 101]. Recently, Vandevraye *et al.* [72] carried out a new measurement at the Nd:YAG laser wavelength, 1064 nm. Their result, $4.5(6)\times10^{-21}$ m^2, lies 1.5 σ above the value of $3.5 - 3.6 \times 10^{-21}$ m^2 obtained by most theoretical studies. This discrepancy calls for further investigation to be carried out, as this cross section is a commonly used benchmark for atomic theories and numerical methods [102].

2.1.2 Oxygen anion

The one-photon detachment total cross section of the oxygen negative ion $O^-(1s^2 2s^2 2p^5\ ^2P^o)$ between the ground state $O(1s^2 2s^2 2p^4\ ^3P)$ and first excited state $O(1s^2 2s^2 2p^4\ ^1D)$ thresholds was first investigated some sixty years ago by Branscomb and Smith [97] and then by Branscomb *et al.* [49]. A third, absolute measurement by Smith [98] provided slightly different cross sections, while the relative measurement of Branscomb *et al.* [80] extended the photon energy range. Two later independent absolute measurements [73, 103], albeit over a limited energy range, confirmed the values of [80, 98]. These were thus considered as a reference and have since been used to normalize relative photodetachment cross sections for other ions such as C^-, B^- and O_2^- [104–107]. The determination of photodetachment cross sections for the open-shell O^- ion remains a challenging task for theories, as electron correlations and polarization effects play an important role. A number of attempts over the past few decades (see [108] and references therein) yielded results that vary widely and do not match the experimental data, neither in magnitude nor in shape. The values of the latest and most extensive calculation [108] lie significantly higher than those of [80, 98]. The pronounced disagreement between theory and experiment and the use of the latter for normalizing other quantities calls for further investigation.

The total cross section above the first excited state threshold (^{1}D), where a steep rise is expected due to the threshold opening, has only been measured by Branscomb *et al.* [80]. Again, pronounced disagreements exist between theory and experiment, and also between different theoretical calculations [108–111]. Such a photon energy range (> 3.5 eV) is harder to reach from an experimental standpoint since tunable UV laser sources are in general rarer and of increased complexity.

The partial cross sections $\sigma_{^3\mathrm{P}}$ and $\sigma_{^1\mathrm{D}}$ for leaving the oxygen atom in its ground and first excited states are seldom encountered in the

literature and the lack of experimental data may be attributed to challenges associated with the need for final-state selectivity and tunable UV laser sources. With the noticeable exception of the work by Domesle *et al.* [112], which provides branching ratios and asymmetry parameters for a photon energy of 4.66 eV, work above the $O(^1D)$ threshold is only theoretical [110, 113–115].

The differential cross section $d\sigma/d\Omega$ into a particular final state can be described, as explained in Sec. 1.4, by an asymmetry parameter β which conveniently reduces the former vectorial quantity to a single scalar value, thereby simplifying representation and discussion. The behavior of the asymmetry parameter for increasing photoelectron energies was studied by Cooper and Zare [57] and resulted in the well-known homonymous formula. They demonstrated the presence of a broad interference effect between the outgoing s and d partial waves which manifests itself by a strongly asymmetrical emission, perpendicular to the laser polarization, at intermediate electron energies. This effect has been confirmed by all subsequent experiments [76, 77, 116]. In stark contrast with the total cross section, agreement is excellent between theory and experiment in the photon energy range covered by the experiments (1.46 – 2.7 eV) [57, 76–78, 116–119]. Data above the $O(^1D)$ threshold is limited to the work of Domesle *et al.* [112] and no theoretical results is available in the literature.

When the photon energy is tuned below the electron affinity, detachment is only possible by absorption of 2 or more photons. The two-photon detachment of O^- has not been widely studied and the agreement between the few results available is not particularly good. The only existing experiment gives a generalized cross section of $\left(4.2\,^{+1.9}_{-1.6}\right) \times 10^{-58}\,\mathrm{m}^4\,\mathrm{s}$ at a wavelength of 1064 nm [120]. An early calculation based on perturbation theory and a one-electron model potential [109] yields, after interpolation, a value of $1.8 \times 10^{-57}\,\mathrm{m}^4\,\mathrm{s}$, which is more than four times larger. The results obtained using an adiabatic theory [121] are almost an order of magnitude larger than experiment. Clearly, there is room for improvement.

2.2 Experimental techniques

2.2.1 Animated-crossed-beam technique

The aim of the present section is to develop a method for measuring absolute total photodetachment cross sections σ with a crossed beams experiment. In such an experiment, a fast ion beam is crossed at right angle by a laser beam and the neutral atoms produced by photodetach-

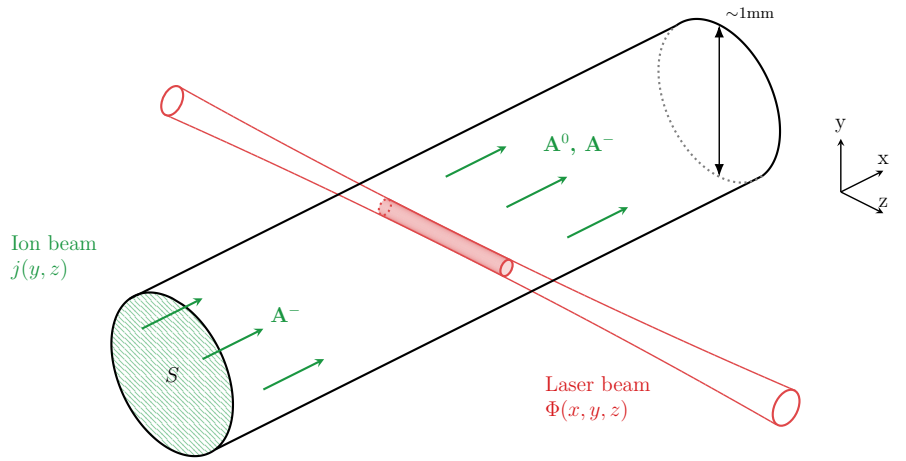

Figure 2.1: *Crossed beam configuration where the laser beam (red) intersects the ion beam at right angle. The interaction volume is the shaded red region.*

ment are counted downstream. The anion current and laser power are measured for normalization purposes and the cross section can be, in principle, determined. However photodetachment occurs over a certain interaction volume, defined by the overlap between the ion and laser beams and shown in Fig. 2.1, which needs to be determined to account for volume averaging effects. In most experiments, σ can be obtained only by assuming a certain profile for the beams. A Gaussian profile is usually assumed for the laser beam while the anion beam profile is in general supposed uniform. The temporal profile of the laser pulses, if any, must also be included. While these assumptions are in general justified, they might not be suitable for measuring absolute cross sections, for which every possible source of error must be tracked down and minimized in order to ensure the accuracy of the measurement.

Continous ion and laser beams

One way to overcome this problem is the so-called animated-crossed-beam technique (ACBT), originally developed for electron-ion collisions by Brouillard and Defrance [79, 122] and later adapted to laser-ion interaction (see Blangé *et al.* [123]). The underlying idea is simple: instead of using two crossed *static* beams, one of the beams is *moved* across the other. The dependence of the cross section on the profiles of the two beams is then "erased" by integrating the signal over the beam displacement, leaving only integrated quantities to be measured. Let us start

from the detachment rate p,

$$p(x, y, z) = \sigma\, \Phi(x, y, z), \tag{2.1}$$

where σ is the detachment cross section and Φ is the photon flux at position (x, y, z) in the reference defined in Fig. 2.1. We assume that anions are traveling along the x-axis at a constant velocity v, hence the time coordinate t is related the x coordinate by x/v. The cumulated detachment probability P obeys the following differential equation,

$$\frac{\mathrm{d}P(x, y, z)}{\mathrm{d}x} = \frac{p(x, y, z)}{v} \left[1 - P(x, y, z)\right]. \tag{2.2}$$

Solving the above equation with appropriate boundary conditions and taking the limit $x \to \infty$, one readily obtains the final detachment probability P_f, given by

$$P_f(y, z) = 1 - \exp\left(-\int_{-\infty}^{+\infty} \sigma\ \Phi(x, y, z) \frac{dx}{v}\right). \tag{2.3}$$

The origin of the reference frame is the center of the laser waist, *i.e.* , the point of maximum intensity.

Let us consider the linear regime of photodetachment, *i.e.* , reasonably low laser intensities, for which the argument of the exponential in the above equation is small. In this case, the exponential can be expanded around the origin in terms of a power series and, by keeping only the two first terms of the series ($\mathrm{e}^{-x} \simeq 1 - x$), we obtain a linear relation between the final detachment probability and the cross section,

$$P_f(y, z) \simeq \sigma \int\ \Phi(x, y, z) \frac{dx}{v}. \tag{2.4}$$

The counting rate N of the detector is the detachment probability, averaged over the atomic beam section S and weighted by the neutral atom detection efficiency η,

$$N \simeq \sigma\eta \iint_S \frac{j(y, z)}{e}\ dy\ dz \int \Phi(x, y, z) \frac{dx}{v}, \tag{2.5}$$

where $j(y, z)$ is the local ion current density at a given position (y, z) on the beam section, and e is the elementary charge. This formula is valid for beams intersecting at right angle.

The variable measured in the experiment is the counting rate $N(Y)$ as a function of the vertical displacement Y of the laser beam. The photon flux must thus read $\Phi(x, y - Y, z)$. Integration over Y then yields

$$\int N(Y)\ dY \simeq \frac{\sigma}{e}\frac{\eta}{v} \iint_S j(y,z)\ dydz \times \iint \Phi(x, y-Y, z)\ dxdY. \tag{2.6}$$

The photon flux Φ is the ratio of the laser intensity to the photon energy $\hbar\omega$, hence the second integral on the right-hand side is nothing else than the laser power P_{laser} divided by $\hbar\omega$, which is independent of z. Thus only $j(y,z)$ depends on the spatial coordinates and its integration over the ion beam section is simply the anion current I_{ion}. We obtain the following expression for the photodetachment cross section:

$$\sigma \simeq \frac{1}{\eta}\frac{\hbar\omega}{P_{\text{laser}}}\frac{e\ v}{I_{\text{ion}}}\int N(Y)\ dY, \tag{2.7}$$

where the numerical integration over the discrete experimental signal is performed using Simpson's rule.

The sole assumption of a linear photodetachment regime, yielding the above formula, is much less stringent than that of a Gaussian laser beam and a uniform atomic beam. By integrating the signal, we can express the cross section in terms of a simple set of easily measurable quantities. This highlights the ease of implementation and robustness of the animated-crossed-beam technique method, which does not require the laser and ion beam profiles to be fully characterized (*e.g.* M^2 factor, inhomogeneity).

In practice, the laser beam is vertically displaced by a tilted glass plate, as shown in Fig. 2.2. The detachment rate is measured at different tilt angles and the corresponding vertical spacing ΔY can in principle be determined by application of the Snell-Descartes law of refraction. We verified that this is indeed the case by passing a razor blade, mounted on a high-accuracy translation stage, across the laser beam at a distance after the glass plate corresponding to the position of the ion beam. By recording the transmitted power as a function of the blade position, one can recover the vertical position of the beam center. The vertical increment is subsequently obtained by repeating the measurement at different angles of the plate. We also imaged the transverse profile of the laser beam as seen by the anion beam with a beam-profiling camera and recorded its vertical position for a series of tilt angles and for different wavelengths. Both independent measurements validated the use of the Snell-Descartes law. Changes of the refraction index with wavelength are taken into account when computing the vertical displacement from the tilt angle.

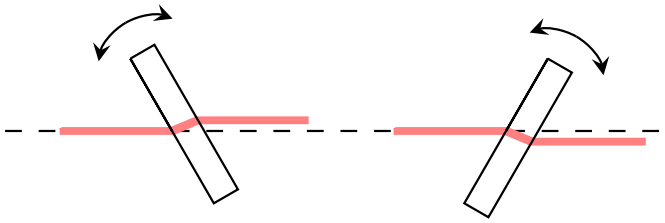

Figure 2.2: *Laser beam passing through a glass plate. Refraction within the plate displaces the beam along the vertical axis.*

Pulsed ion and laser beams

In the previous section, we considered the case of continuous laser and ion beams, whose fluxes do not depend on time. However, pulsed laser systems are ubiquitous in atomic and molecular physics. Pulsed ion beams are also frequent, *e.g.* , when using a pulsed supersonic expansion or when buffer-gas cooling is applied prior to the interaction with the laser beam. The present section shows how the ACBT equations can be modified in order to account for such situations.

The time-dependence of the two pulsed beams prompts the introduction of two time coordinates for the ions: (i) the coordinate t, relative to the beginning of the ion burst; (ii) the coordinate τ, relative to the center of the laser pulse envelope. The delay T between the beginning of the ion burst ($t = 0$) and the center of the laser pulse envelope ($\tau = 0$) is an experimental parameter and in principle can be adjusted at will. The coordinates t and τ are related through $\tau = t - T$.

The yield $N(Y,T)$ of neutrals now depends on the delay T and equation (2.5) must be modified accordingly:

$$\begin{aligned} N(Y,T) &= \frac{\eta\sigma}{\mathrm{e}\ v} \int dt \iint_S dy\, dz\, j(y,z,t) \\ &\qquad \int_{-\infty}^{+\infty} dx\, \Phi\left(x, y-Y, z, t-T+\frac{x}{v}\right). \end{aligned} \tag{2.8}$$

By integrating both sides of (2.8) over Y and T, we obtain an expression similar to (2.6),

$$\begin{aligned} &\iint dY\, dT\, N(Y,T) = \frac{\sigma}{e}\frac{\eta}{v} \times \\ &\int dt \iint_S dy\, dz\, j(y,z,t) \iiint_{-\infty}^{+\infty} dT\, dY\, dx\, \Phi\left(x, y-Y, z, t-T+\frac{x}{v}\right). \end{aligned} \tag{2.9}$$

The integral of the photon flux Φ over T, Y and x reduces to the number of photons per pulse, *i.e.* the laser pulse energy E_{laser} divided by the photon energy $\hbar\omega$. The integral of the current density j over t, y, and z is the number of ions per pulse multiplied by the elementary charge, eN_{ion}. Therefore equation (2.9) becomes:

$$\sigma = \frac{v}{\eta}\left[\iint dT\, dY\, N(Y,T)\right]\frac{\hbar\omega}{N_{\text{ion}}E_{\text{laser}}}. \tag{2.10}$$

In the case where only one of the beams is pulsed, *e.g.* , the laser beam, the time delay T is to be removed from the above formulas and $j(y,z)$ is time-independent. The remaining time integration in Eq. (2.9) runs over the photon flux and, along with the integrals over x and Y, yields the laser pulse energy divided by $\hbar\omega$. The cross section is thus given by

$$\sigma = \frac{v}{\eta}\left[\iint dY\, N(Y)\right]\frac{e\hbar\omega}{I_{\text{ion}}E_{\text{laser}}}. \tag{2.11}$$

The ACBT can therefore accommodate the use of continuous beams, pulsed beams and a combination thereof. If both beams are pulsed, it comes at the expense of an additional scan of the delay between the ion and laser pulses.

2.2.2 Multiphoton extension

The ACBT developed above deals with one-photon detachment, for which the detachment rate is proportional to the photon flux. However, it cannot be straightforwardly applied to multiphoton processes, as we shall see below. Extension of standard ACBT into the multiphoton regime is nonetheless possible using inverse problem theory, and at the price of a few additional and reasonable assumptions.

ACBT breakdown

In the case of non-resonant multiphoton processes, the detachment rate p is the product of the generalized n-photon detachment cross section $\sigma^{(n)}$ with the n-th power of the photon flux Φ:

$$p(x,y,z,\tau) = \sigma^{(n)}\Phi^n\left(x,y,z,\tau+\frac{x}{v}\right), \tag{2.12}$$

where the coordinates (x,y,z) are as defined in Fig. 2.1 and the time $\tau = 0$ corresponds to the maximum of the laser pulse envelope. As before, v is the ion velocity. We consider in the following a continuous ion beam and a pulsed laser beam, the latter being typical of multiphoton experiments as the light intensities required are higher than for 1-photon

processes. The final detachment probability $P(y,z,\tau)$, after the ion has travelled through the laser spot, is given by

$$P(y,z,\tau) = 1 - \exp\left[-\frac{1}{v}\int_{-\infty}^{+\infty} dx\; p(x,y,z,\tau)\right]. \qquad (2.13)$$

As for the one-photon ACBT, we assume that the photon flux is sufficiently low for n-photon detachment to occur in the perturbative regime. Following the same steps as in Sec. 2.2.1, one can obtain an expression for the cross section,

$$\begin{aligned}\sigma^{(n)} = {} & \frac{\mathrm{e}\, v}{\eta}\left[\int dY N(Y)\right] & (2.14)\\ & \times\left[\iint_S dy\, dz\, j(y,z) \iiint_{-\infty}^{+\infty} d\tau\, dY\, dx\, \Phi^n\left(x, y-Y, z, \tau + \frac{x}{v}\right)\right]^{-1}. &\end{aligned}$$

In the multiphoton case ($n \geq 2$) the integral of Φ^n over τ, Y and x appearing in Eq. (2.14) does not reduce to the n-th power of the number of photons per pulse and the cross section cannot be recovered as straightforwardly as in the standard ACBT. In the next subsection, we present two alternative methods for expressing the cross section in terms of accurately measurable quantities by introducing a small set of reasonable assumptions listed below.

First, in the experiment we performed, the confocal parameter of the laser beam (twice the Rayleigh length) is about 2 cm, 20 times larger than the width of the ion beam along the z-axis. Therefore the variations of the photon flux along z are negligible in the region where photodetachment occurs. Second, it is reasonable to assume that $\Phi(x,y,z,\tau)$ can be factorized into a temporal envelope $g(\tau)$ and a spatial profile $\phi(x,y)$ which, as just explained, does not depend on z,

$$\Phi(x,y,z,\tau) \simeq \phi(x,y)g(\tau). \qquad (2.15)$$

Finally, we define $\rho_y(y)$ as the normalized projection of the current density $j(y,z)$ onto the y-axis,

$$\int dz\, j(y,z) = I_{\text{ion}}\, \rho_y(y), \qquad (2.16)$$

where I_{ion} is the ion beam current.

With the above assumptions, Eq. (2.8) for the yield $N(Y)$ can be

written, in the case of a continuous ion beam, as

$$N(Y) = \frac{\eta\sigma^{(n)}}{\mathrm{e}\ v}\Delta^{(n)} I_{\mathrm{ion}} \times \int dy\ \rho_y(y) \int_{-\infty}^{\infty} dx\, \phi^n\left(x, y - Y\right), \tag{2.17}$$

where $\Delta^{(n)}$ is the integral of the n-th power of the time profile of the laser pulse,

$$\Delta^{(n)} = \int_{-\infty}^{+\infty} d\tau\, g^n(\tau + x/v) = \int_{-\infty}^{+\infty} d\tau\, g^n(\tau). \tag{2.18}$$

Generalized two-photon cross sections

We present two alternative methods for expressing the generalized two-photon cross section ($n = 2$ in Eq. 2.17) in terms of precisely measurable quantities. Generalization of these methods to higher numbers of photons ($n \geq 3$) is straightforward.

The first and simplest approach is to approximate the spatial distribution of the photon flux by a Gaussian,

$$\phi(x, y) = \frac{1}{\hbar\omega}\frac{2E_{\mathrm{laser}}}{\pi w_0^2 \Delta} e^{-2(x^2+y^2)/w_0^2}, \tag{2.19}$$

where w_0 is the laser waist and $\Delta = \int d\tau\, g(\tau)$. The choice of a Gaussian distribution is justified by the fact that our pulsed laser operates near the TEM00 mode. The integral of the square of the photon flux can now be evaluated analytically and the generalized two-photon cross section is thus given by

$$\sigma^{(2)} = \frac{\mathrm{e}v}{\eta I_{\mathrm{ion}}}\left(\frac{\hbar\omega}{E_{\mathrm{laser}}}\right)^2 \frac{\Delta^2}{\Delta^{(2)}}\, \pi w_0^2 \int N(Y) dY. \tag{2.20}$$

Note that we have made no assumptions about the shape of the ion beam.

The second method for expressing the integral of ϕ^2, present in Eq. (2.17), in terms of easily measurable quantities and without modeling the shape of the laser beam exploits the fact that the transit of the ions through the laser focus amounts to a tomography of the intensity profile, as shown in Fig. 2.3.

Let us first define a succession $\mathcal{A}$ of integral transforms, which transforms a function $f(x, y)$ into a function $F(Y)$ as follows:

$$F(Y) = \mathcal{A}[f(x, y)] = \int dy \rho_y(y) \int_{-\infty}^{+\infty} dx\, f(x, y - Y). \tag{2.21}$$

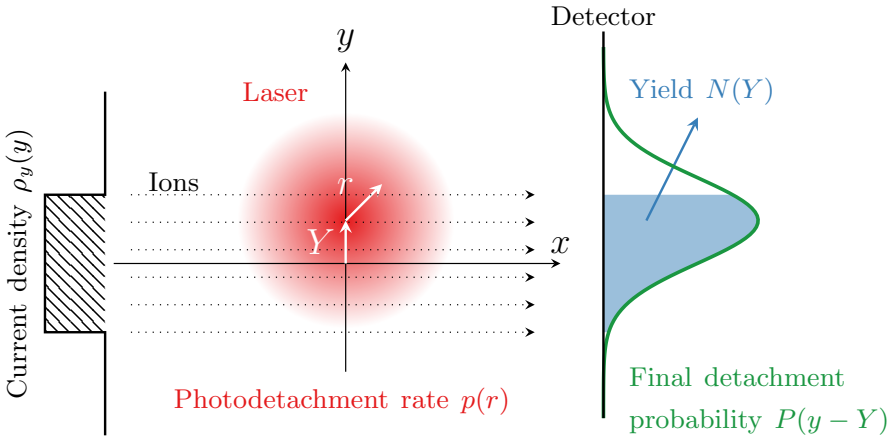

Figure 2.3: *Idealized representation of the experiment. The detachment rate, proportional to the square of the photon flux, is integrated along the ion trajectory (dotted lines) to obtain the final detachment probability (thick curve), as in (2.13). The latter is subsequently convolved with the normalized projection ρ_y of the current density onto the y-axis (hatched area) to obtain the yield N (shaded area) defined in (2.17).*

Equation (2.17) with $n = 2$ can then be rewritten as

$$N(Y) = \frac{\eta\sigma^{(2)}}{\mathrm{e}\ v}\Delta^{(2)} I_{\mathrm{ion}}\, \mathcal{A}[\phi^2(x,y)]. \tag{2.22}$$

It is reasonable to assume that ϕ is symmetric under rotation around the light propagation axis z as our laser operates near the TEM00 mode. The integral over the line of sight x can then be interpreted as the Abel transform of the detachment probability $p = \sigma^{(2)}\phi^2$ [124]. The standard definition of the transform appears immediately when re-writing the integral in cylindrical coordinates,

$$\begin{aligned} N(Y) =& \frac{\eta}{\mathrm{e}\ v}\Delta^{(2)} I_{\mathrm{ion}} \\ &\times 2\int dy \rho_y(y) \int_{y-Y}^{+\infty} dr \frac{r\ p(r)}{\sqrt{r^2-(y-Y)^2}}. \end{aligned} \tag{2.23}$$

The path integral of an atom travelling in a straight line through the laser spot corresponds to the Abel transform $P(y-Y)$ of the detachment rate $p(r)$ at a vertical position $y-Y$. The convolution with the normalized current density $\rho_y(y)$ in the second integral subsequently "blurs" the transform $P(y-Y)$, similar to the point-spread function of an imaging device [125]. It is possible to recover $p(r)$ from the measured yield

$N(Y)$ by numerically inverting the two integral transforms using one of the techniques from the extensive range available [126].

The comparison of ρ_y with a point-spread function highlights the importance of the respective sizes of the ion and laser beams. If the laser beam is much narrower than the ion beam, the blurring effect becomes too strong to recover the final detachment probability. The radius of the ion beam along the vertical direction must be kept of the order of or smaller than the waist of the laser beam. To do so, an aperture of 100 μm in height was used to define the ion beam, matching the $\sim$ 120 μm diameter of the laser spot.

Although an analytical formula can be obtained for inverting $\mathcal{A}$, it is in practice cumbersome and involves derivatives of the measured signal. A more efficient method for performing the Abel inversion consists in expanding the measured yield in a basis of functions ψ_m spanning the "detection" space,

$$N(Y) = \sum_{m=1}^{m_{\max}} c_m \psi_m(Y), \tag{2.24}$$

and the detachment rate in a basis of functions φ_m spanning the "detachment" space,

$$p(r) = A \sum_{m=1}^{m_{\max}} c_m \varphi_m(r), \tag{2.25}$$

where A is a constant. The two basis sets are related through

$$\psi_m(Y) = 2 \int dy \rho_y(y) \int_{y-Y}^{+\infty} dr \frac{r\varphi_m(r)}{\sqrt{r^2 - (y-Y)^2}}. \tag{2.26}$$

Comparing equations (2.26) and (2.23) gives

$$A = \frac{\mathrm{e}\ v}{\eta \Delta^{(2)} I_{\mathrm{ion}}}. \tag{2.27}$$

Since the pulsed laser used for the present study operates near the TEM00 mode, a basis of Gaussian functions with varying widths is appropriate:

$$\varphi_m(r) = \mathrm{e}^{-r^2/[a+(m-1)b]^2}. \tag{2.28}$$

The parameters a and b and the number $m_{\max}$ of functions define the interval spanned by the widths of the functions and their density. They are chosen so that the estimated width of the laser beam lies close to the center of this interval and that the upper and lower limits lie sufficiently far away.

The functions ψ_m are then computed from φ_m using (2.26). The Abel transform of a Gaussian function is another Gaussian function [124]. If

ρ_y is analytical and well-behaved, the convolution by ρ_y can be derived analytically, otherwise it must be performed numerically. This is for example the case when ρ_y is provided as a set of experimental data. The ion beam in the experiment is well collimated so that we can assume that ρ_y is a uniform distribution. Therefore, the basis functions ψ_m can be expressed as the difference of two error functions,

$$\psi_m(Y) = \frac{\pi w_m^2}{2L}\left[\mathrm{erf}\left(\frac{Y+L/2}{w_m}\right) - \mathrm{erf}\left(\frac{Y-L/2}{w_m}\right)\right], \tag{2.29}$$

with $w_m = a + (m-1)b$ and where L is the width of the ion beam along the y-axis. Since in practice N is measured for a discrete set of vertical displacements $(Y_1, \ldots, Y_k)$, expansion (2.24) is written as

$$\mathbf{N} = \mathbf{C}\Psi, \tag{2.30}$$

where $\mathbf{N}$ is the row vector of data, $\mathbf{C}$ is the row vector of unknown coefficients $(c_1, \ldots, c_{m_{\max}})$ and Ψ is the matrix with elements $\Psi_{ij} = \psi_i(Y_j)$. The problem of finding the coefficients $\mathbf{C}$ in (2.30) is in general underdetermined as the number $m_{\max}$ of basis functions is larger than the number k of data. An approximate solution to (2.30) is found by using the non-negative least-square (NNLS) algorithm [127, 128]. The NNLS result was further checked using a Tikhonov regularization [129], whose free, smoothing parameter q was chosen at the maximum curvature of the L-curve [130]. After the coefficients $\mathbf{C}$ have been found, the expansions of both $N(Y)$ and $p(r)$ are known.

Integrating the photon flux over polar coordinates and over the pulse duration, we obtain

$$2\pi\Delta \int dr\ r\ \phi(r) = \frac{E_{\mathrm{laser}}}{\hbar\omega}. \tag{2.31}$$

Substituting $\phi(r) = \sqrt{p(r)/\sigma^{(2)}}$ in (2.31), squaring both members and rearranging, we finally obtain the expression of the generalized two-photon cross section in terms of known quantities:

$$\begin{aligned}\sigma^{(2)} =& \frac{\mathrm{e}\ v}{\eta\ I_{\mathrm{ion}}}\left(\frac{\hbar\omega}{E_{\mathrm{laser}}}\right)^2 \frac{\Delta^2}{\Delta^{(2)}} \\ & \times 4\pi^2 \left(\int dr\ r\sqrt{\sum c_m \varphi_m(r)}\right)^2.\end{aligned} \tag{2.32}$$

The measured signal $N(Y)$ is included in this expression through the coefficients c_m. All other factors can be measured precisely and only

reasonable assumptions concerning the ion and laser beams are necessary.

Let us finally note that the generalization of the ACBT was derived above for the case of a continuous ion beam and a pulsed laser beam, but it is in principle applicable when both beams are pulsed.

2.2.3 Velocity map imaging

The present section introduces the velocity map imaging (VMI) technique. We also present the procedure used to extract the *relative* partial and differential cross sections of the photodetachment of O^- from VMI images. The technique finds its origin in the development of photoelectron and photoion imaging experiments, which aimed at recording the 3D velocity distributions of particles emitted, *e.g.* , upon photoionization or photodissociation. Such imaging experiments relied on (i) the extraction of the charged fragments by a static electric field, which are then sent onto a 2D position sensitive detector (PSD) typically consisting in a stack of multichannel plates, a phosphor screen and a camera; (ii) the reconstruction of the 3D distribution from the 2D image following kinematical considerations and numerical inverse transform techniques [131]. However, the energy and angular resolution of these early experiments were strongly limited by the interaction volume, since particles emitted at different locations but with the same velocity vector would hit the detector at different positions, consequently blurring the image.

The VMI technique, first developed by Eppink and Parker [132] in 1997, came as an important breakthrough in imaging experiments since it proved to be, to a large extent, volume-independent and did not require the use of grid electrodes which lower transmission and may alter the particles' trajectories. The VMI setup, schematically shown in Fig. 2.4, relies on the use of an electrostatic "immersion" lens and a position sensitive detector placed at its back focal length. As is standard in Fourier optics and within the paraxial approximation [125], if the charged fragments are emitted in the front focal plane, their Fourier transform will be formed on the back focal plane, hence the PSD will image the particles' *momentum*-space distribution. Conveniently, this property is robust against small displacements of the emission point from the exact focal length, yielding the approximate interaction-volume independence of VMI. The images recorded with the position sensitive detector are, as for other imaging techniques, the 2D projection of the initial 3D velocity distribution[1]. The initial distribution is then recon-

[1]The velocity distribution for a given fragment is usually called a *Newton sphere*

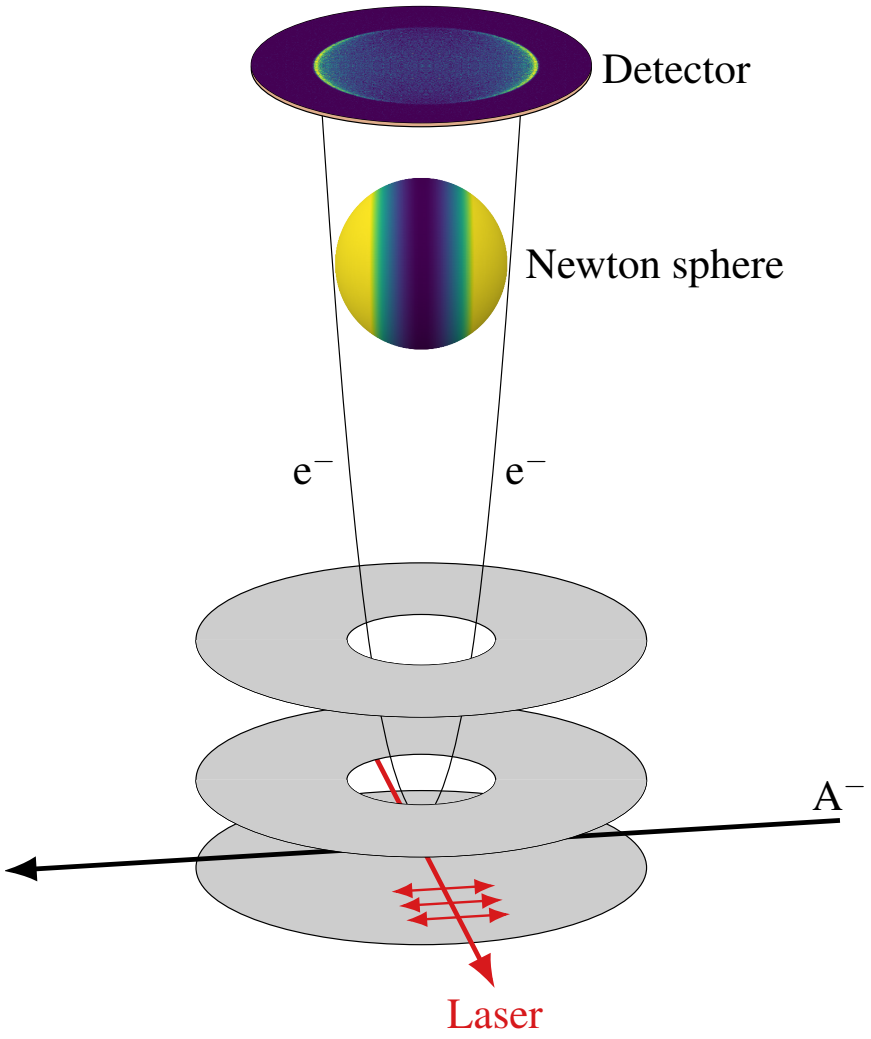

Figure 2.4: *Schematic operation of a VMI system. The stack of electrodes (gray plates) is the VMI electrostatic lens. A beam of anion A^- is intersected, at the lens focal point, by a laser beam. Photoelectrons e^- are emitted, extracted from the interaction region and accelerated onto the position sensitive detector. The laser polarization, indicated by the arrows, is horizontal in order to ensure cylindrical symmetry of the Newton sphere about an axis parallel to the plane of the detector. The image on the PSD was measured for the photodetachment of O^-. The position of photoelectron impacts on the PSD is the forward Abel transform (projection) of their initial 3D velocity distribution, represented by the Newton sphere.*

structed from the recorded image by means of inverse Abel transformation, provided the former possesses cylindrical symmetry.

Further advantages of VMI systems lie in their 4π collection efficiency, in their capability of imaging the complete Newton spheres of all fragment types in a single experiment, thereby significantly reducing acquisition times, and, last but not least, in their relative simplicity concerning building and implementation. Literature on velocity map imaging is abundant and a good introduction by Eppink and Parker can be found in [126].

We have used VMI to perform photoelectron spectrometry of the photodetachment of O^- and determine both branching ratios between the various final states of the oxygen atom, related to partial cross sections, and 3D angular distributions, related to differential cross sections. Details of the experimental VMI setup are presented in Sec. 2.3.2. Once velocity map images are recorded with the PSD, they are processed in order to recover the desired quantities. Details of the analysis procedure are presented below, after a description of the main features of the images and their physical meaning.

The raw images measured with the present setup show an arrangement of concentric discs with bright edges (see Fig. 2.5) corresponding to the 2D projections of the sumperimposed Newton spheres of the various fragments. In the present case, these fragments are photoelectrons that leave the oxygen atom into its different final states. The radius R of each disc is proportional to the photoelectron velocity v, that is,

$$v = \alpha R, \tag{2.33}$$

and the proportionality constant α is an experimental parameter to be determined. The angular distribution of electron impacts across the discs is reminiscent of the photoelectron angular distribution. Since we use a fast O^- beam, the center of the discs is shifted with respect to the center of the detector by the ion velocity, thus preventing to use the full size of the detector. Given the anions velocity of 2.5×10^5 m/s, the shift is of the order of 1/4 of the distribution's radius for 4 eV photoelectrons, and reaches a value close to the distribution's diameter for threshold electrons. The raw image is slightly distorted, an effect we tentatively ascribe to imperfect magnetic shielding of the spectrometer and small inhomogeneities of the electric potential inside the detachment region. If the Abel transform is performed on the raw image, the lack of circularity strongly degrades the energy and angular resolution. The image must therefore be circularized prior to Abel inversion.

The circularization procedure is based on the idea of Cavanagh *et*

al. [78]. It consists in expressing the coordinates of the electron impacts, thereafter termed events, in terms of polar coordinates (r, θ) and scaling r with a scaling function $f(r, \theta)$. Let us start with an illustrative example. If an image is, *e.g.* , a circle of radius a which is distorted into an ellipse with semi major axis a and semi minor axis b, the radius depends on θ as

$$r(\theta) = \sqrt{\frac{a^2 b^2}{b^2 \cos^2\theta + a^2 \sin^2\theta}}. \tag{2.34}$$

In order to retrieve the circle, all r coordinates must therefore be scaled by

$$f(\theta) = a/r(\theta). \tag{2.35}$$

The scaling function $f(\theta)$ does not depend on r for this specific case, but does so in the general one.

In order to determine the scaling function for real images, we track the radial position r_e of the bright outer edge of a disc, corresponding to a given Newton sphere, for all angles θ. In practice, we obtain a set of radial positions $r_e(\theta_i)$ by fitting the radial distribution of events contained within consecutive angular slices $[\theta_i, \theta_{i+1}]$ with the Abel transform of a Gaussian function whose widths and centers are fit parameters. The discrete scaling function is then given by

$$f_e(\theta_i) = \bar{r_e}/r_e(\theta_i), \tag{2.36}$$

where $\bar{r_e}$ is the average of all $r_e(\theta_i)$ values. In the case where several Newton spheres coexist in the image, we use an ensemble of Gaussian functions to fit the radial distributions and determine the ensemble of radial positions $\boldsymbol{r}_e(\theta_i) = [r_{1e}(\theta_i), r_{2e}(\theta_i), \ldots]$ and the corresponding scaling functions $\boldsymbol{f}_e(\theta_i)$. A continuous scaling function $f(r, \theta)$ is subsequently obtained by interpolation over all θ_i's and over the mean radii $\bar{r_e}$ of all Newton spheres.

It should be noted that radial scaling modifies the local density of events and, in particular, creates artificial angular structures in the image that, after Abel inversion, may yield incorrect values of β parameters. This effect is eliminated by scaling the number of events in each image pixel by $f^2(r, \theta)$, corresponding to the change in area induced by the radial scaling. We verified that the combination of radial scaling and density rescaling yields, indeed, correct β parameters by generating artificial images through random generation of electrons velocities on a

set of Newton spheres with given velocities and β parameters. If distorsion is important, the offset of β due to circularization without density rescaling can be as large as -0.2.

After circularization, the inverse Abel transformation of the processed images is performed using the MEVELER code of Dick [133], which showed good performances in terms of resolution, noise resistance, and excellent behavior even for low numbers of events. It computes the inverse image based on statistical and information criteria and possesses the advantage not to introduce in the analysis more information than is already contained in the raw image, compared to other methods which do so by, *e.g.* , fitting [134].

An example of circularized and inverted images is shown in Fig. 2.5 and was obtained by photodetaching O^- anions at a wavelength of 357.14 nm, where the oxygen atom is left either in its ground (^{3}P) or first excited (^{1}D) state. The left half of the upper image is the circularized image, the right half is the inverted image and the bottom graph is the radial distribution of photoelectrons, corresponding to the integral of the inverted image over all polar angles. Three different electron velocities can be observed, which we can straightforwardly attribute, from left to right, to the transitions from the $J = 3/2$ and $J = 1/2$ fine structure components of O^- to the $^1D_2$ excited state of oxygen and from O^- to the ground ^{3}P state of oxygen. The six different transitions between the fine structure components of O^- and O(^{3}P) are not resolved in this spectrum. The remaining part of the section explains how branching ratios and asymmetry parameters can be extracted from the VMI images, with illustrative examples based on the data presented in Fig. 2.5.

In order to obtain the branching ratios, one needs to compute the intensity of the transitions to the various final atomic states. This is done by fitting each peak in the velocity distribution, labeled by an index i, with a Gaussian function and computing its integral $\mathcal{P}_i$. The branching ratio to a given final state j can then be obtained using

$$R_j = \frac{\mathcal{P}_j}{\sum_i \mathcal{P}_i}. \tag{2.37}$$

The uncertainty on the branching ratio is taken as the 1σ standard deviation computed from the relevant covariance matrix elements calculated during the fitting procedure. For the distribution presented in Fig. 2.5, we obtain for example

$$R_{^3\mathrm{P}} = \frac{\mathcal{P}_{^3\mathrm{P}}}{\mathcal{P}_{^3\mathrm{P}} + \mathcal{P}_{^1\mathrm{D}}} = 0.898 \pm 0.007, \tag{2.38}$$

where $\mathcal{P}_{^1\mathrm{D}}$ is the sum of the areas under both leftmost peaks in the

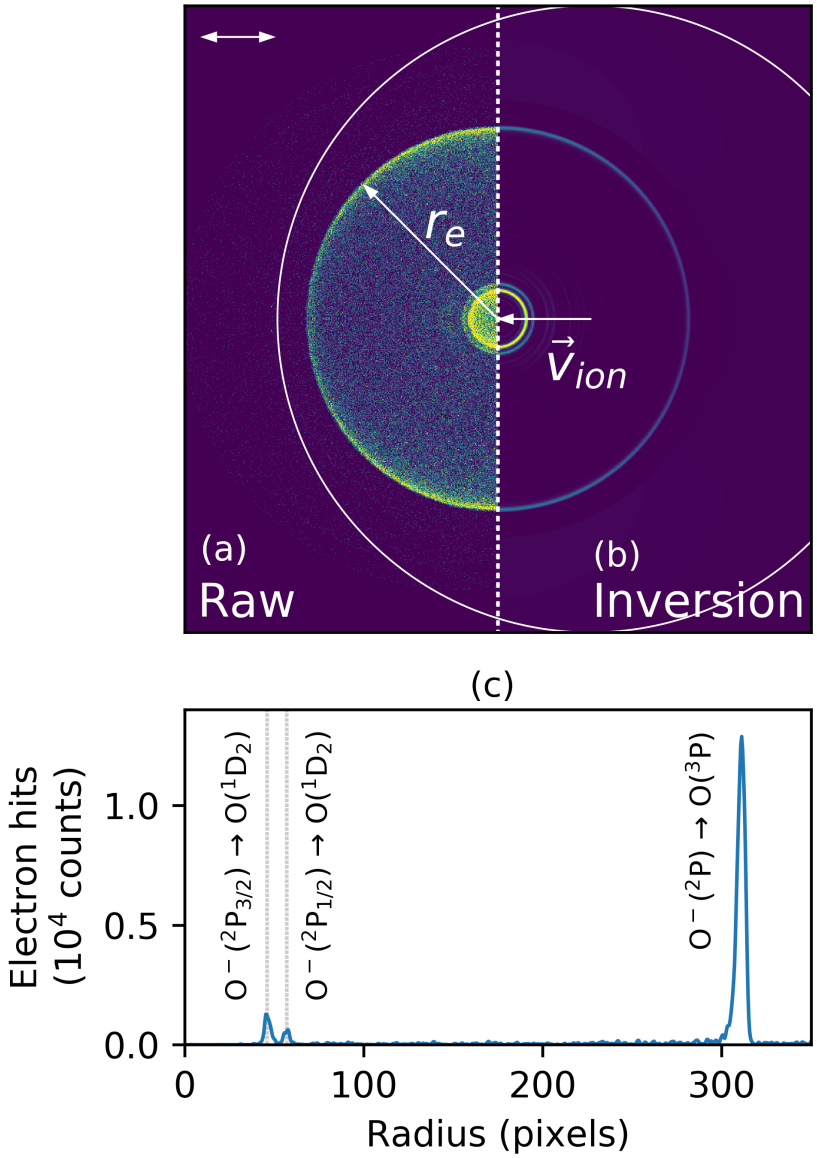

Figure 2.5: *Data for the photodetachment of O^- at $\lambda = 357.14$ nm (3.47 eV). (a) Circularized raw image (1024 × 1024 pixels). (b) inverse-Abel transform image computed with the MEVELER algorithm [133]. The horizontal double arrow indicates the direction of the laser polarization. The white circle indicates the PSD edges. The Newton sphere of radius r_e is shifted with respect to the center of the PSD by the ions' velocity $\vec{v}_{ion}$. (c) Radial distribution of the electrons after Abel inversion.*

velocity distribution, so as to include both fine structure states of the anion.

The asymmetry parameter β for each final state is given by the ratio between the $Q_2(r)$ and $Q_0(r)$ radial distributions calculated by the MEVELER program. $Q_0(r)$ is the total distribution, as shown in the radial spectrum of Fig. 2.5, and $Q_2(r)$, when divided by r^2, represents the contribution of the 2nd-order Legendre polynomial to the angular distribution. In practice, for each peak in the velocity distribution, β is computed using

$$\beta = \frac{\sum_i Q_2(r_i)}{\sum_i Q_0(r_i)}, \tag{2.39}$$

which corresponds to the weighted mean of Q_2/Q_0, with weights given by total velocity distribution, *i.e.*, Q_0. The summations runs over r values around the peak center where $Q_0(r)$ is higher than, typically, 10% of the maximum value. In the cases where noise is important, the peaks in the Q_0 and Q_2 distributions are fitted with functions of the form

$$f(r) = \mathrm{e}^{-(r-a)^2/b^2} \times (cr + d). \tag{2.40}$$

The area under the Gaussian function in the above equation is then used to determine β. The accuracy $\Delta\beta$ on the value of the β parameter is in principle limited by the angular resolution of the detection system, given by $\Delta\theta = 1/r_e$ with r_e being the radius, in pixels, of the Newton sphere on the image. In our setup, $\Delta\theta$ reaches values from, typically, 0.2° to 0.6°. However, the image circularization and the Abel inversion procedures cause further uncertainties and increase $\Delta\beta$ to about 0.05. When the number of background electrons is large, the VMI images are significantly altered and the uncertainty is estimated to reach $\Delta\beta = 0.1$. For the velocity distribution presented in Fig. 2.5, we obtain $\beta_{^3\mathrm{P}} = -0.54 \pm 0.05$ and $\beta_{^1\mathrm{D}} = -0.11 \pm 0.05$.

Although not relevant for the present study, the energy resolution $\Delta E/E$ is of the order of 2% for the largest images and when potentials on the VMI electrodes are carefully optimized. We did not optimize potentials for each repeller voltage, thus resolution fluctuates from 2% to 4% throughout the measurements. It also degrades close to thresholds, where photoelectron velocities are low and images become small. Although the present resolution does not reach the 0.5% resolution of León *et al.* [135], it is considered as satisfactory since the ion beam velocity prevents us from using the full detector size. Enhancing the magnetic shielding and reducing the velocity spread of the ion beam may further enhance the resolution for future studies.

2.3 Experimental setups

2.3.1 Animated-crossed-beam setup

The experimental setup for measuring the total photodetachment cross section of H^- is presented in the following. The setup for studying the photodetachment of O^- is essentially the same and those differences between the two apparatuses, *e.g.* , different laser systems, are described at the end of the section.

Photodetachment of H^-

The first stage of the experimental setup, sketched in Fig. 2.6, comprises a duoplasmatron source providing a 4 keV beam of H^- anions. After mass-selection by a permanent magnet, a set of planar deflectors brings the beam to the interaction region, pumped to high vacuum (3×10^{-8} mbar). Two diaphragms, located on either side of the ion-laser interaction region, define the beam direction. These two diaphragms have further been carefully aligned with the apertures of the quadrupolar deflector and the channel electron multiplier (CEM) cone so that the beam direction and the neutrals detection axis overlap.

The 1 mm H^- beam is illuminated perpendicularly by the light of a CW Ti:sapphire laser pumped by an Ar^+ laser, the latter delivering a maximum output power of 21 W in multiline operation. The Ti:sapphire laser operates at the TEM00 mode and covers the 700-1000 nm wavelength range with an output power of more than 3 W at the center of the range. This range is further extended to 1064 nm by means of a CW diode pumped solid state laser. The light is brought to the vacuum chamber by a set of mirrors and focused by an $f = 40$ cm lens onto the anion beam. A 10 mm thick glass plate mounted on a rotating stage is placed just after the lens. By varying the angle of the plate, the angle of incidence of the laser beam can be varied and its vertical position after the plate can be modified at will, thus "animating" the beam (see Fig. 2.2). The reflectivity of the AR coating on the glass plate changes slightly with the incidence angle, thus changing the transmitted laser power. However, since the laser power is measured *after* the plate, such changes do no affect the measurement.

On the other side of the vacuum chamber, the light is collected by a thermal powermeter measuring the laser power with 3% accuracy. Powers ranging from 0.5 to 2 W are reached in the interaction region throughout the wavelength range covered. A measurement of the laser power before and after the vacuum chamber showed no difference; hence the loss of photon flux due to the exit window of the chamber is contained

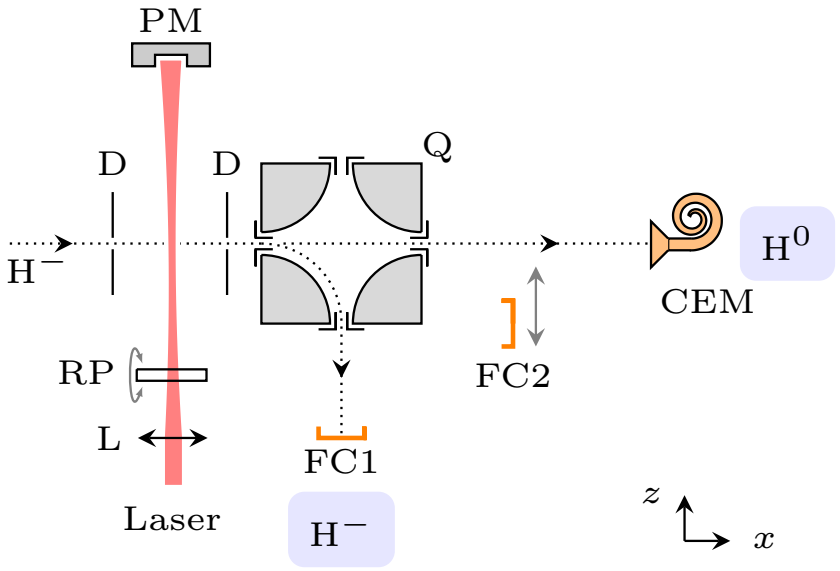

Figure 2.6: *Experimental setup. D: diaphragm; FC: Faraday cup; Q: quadrupolar deflector; CEM: channel electron multiplier; L: lens; RP: rotating fused silica plate; PM: powermeter. The laser beam propagates along the z-direction and its polarization is along the y-axis.*

within the accuracy of the powermeter. This confirms the manufacturer specifications, which give a reflectance of the coated window lower than 0.5% and an absorbance of the order of 0.1% (N-BK7).

After the second aperture, the ion beam enters the detection region. It first passes through a quadrupolar deflector, where negative ions are deflected on one side and collected in a Faraday cup connected to the input of a calibrated electrometer. The neutral hydrogen atoms fly straight through the quadrupole and are detected about 30 cm downstream by a CEM.

Two parameters affect the detection of neutrals by the CEM: the detection efficiency η and the counting rate N. The efficiency is estimated to be 0.98 ± 0.02 according to Naji *et al.* [136], who measured the efficiency of the exact same detector model. Furthermore, test measurements for a 6 keV beam showed no significant increase of the detection efficiency, suggesting that η has reached the asymptotic regime of efficiency versus particle energy, as expected from the CEM specifications. When too high ($\gtrsim$ 50 kHz), the second parameter, the counting rate N, causes a non-negligible deadtime and degrades the pulse height

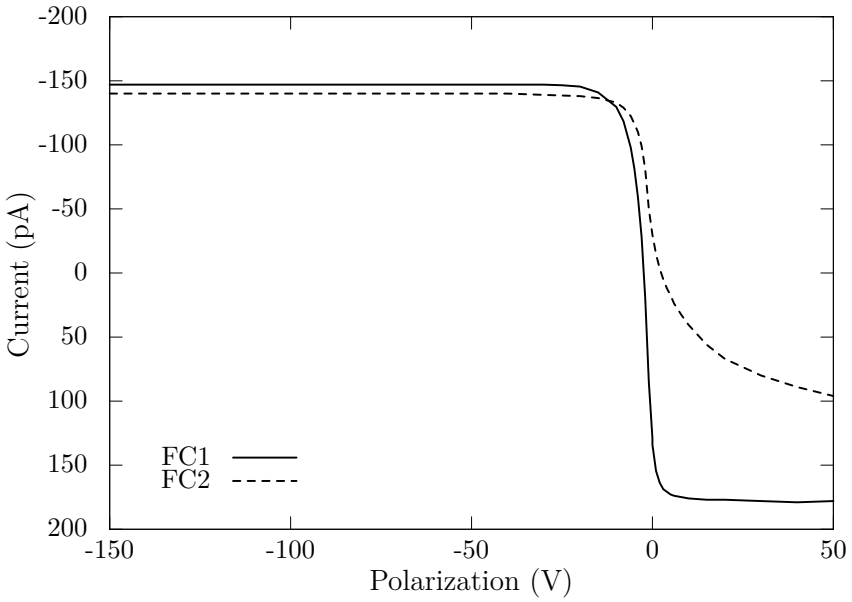

Figure 2.7: *Current (pA) measured by the Faraday cups FC1 and FC2 with respect to the bias voltage (V) applied to the guard electrode of the cup. A bias voltage of -100V is applied to each cup throughout the experiment. The offset at negative voltages is the leakage current on FC1.*

distribution. The main contribution to N comes from the collisional detachment with the residual gas occuring between the first diaphragm and the quadrupole. The ion beam intensity was therefore reduced to $\sim$ 50 pA in order to maintain the counting rate below its maximum threshold. Typical values of 25 kHz are reached in operation.

When the quadrupolar deflector is switched off, a movable Faraday cup (FC2) can be used to collect the negative ions in a straight line aligned with the CEM entrance. The measured current, compared to the current measured in FC1 when the quadrupole is on, gives an accurate estimation of the alignment between the beam and detection axes. When the agreement between the two currents measured is reached, the axes overlap and we therefore ensure that no photodetached hydrogen atom misses the detector, *i.e.* , that the normalization of the counting rate to the H^- current is consistent. After fine-alignment, an agreement better than 1% was obtained between the two currents, which we take as the uncertainty on the H^- current value. A leakage current was observed in the Faraday cup FC1, due to the neighboring high voltages of the quadrupole. The cup current was therefore calibrated accordingly, prior

to each measurement.

Each Faraday cup is equipped with a guard electrode biased by a -100 V voltage. We checked the behavior of the measured current as a function of the bias voltage, as shown in Fig. 2.7. For sufficiently high negative voltages, typically below -50 V, a plateau is reached indicating that all secondary electrons emitted by the ion-surface collisions are confined within the cup, and therefore that the current measured faithfully reproduces the incoming ion beam current. The remaining difference between the currents measured by the two cups is solely the leakage current on FC1 discussed above. Furthermore, the radius of the ion beam is one third of the cup radius, hence excluding edge effects.

The rotating stage and powermeter are servo-controlled by an external computer. A data acquisition system monitors the Faraday cup current, given by the analog output of the electrometer, and the CEM counting rate. All the variables required to obtain the cross section can thus be measured and stored in the computer. The experiment therefore consists in moving the rotating stage to a given angle and sequentially recording the laser power, neutrals count rate and negative ion current.

Photodetachment of O^-

The one- and two-photon detachment cross sections of O^- have been determined by three experiments which make use of, essentially, the same apparatus as the one described in the previous subsection, barring a few alterations. Three different laser sets were used for these measurements and are described in the following. Modifications concerning the anion beam are only minor and presented at the end of the subsection.

Two series of measurements were run for the one-photon detachment cross section. The first makes use of a set of CW lasers to span a relatively wide range of wavelengths. Light between 700 nm and 845 nm is provided by a tunable Ti:Sapphire laser pumped by an Ar^+ laser. The lines from the same Ar^+ laser cover the range from 457.9 nm to 514.5 nm. A diode-pumped solid-state laser supplies light at a wavelength of 532 nm and a diode laser at 405 nm. Laser powers in the interaction region range from 60 mW to a few hundred mW. The second measurement spans a significantly broader wavelength range thanks to the use of a pulsed OPO laser system, going from threshold (848.6 nm) to 225 nm. It produces nanosecond pulses with an energy in the mJ range and at repetition rate of 30 Hz. The light pulses are intense enough to saturate photodetachment and their energy must be lowered prior to the interaction region for the ACBT to be applicable. The combination of a $\lambda/2$ plate mounted on a high-accuracy rotation stage and a polarizing beam

splitter serves as an attenuator whose transmittance can be adjusted at will by rotating the waveplate. The pulse energy is measured with a pyroelectric energy meter. All the optical elements used are coated with broadband anti-reflection (AR) coatings, and several sets of optics were needed to span wavelengths ranging from 225 nm to 848.6 nm. We verified that transmission losses due to absorption and reflection on the exit laser window are negligible and thus that the measured laser pulse energy is indeed the one seen by the ions inside the vacuum chamber.

Two-photon experiments require higher intensities, only attainable with pulsed lasers, and are limited to below the one-photon threshold (848.6 nm). We used a Q-switched Nd:YAG laser providing nanosecond pulses with an initial energy of about 500 mJ, which is reduced to a few mJ by the combination of three methods: (i) varying the delay between the optical pumping of the Nd:YAG rod and the opening of the Q-switch; (ii) selecting the reflection of the beam on a bare glass plate; (iii) combining a $\lambda/2$-plate and a polarizing beam splitter. The pulsed Nd:YAG laser is inherently a multimode laser, producing chaotic light which can affect the measurement of multiphoton cross sections [137–139]. To assess the importance of this in our experiment, we also operated the Nd:YAG laser with a single mode by injecting the light of a seeding laser (temperature-controlled laser diode) into its cavity. The time-envelope of the output pulse was monitored with a fast photodiode, and deviation from the single mode regime due to temperature variations of the diode clearly appeared as intensity beatings. The fast photodiode has a rise time of 1 ns, according to the manufacturer.

On the ion side, oxygen anions are produced from the same duoplasmatron source used for H^-, fed with N_2O gas. The second diaphragm defining the direction of the beam in the interaction and detection regions is now rectangular (1 mm along z, 100 μm along y). Its width is of the order of the laser spot size so as to maximize the signal-to-noise ratio. An electrostatic deflector located before the diaphragms is also switched on and off in order to pulse the ion beam and limit the number of background atoms hitting the CEM, hence limit CEM aging. A duty cycle of 10% is chosen to maintain sufficient beam intensity so that the beam current can be reliably measured.

After the interaction region, detection of the neutral atoms must be modified when using pulsed lasers. Their low repetition rates indeed drastically reduces the photodetachment signal, which becomes much smaller than the background one, impeding the use of time-gated measurements. The neutrals are counted during a narrow time window (~ 20 ns) delayed with respect to the laser shot by the neutrals' time of flight (~ 2.3 μs). A second, identical window delayed in time is used to

determine the background signal. The background mainly arises from collisional detachment with the residual gas and is below 1 kHz for an ion beam current of ~ 10 pA. Note that counting rates must be corrected for the Poisson distribution of the photodetachment events in order to obtain the exact mean detachment rate. Finally, a multi-channel plates (MCP) detector was used in the two-photon cross section experiment, instead of the CEM used otherwise. Its detection efficiency is estimated to be 56 % by comparing its count rate with that of a CEM whose efficiency is known [136].

2.3.2 Velocity map imaging setup

We have built a velocity map imaging (VMI) spectrometer aimed at measuring low-energy photoelectrons. The design of the electrostatic lens is taken from León *et al.* [135], who carefully optimized the lens dimensions and added guarding and shielding electrodes so as to obtain optimal focusing and thus reach one of the best resolution available with $\Delta E/E = 0.5\%$. The reason for that choice is that, while we do not aim at measuring high resolution photoelectron spectra, the use of fast beams prevents one to use the full size of the detector which, in turn, worsens the energy resolution. The design of León *et al.* was therefore chosen in order to maintain good resolution even for small images while keeping the setup complexity sufficiently low. A detailed drawing of the present VMI lens can be found in Appendix B.

A schematic view of the experiment is presented in Fig. 2.8. Oxygen anions are produced from the same duoplamastron source that was used in the previous experiments, mass selected and accelerated to 5 keV. The anion beam is pulsed by switching on and off a deflector (DH_1) using a fast, high-voltage switch. When the deflector is off, the ions fly straight to a Faraday cup (FC_1) and the ion current can be monitored. When the deflector is on, ions fly through the chicane (DH_1 and DH_2) and are collimated by two diaphragms of diameter 2 mm and 1 mm respectively, housed in a re-referencing tube. The deflector is switched on for about 400 ns and its delay with respect to the laser pulse is chosen so that the center of the ion bunch reaches the center of the VMI at the same time as the laser pulse. Beam pulsing is implemented in order to lower the number of background electrons, mainly arising from collisions between anions and residual gas, and thus to limit detector aging.

The fast anion beam enters the VMI perpendicularly to the lens axis. Photoelectrons are emitted within the interaction region at the center of VMI, where the anion beam is crossed at right angle by the laser beam. They are extracted towards the detector, perpendicularly to the laser-

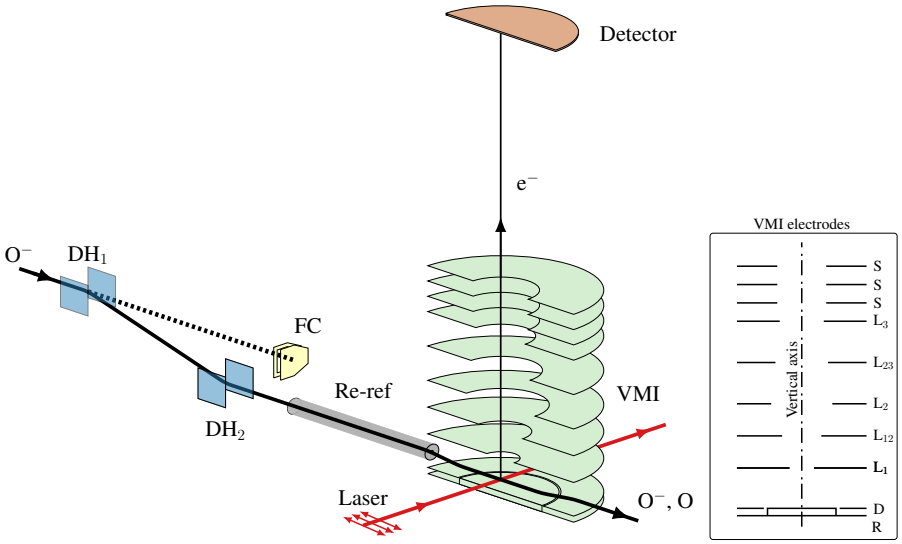

Figure 2.8: *Schematic view of the velocity map imaging experiment. DH_1 and DH_2: electrostatic horizontal deflectors; FC: Faraday cup; Re-ref: re-referencing tube; VMI: velocity map imaging spectrometer. The VMI electrodes are labeled according to the inset on the right, which shows a vertical slice through the lens. R: repeller; D: deflector; L_1: extractor; L_{12}, L_{23}: guarding electrodes; S: shielding electrodes.*

ion plane, by the $\sim$ 50 V/cm electric field created by the repeller and extractor electrodes. After traveling through the lens and a 37.5 cm–long flight tube, the electrons hit a PSD detector and the positions of the impacts are recorded [140].

The perpendicular detection geometry combined with the use of a fast beam of oxygen anions (5 keV, 2.5×10^5 m/s) prompts two modifications to the design of the VMI lens. First, the ion beam traveling through the VMI is substantially deflected by the extraction field. In order to compensate for that deflection, the repeller electrode is split into two concentric discs, as in the setup of Johnson *et al.* [141]. The inner disc acts as the standard repeller electrode, providing a homogeneous extraction field to repel photoelectrons. The outer disc serves as a deflector which counteracts the upwards deflection above the inner disc by downwards deflection before and after. The deflector voltage can be adjusted so that the anions exit the VMI following the same trajectory along which they entered. The exiting anions are collected downstream on a Faraday cup and the deflector voltage is optimized by maximizing the measured current. The second modification is prompted by the fact that photoelectrons are emitted within the moving frame of the ion

and their velocity in the lab frame is therefore the vectorial sum of the photodetachment velocity and the anions velocity. As a result, photoelectrons are emitted more off-axis than in the case of slow particles or collinear injection and the diameter of the aperture in the extracting electrode had to be enlarged to 20 mm, instead of 14 mm in the original design.

The voltage V_R on the repeller ranges from -150 V for low energy photoelectrons to -1200 V for 4 eV photoelectrons. For each value of V_R, the voltages V_1 and V_2 on L_1 and L_2 are coarsely optimized so as to obtain reasonable energy resolution. We found that, in most cases, setting $V_1 = 0.89V_R$ and $V_2 = 0.66V_R$ fulfills the present needs. Guarding electrodes are set to $V_{12} = (V_1 + V_2)/2$ for L_{12} and $V_{23} = V_2/2$ for L_{23}. The L_3 and shielding electrodes are grounded. Voltage on the deflector is higher than that of L_1 and is optimized on the measured ion current. It is subsequently adjusted in order to maximize the photoelectron signal.

Along with these modifications of the original VMI design, we have added a re-referencing tube in order to minimize adverse effects due to the deceleration of ions as they enter the VMI lens. When the ion bunch flies through the tube, it is rapidly switched from the ground to a high voltage whose value lies between that of the extractor and deflector electrodes. This effectively re-references the ion bunch from the ground to the VMI voltage and, when the ions exit the tube, the potential gradient at the VMI entrance is almost suppressed and deceleration strongly reduced. However, in regard of the high beam energy (5 keV) and the comparably small VMI voltages (150 V – 1200 V), we have seen no particular improvement on the energy resolution when the re-referencing tube is used.

The screening of magnetic fields is critical for photoelectron spectroscopy, therefore the VMI lens and flight tube are surrounded by two concentric μ-metal cans and tubes. The repeller electrode is manufactured with ARCAP non-magnetic alloy and all other electrodes are made of non-magnetic stainless steel. The setup is placed in a stainless steel chamber pumped to high vacuum (10^{-8} mbar).

Light pulses are produced by the OPO laser system also used for the animated-crossed-beam experiment described above. At the exit of the OPO, light passes through a $\lambda/2$ plate and a polarizing beam splitter. This combination provides control over the laser pulse energy and sets the polarization of the light parallel to the plane of the imaging detector. In the infrared and visible range, light is focused by an $f = 40$ cm lens onto the anion beam at the center of the VMI. It enters and leaves the vacuum chamber through laser windows. All optics are AR-coated.

In the ultraviolet range, scattered photons hitting the VMI elec-

trodes, in particular the repeller, are an important source of background photoelectrons which, in turn, strongly affect the measured images. In order to reduce background as much as possible, we have disposed a series of baffles along the laser beam path (10 before the entrance of the VMI and 5 after). Each baffle has a 4 mm hole at its center, where light passes through, and is coated with colloidal graphite to reduce reflection. The μ-metal shields are also coated with colloidal graphite. In addition, the $f = 40$ cm lens was removed and the laser windows were tilted at an angle to prevent light reflected onto the windows from penetrating inside the VMI. For wavelengths below 280 nm, we have also replaced the repeller electrode by a grid with 90% transparency and a positively biased plate located ~ 5 mm underneath. This design strongly reduces the number of background photoelectrons [141, 142] while maintaining good focusing properties. Note that the positive bias on the plate must be kept low enough, roughly 300 V higher than the repeller voltage, in order not to modify the electrical potential seen by the photodetached electrons in the interaction region.

The correlation between brightness and amplitude (COBRA), position sensitive detector [140] is used to image photoelectrons. It consists in a stack of 2 microchannel plates (MCP), a waveform digitizer, a phosphor screen and a CMOS camera. The arrival time of photoelectrons onto the detector can be measured by COBRA but is not required in the present study and therefore not recorded. Injecting the anion beam perpendicularly to the VMI axis yields a detection system simpler than that used for collinear injection [78, 135], where the voltage on the MCP must be rapidly lowered before the ion pulse hits the detector. Measurements are performed at 30 Hz, the repetition rate of our laser, and images are processed in real time. Each image is 512×512 pixels in size and the position of each electron hit is determined with sub-pixel accuracy using a centroiding algorithm. We work, in average, with 3 or 4 electrons per laser shot and data for each wavelength is acquired until about 100,000 events are recorded.

2.4 Photodetachment of H^-: total cross section

The absolute total photodetachment cross section of H^- was measured using the ACBT in a wavelength range from 700 nm to 1064 nm. Raw results as obtained from the experiment are shown in Sec. 2.4.1. The measured total cross section is presented in Sec. 2.4.2 and compared against available experimental and theoretical data.

2.4.1 Animated-crossed-beam result

At each wavelength, the laser beam is scanned across the ion beam while counting neutrals and monitoring the anion current and laser power. This procedure is repeated many times in order to secure good statistics. The resulting data, corrected for the laser power and the ion current, are shown in Fig. 2.9 for a laser wavelength of $\lambda = 850$ nm (1.4586 eV). On either side of the graph, the displacement of the laser beam is larger than the ion beam radius and the two beams do not overlap. Switching the laser on and off at large displacements did not change the neutrals counting rate of the CEM, thus ensuring that only the background counts are present. As the vertical displacement moves towards 0, there is an increasing overlap between both beams and the photodetachment signal rises on top of the background signal. The background is estimated by averaging three points at each extremity of the graph and then subtracted from the total counts to obtain the net photodetachment signal, from which the cross section can be computed according to Eq. 2.7.

Figure 2.9 shows 40 scans of the vertical position at $\lambda = 850$ nm. For each, a value of the cross section is computed and the total cross section is the mean value, 3.96×10^{-21} m^2. The standard deviation of the mean [143] is 0.02×10^{-21} m^2, about 0.5% of the mean, highlighting the excellent repeatability of our measurements and providing the statistical error. Uncertainties arising from systematic effects are estimated as follows: the powermeter accuracy of 3% is given by the manufacturer; the vertical displacement of the laser beam is known with 2% precision, as estimated from the comparison of measured and calculated values; the 1% error on the current measurement is obtained by comparing the current measured by the two Faraday cups FC1 and FC2 and corresponds to the calibration accuracy of the electrometer; an uncertainty of 1% on the ions' velocity is given by the small variations of the source's acceleration voltage (4 kV); the uncertainty of 2% on the detection efficiency of the CEM has been previously established by Naji *et al.* [136]. Each of these values provide an upper limit a_+ and a lower limit a_- to the

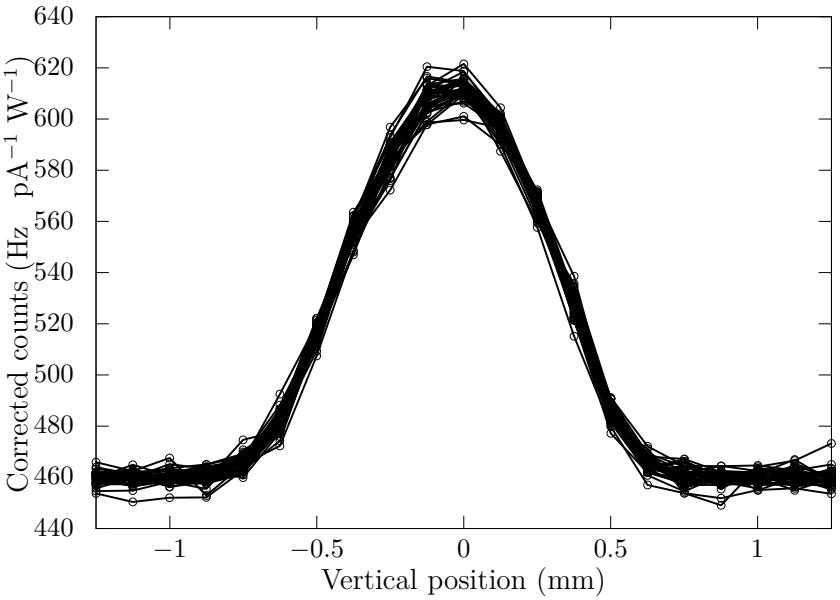

Figure 2.9: *Normalized count rate of the channel electron multiplier for different vertical displacements of the laser beam. The measured count rate was divided by the H^- current and the laser power to obtained the normalized count rate.*

exact value a. As no further information is available about the probability distribution of a amongst the interval, we consider $[a_-, a_+]$ as a one- standard deviation confidence interval. The associated uncertainty is consequently, following NIST's guidelines [143], $(a_+ - a_-)/2$ and the total error $\Delta\sigma$ is the quadrature sum of the various uncertainties. The above procedure was repeated by steps of 50 nm in the 700-1000 nm range, with an additional measurement at 1064 nm, yielding the results presented in Table 2.1 and compared to the existing data in Figs. 2.10 and 2.11 (circles).

2.4.2 Total cross section

As shown in Fig. 2.10, the present measurement agrees well with the absolute measurement of Popp and Kruse [99]. These authors used the spectrum of a well-characterized hydrogen-arc lamp and, by modeling the partial local thermal equilibrium within the arc, could infer absolute values for the photodetachment cross section. The wavelength dependence of our measured cross section matches the relative measurement of Smith and Burch [98], which is put on an absolute scale for compar-

Photon energy (eV)	σ (10^{-21} m^2)	$\pm\Delta\sigma$ (10^{-21} m^2)
1.1654	3.48	0.15
1.2398	3.74	0.17
1.3051	3.82	0.17
1.3776	3.96	0.17
1.4586	3.96	0.17
1.5498	3.91	0.17
1.6531	3.90	0.17
1.7712	3.74	0.16

Table 2.1: *Present photodetachment cross sections (10^{-21} m^2) as a function of the photon energy (eV).*

ison, using one of the most robust theoretical data available, namely that of Venuti and Decleva [47]. Smith and Burch performed the measurement of the photodetachment cross section of the D^- ion within a crossed-beam configuration. The light source was a carbon projection arc lamp combined with narrow bandpass filters, providing intense, quasi-monochromatic light. The measurement of the free electron current, the ion current and the light power yielded a relative value for the cross-section. These two methods are different from the present experiment, and the good agreement both in shape and magnitude therefore gives confidence in the validity of the values obtained.

A measurement of the photodetachment cross section has been recently performed by Vandevraye *et al.* [72] with a pulsed Nd:YAG laser, and is also shown in Fig. 2.10. The cross-section was measured by means of several saturation-based techniques, thus avoiding the approximation of the linear regime. To obtain the cross section, the spatial and temporal profiles of the photon flux had to be assumed Gaussian while the ion density was assumed uniform. Although justified, these assumptions are not exact and may therefore introduce discrepancies. This measurement lies at the higher limit of compatibility with the results of Popp and Kruse [99] compiled in their table. Note that the value of $3.6(3) \times 10^{-21}$ m^2 quoted in [72] was obtained from the crossed beam values of Smith and Burch [98] scaled by Popp and Kruse [99].

For the sake of completeness, one must mention the first absolute measurement made by Branscomb and Smith [97] in the mid-fifties. They measured the integrated cross section of the photodetachment of H^- by illuminating the anion beam at right angle with a tungsten lamp combined with a set of sharp cutoff filters. The cross section being integrated over a wide range of photon energies, no direct comparison can be made. The authors however computed the ratio of their cross section to

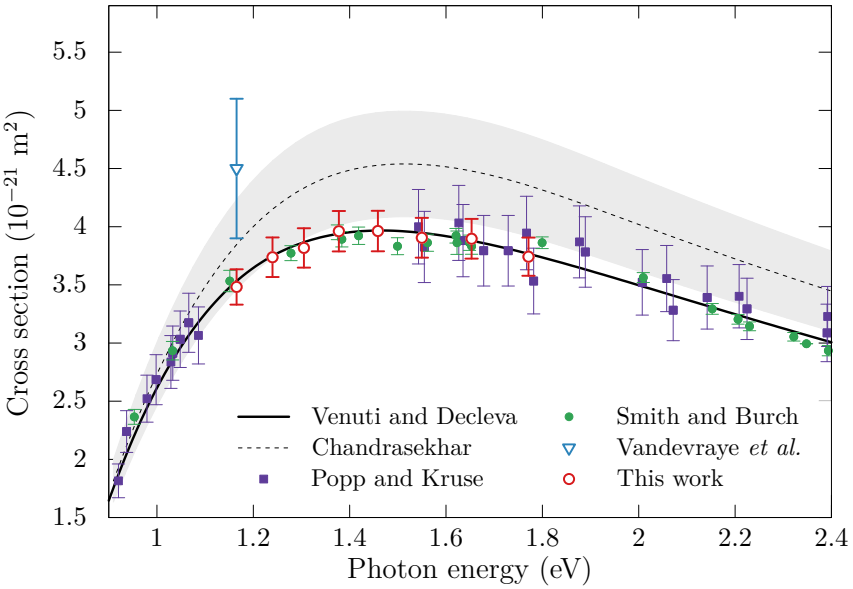

Figure 2.10: *Experimental photodetachment cross section (10^{-21} m^2) as a function of the photon energy (eV). The empty circles and the triangle are, respectively, the present work and the work of Vandevraye et al. [72]. The full squares are from Popp and Kruse [99] and the discs are the relative measurement of Smith and Burch [98] set on an absolute scale using the calculation of Venuti and Decleva [47] (shown by the full line). The absolute, wavelength-integrated measurements of Branscomb and Smith [97] lie within ±10% of the calculation of Chandrasekhar [84] multiplied by 1.01 (dashed line), as depicted by the shaded area.*

the values obtained by Chandrasekhar [84], obtaining an average of 1.01 ±0.10. Therefore, the cross section computed by Chandrasekhar, multiplied by 1.01, is plotted in Fig. 2.10 along with a shaded area defining a 10% interval around the theoretical curve. It appears to be fully compatible with the measurements of Popp and Kruse [99] and Vandevraye *et al.* [72].

The absolute photodetachment cross section was also investigated by Bacal and Hamilton [100] and Nishiura *et al.* [101] by means of lasers in an attempt to monitor the production of H^- and D^- ions within fusion plasmas. The fraction of photodetached ions as a function of the laser pulse energy was measured, and a subsequent fit with the theoretical photodetachment probability, depending on the cross section, ensured the validity of the method. However, the important spread of the data points allows to confirm only the order of magnitude of the cross section.

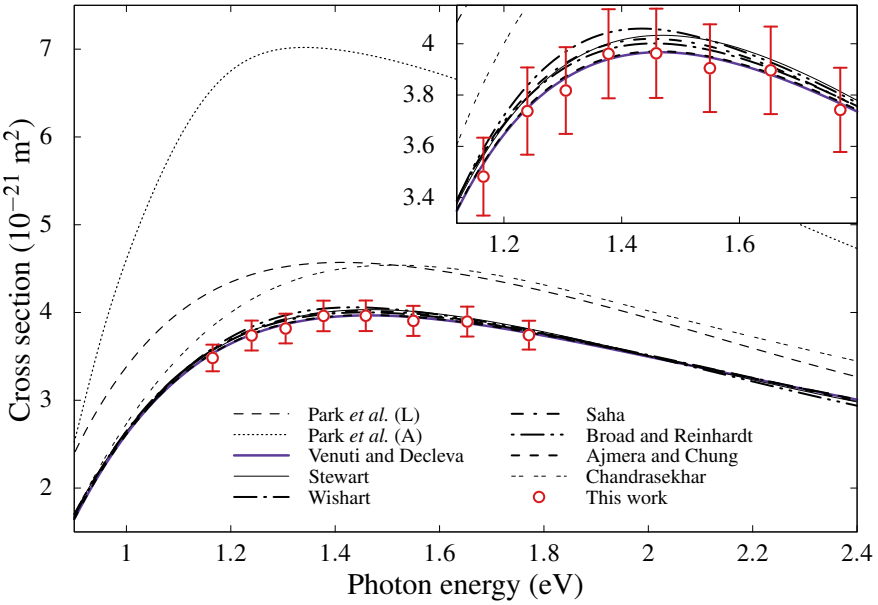

Figure 2.11: *Photodetachment cross section (10^{-21} m^2) as a function of the photon energy (eV). The empty circles are the present work. The curves are theoretical values from Park et al. [95] in the length (dashed) and acceleration (densely dotted) gauges, Venuti and Decleva [47] (full thick), Stewart [86] (full thin), Wishart [87] (long dash-dotted), Saha [88] (dash-dotted), Broad and Reinhardt [89] (dash-doubly dotted), Ajmera and Chung [90] (dotted), Chandrasekhar [84] (doubly dotted).*

As shown in Fig. 2.11, the agreement of the present measurement with most theoretical results is excellent over the whole wavelength range covered by the experiment, particularly with that of Ajmera and Chung [90] and of Venuti and Decleva [47]. The latter is a state-of-the-art calculation which was internally validated by the perfect matching of the cross section values obtained within the different gauges (length, velocity and acceleration), and its accuracy is estimated to be better than 0.001 $\times 10^{-21}$ m^2. The value computed at 1064 nm (1.1653 eV) is $\sigma = 3.52 \times 10^{-21}$ m^2 and agrees within error bars with the present value $\sigma = 3.48(15) \times 10^{-21}$ m^2. The value of Vandevraye *et al.* [72] is $\sigma = 4.5(6) \times 10^{-21}$ m^2 and lies 1.5 σ above that of Venuti and Decleva.

A few theoretical values depart from the commonly obtained cross section. In particular the adiabatic approximation in hyperspherical coordinates, adopted both by Fink and Zoller [96] and Park *et al.* [95], led to the significantly higher results shown in Fig. 2.11. Park *et al.* gave a detailed account of the possible causes of the discrepancy, accounting

for the lower reliability of the adiabatic hyperspherical approximation in the regions of the configuration space where the gauges used have the largest weight. It also applies to Fink and Zoller's calculation, who obtained results identical to Park *et al.* within numerical accuracy. The adiabatic hyperspherical approach was later extended from single channel to coupled channels calculations by, *e.g.* , Masili and Starace [92]. Including no more than 4 channels, their computed photodetachment cross section converged to the values of Stewart [86], which lie in the range of most theoretical works. The early work of Chandrasekhar [84] also departs from the commonly obtained values. This pioneering calculation was performed with a model potential without explicitly taking into account electron correlations.

2.5 Photodetachment of O^-: the full picture

2.5.1 One-photon total cross section

Results for the total one-photon detachment cross section of O^- are shown in Fig. 2.12 and compared against available experimental data [73, 80, 98, 103]. The cross section measured with CW lasers is shown by the light brown inverted triangles. Values measured with the OPO laser system are represented by the blue squares and span photon energies ranging from 1.46 eV to 5.51 eV by steps of 0.062 eV (500 cm^{-1}), and by even smaller steps close to thresholds. The present measurements thus extends by more than 1.5 eV the range over which experimental data is available. The error bars shown in Fig. 2.12 represent the 2σ statistical uncertainty, where σ is the standard deviation of the mean. Uncertainties arising from systematic effects are estimated to lie below 7% and include uncertainties on the detection efficiency (4%), laser pulse energy (5%), ion current (1%), ion velocity (1%) and laser beam vertical displacement (2%), as in Sec. 2.4.1.

The present data is in good self mutual agreement over the common photon energy range covered. Just above threshold, the present measurements are also in agreement with that by Lee *et al.* [103]. For photon energies above 2.2 eV however, the measured cross sections are about 20% larger than the three other experiments and increases with energy while the experimental data of [73, 80, 98] present a plateau with a slightly negative slope.

The measurements by Smith and by Branscomb *et al.* were performed in a crossed beam configuration [80, 98]. The light from a carbon arc lamp was sent through quasi-monochromatic filters onto a beam of O^- and the cross section was inferred by carefully measuring the pho-

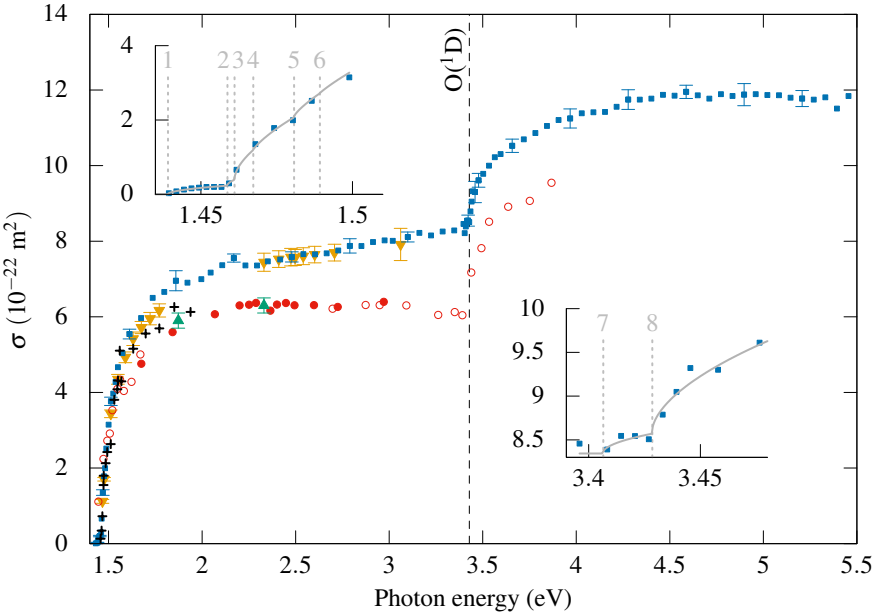

Figure 2.12: *Total photodetachment cross section of O^-. Full squares: absolute values from the present experiment with the OPO laser, full triangles: absolute measurement of Hlavenka et al. [73], full inverted triangles: absolute values of the present experiment with CW lasers, full circles: absolute measurement of Smith [98], open circles: relative measurement of Branscomb et al. [80], crosses: absolute measurement of Lee and Smith [103]. The vertical dashed line shows the $O(^1D)$ threshold. The insets show results from the present experiment around the $O(^3P)$ and $O(^1D)$ thresholds, from left to right. The vertical dotted lines indicate the position of the various fine-structure thresholds, numbered as in Fig. 2.15.*

toelectron current [97]. The origin of the differences with the present experiment is yet not understood. The recent experiment of Hlavenka *et al.* [73] yields values for the cross section matching those of earlier work. It is based on negative ion depletion in a multipole trap and thus avoids the possible loss of photoelectrons just mentioned. As in the present work, the measurement relies on scanning the laser beam across the ion trap in order to avoid having to determine the interaction volume but the assumptions made concerning the ion density are more stringent. The quoted uncertainty seems rather low, considering the typical accuracy of powermeters and the laser beam deflection technique employed to scan the trapping volume.

For the sake of completeness, one must mention the early absolute measurements by Branscomb and Smith [97] and later by Branscomb

et al. [49], performed with a similar experimental setup. These early values were omitted from a subsequent publication by the same authors [80] and are thus not reproduced here. Their magnitudes are lower than those of the present experiment, while their shape is very similar.

The opening of the first excited state (^{1}D) threshold manifests itself as a steep rise in the cross section above 3.43 eV. The present cross section does not match that measured by Branscomb *et al.* [80], which was put on an absolute scale using the data of Smith [98]. As stated by Branscomb *et al.* , calibration of their apparatus was challenging for photon energies above 3.7 eV because of stray photoelectrons produced by UV light on the walls of the vacuum chamber. Detection of these stray photoelectrons may change the observed cross section and, while no uncertainty is given, the difference of more than 2.5×10^{-22} m^2 (25%) between the measured cross section and a crude theoretical estimate was regarded by the authors as non contradictory [80]. The present results above the O(^{1}D) threshold also lie within 25% of the values of Branscomb *et al.* . For photon energies above 3.93 eV, no other experimental data is available.

The present results obtained with the OPO laser are compared in Fig. 2.13 against theoretical calculations. The cross section from a *R*-Matrix Floquet (*R*MF) calculation falls in reasonable agreement with our results below the O(^{1}D) threshold [117]. The calculation employs a restricted configuration interaction (CI) description of the anion and atomic target which includes pseudo-orbitals chosen to optimize the polarizability of ground state oxygen. The CI basis is voluntarily limited to essentially Hartree-Fock wave functions for the three physical atomic states in order to keep the *R*MF calculation simple. The electron affinity of O^- and polarizability of ground state oxygen are well reproduced but the energies of the two first excited states of oxygen (^{1}D, ^{1}S) are not accurate. This is evident in Fig. 2.13 where the opening of the O(^{1}D) threshold occurs at a significantly higher photon energy. Despite this energy difference, the magnitude of the experimental cross section is reasonably well reproduced while its shape deviates from the *R*MF results by a steeper rise above both thresholds and a more gentle slope at higher energies. A standard *R*-matrix calculation was also performed and its results in the length form are essentially identical to the *R*MF ones, which use the most appropriate gauge in each region of configuration space [117]. Results in the velocity gauge, shown in Fig. 2.13, lie some 25% lower. The dotted curve is the result, in the length form, of the calculation by Zatsarinny and Bartschat using the B-spline *R*-matrix method [108]. Results in the velocity gauge are in relatively good mutual agreement with the length ones. Their calculation includes a large

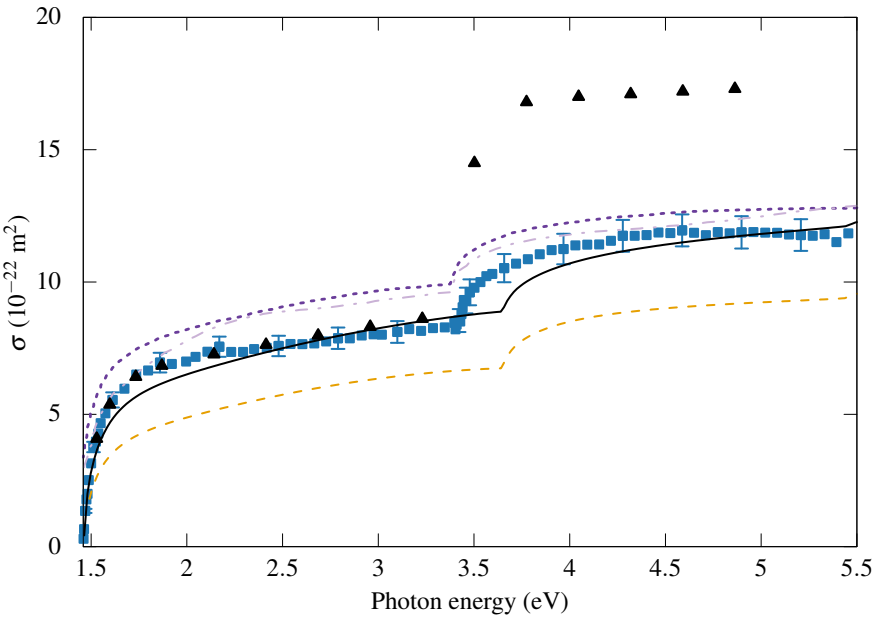

Figure 2.13: *Total photodetachment cross section of O^-. Full squares: present experiment with the OPO laser, full triangles: model potential calculation of Robinson and Geltman [109], full line: RMF calculation [117], dashed line: R-matrix calculation in the velocity gauge [117], dotted and chained lines: BSR calculation of Zatsarinny and Bartschat [108] in the length and velocity gauges.*

number of accurate target states so as to describe as well as possible the oxygen ground and low-lying excited states. The calculated cross section lies about 15% higher than the present measurement below the O(^{1}D) threshold, but is only 6% higher above the O(^{1}D) threshold, a value that matches the experimental uncertainty. We may note that the amplitude of the step corresponding to the opening of the O(^{1}D) channel is smaller in the calculation than in the experiment. Agreement with the early calculation of Robinson and Geltman [109] is surprisingly good below the O(^{1}D) threshold, considering that the calculation is based on a one- electron model potential adjusted to the experimental electron affinity. The cross section above the O(^{1}D) threshold is much higher than the present data and may reflect, as suggested by Robinson and Geltman, the fact the polarizability α of oxygen is different between O(^{3}P) and O(^{1}D). Due to the lack of available data, the experimental value of α for the oxygen ground state was used for both final states in their calculation. Finally, let us note that most theoretical results presented here are 20% to 35% larger than the previous experimental

cross sections [73, 80, 98, 103]. There is no agreement in shape either, in particular above 2.2 eV where previous experimental data are nearly constant with photon energy while theoretical values increase monotonically.

One must mention that the photodetachment cross section of O^- was calculated in a number of other theoretical works, ranging from semiempirical calculations to equation-of-motion coupled-cluster Dyson orbitals or density functional theory calculations [111, 114, 115, 144–146]. They substantially differ from the data presented in Figs. 2.12 and 2.13 both in shape and magnitude.

The good agreement reached between the results obtained with CW and pulsed OPO lasers illustrates the robustness of the animated-crossed-beam technique and validates its use with pulsed laser sources. The CW experiment is indeed performed mainly with CW Ar^+ and Ti:Sa lasers operating at the TEM00 mode and providing a light beam of superior quality, with a spatial profile very close to Gaussian and excellent power stability. In the OPO laser system, light pulses are generated through a series of nonlinear processes in optical crystals and, as such, the light beam quality is strongly reduced. The spatial profile is far from Gaussian and strongly varies with the wavelength. Pulse-to-pulse energy fluctuations reach standard deviations of more than 30% and important fluctuations in the time profile of a single laser pulse can also be observed since the Nd:YAG pump laser is multimode. In theory, the ACBT does not set restrictions on the laser intensity profile as long as it remains constant throughout a vertical scan. It also stands when pulsed lasers are used, as shown in Sec. 2.2.1. Moreover, pulse-to-pulse fluctuations of the time profile of the laser pulses can be averaged out by measuring over a sufficiently large number of pulses, as in the present work. The excellent mutual agreement between the CW and pulsed measurements certainly confirms such considerations.

The insets in Fig. 2.12 show details of the cross section around the $O(^3P)$ and $O(^1D)$ thresholds. The positions of the various fine structure thresholds are indicated by the vertical dotted lines, numbered according to Fig. 2.15, and the most intense fine structure transitions can be observed as sharp rises in the cross section curve. Note that the region around the $O(^3P)$ threshold has been measured in much greater detail by Neumark *et al.* [147] and Suzuki and Kasuya [148], and reaching such a level of detail is certainly not the goal of the present study. The cross section can be fitted by a sum of Wigner threshold laws [44] associated to each fine structure threshold and including only s-wave contributions since these are predominant for low energy photoelectrons. Such a fit

function reads

$$\sigma(\epsilon) = A \sum_{J=1/2}^{3/2} \mathcal{P}_J \sum_{J'=0}^{2} R_{JJ'}(\epsilon - E_{JJ'})^{1/2}, \tag{2.41}$$

where ϵ is the photon energy, A a proportionality constant and $\mathcal{P}_J$ is the initial population of the fine structure component $O^-(^2P_J)$. A and $\mathcal{P}_J$ are fit parameters. $R_{JJ'}$ and $E_{JJ'}$ are the branching ratio and transition energy of the JJ' transition from the initial $O^-(^2P_J)$ state to the final $O(^3P_{J'})$ or $O(^1D_{J'})$ states. Transition energies are computed using electron affinities and energy levels from [149] and [150]. Branching ratios[2] $R_{JJ'}$ to the $O(^3P)$ and $O(^1D)$ states are obtained from [78, 151, 152]. The fit of the measured cross section with Eq. (2.41) can be used to estimate the initial populations $\mathcal{P}_J$ of the fine structure components of O^-. They are found to be 0.34 ± 0.02 and 0.66 ± 0.02 for the $J = 1/2$ and $J = 3/2$ components respectively when fitting the ground state threshold. The fit of the $O(^1D)$ threshold yields populations of 0.30 ± 0.14 and 0.70 ± 0.14 for $J = 1/2$ and $J = 3/2$ respectively.

2.5.2 One-photon partial cross sections

Term-resolved partial cross sections

The branching ratio $R_{^1D}$ to the $O(^1D)$ final state, obtained from VMI measurements, is represented in Fig. 2.14(a). It raises rapidly above threshold and soon reaches a plateau-like region where, on average, photodetachment leaves 21.6% of the oxygen atoms in the ^1D state and the rest in the ground state. For a photon energy of 3.20 eV ($\lambda = 266$ nm), the present branching ratio of 0.21 ± 0.02 agrees within error bars with the value of 0.24 ± 0.04 measured by Domesle *et al.* [112]. The solid line in Fig. 2.14(a) represents a tentative fit of the branching ratio using

$$R_{^1D}(\epsilon) = C \sum_{J=1/2}^{3/2} \mathcal{P}_J \frac{(\epsilon - E_{J2})^{1/2}}{1 + b(\epsilon - E_{J2})^a}, \tag{2.42}$$

where $\mathcal{P}_J$ is the initial population of the J-th fine structure component of O^-, taken from Sec. 2.5.2, E_{J2} is its energy difference with respect to the the $O(^1D_2)$ state of oyxgen and a, b and C are fit parameters. The rationale behind this choice of function is that $R_{^1D}(\epsilon)$ tends to a Wigner threshold law for low photoelectron energies and is almost

[2] Details on these branching ratios and on the populations $\mathcal{P}_J$ will be presented in Sec. 2.5.2

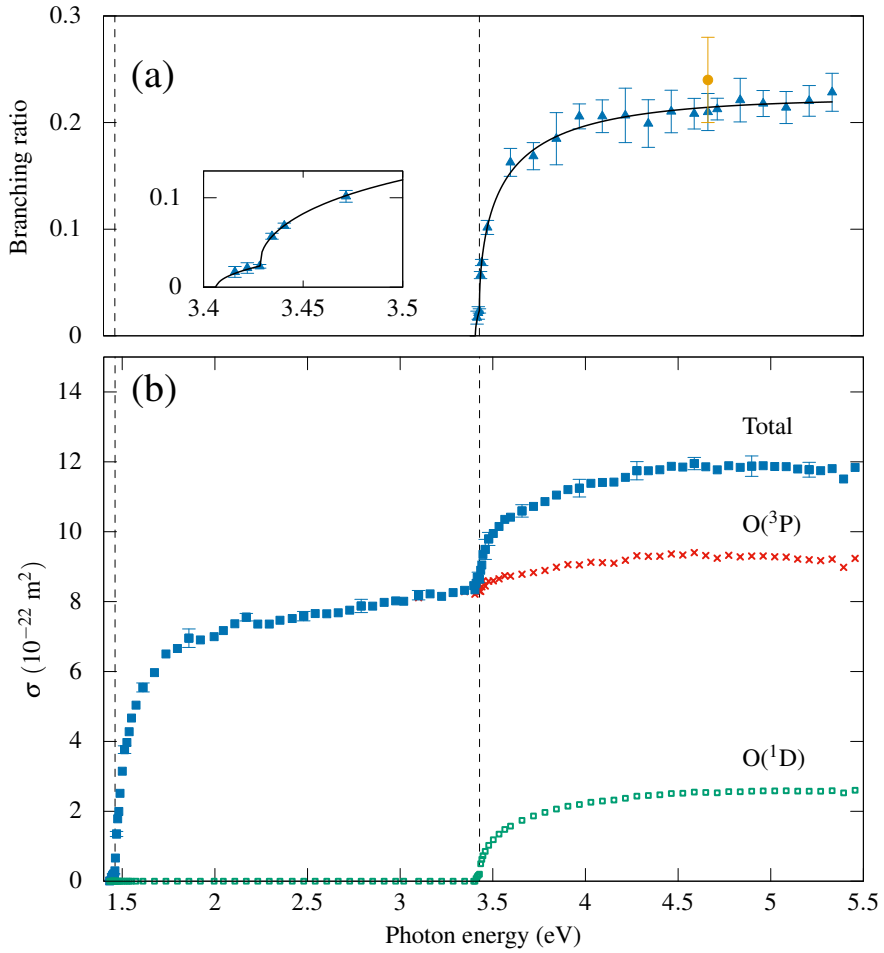

Figure 2.14: *(a) Branching ratio to the $O(^1D)$ final state and (b) total and partial photodetachment cross sections. (a) Full triangles: present measurement, disc: measurement of Domesle et al. [112], full line: fit of the present data (see text). The inset is magnified view of the data at threshold. Uncertainties are 1σ values coming from the least-square fitting procedure of the peaks in the photoelectron velocity distribution. (b) Full squares: total cross section, crosses: partial cross section to the $O(^3P)$ state, empty squares: partial cross section to the $O(^1D)$ state. The dashed lines indicate, from left to right, the positions of the $O(^3P)$ and $O(^1D)$ thresholds.*

constant in the high energy region. Note that while the partial cross section to O(^{1}D) must follow a Wigner law at threshold, this is not the case for the branching ratio. However, since the partial cross section to O(^{3}P) remains essentially flat across the O(^{1}D) threshold region, the partial cross section and branching ratio to O(^{1}D) exhibit essentially the same behavior and $R_{^1\mathrm{D}}$ raises, in good approximation, according to the Wigner law. The best fit is obtained for $a = 0.61$, $b = 8.1 \times 10^{-3}$ cm$^{-0.61}$ and $C = 6.8 \times 10^{-3}$ cm$^{1/2}$.

The partial photodetachment cross sections to the O(^{3}P) and O(^{1}D) final states can be straightforwardly obtained from the total cross section and the fit of the branching ratio,

$$\sigma_{^1\mathrm{D}} = R_{^1\mathrm{D}}\ \sigma, \tag{2.43}$$

$$\sigma_{^3\mathrm{P}} = (1 - R_{^1\mathrm{D}})\ \sigma. \tag{2.44}$$

They are represented in Fig. 2.14(b) along with the total cross section.

Fine structure-resolved branching ratios

For a given final term (^{3}P or ^{1}D), branching ratios[3] also exist between the various fine structure components of both the initial anionic state ($J = 1/2, 3/2$) and the final atomic state (see Fig. 2.15). It is well established that these ratios are not a simple product of the statistical weights of the initial and final states [68, 151]. For detachment of a p-electron close to threshold, they can be expressed as ratios between geometrical factors $G_{JJ'}$ obtained through angular momentum conservation and coupling between the atomic target and the outgoing photoelectron [152]. Such geometrical factors read

$$G_{JJ'} = (2J'+1) \sum_{\lambda} (2\lambda+1) \begin{Bmatrix} L' & S & \lambda \\ \frac{1}{2} & J' & S' \end{Bmatrix}^2 \begin{Bmatrix} L' & S & \lambda \\ J & \ell_0 & L \end{Bmatrix}^2, \tag{2.45}$$

where the quantum numbers (L, S, J) and (L', S', J') are relative to the anion and the atom, respectively. ℓ_0 is the initial orbital quantum number of the electron and is 1 for a p-electron. Numerical values of the branching ratios, calculated from these geometrical factors as $R_{JJ'} = G_{JJ'} / \sum_{J'} G_{JJ'}$, are given in Table 2.2 for the ground state. Since the first excited state (^{1}D$_2$) has only one fine structure component,

[3]The related quantity of intensity ratios is sometimes favored in the literature, and represent the intensity of a given $J \to J'$ transition relative to the $J \to 2$ transition.

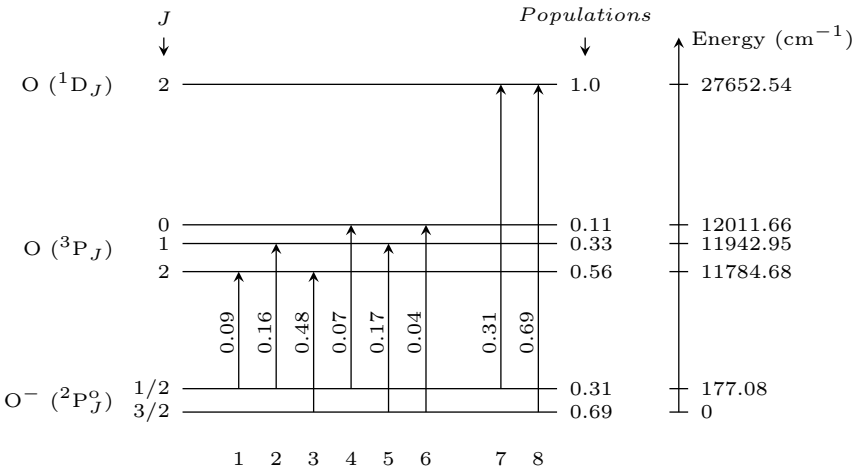

Figure 2.15: *Sketch of the fine structure energy levels of O^- and of the ground and first excited states of O. The arrows depict the various fine structure transitions, labeled by numbers and ordered by increasing energy. The numbers next to the arrows are the transition intensities, given by $\mathcal{P}_J R_{JJ'}$ in Eq.* (2.41)*. The population distributions of the initial anion state and final atomic state are shown on the right. All quantities are normalized so that their sum for a given term is 1. The scheme is not to scale, however transition energies are indicated on the right and were computed using [149] and [150].*

both ratios are obviously 1 in this case. We may finally note that, following the symmetry and orthogonality properties of the $6j$ symbols [153],

$$\sum_{J'} G_{JJ'} = \frac{1}{(2S+1)(2L+1)} = \frac{1}{6}, \tag{2.46}$$

independent of the initial fine structure component J and of the values of (L', S'). Therefore, close to threshold, the difference between the photodetachment cross sections of the $J = 3/2$ and $J = 1/2$ states is due only, through the Wigner law, to differences in threshold energies. This difference is, to the first order, proportional to $\Delta E/\sqrt{\epsilon}$, where ΔE is essentially the fine structure splitting of O^- (0.02 eV) and ϵ is the photon energy. It therefore rapidly vanishes with increasing photon energies.

For the oxygen ground state ($J' = 0, 1, 2$), branching ratios similar to those of Table 2.2 have been measured up to photon energies of 2.54 eV [77, 78, 119]. The purely geometrical picture is strictly valid only if a single partial wave contributes to detachment [152], as is the case close to threshold where s-wave detachment predominates. How-

$J \backslash J'$	2	1	0
3/2	0.69	0.25	0.06
1/2	0.28	0.5	0.22

Table 2.2: *Fine structure branching ratios for the oxygen ground state. The sum over J' for each J is 1.*

ever, increasing photon energies see the onset of d-wave detachment and the ratios determined from Eq. (2.45) should not be valid since geometrical factors cannot be separated from radial dipole matrix elements in the various summations involved in the calculation of the cross sections. Pan and Starace showed that the geometrical picture still holds far from threshold if one-electron dipole matrix elements are term-independent and Cavanagh *et al.* observed, following their experimental results, that this must be the case for ground state oxygen [78, 152]. Interestingly, we note that term independence is a characteristic of central potential models and the sustained validity of the geometrical approach may therefore be associated to the excellent agreement between the present total cross section and the model potential calculation of Robinson and Geltman [109].

In the present VMI measurement, fine structure transitions are resolved up to ~ 0.3 eV above threshold. The transition intensities and the branching ratios can be obtained, as for the term resolved quantities, by fitting the fine structure peaks in the photoelectron velocity distribution with Gaussian functions and computing their areas. The corresponding results show no deviation from the geometrical distribution and branching ratios match the theoretical ones within 15–20 % for the brightest transitions and 30% for the less intense one. Moreover, since they have been experimentally verified, theoretical branching ratios for the $O(^3P_{J'})$ channels can be used to estimate the initial populations of the fine structure components of O^-. Doing so, we obtain 0.69 ± 0.01 and 0.31 ± 0.01 for the $J = 3/2$ and $J = 1/2$ components, in agreement within error bars with the populations determined by fitting the total cross section close to the $O(^3P)$ and $O(^1D)$ thresholds (see Sec. 2.5.1). Identical values are obtained when considering data close to the $O(^1D)$ threshold, albeit with an uncertainty that is twice larger (0.02).

The measured fine structure population distribution departs from a purely statistical mixture (2:1), which would correspond to production from an infinitely hot source. The distribution can be used to estimate the temperature of the ion source, given, *via* the Boltzmann distribution,

by

$$T = -\frac{\Delta E}{k \ln(2R)}, \tag{2.47}$$

where ΔE is the fine structure splitting of O^-, k is the Boltzmann constant and R is the ratio between the populations of the $J = 1/2$ and $J = 3/2$ components. The above equation yields an ion source temperature of 2382 ± 787 K, a value we consider as reasonable. We have further measured the fine structure populations for different ion source conditions, and found that the populations depend only weakly on the discharge current. This is expected since we are already in the asymptotic regime of Eq. (2.47).

Finally, it is interesting to note that, although the branching ratios are not statistical, since the initial fine structure distribution is close to statistical, the population distributions of the final $O(^3P'_J)$ and $O(^1D_{J'})$ states also are. From the measured populations and theoretical branchings ratios, we obtain, *e.g.* , 0.56 ± 0.03 for the $J' = 2$ component of the ground state, 0.33 ± 0.04 for its $J' = 1$ component and 0.11 ± 0.04 for $J' = 0$. This is to be expected since, for an initial statistical distribution, the symmetry and orthogonality properties of the $6j$ symbols give

$$\sum_J (2J+1) G_{JJ'} = \frac{2J'+1}{(2S'+1)(2L'+1)}. \tag{2.48}$$

Hence we are able to completely define the initial state of the anion and the final state of the atom, down to the fine structure populations. These results are shown in Fig. 2.15 along with transition intensities, relative to the most intense $3/2 \rightarrow 2$ transition, calculated using geometrical factors and experimental initial O^- populations. Such a level of detail can be reached, as we show here, either through velocity map imaging or by examining the total cross section at threshold.

2.5.3 One-photon differential cross section

The differential cross section for emission of a photoelectron of energy ε from an unpolarized atom or ion by linearly polarized light and under the dipole approximation can be written as

$$\frac{\mathrm{d}\sigma_f(\varepsilon)}{\mathrm{d}\Omega} = \frac{\sigma_f(\varepsilon)}{4\pi} \left[1 + \beta_f(\varepsilon) P_2(\cos\theta)\right]. \tag{2.49}$$

In the above equation, σ_f is the partial cross section to a given final state f, β_f is the asymmetry parameter, $P_2(\cos\theta) = \left(3\cos^2\theta - 1\right)/2$ and θ is the photoelectron ejection angle with respect to the quantization axis.

Therefore, under the above assumptions, the 3D differential cross section boils down to a single scalar parameter β. Discussion below is based on the latter.

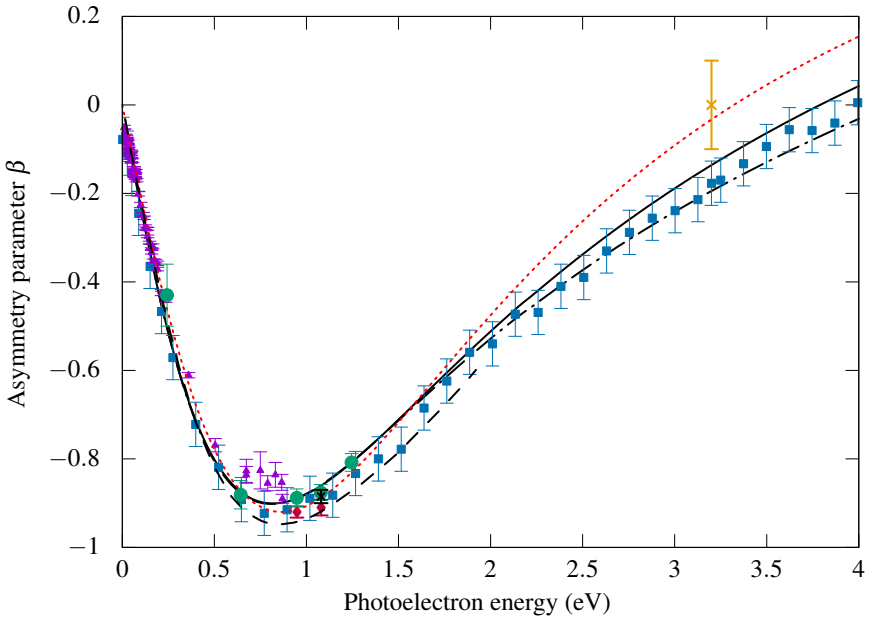

Figure 2.16: *Asymmetry parameter for photodetachment of O^- leaving O in the ^{3}P ground state. Full squares: present experiment, full triangles: Cavanagh et al. [78, 119], full circles: Hanstorp et al. [116], diamonds: Breyer et al. [77], crosses: Hall and Siegel [76], empty square: Domesle et al. [112]. Dotted line: model of Hanstorp et al. [116], dashed line: Cooper and Zare [57], full and chain lines: R-matrix results in the length and velocity forms.*

The measured asymmetry parameter for photodetachment of O^- leaving the oxygen atom in its ground state is shown in Fig. 2.16 and compared against available experimental and theoretical data. The present results follow the general trend established by Cooper and Zare [57], with isotropic emission at threshold ($\beta = 0$), emission preferentially perpendicular to the polarization axis ($\beta \simeq -1$) for intermediate photoelectron energies and emission preferentially parallel to the polarization axis at higher energies ($\beta \simeq 1$). The convergence of the asymmetry parameter to $\beta = 1$ at higher photoelectron energies, which is the signature of a pure d-wave behavior, is not observed in the energy range spanned by the experiment. This curve, characteristic of the photodetachment of electrons with $\ell \geq 1$, is the result of an interference between the competing s and d outgoing waves.

For photoelectron kinetic energies below 1.5 eV, the present data

agrees with all four existing measurements within error bars [76–78, 116, 118, 119]. Hall and Siegel pioneered measurements of the photoelectron angular distribution by photodetaching a beam of O^- inside the cavity of an Ar^+ laser and collecting photoelectrons with a hemispherical energy analyzer of low solid angle acceptance [76]. By measuring the yield of photoelectrons while rotating the polarization of the laser light with a $\lambda/2$ plate, the angular distribution could be retrieved. A similar setup was later used by Breyer *et al.* [77]. Hanstorp *et al.* were able to measure β by using an Ar^+ laser and a ring dye laser to photodetach O^- ions inside a graphite tube drilled with thin holes, and outside of which a channel electron multiplier was used to collect photoelectrons [116]. Again, rotating the polarization of the laser light while recording the electron yield allows one to determine the angular distribution. Recently, Cavanagh *et al.* [78, 118, 119] have measured the asymmetry parameter for photoelectron energies ranging from threshold to 1.2 eV using a high resolution velocity map imaging spectrometer.

In the higher energy region, the sole data available is the measurement of Domesle *et al.* at a wavelength of 266 nm (4.66 eV) [112]. They obtained β by measuring the photoelectron time of flight (TOF) inside a magnetic-bottle spectrometer and subsequently modeling trajectories with Monte Carlo methods. Their result (0.0 ± 0.1) is in disagreement with our measurement (-0.177 ± 0.05). The reason for such a discrepancy is unclear. If we note that good agreement is reached for the $O(^1D)$ channel, where distribution is strongly asymmetrical ($\beta \simeq -1$), we may speculate that the fitting of the experimental electron TOF distribution with the Monte Carlo model is appropriate only for directional emission, and fails in the case of emission close to isotropic due to non isotropic spurious effects.

The present results fall in fair agreement with the results of Cooper and Zare [57], who established the eponymous formula for the asymmetry parameter and computed β using radial dipole matrix elements obtained from the model potential of Robinson and Geltman [109]. The Cooper and Zare formula is further simplified by the formula due to Hanstorp *et al.* [116], under the assumption that radial dipole matrix elements follow the Wigner threshold law,

$$\beta = 2A_2\varepsilon\frac{A_2\varepsilon - 2c}{1 + 2A_2^2\varepsilon^2}, \tag{2.50}$$

where ε is the photoelectron energy. The parameter A_2 is related to the ratio between the radial dipole matrix elements coupling the initial state to the s and d continua, and the parameter c is the cosine of the phase shift difference between the s and d outgoing waves. We have fitted

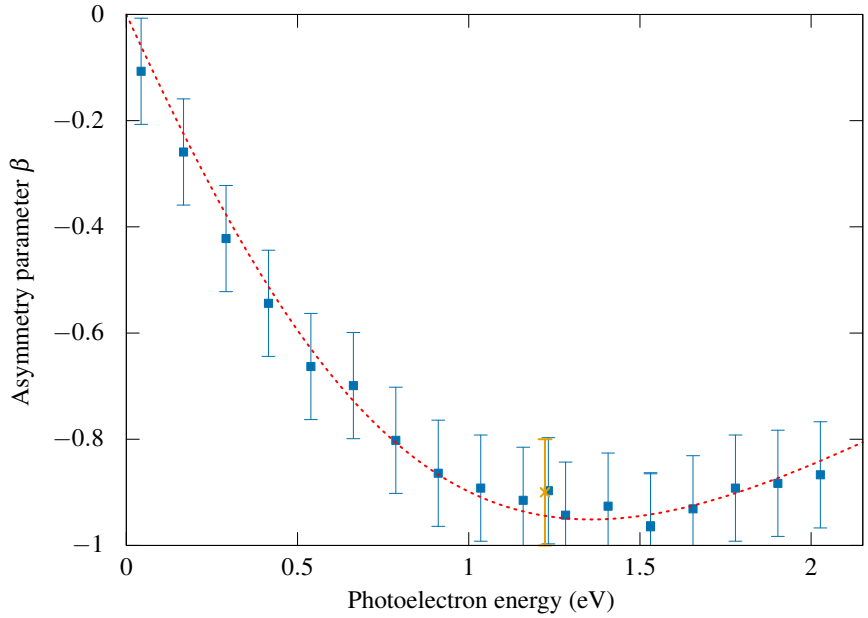

Figure 2.17: *Asymmetry parameter for photodetachment of O^- leaving O in the ^{1}D state. Full squares: present experiment, empty square: Domesle et al. [112], shifted by -0.01 eV for clarity. Dotted line: best fit to the present results using the model of Hanstorp et al. [116].*

the available experimental data below 2 eV with the above formula, obtaining $A_2 = 1.132$ eV^{-1} and $c = 0.940$, values close to those of Hanstorp *et al.* [116]. Agreement between the fit and the present values is satisfactory at low energies and degrades for photoelectron energies above 1.5 eV. This energy is already well beyond the range of validity of the Wigner threshold law used to derive Eq. (2.50), and such an extended agreement may be due to the fact that the Wigner law is used only to determine a ratio between two dipole matrix elements [116].

The asymmetry parameter obtained from the same *ab initio*, *R*-Matrix calculation used to determine the total cross section [117] is also shown in Fig. 2.16. Results from calculations using the length and velocity forms of the dipole matrix, shown by the full and chain lines, both fall in good agreement with the present measurement over the whole energy range covered. Length form results lie a few percent above the experimental values at higher photoelectron energies and velocity form data are a few percent lower, but the two remain within error bars. As a final note, we mention that the asymmetry parameter was also computed using density functional theory by Liu and Ning [146], however

its shape largely differs from that represented in Fig. 2.16.

Data concerning the asymmetry parameter for photodetachment leaving oxygen in its first excited state $O(^1D)$ is much scarcer, and is represented in Fig. 2.17. As expected, the β parameter follows the general trend given by the Cooper and Zare formula for p-electron photodetachment. At a wavelength of 266 nm (4.66 eV), the agreement is excellent between the present β parameter (-0.90 ± 0.10) and the value of -0.90 ± 0.10 measured by Domesle *et al.* [112]. The dotted line represents our best fit of the present results using the formula of Hanstorp *et al.* [116], with parameters $A_2 = 0.727$ eV^{-1} and $c = 0.963$.

2.5.4 Two-photon total cross section

The two-photon detachment of the oxgyen anion was studied at the Nd:YAG laser wavelength, $\lambda = 1064$ nm, using the extension of the animated-crossed-beam technique we developed earlier. Results related to the extension itself are first presented, followed by the experimental value of the two-photon generalized cross section. The influence of the photon statistics is discussed in details at the end of the section.

In Fig. 2.18, we show an example of the measured detachment yield as a function of the vertical position of the laser beam, normalized for the laser pulse energy and the ion current. The corresponding basis expansion is shown by the full line and relies on a set of 300 Gaussian functions with widths corresponding to laser waists from 30 μm to 200 μm. We intentionally chose an oversized basis to test the robustness of the method. The NNLS algorithm and the Tikhonov regularization method give the same expansion coefficients to within 2%. They are non-zero only for two functions with widths corresponding to laser waists of 60 μm and 60.7 μm, in excellent agreement with an independent measurement of the waist. Indeed, by passing a razor blade at the focal point and measuring the transmitted energy, we estimated the radius of the laser spot to be 60 μm. Using (2.20), the value obtained for the cross section is $\sigma^{(2)} = 1.49 \times 10^{-57}$ m^{4}s, while (2.32) gives $\sigma^{(2)} = 1.50 \times 10^{-57}$ m^{4}s.

The uncertainties arising from systematic effects are listed in Table 2.3. The finite response time of the fast photodiode yields an uncertainty in the ratio $\Delta^2/\Delta^{(2)}$, which is estimated to lie below 2%. The energy meter has a 3% calibration accuracy according to the manufacturer, and a comparison with another energy meter gives a 5% uncertainty. The latter thus provides a conservative estimate for the pulse energy error. The uncertainty in the coefficients of the expansion is lower than 3%. The 3% uncertainty in the height L of the slit, which enters the determination of the basis functions Ψ_m in equation (2.29), results in

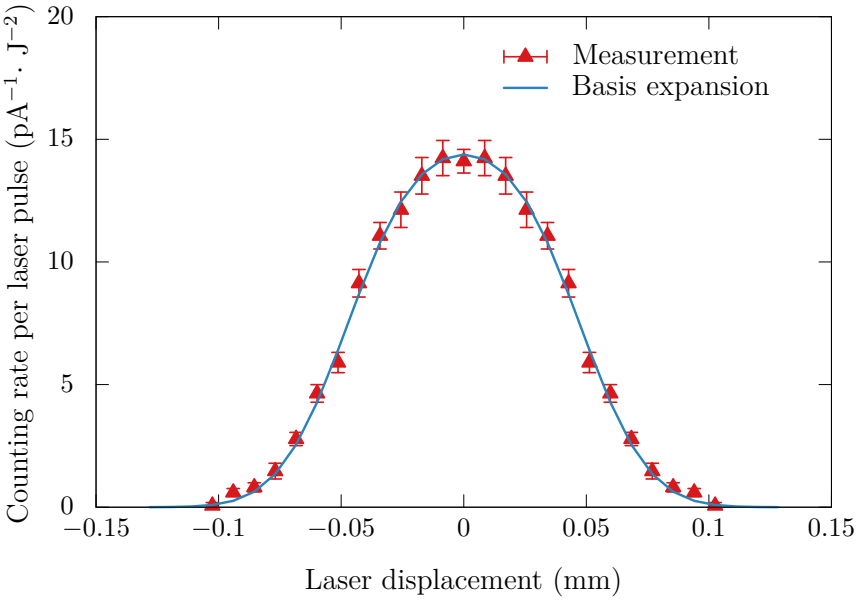

Figure 2.18: *Number of neutrals per laser pulse (triangles) as a function of the vertical displacement Y of the laser beam. The data is an average over 31 vertical scans. It has been normalized for the laser pulse energy and the ion beam current, and was subsequently symmetrized. The full line is the result obtained from the basis expansion.*

an uncertainty from 7% to 15% in the cross section depending on the quality of the measurement. The total error is then computed following the NIST guidelines [143], and is a simple quadrature sum of the different uncertainties.

The experimental generalized two-photon detachment cross section is shown in Fig. 2.19 and compared against available data. The dot-dashed, broken and full curves correspond respectively to the results of an R-Matrix Floquet calculation for the $M_L = 0$ and $\mid M_L \mid = 1$ magnetic sublevels of the initial $O^-(^2P^o)$ state and their statistically averaged sum [117]. The characteristics of the RMF calculations are the same as for one-photon detachment results presented above. The averaged sum displays a maximum for a photon energy in the region of 0.95 eV, corresponding to a photoelectron energy of about 0.234 eV, coming mainly from the $\mid M_L \mid = 1$ contribution which is dominant over most of the energies considered here. The results of the perturbation theory calculation by Robinson and Geltman [109] also display a similar maximum albeit some 10% larger than in the R-matrix Floquet case.

	Relative uncertainty
Vertical displacement Y	2%
Ions velocity v	1%
Power/energy meter $P_{\text{laser}}/E_{\text{laser}}$	5%
Detection efficiency η	5%
Photodiode rise time	2%
Slit height L	7 to 15%

Table 2.3: *Experimental uncertainties arising from systematic effects.*

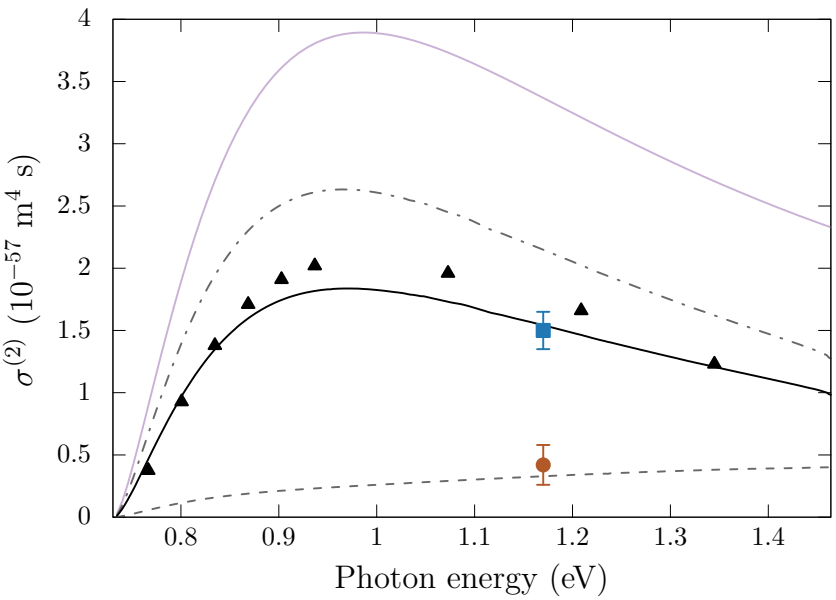

Figure 2.19: *Generalized cross section for two-photon detachment of $O^-(1s^2 2s^2 2p^5\ {}^2\mathrm{P}^o)$. The dot-dashed and broken lines are the results of an R-matrix Floquet calculation for the $M_L = 0$ and $\mid M_L \mid = 1$ sublevels of the initial anion state respectively, while the solid line is their statistical average [117]. The full triangles are the results from perturbation theory based on a one-electron model potential [109]. The thin solid line is the results obtained from the adiabatic-theory approach [121]. The full circle is the experimental value of [120] while the full square is our new absolute experimental result. The error bars are the combined statistical and systematic uncertainties.*

The results of Gribakin and Kuchiev [121, 154] are about twice those of the *R*MF calculation. They were obtained from an analytical formula for the n-photon detachment cross sections ($n \geq 2$) of negative ions, derived from an adiabatic-theory approach. This expression should give better results when more photons are absorbed.

At the photon energy of 1.165 eV, corresponding to the Nd:YAG laser wavelength, the *R*MF calculations yield a generalized cross section of $1.55 \times 10^{-57}\,\mathrm{m}^4\,\mathrm{s}$, some 20% smaller than that obtained using perturbation theory [109] and thus much larger than the older experimental value [120]. Our new measurement gives a generalized cross section of $(1.50 \pm 0.16) \times 10^{-57}\,\mathrm{m}^4\,\mathrm{s}$, almost four times larger than the previous experiment and thus in very good agreement with the results of our *R*-Matrix Floquet calculations and those obtained by Robinson and Geltman [109].

Let us now consider the influence of the photon statistics on the experimental generalized cross section. It is well established that temporal fluctuations of the intensity due to mode beating enhance the efficiency of n-photon ionization and detachment [137–139]. In the limit of an infinite number of modes, the enhancement factor reaches $n!$. Pulsed, high power lasers exhibit in general a large number of modes and previous studies of two-photon detachment have taken the photon statistics into account by dividing the value of the cross section extracted from the data by two [120]. Our Nd:YAG laser also operates in the multimode regime, but can be seeded to force single-mode operation. It is further possible to characterize the distribution of the modes by measuring the temporal profiles of the laser pulses. Figure 2.20 (a) shows such profiles measured with a 25 GHz photodiode connected to a 3 GHz oscilloscope, with the full line corresponding to the unseeded case and the dashed line to the seeded one. Figure 2.20 (b) shows the norm of the Fourier transform of the difference between the temporal envelope of a single pulse and the mean temporal envelope, averaged over 500 pulses. In the seeded case, the temporal envelope is smooth, as expected for single-mode operation, and, in the Fourier spectrum, the single peak centered at the origin is reminiscent of the Fourier transform of the envelope. In the multimode case (full line), intensity modulations due to mode beating appear on the temporal profile and, in the Fourier spectrum, 8 additional peaks are observed at integer multiples of the 237 MHz frequency, which matches the free spectral range of the cavity. The laser pulse therefore consists of at least 9 modes.

The generalized cross section extracted from the data is $(1.59 \pm 0.27) \times 10^{-57}\ \mathrm{m}^4\mathrm{s}$ in the multimode case and $(1.50 \pm 0.16) \times 10^{-57}\ \mathrm{m}^4\mathrm{s}$ in the single mode case, therefore, surprisingly, no effect of photon statis-

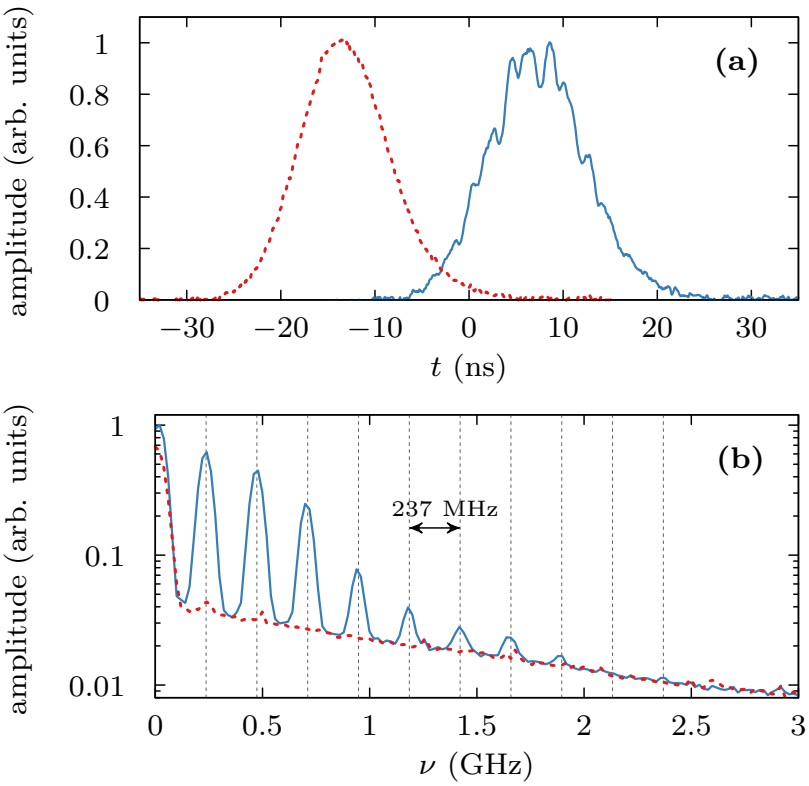

Figure 2.20: *(a) Temporal profile of the pulses from the seeded (dashed) and unseeded (full) Nd:YAG laser, and (b) norm of the Fourier transform of the difference between the temporal profile of a single pulse and the mean temporal profile, averaged over 500 pulses. The temporal profile of the seeded laser has been shifted in time for clarity. The vertical dashed lines indicate integer multiples of the free spectral range of the laser cavity.*

tics is observed within the error bars. The possible reasons for such an absence are twofold. First, the number of modes is low, hence deviations due to photon statistics may be lower than $n!$. As an example, the experiment of Lecompte *et al.* [138] considered the 11-photon ionization of xenon for an increasing number of modes and approximately reached the $n!$ factor when more than 100 modes were present in the cavity. Second, in the present crossed-beam configuration, the traversal time of the anions through the diameter of the square of the spatial intensity profile is about 273 ps while the intensity modulations due to mode beating have a period higher than ~ 1 ns. As the ions travel through the laser spot, the pulse envelope is essentially constant, and photon statistics do not influence the two-photon detachment process.

2.6 Conclusion

The animated-crossed-beam technique (ACBT), originally developed for electron-ion collisions, was used to measure absolute, total photodetachment cross sections. We demonstrated that it can be adapted to the laser-atom case irrespective of whether the beams are pulsed or continuous. It provides with a direct link between the one-photon cross section and easily measurable quantities: laser power, ion current and integrated detachment signal. The absence of any assumption on the shape of the interacting beams makes for a robust and reliable technique, capable of providing benchmark data. Its attractive features can be extended to the case of multiphoton ionization and detachment at the price of an increased mathematical complexity and a few necessary assumptions on the shape of the beams, which, we believe, are less stringent than in usual techniques. The extension relies on the deconvolution and Abel inversion of the detachment signal through a basis expansion.

In a first step, the one-photon detachment cross section of H^- was measured in the 700-1064 nm wavelength range. The results obtained with the ACBT are found to be in excellent agreement with most of the previous experimental determinations and with recent, compelling theoretical studies. This, we believe, confirms the benchmark capabilities of the technique. In a second step, the one-photon total detachment cross section of O^- was measured and the results obtained are significantly larger than those from previous experiments, but in agreement with the most recent, *ab initio* R-Matrix Floquet calculation [117]. This resolves, in turn, a long lasting discrepancy between theory and experiment and has important implications since the O^- photodetachment cross section was often used to put relative cross sections for other negative ions

on an absolute scale. The cross section behavior around the opening of the $O(^1D)$ threshold has been measured in details for the first time and the available experimental data was extended up to just below the $O(^1S)$ threshold. The two-photon generalized detachment cross section was measured at the Nd:YAG frequency and falls in excellent agreement with the same *R*MF calculation, thus resolving another long-standing discrepancy.

A VMI spectrometer was designed and built so as to permit the use of a fast anion beam and a perpendicular detection geometry. It allowed us to study photoelectrons emitted upon the one-photon detachment of O^- and measure the branching ratio between the ground and first excited states of oxygen and the asymmetry parameters of each channel. Branching ratios fall in fair agreement with the single experimental data point available, and, sufficiently far above the $O(^1D)$ threshold, indicate that photodetachment leaves about 20% of the atoms in the $O(^1D)$ excited state while the rest is in the ground state. Fine structure branching ratios were also measured close to thresholds and fall in fair agreement with previous works. Their theoretical values were further used to determine the initial fine structure population distribution of O^-, which corresponds to a temperature of above 2000 K. Asymmetry parameters were measured for both $O(^3P)$ and $O(^1D)$ final states and up to photon energies of 5.5 eV. They exhibit the characteristic behavior of p-electron detachment, resulting in electron emission perpendicular to the laser polarization axis at intermediate photoelectron energies. Agreement is good with most other experimental and theoretical works and we could, again, substantially extend the photon energy range over which experimental data is available.

The present work shows that, by combining both the animated-crossed-beam technique and velocity map imaging technique with widely tunable broadband laser systems, one can determine the complete set of parameters governing photodetachment in an absolute manner. The resulting data gives information on even minute details, such as fine structure branching ratios, and provides with stringent tests of theoretical methods both for benchmark anions and for open-shell systems which still somewhat challenge theories.

Chapter 3

Double photodetachment of He^- in strong laser fields

3.1 Introduction

3.1.1 State of the art

Helium can not attach an extra electron and form a stable negative ion, and the same is true of all rare gas atoms. It possesses nevertheless a rich spectrum of quasi-bound states with energies higher than the helium ground state, and thus embedded in the detachment continuum. One of these states, $He^-(1s2s2p\ ^4P^o)$, is *metastable* against spontaneous decay back to $He(1s^2\ ^1S)$ since the ejection of an electron does not fulfill the selection rules for Coulomb autodetachment. Indeed, the total spin S is not conserved and decay occurs only *via* weak spin-orbit and spin-spin interactions. Furthermore, spontaneous decay to other states of helium is not permitted since it lies 77.5 meV below the first excited state $He(1s2s\ ^3S)$ [38]. The He^- anion is thus metastable, with lifetimes from 7.8 μs to 359 μs depending on the fine structure component considered (J =1/2, 3/2 or 5/2) [39]. This is sufficiently long for most studies to be carried out and, because it is a doubly-excited system in which electron-electron correlations are important, it has received a lot of attention over the years [36].

Double photodetachment (DPD) is the absorption of one or several photons by a negative ion and the ejection of two electrons. While double photoionization, its counterpart for atoms, has been extensively studied, data is scarcer concerning double photodetachment, in particular on the experimental side [36]. Notwithstanding experimental challenges, and in particular producing sufficient anion densities, the important structural

differences between negative ions and atoms are expected to alter the dynamics of double electron ejection and makes the study of DPD and its comparison with double photoionization attractive.

If its energy is chosen above the double detachment threshold[1], a single photon is sufficient to induce DPD through the direct or sequential emission of two electrons and these processes have been studied for a number of anions [6, 155–157]. We consider in the following photon energies *below* the double detachment threshold, for which DPD can only occur through multiphoton absorption. Because the electron affinity is much lower than the first ionization potential, multiphoton DPD involves, in general, the one-photon single detachment of the anion followed by the multiphoton ionization of the intermediate atom. The second, multiphoton ionization step is efficient only for high light intensities hence multiphoton DPD is best observed with pulsed, high energy lasers. Early work on double photodetachment involved moderately strong fields ($\sim 10^{10}$ W/cm^2) and aimed either at studying excess photon detachment, *i.e.* , the absorption by the system of more photons than is energetically required, or at performing the spectroscopy of autoionizing states embedded in the continuum [158, 159]. The detection of positive ions following photodetachment is also at the basis of resonant ionization spectroscopy, although in this case the atom is optically excited to a Rydberg state and ionized by a static electric field [74]. This technique has been used a number of times to explore autoionizing states of He^- [75, 160–162]. Yet, in all the above studies, the production of positive ions is only a means to study the negative ion and the ionization dynamics of the second electron are not considered in detail. More recently, a number of works were devoted to the search for genuine strong field effects in double photodetachment [163–168]. Within the much higher light intensities reached with modern femtosecond lasers ($> 10^{13}$ W/cm^2), additional DPD dynamics were observed involving rescattering of the first photoelectron onto the atomic target [168]. Interestingly, the influence of the magnetic quantum number M_L on strong field DPD has also been discussed within the frame of Ammosov-Delone-Krainov or Keldysh-like models [166, 167], and it was shown to be of some importance in the saturation of the second, ionization step.

Within a purely sequential picture and for moderately strong fields, the DPD of He^- first proceeds by the one-photon detachment of the anion, leaving helium atoms in the $1s2s\,^3S$ and $1s2p\,^3P^o$ states which can then ionize by absorption of n additional photons. Therefore DPD of He^- can be viewed as a means to (i) produce excited, triplet states of he-

[1]That is, the sum of the electron affinity and first ionization potential of the atom

lium which are hard to produce with other, conventional methods and (ii) study their subsequent photoionization. While photoionization of ground state helium has been extensively studied and is today very well understood both theoretically and experimentally [169], little is known concerning the photoionization of its excited states. Early experiments by Stebbings *et al.* [170] gave a first account of the photoionization cross sections from the $1s2s\,^{1,3}S$ states, along with theoretical work by, for example, Burgess and Seaton [171] and by Jacobs [172]. Later, Gisselbrecht *et al.* [173] used high-harmonic generation techniques to measure photoionization cross sections of the 1s2p and 1s3p singlet states, obtaining satisfactory agreement with theoretical work by Chang and Zhen [174] and Chang and Fang [175].

Data concerning *multiphoton* ionization (MPI) of excited states of helium are even scarcer. In 1974, Dunning and Stebbings [176] used a 2-photon ionization scheme, but focused on the determination of single-photon ionization cross sections of $^3P^o$ states. Lompré *et al.* [177] investigated two-photon ionization of the $1s2s\,^{1,3}S$ excited states of helium for two wavelengths, a phenomenon Haberland *et al.* [178] also considered in a narrow wavelength region around 500 nm where the process is resonantly enhanced. More recently, Madine and van der Hart [179, 180] used R-matrix Floquet theory (RMF) to examine the competition between multiphoton ionization of inner and outer shell electrons of the $1s2s\,^1S$ and $1s3s\,^1S$ states of helium in a vacuum ultraviolet radiation field.

3.1.2 Double detachment of He^-

A schematic view of the double detachment process and the energy levels involved is shown in Fig. 3.1. Two different wavelength ranges are considered: the range from 530 nm to 560 nm (range I, dotted arrows), where the $1s2s\,^3S$ transient state gives the dominant DPD contribution, and the range from 685 nm to 730 nm (range II, full arrows), where DPD proceeds *via* the $1s2p\,^3P^o$ transient state.

In both ranges, the first step, shown on the left, involves the one-photon detachment of He^- and leaves an helium atom in the $1s2s\,^3S$ and $1s2p\,^3P^o$ states. In range I, the helium atom must absorb at least three photons to ionize from the $1s2s\,^3S$ state and two photons to do so from the $1s2p\,^3P^o$ state. It is well known that ionization efficiency can be enhanced by intermediate resonant states, *e.g.*, one of the many high-lying $1sns$ and $1snd$ states that can be reached by two-photon absorption from the $1s2s\,^3S$ state. Absorption of one further photon leads to the emission of an electron in the $\ell = 1, 3$ continua, and the whole process

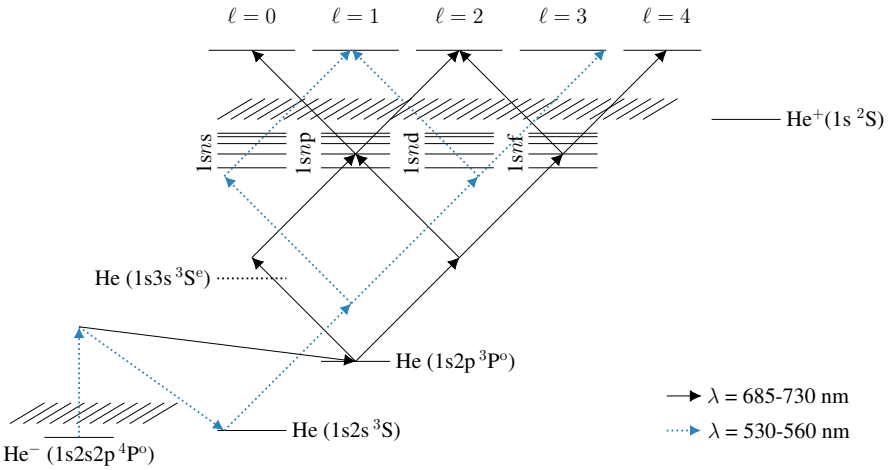

Figure 3.1: *Schematic energy level diagram of He^- and He. The dotted arrows show the pathway responsible for double detachment of He^- via the 1s2s transient state and its (2+1) REMPI in wavelength range I. The solid arrows show the pathway via the 1s2p state and its (1+1+1) and (2+1) REMPI in wavelength range II.*

may be described as following a (2+1) resonance-enhanced multiphoton ionization (REMPI) scheme. One may thus expect double detachment to proceed preferentially through REMPI of the 1s2s transient state[2], even though the number of photons required is higher than through the *non resonant*, 2-photon ionization of the 1s2p state.

In range II, the helium atom must absorb at least three photons to ionize from both the 1s2s ^{3}S and 1s2p ^{3}P^o states. High-lying 1snp and 1snf states can be reached by resonant two-photon absorption from the 1s2p ^{3}P^o state, from which absorption of one further photon leads to the emission of an electron in the $\ell = 0, 2, 4$ continua. The whole process thus follows a (2+1) REMPI scheme. Figure 3.1 also reveals the existence of another possible REMPI scheme: for $\lambda \approx 706.7\,\mathrm{nm}$, the photon energy $\omega \approx 1.7543$ eV coincides with the energy difference between the field-free He(1s2p ^{3}P^o) and He(1s3s ^{3}S) states. The latter is in one-photon resonance with the 1s11p state which can emit a photoelectron in the $\ell = 0, 2$ continua by absorbing one further photon. Such a (1+1+1) REMPI scheme is rare in atomic multiphoton ionization since the most studied initial state, the ground state, is far below the excited states. The presence of two intermediate resonant states instead of only one significantly enriches the ionization behaviour. The

[2]It should be clear that, although we shall omit to specify the term sometimes, all 1s$n\ell$ states belong to the triplet symmetry

competition between the two REMPI schemes is also interesting as their respective importance depends on the magnetic quantum number M_L of the initial state 1s2p ^{3}P^o. For $M_L = \pm 1$, only the well-known (2+1) scheme is allowed while for $M_L = 0$, the (1+1+1) process is also permitted. We shall see that these different pathways and properties induce a very unusual behavior in the double photodetachment rates as a function of the laser wavelength, which extends quite far from the resonance between the field-free He(1s2p ^{3}P^o) and He(1s3s ^{3}S) states due to their one-photon dynamic Stark mixing.

3.2 Experimental setup

The first stage of the experimental setup, sketched in Fig. 3.2, comprises a duoplasmatron source fed with He gas and producing an He^+ beam that is mass selected by a permanent magnet and accelerated to 4 keV. The beam is then passed through a cesium vapour cell, where single and double charge transfer converts He^+ ions into He(1s2s ^{1,3}S) and He^-(1s2s2p ^{4}P^o) respectively. The production of He^- requires a large target density for multiple collisions to occur, resulting in a conversion efficiency of around 1%. After the vapor cell, a double deflection, using electrostatic plates, cleans the beam of its neutral and positive components. The remaining He^- beam is passed into the laser interaction region which is pumped to a high vacuum of about 10^{-8} mbar. Although He^- is metastable, the lifetimes of its various fine structure components, 359 μs for $J = 5/2$, 12.3 μs for $J = 3/2$ and 7.8 μs for $J = 1/2$ [39], are sufficiently long to allow the use of conventional beam transport techniques. Contamination of the beam by ground state helium atoms due to spontaneous detachment only occurs at the percent level.

The 1 mm ion beam is illuminated perpendicularly by nanosecond pulses from a tunable dye laser pumped by the second or third harmonics of a Nd:YAG laser. Coumarin 500 and Pyridine 1-2 dyes were used to cover wavelength ranges from 530 nm to 560 nm (range I) and 685 nm to 730 nm (range II) respectively. A pyroelectric detector constantly monitors the pulse energy, which can be attenuated using a half-wave plate mounted on a high accuracy rotation stage and a polarizing beamsplitter cube, both placed at the output of the dye laser. The $\lambda/2$-plate is servo-controlled by the detector to ensure a constant pulse energy along the dye gain curve. Laser light is then focused onto the ion beam inside the vacuum chamber by an $f = 40$ cm lens and collected, at the exit of the chamber, by the pyroelectric detector. The size of the waist at focus is about 54 μm, resulting in a peak intensity of 3.9×10^{10} W/cm^2

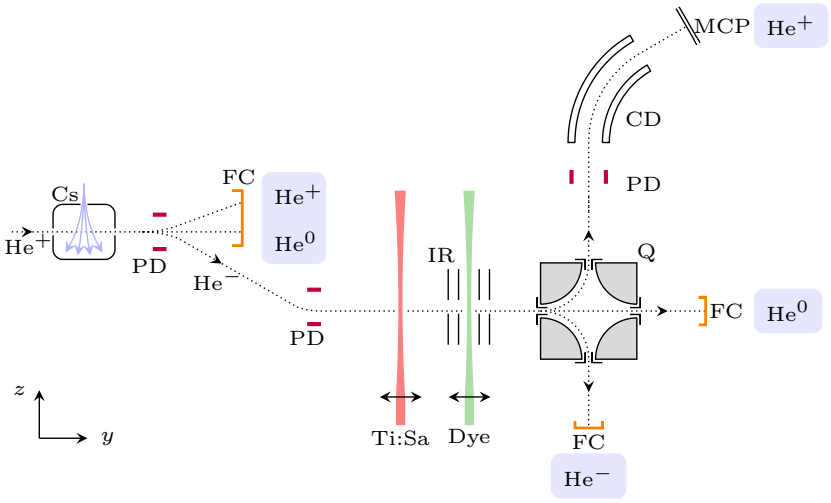

Figure 3.2: *Experimental setup. Cs: cesium vapor cell; PD: planar deflector; FC: Faraday cup; CD: cylindrical deflector; IR: interaction region; Q: quadrupolar deflector; MCP: multichannel plates; Ti:Sa: Ti:Sapphire laser beam; Dye: dye laser beam. Double arrows indicate convergent lenses. The laser beams propagate along the z direction and their polarizations, when linear, are along the y axis.*

for 8 mJ pulses. A $\lambda/4$-plate can be disposed between the lens and the attenuator to change the polarization of the laser beam from linear to circular or elliptic. No mirrors are used after it in order to avoid spurious depolarization.

Ions traverse the laser spot (twice the waist) in about 250 ps, which is much shorter than the pulse duration whose full width at half maximum is 4.8 ns. During their transit, a few He^- ions are converted into He^+ by double detachment. Because of the spatial and temporal profiles of the laser and ion beams, the measured signal is averaged over the focal volume and integrated over the pulse duration.

The resulting He^+ ions are subsequently analyzed in energy by a quadrupolar deflector [181] coupled with a 60° cylindrical deflector in order to ensure the detection of laser-induced double detachment events only. Negative ions are collected at the opposite side of the quadrupole in a Faraday cup. In addition to the energy analysis, a temporal gating of the 60° deflection and the signal acquisition is performed: the cylindrical deflector is switched on only during a narrow time window centred around the time of flight of laser-produced He^+, whose hits on the multi-channel plates are subsequently recorded in coincidence with a square signal of a few tens of nanoseconds, appropriately delayed with

respect to the laser pulse. The energy selection and temporal gating reduce the background to less than 3 counts per hundred laser shots, as determined in a shifted time window of the same duration.

The use of multi-channel plates allows the detection of single ions. As a result of this extreme sensitivity, however, it is not possible to distinguish between single and multiple ion formation within the same laser shot. A correction must be applied to the measured rate to account for the Poisson probability distribution of multiple double photodetachment events,

$$N_{\text{corr}} = -N_p \ln(1 - N_{\text{meas}}/N_p), \tag{3.1}$$

where N_{meas} (N_{corr}) is the measured (corrected) number of events measured after N_p laser pulses. The corrected results are further normalized by the measured He^- current. In the spectra presented below, the ionization yield at each wavelength is recorded over more than 1000 laser pulses. The overall uncertainty is of the order of 5-10% and is dominated by counting statistics with small contributions from the pulse energy readout and variations in the laser pulse shape.

In order to assess the sequential nature of the double detachment process, light from a tunable, CW Ti:Sapphire laser was focused onto the anion beam before it entered the interaction region in order to photodetach He^- ions prior to their exposure to the dye laser light. The Ti:Sapphire laser was tuned to $\lambda = 1005$ nm in order to maximize the detachment cross section to the He(1s2p $^3P^o$) state, which reaches 3.6×10^{-19} m^2 [182, 183], and thus produce, in vast majority (99%), atoms in the 1s2p state. The atoms then fly to the interaction region where they are intersected by the dye laser beam. The 5 mm spatial separation between the light beams ensures that the detachment and REMPI events are sequential. During transit between the two laser foci, about 10% of the He(1s2p $^3P^o$) states decay spontaneously into He(1s2s ^3S).

When detecting He^+ ions, we must be able to discriminate between the two color process, with detachment by the Ti:Sapphire laser and ionization by the dye laser, and the dominant one color process, where detachment and ionization occur within the same dye laser pulse. To do so, a bias of 100 V is applied to the region of interaction with the dye laser. He^+ ions produced by double detachment in this region gain an energy of 200 eV while those produced by ionization of incoming He atoms gain only 100 eV. He^+ ions produced by either the Ti:Sapphire laser or collisions with the residual gas outside the interaction region gain no energy. The subsequent energy analysis performed by the quadrupolar and cylindrical deflectors readily separates the various contributions.

3.3 Theoretical methods

Double photodetachment (DPD) is treated theoretically in two separate steps. First, an R-Matrix calculation treats the single photodetachment of He^- and provides partial cross sections to the various final states and magnetic sublevels of the atom. Multiphoton ionization (MPI) of He is then treated within the R-Matrix Floquet (RMF) theory framework, which provides *ab initio*, non perturbative and time-independent data. In order to model the experiment in details, an effective Hamiltonian treatment of MPI is developed, checked against RMF and then used to simulate the experimental DPD yields. Atomic units ($\hbar = 1, e = 1, m_e = 1$) are used unless otherwise stated.

3.3.1 R-Matrix theory for single photodetachment

One-photon detachment of He^- has been studied in some detail over the past few decades, with particular emphasis on resonances with doubly excited states (see for example the review article [36] and references therein). In the wavelength ranges spanned by the present study (685-730 nm and 530-560 nm), no such resonances are accessible and the cross section is smooth. Overall, there is relatively good agreement between the various theoretical and experimental results in this region [182–190]. Previous studies have however dealt only with *linear* polarization, whilst our present goal is to study double detachment under arbitrary elliptical polarization. Moreover, while partial cross sections into the He(1s2s ^{3}S) and He(1s2p ^{3}P^o) states have been considered by some authors, no information exists on partial cross sections to the various magnetic sublevels of a given term, *e.g.* He(1s2p ^{3}P^o) with $M_L = 0, \pm 1$. Such partial cross sections are not anecdotal since, as we shall see in the next chapters, the dynamics of resonance-enhanced multiphoton ionization of He(1s2p ^{3}P^o) strongly depend on the magnetic quantum number M_L.

The required partial cross sections σ_j can be calculated by first establishing a formula relating them to reduced dipole matrix elements, which do not depend neither on polarization nor on M_L, and later calculating these matrix elements with the R-Matrix method. Let us first investigate how the σ_j's can be expressed, via angular momentum algebra, in terms of matrix elements coupling the initial and final states. We assume L-S coupling and consider only dipole-allowed transitions. Since the initial state, 1s2s2p ^{4}P^o, has a total spin $S_i = 3/2$, the dipole selection rules impose that the residual atom must be left in a triplet state. For ease of notation, we therefore do not explicitly specify the spin quantum numbers in what follows.

We consider an initial state of the unpolarized anion, denoted by $|\alpha_i L_i M_{L_i}\rangle$, where L_i is the orbital angular momentum of the state i, M_{L_i} its magnetic quantum number and where α_i represents all other numbers required to specify the state. The final state in channel c $|\alpha_c L_c \ell L M_L\rangle$ is, asymptotically, the product of the wave functions of the residual atomic state $|\alpha_c L_c M_{L_c}\rangle$ and of the ejected electron $|\epsilon_c \ell m_\ell\rangle$, coupled to give a total angular momentum L and total magnetic quantum number M_L. The partial cross section for photodetachment to a particular magnetic sublevel M_{L_c} averaged over the initial magnetic sublevels is given in the length form by,

$$\sigma_{L_c,M_{L_c}}(\hat{\boldsymbol{\epsilon}}) = \frac{4\pi^2 \alpha a_0 \omega}{2L_i+1} \sum_{M_{L_i}} \sum_{L,M_L,L'} \sqrt{(2L+1)(2L'+1)}$$
$$\sum_{\ell,m_\ell} \begin{pmatrix} L_c & \ell & L \\ M_{L_c} & m_\ell & -M_L \end{pmatrix} \begin{pmatrix} L_c & \ell & L' \\ M_{L_c} & m_\ell & -M_L \end{pmatrix}$$
$$\times \langle \alpha_c L_c \ell L' M_L | D(\hat{\boldsymbol{\epsilon}}) | \alpha_i L_i M_{L_i} \rangle^* \langle \alpha_c L_c \ell L M_L | D(\hat{\boldsymbol{\epsilon}}) | \alpha_i L_i M_{L_i} \rangle \,, \quad (3.2)$$

which is derived from the general expression of the dipole matrix elements given by Burke [51]. α is the fine-structure constant, a_0 is the Bohr radius, ω is the photon angular frequency and $D(\hat{\boldsymbol{\epsilon}})$ is the dipole length operator for a given polarization vector $\hat{\boldsymbol{\epsilon}}$. The dipole matrix elements for arbitrary elliptical polarization can be related to the reduced dipole matrix elements $(\alpha_c L_c \ell L || \boldsymbol{D} || \alpha_i L_i)$ using the Wigner-Eckart theorem,

$$\langle \alpha_c L_c \ell L M_L | \, D(\hat{\boldsymbol{\epsilon}}) \, | \alpha_i L_i M_{L_i} \rangle = (\alpha_c L_c \ell L || \boldsymbol{D} || \alpha_i L_i) \times (-1)^{-L-M_L}$$
$$\times \left[\begin{pmatrix} L & 1 & L_i \\ -M_L & 0 & M_{L_i} \end{pmatrix} \sqrt{\cos 2\varepsilon} - \begin{pmatrix} L & 1 & L_i \\ -M_L & \pm 1 & M_{L_i} \end{pmatrix} \sqrt{2} \sin \varepsilon \right] \quad (3.3)$$

where $\boldsymbol{D}$ is the tensor operator corresponding to $D(\hat{\boldsymbol{\epsilon}})$. The polarization vector $\hat{\boldsymbol{\epsilon}}$ is expressed within the "natural" frame of reference of Tumaikin and Yudin [191, 192],

$$\hat{\boldsymbol{\epsilon}} = \mathbf{e}_0 \sqrt{\cos 2\varepsilon} - \mathbf{e}_{\pm 1} \sqrt{2} \sin \varepsilon. \quad (3.4)$$

where $\mathbf{e}_{0,\pm 1}$ are spherical unit vectors [53] and the ellipticity angle ε can take the values $-\pi/4 \leq \varepsilon \leq \pi/4$. On the right-hand side, the helicity of the vector $\mathbf{e}_{\pm 1}$ corresponds to the sign of ε. The polarization is linear when $\varepsilon = 0$, left circular when $\varepsilon = \pi/4$ and right circular when $\varepsilon = -\pi/4$. Similarly, the complex conjugate of the dipole matrix

element appearing in Eq. (3.2) is calculated from the reduced dipole matrix element using

$$\langle \alpha_c L_c \ell L' M_L | \, D(\hat{\boldsymbol{\epsilon}}) \, | \alpha_i L_i M_{L_i} \rangle^* = (\alpha_c L_c \ell L' || \boldsymbol{D} || \alpha_i L_i)^* \times (-1)^{-L'-M_{L_i}}$$

$$\times \left[\begin{pmatrix} L' & 1 & L_i \\ -M_L & 0 & M_{L_i} \end{pmatrix} \sqrt{\cos 2\varepsilon} + \begin{pmatrix} L' & 1 & L_i \\ -M_L & \mp 1 & M_{L_i} \end{pmatrix} \sqrt{2} \sin \varepsilon \right]. \quad (3.5)$$

The present expression for $\hat{\boldsymbol{\epsilon}}$ differs from the usual choice for elliptical polarization which reads $\hat{\boldsymbol{\epsilon}} = -\mathbf{e}_{+1} \sin(\varepsilon + \pi/4) + \mathbf{e}_{-1} \cos(\varepsilon + \pi/4)$ and corresponds to a choice of the quantization axis ($\hat{\boldsymbol{z}}$) along the light propagation axis, typical of circular polarization. However, when $\varepsilon = 0$, this usual expression is in contradiction with the convention for linear polarization, in which the electric field vector is chosen as the quantization axis ($\hat{\boldsymbol{\epsilon}} = \mathbf{e}_0$). Conveniently, the natural frame bridges the linear and circular conventions together by performing a continuous rotation of the reference frame as the ellipticity angle evolves from 0 to $\pi/4$, going from $\hat{\boldsymbol{z}}$ along $\vec{E}$ to $\hat{\boldsymbol{z}}$ along the light propagation direction. The reference frame thus *depends* on the ellipticity angle, although comparison with standard conventions is straightforward in the limiting cases of linear and circular polarization. Since the choice of the reference frame is arbitrary, any other frame would yield identical results for the partial photodetachment cross sections, keeping in mind that the M_L values are projections of the angular momentum along the quantization axis and must thus be appropriately rotated for meaningful comparison.

The cumulated photodetachment probability to a particular final state $|\alpha_c L_c M_{L_c}\rangle$ is readily obtained from the partial cross sections by solving the rate equation $dN(t)/dt = -\sigma\phi(t)N(t)$ with appropriate boundary conditions,

$$P_{\alpha_c, L_c, M_{L_c}}(t) = \frac{\sigma_{\alpha_c, L_c, M_{L_c}}}{\sigma} \left[1 - \mathrm{e}^{-\int_{-\infty}^{t} dT \sigma \phi(T)} \right], \quad (3.6)$$

where $\phi(T)$ is the instantaneous photon flux and the total cross section σ is obtained by summing the partial cross sections over all quantum numbers. Note that the intensity, or photon flux, required for double detachment is very high and therefore, in the region where it occurs, the exponential term on the right hand side of the above equation is essentially zero, *i.e.* , photodetachment is saturated.

In order to compute the partial cross sections (3.3) and hence the cumulated photodetachment probability, we require the reduced dipole matrix elements $(\alpha_c L_c \ell L || \boldsymbol{D} || \alpha_i L_i)$, which are independent of the polarization. These can be extracted from standard R-matrix calculations

using the UK APAP (Atomic Processes for Astrophysical Plasmas) suite of computer codes [193]. In the rest of the section we give details on the calculation, together with some illustrative results to assess the reliability of the reduced dipole matrix elements thus obtained.

In the R-matrix approach, configuration space is divided into two regions by a sphere encompassing the charge density of all states of the residual atom included in the calculation. Within this sphere, the states of the $(N+1)$-electron system are represented by a discrete set of antisymmetrized basis functions built from linear combinations of the residual atomic states coupled with a set of continuum orbitals representing the ejected electron, supplemented by a number of bound or short-range correlation configurations. The $(N+1)$-electron Hamiltonian is diagonalized in this basis, and the resulting eigenvalues and eigenvectors are used to construct the inverse logarithmic derivative matrix or R-matrix on the boundary of the inner region. In the outer region, the ejected electron moves far from the target while the other electrons remain bound. Exchange between the ejected and bound electrons can then be neglected, so that the wavefunctions for the full system can be represented by a standard close-coupling expansion involving products of the residual atomic states and a set of unknown functions representing the ejected electron. These unknown functions satisfy an infinite set of coupled second-order differential equations, with the appropriate asymptotic boundary conditions determining if the solutions represent a bound state of the initial anion or a continuum state of the atom plus ejected electron. The initial bound state and final continuum states are then determined by matching the solutions in the inner and outer regions at their common boundary. For the initial bound state, this matching can only be performed at discrete energies, which are found by an iterative search algorithm.

Since the initial He^- anion has a $^4P^o$ symmetry, after photodetachment the residual oxygen atom can only be left in a triplet state. The present calculation includes the five lowest triplet states of helium, whose wave functions were obtained using the `CIV3` atomic structure computer code [194, 195]. The energies and excitation thresholds thus obtained are presented in table 3.1, where they are compared with those of a more accurate calculation [196] and with the values recommended by the National Institute of Standards and Technology (NIST). Oscillator strengths and transition probabilities are compared with the NIST values in table 3.2.

In the R-matrix calculation, the inner region extends out to $40\,a_0$, and 30 continuum orbitals per angular momentum ℓ are used to represent the ejected electron. The $(N+1)$-electron Hamiltonian in the inner

Table 3.1: *Energies and excitation thresholds for the five lowest triplet states of helium. The theoretical values are compared with the accurate, non-relativistic energies taken from Drake [196] and the thresholds recommended by the National Institute of Standards and Technology (NIST) [150].*

	Present (au)	Drake (au)	Present (au)	NIST (au)
1s2s 2^3S	-2.17513	-2.17523	0.0	0.0
1s2p 2^3P^o	-2.13294	-2.13316	0.04219	0.04206
1s3s 3^3S	-2.06866	-2.06869	0.10647	0.10653
1s3p 3^3P^o	-2.05798	-2.05808	0.11714	0.11714
1s3d 3^3D	-2.05562	-2.05564	0.11951	0.11958

Table 3.2: *Oscillator strengths f and rates A in length (L) and velocity (V) forms for dipole allowed transitions involving the five lowest triplet states of helium, compared with the values recommended by NIST [150]. The figures in parentheses are the powers of ten by which the preceeding number must be multiplied.*

Transitions		f		A ($\sec^{-1}$)	
		Present	NIST	Present	NIST
1s2s – 1s2p	L	0.5421	0.5394	0.1033 (8)	0.1022 (8)
	V	0.5320		0.1014 (8)	
1s2s – 1s3p	L	0.5744 (-1)	0.6448 (-1)	0.8442 (7)	0.9475 (7)
	V	0.6378 (-1)		0.9373 (7)	
1s2p – 1s3s	L	0.7019 (-1)	0.6951 (-1)	0.2795 (8)	0.2785 (8)
	V	0.6786 (-1)		0.2703 (8)	
1s2p – 1s3d	L	0.6161	0.6102	0.7100 (8)	0.7070 (8)
	V	0.6085		0.7012 (8)	
1s3s – 1s3p	L	0.9126	0.8914	0.1114 (7)	0.1074 (7)
	V	0.8693		0.1061 (7)	
1s3p – 1s3d	L	0.1095	0.1120	0.1179 (5)	0.1292 (5)
	V	0.1055		0.1136 (5)	

region is diagonalized for the initial $^4\mathrm{P^o}$ symmetry and the three final symmetries $^4\mathrm{S^e}$,$^4\mathrm{P^e}$, $^4\mathrm{D^e}$ allowed by the dipole selection rules. In the outer region, imposing decaying boundary conditions on the solutions of the coupled second-order differential equations in the $^4\mathrm{P^o}$ symmetry yields an electron affinity of about 75.5 meV for the initial He^- state. This compares favourably with the value of 77.5 meV obtained both by experiment [38] and by a more extensive calculation [197], and is slightly better than that of an earlier R-matrix calculation [182], in which the computed electron affinity was then slightly adjusted to agree with the accurate value. While such small differences may be important close to threshold, they have little effect on the overall cross sections in the range of photon wavelengths (500-800 nm) considered in this study, and we do not perform such an adjustment here.

3.3.2 R-Matrix Floquet theory for multiphoton ionization

R-Matrix Floquet theory [198, 199] allows atomic processes in a laser field to be described in an *ab initio* and non-perturbative way. The theory has been successfully applied to the investigation of multiphoton ionization, laser-assisted scattering, harmonic generation and laser-induced continuum states. Details of the theory together with particularly illustrative examples of its application can be found in the recent books [200] and [51]. Here, only those features that are relevant to the current study will be outlined.

The wave function of an $(N+1)$-electron system in a linearly polarized laser field described in the dipole approximation by the vector potential $A_0\hat{\boldsymbol{\epsilon}}\cos\omega t$ can be expressed in terms of a Floquet-Fourier expansion

$$\Psi(\boldsymbol{X}_{N+1},t) = \mathrm{e}^{-\mathrm{i}Et}\sum_{n=-\infty}^{\infty}\mathrm{e}^{-\mathrm{i}n\omega t}\Psi_n(\boldsymbol{X}_{N+1}), \tag{3.7}$$

where $\boldsymbol{X}_{N+1}$ is the set of space and spin coordinates of all $N+1$ electrons. Inserting (3.7) into the time-dependent Schrödinger equation

$$\mathrm{i}\frac{\partial}{\partial t}\Psi(\boldsymbol{X}_{N+1},t) = \left[H_{N+1} - \frac{\mathrm{i}}{\mathrm{c}}\boldsymbol{A}(t)\cdot\sum_{e=1}^{N+1}\boldsymbol{\nabla}_e + \frac{N+1}{2\mathrm{c}^2}\boldsymbol{A}^2(t)\right]\Psi(\boldsymbol{X}_{N+1},t)$$

yields an infinite set of time-independent coupled equations for the Floquet components $\Psi_n(\boldsymbol{X}_{N+1})$. These equations can be solved efficiently using the R-matrix approach of partitioning configuration space into sub-regions with locally adapted gauges and reference frames.

The inner region is defined as the sphere of radius a encompassing the N-electron states $\Phi_i(\boldsymbol{X}_N)$ retained in the calculation to describe the residual ion. The components $\Psi_n(\boldsymbol{X}_{N+1})$ are expanded in a basis of fully antisymmetrized wave functions built from $\Phi_i(\boldsymbol{X}_N)$ and continuum orbitals $u_{n\ell}$ satisfying a fixed logarithmic boundary condition at $r = a$. The most appropriate gauge to use in this region is the length gauge, in which the interaction of the atomic system with the laser field is proportional to the distance of the electrons from the nucleus. The corresponding Hamiltonian is diagonalized in the Floquet $(N + 1)$-electron basis. The amplitudes of the eigenvectors at $r = a$ and the eigenvalues are used to calculate the R-matrix elements, *i.e.* the inverse of the logarithmic derivatives in the reaction channels.

In the outer region, the photoelectron moves far from the nucleus while the other electrons remain bound. Since the radiative interaction in the length gauge diverges at large distances, a transformation to the velocity gauge is performed on the photoelectron, while the interaction of the field with the other electrons is still described in the length gauge. In the outer region, exchange of the photoelectron with the remaining bound electrons is negligible so that (3.7) reduces to an infinite set of ordinary differential equations that can be solved using a close-coupling approach combined with a log-derivative propagation method. At sufficiently large distances, the solutions are matched to Siegert outgoing boundary conditions defined in the acceleration frame where the close-coupling equations are asymptotically uncoupled and propagated inwards using an asymptotic expansion technique. The matching is possible only at particular complex quasi-energies E, whose real part gives the Stark-shifted energy of the dressed atomic states and whose imaginary part is minus half the dressed state ionization rate. The quasi-energies for each state are found by an iterative search in the complex energy plane, usually starting from the zero-field values, and followed adiabatically as the laser frequency or intensity changes. Near resonance, this can require very small steps and hence a very large number of individual calculations. This is also true when the imaginary part of the state being followed is extremely small, for example the 1s2p state.

As the photon energy is relatively small, the residual He^+ ion can be assumed to be left in its ground state. Since the initial state is $He(1s2p\,{}^3P^o)$, the set of N-electron states $\Phi_i(\boldsymbol{X}_N)$ is limited to $He^+(1s)$. Due to this approximation, the ionization potentials of $He(1s2p\,{}^3P^o)$ and $He(1s3s\,{}^3S)$, respectively 3.5333 eV and 1.8637 eV, are underestimated by 0.05 eV and 0.005 eV. The radius of the inner region was taken to be $6\,a_0$. Seven Floquet components (5 absorption and one emission) were retained in expansion (3.7), together with angular momenta ℓ up to 11.

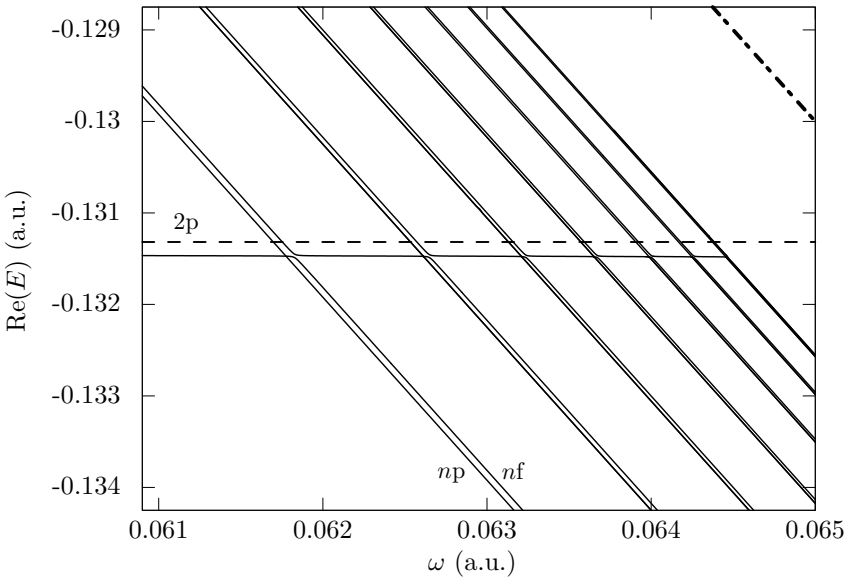

Figure 3.3: *Real part of the RMF quasi-energies for $M_L = \pm 1$ and dressed Rydberg states from $n = 8$ to $n = 14$, as a function of the laser angular frequency at a fixed intensity of 3.6×10^{10} W/cm^2. The dashed line indicates the zero-field energy of the 1s2p state and the thick dot-dashed line in the upper right corner is the two-photon ionization threshold.*

The inner region solutions were propagated to $65\,a_0$ where they were matched to outgoing Siegert boundary conditions.

The real part of the quasi-energies obtained are shown in Fig. 3.3 for $M_L = \pm 1$ and Fig. 3.4 for $M_L = 0$ as a function of the photon energy ω. In Fig. 3.3, the horizontal line corresponds to the energy of He(1s2p ^{3}P^o) state while the slanted lines correspond to the energy of the Rydberg He(1snp) and He(1snf) states dressed by two photons. Figure 3.4 also includes the He(1s3s ^{3}S) state dressed by one photon. A detailed explanation of these figures will be given in section 3.6, but one can already see major differences between the $M_L = \pm 1$ and $M_L = 0$ cases, hinting at different physical behaviours depending on the value of the magnetic quantum number. For $M_L = 0$, the presence of the 1s3s state dressed by one photon gives rise to a very large avoided crossing around $\omega_r = 0.06282$ a.u. between the 1s2p and 1s3s energy curves, reflecting the strong interaction between these two states which is absent in the $M_L = \pm 1$ case. The energy of He(1s2p ^{3}P^o) is shifted down for $\omega < \omega_r$ and up for $\omega > \omega_r$, in contrast to the $M_L = \pm 1$ case where the energy is always shifted down. The Stark shift of the Rydberg states

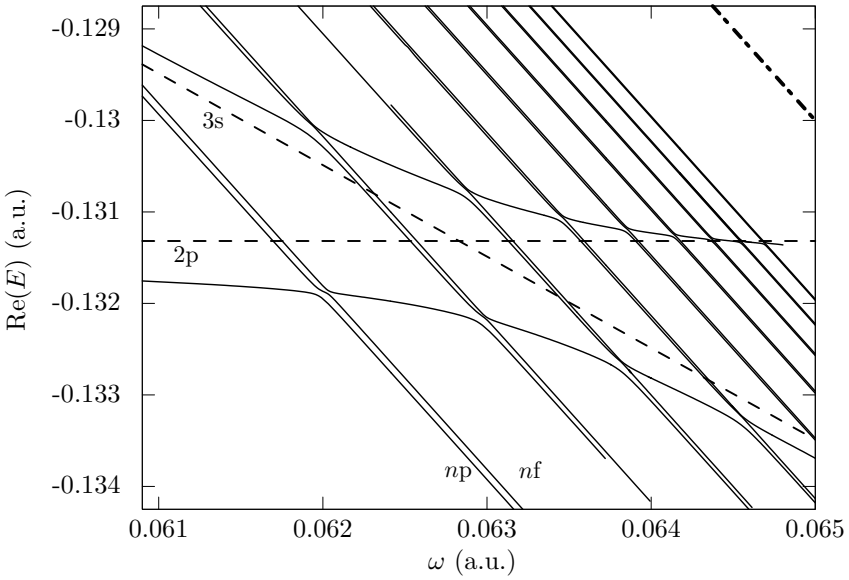

Figure 3.4: *Real part of the RMF quasi-energies for $M_L = 0$ and dressed Rydberg states from $n = 8$ to $n = 16$, as a function of the laser angular frequency at a fixed intensity of 3.6×10^{10} W/cm^2. The horizontal dashed line indicates the zero-field energy of the 1s2p state, while the oblique dashed line represents the zero-field energy of the 1s3s state shifted down by ω. The thick dot-dashed line in the upper right corner is the two-photon ionization threshold.*

(present as a series of lines with slope -2ω) is negligible.

The RMF calculation corresponds to a well-defined intensity but a simple time-dependent picture can be built using a naive two-state model involving the strongly interacting 1s2p and 1s3s states. This is justified by the observation that in the RMF calculation the Rydberg states are not appreciably perturbed by the field. The field-dressed wave functions can be written as

$$|\psi_+(t)\rangle = \sin\theta(t)\,|2\mathrm{p}\rangle + \cos\theta(t)\,|3\mathrm{s}\rangle\,, \tag{3.8}$$

$$|\psi_-(t)\rangle = \cos\theta(t)\,|2\mathrm{p}\rangle - \sin\theta(t)\,|3\mathrm{s}\rangle\,, \tag{3.9}$$

with

$$\theta(t) = \frac{1}{2}\arctan\left(\frac{\Omega(t)}{\Delta}\right), \qquad 0 \le \theta(t) \le \pi/2. \tag{3.10}$$

The detuning Δ is defined by $\Delta = E_{3\mathrm{s}} - \omega - E_{2\mathrm{p}}$ while $\Omega(t)$ is the Rabi frequency

$$\Omega = \mathscr{E}_0(t)\,\langle 3\mathrm{s}|\,\hat{\boldsymbol{\epsilon}}\cdot\boldsymbol{r}\,|2\mathrm{p}\rangle \tag{3.11}$$

with $\mathscr{E}_0(t)$ the amplitude of the electric field at time t, $\hat{\boldsymbol{\epsilon}}$ the polarization vector and $\boldsymbol{r}$ the radial coordinate of the electron. Defining $E_0 = (E_{3s} - \omega + E_{2p})/2$, the energies of the two states are given by

$$E_\pm = E_0 \pm \frac{1}{2}\sqrt{\Omega^2(t) + \Delta^2} \tag{3.12}$$

which tend to $E_0 \pm |\Delta|/2$ as the electric field and hence $\Omega(t)$ tends to zero.

We first consider $\Delta > 0$, corresponding to photon energies below the 1s2p-1s3s resonance. For vanishing fields, θ tends to 0 and the 1s2p state corresponds to $|\psi_-\rangle$ while the 1s3s state corresponds to $|\psi_+\rangle$. As the electric field increases, the energy of the 1s2p evolves adiabatically as E_-, *i.e.* is shifted down with respect to the field-free energy. As the Rydberg states are not appreciably perturbed by the field, this results in a blue shift of the 1s2p-1snp resonances. When the photon energy is above the 1s2p-1s3s resonance, we have $\Delta < 0$ and hence $\theta = \pi/2$ for vanishing fields. The 1s2p state thus corresponds to $|\psi_+\rangle$ and its energy evolves adiabatically as E_+, inducing a red-shift in the resonance positions.

This naive approach provides some insight on the mechanisms taking place in the ionization process under study. In particular, the sign of the shift is determined uniquely by the laser frequency ω, while its amplitude varies in time following $\mathscr{E}_0(t)$. The change from blue to red shift is expected to leave a strong signature in the experimental ionization spectra, along with major differences between the $M_L = 0$ and $M_L = \pm 1$ cases.

The next section is dedicated to a more realistic model of the experiment.

3.3.3 Effective Hamiltonian theory for multiphoton ionization

The RMF theory is a powerful tool for studying multiphoton ionization of complex atoms but may require lengthy computation, especially close to resonance. It is therefore not adapted to a detailed modeling of an actual experiment where ionization rates over a large range of laser intensities are required. A more practical and versatile approach is provided by effective Hamiltonian (EH) theory [201], whose scope goes well beyond atom-laser interactions, as shown in the comprehensive reviews by Killingbeck and Jolicard [202, 203].

The underlying idea of EH theory is twofold. First, the Hilbert space is partitioned into two different subspaces: the *model* space $\mathscr{P}$,

containing the most relevant states of the problem, which in our case are the quasi-resonant bound states, and its orthogonal complement $\mathscr{Q}$, spanning the rest of the Hilbert space. Second, the exact Hamiltonian is "folded" into a smaller, effective Hamiltonian which couples explicitly only those states belonging to the model space. The effect of states in the $\mathscr{Q}$-space is treated through additional perturbative matrix elements, illustrating the *semi-perturbative* nature of the EH approach. The choice of which states to include in the model space is of critical importance since the effective Hamiltonian aims at preserving the main physical properties of the process under study while treating perturbatively or even omitting the remaining states.

We have built two effective Hamiltonian aiming at describing the REMPI of the He(1s2s ^{3}S) and He(1s2p ^{3}P^o) states respectively. For the 1s2s state, the $\mathscr{P}$-space includes the 1s2s ^{3}S, 1sn ^{3}S and 1snd ^{3}D states with n spanning the 4–27 range. In the case of the 1s2p state, the $\mathscr{P}$-space includes the 1s2p ^{3}P^o, 1s3s ^{3}S, 1s3d ^{3}D, 1snp ^{3}P^o and 1snf ^{3}F^o states, with n spanning the range 6–45. The $\mathscr{Q}$-space is truncated to a finite size and includes ^{3}S, ^{3}D and ^{3}G states together with high-lying ^{3}P^o and ^{3}F^o states with n up to 70. Continuum states with $\ell = 0 - 5$ are included up to energies where bound-free couplings are negligible. The energy of the 1s2p ^{3}P^o, 1s3s ^{3}S and 1s3d ^{3}D states, respectively -0.133154, -0.0686816 and -0.0556288 a.u. are taken from the NIST database [150], while the energy of the Rydberg states is calculated from their principal quantum number and quantum defect [196].

The effective Hamiltonian H_{eff} gives rise to the following eigenvalue equation:

$$H_{\text{eff}} \left|\psi_p\right\rangle = E \left|\psi_p\right\rangle , \tag{3.13}$$

where the wave function $|\psi_p\rangle$ spans the model space and the complex eigenvalue E has a real part ideally identical to an eigenvalue of the exact Hamiltonian. A complete and rigorous derivation of general effective Hamiltonians has been given by Durand [204] while the application of EH theory to multiphoton ionization is described by Baker [201]. A detailed account on the derivation of an effective Hamiltonian for the present problem is given in Appendix A. The effective Hamiltonian, valid up to the second-order in the atom-field interaction, is written as

$$H_{\text{eff}} = PH_0P + PVP + P\left(S + \Omega - \mathrm{i}\frac{\Gamma}{2}\right)P \tag{3.14}$$

where V is the exact atom-field interaction operator and H_0 the exact "free" Hamiltonian, containing the field-free atomic Hamiltonian and the light-field Hamiltonian. The eigenvalues of the bound states of H_0 will

be denoted by $E_i = \mathcal{E}_i - m\omega$, where $\mathcal{E}_i$ is the energy of the field-free bound states and m is the number of photons absorbed. By convention, m is 0 for 1s2s ^{3}S and 1s2p ^{3}P^o, 1 for 1s3s ^{3}S and 1s3d ^{3}D , and 2 for the Rydberg states in the model space. The eigenvalues of the continuum states of H_0 are, similarly, $e = \varepsilon - 3\omega$, where ε is the photoelectron energy. P is the Feshbach projection operator, projecting the wave function onto the $\mathscr{P}$-space:

$$P = \sum_{i \in \mathscr{P}} |i\rangle \langle i| . \tag{3.15}$$

The operators S, Ω and Γ are perturbations of the states in the model space due to those in $\mathscr{Q}$-space. Their physical significance is standard in second-order perturbation theory: S and Ω are two-photon transition operators connecting quasi-resonant bound states via, respectively, the non-resonant bound states and the ionization continuum states ($\mathscr{Q}$-space), while Γ is the ionization width of the model space states. They are given by

$$S = \sum_{k \in \mathscr{Q}} \frac{V |k\rangle \langle k| V}{E_i - E_k}, \tag{3.16}$$

$$\Omega = \mathcal{P} \int \mathrm{d}e \frac{V |e\rangle \langle e| V}{E_i - e}, \tag{3.17}$$

$$\Gamma = 2\pi V |e\rangle \langle e| V \Big|_{e=E_i}, \tag{3.18}$$

where $|e\rangle$ is an ionization continuum state, identified by the photoelectron energy ε, its angular momentum ℓ and magnetic quantum number m_ℓ. Similarly, $|k\rangle$ is a bound state in $\mathscr{Q}$-space identified by the principal, angular and magnetic quantum numbers n, ℓ and m_ℓ. $\mathcal{P}\int$ represents a Cauchy principal value integration.

In practice, the calculation of the various elements of H_{eff} is performed within the dipole and rotating-wave approximations [205], justified by the moderate laser intensities involved and the treatment of only quasi-resonant bound states. The interaction of the j-th electron with the laser field is given by the dipole moment operator $\hat{\boldsymbol{\epsilon}} \cdot \boldsymbol{r}_j$, with $\hat{\boldsymbol{\epsilon}}$ the polarization vector and $\boldsymbol{r}_j$ the radial coordinate of the electron.

The two-photon dipole matrix elements between the 1s2p and 1s$n\ell$ bound states are calculated using perturbation theory:

$$V^{(2)}_{2\mathrm{p}n\ell} = \frac{\mathscr{E}_0^2}{4} \sum_k \frac{\langle 1\mathrm{s}n\ell \mid \hat{\boldsymbol{\epsilon}} \cdot \boldsymbol{R} \mid k\rangle \langle k \mid \hat{\boldsymbol{\epsilon}} \cdot \boldsymbol{R} \mid 1\mathrm{s2p}\rangle}{\mathcal{E}_{1\mathrm{s2p}} + \omega - \mathcal{E}_k}, \tag{3.19}$$

where $\mathscr{E}_0$ is the amplitude of the electric field, $\boldsymbol{R} = \boldsymbol{r}_1 + \boldsymbol{r}_2$, and the sum is over all intermediate bound and continuum states coupled to the initial and final states. The one-photon dipole matrix elements appearing in (3.19) are obtained from a two-electron Coulomb Discrete Variable Representation (DVR) [206] calculation which is able to furnish accurate energies for a large number of states, as well as their oscillator strengths. In this method, the two-electron wavefunctions are expanded in a basis of antisymmetrized linear combinations of the product of two one-electron DVR basis functions, themselves constructed from zeroes of a reference Coulomb function. Diagonalizing the two-electron Hamiltonian in this basis yields a set of energies and wavefunctions, of which the lowest correspond to the physical bound states while the others are pseudostates representing higher lying excited states and the continuum. The infinite sum appearing in (3.19) is then replaced by a finite sum over these states and pseudostates.

The dipole moments connecting Rydberg and continuum states are calculated using Quantum Defect theory (QDT) [207]. Their angular parts are given by straightforward angular momentum algebra whereas their radial parts

$$\int_0^\infty \mathrm{d}r R^*_{\varepsilon\ell}(r) r^3 R_{\bar{n}\ell}(r) \tag{3.20}$$

are obtained by numerical integration of the bound and continuum QDT radial wave functions:

$$rR_{\bar{n}\ell}(r) = K(\bar{n},\ell) W_{\bar{n},\ell+1/2}(2r/\bar{n}), \tag{3.21}$$

$$rR_{\varepsilon\ell}(r) = s(\varepsilon,\ell;r)\cos[\pi\delta_\ell(\varepsilon)] + c(\varepsilon,\ell;r)\sin[\pi\delta_\ell(\varepsilon)] \tag{3.22}$$

where $\delta_\ell(\varepsilon)$ is the quantum defect extrapolated to positive photoelectron energy ε; $s(\varepsilon,\ell;r)$ and $c(\varepsilon,\ell;r)$ are the normalized regular and irregular Coulomb functions [153]; $K(\bar{n},\ell)$ is a normalization factor [207] and $W_{\bar{n},\ell+1/2}(2r/\bar{n})$ a Whittaker function. In order to avoid divergence at $r = 0$, the irregular Coulomb and Whittaker functions are also multiplied by a cut-off factor $[1-\exp(-\tau_\ell r)]^{2\ell+1}$ [171]. In QDT, the effective principal quantum number $\bar{n}$ is given by the difference of the principal quantum number n and the associated quantum defect $\delta_\ell(n)$. The values used here are calculated from Ritz's expansion with coefficients taken from Drake [196]. Coulomb and Whittaker functions are calculated using the routines by Barnett [208] and Noble [209] respectively, while quadratures are performed with the standard QUADPACK routines [210] requesting a 10^{-6} relative accuracy. We have verified that this numerical approach allows the fast generation of bound-free dipole moments for

photoelectron energies ranging from 0 to a few a.u. and Rydberg bound states up to $n = 98$, the limit of the Whittaker function routine.

It is then straightforward to obtain the numerical values of the two-photon matrix elements

$$\Gamma_{ij} = \frac{\pi \mathscr{E}_0^2}{2} \left\langle j \right| \hat{\boldsymbol{\epsilon}} \cdot \boldsymbol{r} \left| e \right\rangle \left\langle e \right| \hat{\boldsymbol{\epsilon}} \cdot \boldsymbol{r} \left| i \right\rangle \Big|_{e=E_i} \tag{3.23}$$

from the one-photon dipole matrix elements. The matrix element

$$\Omega_{ij} = \frac{\mathscr{E}_0^2}{4} \mathcal{P} \int \mathrm{d}e \frac{\langle j| \hat{\boldsymbol{\epsilon}} \cdot \boldsymbol{r} |e\rangle \langle e| \hat{\boldsymbol{\epsilon}} \cdot \boldsymbol{r} |i\rangle}{E_i - e} \tag{3.24}$$

requires an additional Cauchy principal value integration, performed numerically. The computational costs can be reduced by making extensive use of the $\bar{n}^{-3/2}$ scaling of single photon bound-bound and bound-free dipole moments.

Dipole matrix elements $\langle j|\hat{\boldsymbol{\epsilon}} \cdot \boldsymbol{r}|i\rangle$ are considered above without specifying the polarization vector $\hat{\boldsymbol{\epsilon}}$. As we aim at studying multiphoton ionization under arbitrary elliptical polarization, they should in principle be calculated for all $\hat{\boldsymbol{\epsilon}}$ vectors. Such calculations are prohibitive but can be greatly simplified, as for the photodetachment of He^-, by virtue of the Wigner-Eckart theorem. It is indeed sufficient to notice that the reduced matrix elements $(n'\ell'||\boldsymbol{D}||n\ell)$ and $(e\ell'||\boldsymbol{D}||n\ell)$ are independent of $\hat{\boldsymbol{\epsilon}}$, and thus need be computed only once. Dipole matrix elements can then be obtained from their reduced counterparts using Eq. (3.3). Moreover, since two-photon matrix elements are sums or integrals of products of two one-photon terms, similar observations apply. For example, the coupling Ω_{ij} can be obtained with

$$\Omega_{ij} = \frac{\mathscr{E}_0^2}{4} \sum_{\ell'} p_{\ell',m_{\ell'}\ell_j,m_{\ell_j}}(\varepsilon) p_{\ell_i,m_{\ell_i},\ell',m_{\ell'}}(\varepsilon) \Omega^{\mathrm{R}}_{i\ell' j}, \tag{3.25}$$

where $\Omega^{\mathrm{R}}_{i\ell' j}$ is a "reduced" matrix element given by

$$\Omega^{\mathrm{R}}_{i\ell' j} = \mathcal{P} \int \mathrm{d}e \frac{(j||\boldsymbol{D}||e\ell')(e\ell'||\boldsymbol{D}||i)}{E_i - e}, \tag{3.26}$$

and the factor $p_{\ell,m_\ell,\ell',m_{\ell'}}(\varepsilon)$ results from the Wigner-Eckart theorem,

$$\begin{aligned} p_{\ell,m_\ell,\ell',m_{\ell'}}(\varepsilon) &= (-1)^{-\ell'-m_{\ell'}} \\ &\times \left[\begin{pmatrix} \ell' & 1 & \ell \\ -m_{\ell'} & 0 & m_\ell \end{pmatrix} \sqrt{\cos 2\varepsilon} - \begin{pmatrix} \ell' & 1 & \ell \\ -m_{\ell'} & \pm 1 & m_\ell \end{pmatrix} \sqrt{2} \sin \varepsilon \right]. \end{aligned} \tag{3.27}$$

Note that the reduced matrix element $\Omega^{\mathrm{R}}_{i\ell' j}$ depends on the partial wave ℓ'. In the above 3 equations, ε denotes the *ellipticity angle*. We may finally note that, beyond its usefulness for polarization, the Wigner-Eckart theorem also allows matrix elements to be determined for all magnetic sublevels m_ℓ of a given state in a single calculation.

3.3.4 Detailed modeling of the experiment

The experimental process is, of course, time-dependent, hence its modelling must set the static EH picture developed above "in motion". The helium atom travelling through the laser pulse experiences a time-varying intensity envelope $I(t)$. Hence the quantities V, Ω, Γ and S in the EH theory also vary, V being proportional to $\sqrt{I(t)}$ and S, Ω and Γ to $I(t)$. Up to second-order in perturbation theory, the effective Hamiltonian H_{eff} derived from the time-independent eigenvalue equation also satisfies the time-dependent Schrödinger equation:

$$\mathrm{i}\hbar \frac{\mathrm{d}\,|\psi_p(t)\rangle}{\mathrm{d}t} = H_{\mathrm{eff}}(t)\,|\psi_p(t)\rangle \tag{3.28}$$

as shown by, *e.g.* , Baker [201] . A formal solution may then be written as

$$|\psi_p(t+\Delta t)\rangle = e^{-\mathrm{i}H_{\mathrm{eff}}(t)\Delta t/\hbar}\,|\psi_p(t)\rangle\,. \tag{3.29}$$

The wave function is propagated in time from -2×10^7 a.u. to 2×10^7 a.u. , in steps of $\Delta t \leq 10^4$ a.u., by numerically approximating the matrix exponential $e^{-\mathrm{i}H\Delta t}$ using routines from ExpoKit [211]. When considering REMPI of the 1s2s state, the model space wave function is given by

$$\begin{aligned}|\psi_p(t)\rangle =& c^0_{2s}(t)\,|2s0\rangle \\ &+ \sum_{n=4}^{27}\left[c^0_{ns}(t)\,|ns0\rangle + \sum_{m_\ell=-1}^{1} c^{m_\ell}_{nd}(t)\,|ndm_\ell\rangle\right],\end{aligned} \tag{3.30}$$

where the $1s$ orbital has been omitted in the $|n\ell m_\ell\rangle$ basis vectors for brevity. In the case of REMPI of the 1s2p state, the wave function reads

$$\begin{aligned}|\psi_p(t)\rangle = \sum_{m_\ell}\Big[&c^{m_\ell}_{2p}(t)\,|2pm_\ell\rangle + c^0_{3s}(t)\,|3s0\rangle + c^{m_\ell}_{3d}(t)\,|3dm_\ell\rangle \\ &+ \sum_{n=6}^{45}\Big(c^{m_\ell}_{np}(t)\,|npm_\ell\rangle + c^{m_\ell}_{nf}(t)\,|nfm_\ell\rangle\Big)\Big].\end{aligned} \tag{3.31}$$

The summations over m_ℓ run over the appropriate range for each basis vector. For linear polarizaton, selection rules ($\Delta m_\ell = 0$) permit only those states with the same magnetic quantum number as the initial state to be populated. This in turn keeps the sizes of the wave function and the effective Hamiltonian small, *e.g.* , 83×83 for the 1s2p state. In the general case of elliptic polarization, looser selection rules ($\Delta m_\ell = 0, \pm 1$) yield a significantly larger wave function and effective Hamiltonian, with a size up to 409×409 for the 1s2p state.

Initial conditions are obviously $c_{2\mathrm{s}0}(t = 0) = 1$ and $c_{2\mathrm{p}m_\ell}(t = 0) = 1$ for propagations from the 1s2s and 1s2p states respectively. All other coefficients are zero. Note that 3 independent propagations must be performed for each of the 3 magnetic sublevels ($m_\ell = 0, \pm 1$) of the 1s2p state. Although the wave function is initially normalized to unity, its norm may decrease with time due to the non-hermiticity of H_{eff}. This loss of normalization corresponds to an outgoing flux of electrons and its value after the propagation is the ionization probability P_i^+ of a given intial state $|i\rangle$. The values of the coefficients $c_{n\ell}$ at a particular time t provide the instantaneous amplitudes of the diabatic bound states.

In order to compute the double detachment probability P_{DPD} one must treat, in principle, detachment and ionization as two sequential events. P_{DPD} is related to the product of the instantaneous detachment probability $\frac{\mathrm{d}P^0(t)}{\mathrm{d}t}\big|_{t=t_0}$, evaluated at a time t_0, by the ionization probability $P_i^+(t_0)$, obtained from the numerical propagation of the atomic wave function starting at a time t_0. Moreover, since detachment may occur at any time t_0, the product must be integrated over t_0 and we obtain

$$P_{\mathrm{DPD}} = \int_{-\infty}^{+\infty} \mathrm{d}t_0 P_i^+(t_0) \frac{\mathrm{d}P^0(t)}{\mathrm{d}t}\Big|_{t=t_0}. \tag{3.32}$$

Following the above equation, propagation of the atomic wave function must be performed for a large number of starting times t_0 to compute $P_i^+(t_0)$, thus making the modeling computationally intensive. However, 3-photon ionization occurs at intensities that are much higher than those required for efficient photodetachment, *i.e.* at later times. Therefore the ionization probability P_i^+ is essentially independent of the time at which the atom is created by photodetachment since, in any case, multiphoton dynamics will start much later. In other words, $P_i^+(t_0)$ is in good approximation constant over the time region where instantaneous detachment probability is non-negligible, hence

$$P_{\mathrm{DPD}} \simeq P_i^+(t_0 \to -\infty) \times P^0(t_0 \to +\infty). \tag{3.33}$$

In this case, a single propagation of the wave function is sufficient to compute the double detachment probability, and the detachment and ionization events are considered independent. Note that the validity of this approximation has been successfully verified experimentally (see Sec. 3.6.2).

In the experiment, the laser operates near the TEM00 mode, with a Gaussian spatial profile. The time profile of the pulse, $g(\tau)$, has been measured by a fast photodiode and its analytic fit, used in the modeling, is given by the piecewise function

$$g(\tau) = \begin{cases} \cos^2(\pi \frac{\tau}{7.81}) & \text{if } 0 > \tau \geq -3.9, \\ e^{-(\tau/2.29)^2} & \text{if } \tau \geq 0, \\ 0 & \text{otherwise,} \end{cases} \tag{3.34}$$

where τ is in nanoseconds. This profile has a full width at half maximum of 4.8 ns. The confocal parameter of 2.62 cm, large compared to the diameter of the atomic beam, allows the waist size w_0 to be taken as constant across the atomic beam. The intensity profile is thus given by

$$I(t; x, \tau) \simeq I_0\, g(\tau + t)\, e^{-2(x^2 + (v_{\mathrm{He}} t)^2)/w_0^2}, \tag{3.35}$$

where I_0 is the peak intensity of the pulse, t the travel time through the laser beam, and v_{He} the velocity of the atom. The x-direction is perpendicular to the direction of both the laser and atomic beams. The parameter τ refers to the point on the pulse envelope experienced by the atom when at the center of the laser beam ($t = 0$). The time of flight of the atoms through the laser spot (250 ps) is much shorter than the pulse duration, hence the evolution of the pulse envelope during the time-propagation of the Hamiltonian can be assumed negligible, that is: $g(\tau + t) \sim g(\tau)$. Since the effective Hamiltonian $H_{\mathrm{eff}}(t)$ depends on the instantaneous intensity, it and thus the ionization probability $P_i^+(x, \tau)$ depend parametrically on x and τ.

To reproduce the experimental ionization spectra, a large number of propagations must be performed for different values of x and τ, taking into account the following experimental conditions:

i. the incoming He^- beam has a 1 mm diameter, which is much larger than the laser waist. The modeled ion signal must be averaged over the atomic beam cross section;

ii. the signal must be time-integrated over the pulse duration;

iii. the photodetachment of He^-, producing neutral helium, is not uniform across the beam cross section. Therefore the distribution of neutral helium is not uniform either.

The above considerations, along with the assumption of independent detachment and ionization, lead to the following expression for the simulated yield N_{1s2s} for double detachment *via* the 1s2s state:

$$N_{1s2s} = \int_{\Delta t} \mathrm{d}\tau \int_0^R \mathrm{d}x \; w(x)\, P^+_{1s2s}(x,\tau)\, P^0_{1s2s}(x,\tau)\, \Phi_{He^-}, \tag{3.36}$$

where Δt is the pulse duration, R the atomic beam radius, P^+_{1s2s} the probability to ionize neutral helium in the 1s2s state, P^0_{1s2s} the probability to photodetach He^- in the 1s2s channel and Φ_{He^-} the incoming He^- flux; $w(x)$ is the weight associated with the position x in the atomic beam, obtained from simple geometrical considerations:

$$w(x) = 4\sqrt{R^2 - x^2}. \tag{3.37}$$

The ω-dependence of N, P^+ and P^0 has been omitted from the notation for clarity. The limits $t_0 \to -\infty$ and $t_0 \to +\infty$ in the arguments of P^+_{1s2s} and P^0_{1s2s}, shown in Eq. (3.33), have been omitted for the same reason.

Similarly, the double detachment yield *via* the 1s2p state is the sum of the contributions of its various magnetic sublevels,

$$N_{1s2p} = \sum_{m_\ell} \int_{\Delta t} \mathrm{d}\tau \int_0^R \mathrm{d}x \; w(x)\, P^+_{1s2p,m_\ell}(x,\tau)\, P^0_{1s2p,m_\ell}(x,\tau)\, \Phi_{He^-}, \tag{3.38}$$

where P^0_{1s2p,m_ℓ} is the probability photodetach He^- into the 1s2p (m_ℓ) magnetic sublevel and P^+_{1s2p,m_ℓ} the probability to ionize it.

Let us now estimate the photodetachment probability $P^0_{\alpha_c L_c M_{L_c}}$ into any of the 4 possible final states. As explained above, we suppose that the detachment and ionization steps are independent and thus that P^0 is, in good approximation, the asymptotic value of the cumulated photodetachment probability,

$$P^0_{\alpha_c L_c M_{L_c}} \simeq P_{\alpha_c L_c M_{L_c}}(t \to \infty; x, \tau). \tag{3.39}$$

The cumulated probability $P_{\alpha_c L_c M_{L_c}}$ is given by Eq. (3.6) and now parametrically depends on x and τ since the light intensity and photon flux also do. Replacing the photon flux in Eq. (3.6) by a Gaussian profile identical to Eq. (3.35) and taking the limit $t \to \infty$, the above equation becomes

$$P^0_{\alpha_c L_c M_{L_c}}(x,\tau) \simeq \frac{\sigma_{L_c,M_{L_c}}}{\sigma} \left[1 - \exp\left(-\frac{I(0;x,\tau)}{\hbar\omega} \times \sqrt{\frac{\pi}{2}} \frac{w_0}{v_{He}} \times \sigma\right)\right] \tag{3.40}$$

where $I(0;x,\tau)/\hbar\omega$ is the photon flux and $\sqrt{\frac{\pi}{2}}w_0/v_{\rm He}$ the interaction time. We recall that $\sigma_{L_c,M_{L_c}}$ is the partial photodetachment cross section to a particular state of the atom and σ is the total cross sections. Both depend on the photon energy ω. Since REMPI occurs in regions of space and time where detachment is saturated, the exponential term in the above equation is essentially 0 and the probability is equal the branching ratio,

$$P^0_{\alpha_c L_c M_{L_c}}(x,\tau) \sim \frac{\sigma_{L_c,M_{L_c}}}{\sigma}. \tag{3.41}$$

Let us finally note that the simulated results are further multiplied by 0.56 to account for the MCP detection efficiency.

3.4 Single detachment of He^-

We have studied theoretically the one-photon, single detachment of He^- under elliptic polarization and in the wavelength range from 500 nm to 800 nm. As shown in figure 3.5, presenting the total photodetachment cross section for linear polarization, the agreement with the earlier work is very good. Branching ratios to the different M_L sublevels of the He(1s2s ^{3}S) and He(1s2p ^{3}P^o) final states in the range from 685 nm to 730 nm were calculated from reduced matrix elements using Eq. (3.2). The branching ratios are in fact only weakly dependent on the wavelength. A representative set is presented in Fig. 3.6, for different light polarizations at $\lambda = 690$ nm. They correspond to partial cross sections of 19.5×10^{-22} m^2 and 10.4×10^{-22} m^2 for the 1s2s and 1s2p states respectively, falling in good agreement with those calculated by Ramsbottom and Bell [182]. The population of the 1s2s state ($R_{2s} = 0.66$) is nearly twice that of the 1s2p state ($R_{2p} = 0.34$), and this sharing is independent of the ellipticity. The 1s2p state is slightly less populated at shorter wavelengths ($R_{2p} = 0.34$ for $\lambda = 685$ nm) and more populated at longer wavelengths ($R_{2p} = 0.4$ for $\lambda = 730$ nm).

The branching ratio to the 1s2s state with a single, isotropic sublevel $M_L = 0$ obviously does not depend on the ellipticity. The 1s2p state has three magnetic sublevels with $M_L = 0, \pm 1$. The branching ratio for $M_L = 1$ and $M_L = -1$ respectively increases and decreases slightly as the ellipticity angle goes from 0 to $\pi/4$. The branching ratio for $M_L = 0$ is essentially independent of ellipticity, with only a slight (5%) increase between linear and circular polarization. For linear polarization ($\varepsilon = 0$), the three sublevels are almost equally populated, with 34% in each of the $M_L = 1$ and -1 states and 32% in the $M_L = 0$ state. For left circular polarization σ^+ ($\varepsilon = \pi/4$), the $M_L = 1$ state is preferentially

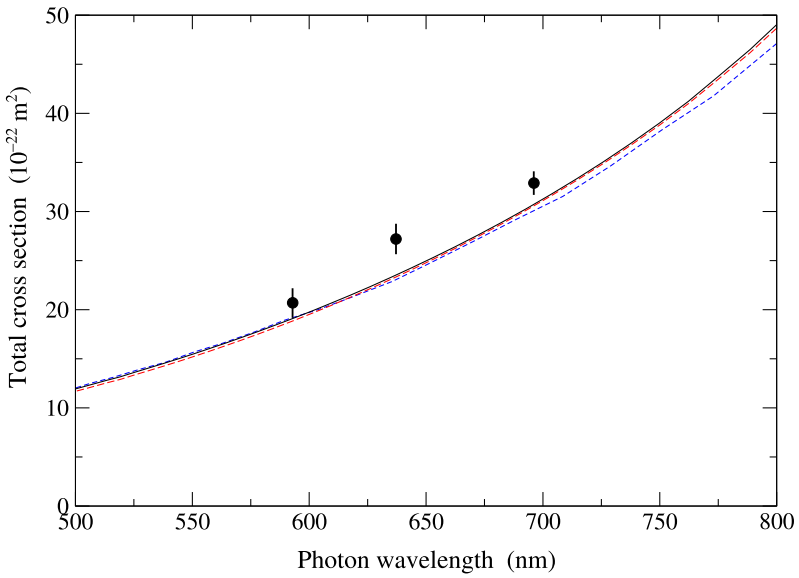

Figure 3.5: *Total cross section for the photodetachment of He^- as a function of the photon wavelength. Full line: R-matrix calculation using the length form of the dipole matrix elements; dashed line: R-matrix calculation using the velocity form of the dipole matrix elements; broken line: reference [182]; circles: experimental results from reference [190].*

populated with 39% of the total 1s2p population, compared to 34% in $M_L = 0$ and 27% in $M_L = -1$. This may be expected since the dipole transition selection rule is $\Delta M_L = +1$. For right circular polarization σ^- ($\varepsilon = -\pi/4$), the opposite behavior is observed with the $M_L = -1$ state being more populated.

The branching ratios to the various magnetic sublevels of the 1s2p state depend on the choice of the reference frame, since M_L values represent the projection of the orbital angular momentum onto the quantization axis z. Furthermore, the natural reference frame, within which polarization is expressed following Eq. (3.4), rotates in the lab frame with the ellipticity angle, hence magnetic quantum numbers for different polarizations correspond to projections onto quantization axes with different orientations. Such dependence however does not affect the final conclusions since all calculations to determine measurable quantities are performed within the same frame, and final results are summed over all M_L values, *i.e.* all orientations, before being compared to experiment.

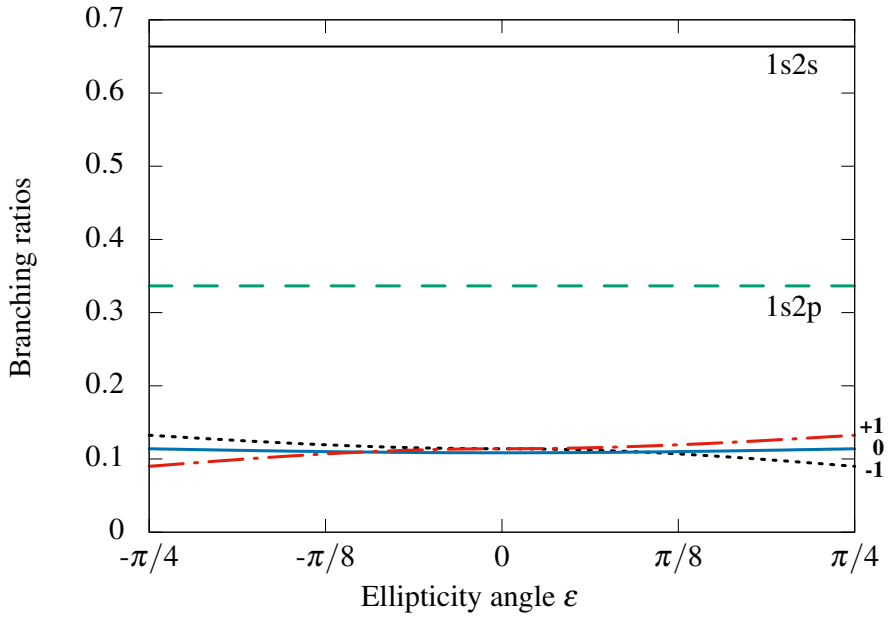

Figure 3.6: *Branching ratios for the photodetachment of He^- into the He(1s2s ^{3}S) and He(1s2p ^{3}P^o) states. Full thin line: 1s2s state, dashed line: 1s2p state. Branching ratios to the various magnetic sublevels of the 1s2p state are also shown, and corresponding M_L values are labeled on the right-hand side of the graph. Dotted line: $M_L = -1$, full thick line: $M_L = 0$, dash-dotted line: $M_L = +1$.*

As noted previously, for linear ($\varepsilon = 0$) and circular ($\varepsilon = \pm\pi/4$) polarizations, the natural frame coincides with the standard choice of reference frame and comparisons with other data are straightforward. Moreover, calculations within other reference frames would yield results equivalent to the present ones and which can be compared to one another after appropriate rotation by means of Wigner D matrices [53].

The behavior of the branching ratios for magnetic sublevels is established here for the photodetachment of He^-, but the the trends observed most certainly hold for other anions. The magnitude of the photodetachment cross sections depends on the reduced dipole matrix elements, but their dependence on magnetic number M_L and polarization $\hat{\boldsymbol{\epsilon}}$ derives from angular momentum algebra. Relatively small variations between different anions or final states are expected to arise since matrix elements and geometrical factors are entangled in the various summations of Eq. (3.2).

3.5 Double detachment *via* He(1s2s ^{3}S)

The experimental double photodetachment (DPD) spectrum of He^- is shown in Fig. 3.7(a) for photon energies ranging from 2.22 eV (558.5 nm) to 2.4 eV (529.8 nm) and for linear polarization. It represents the average number of He^+ ions created from an incoming He^- beam of 1 nA by a 6 mJ laser pulse. The two series of peaks readily observed can be attributed to the following mechanism: He^- is photodetached into the He(1s2s ^{3}S) channel; population transfer occurs from the 1s2s state to the Rydberg 1sns and 1snd states due to a two-photon resonance and the latter states subsequently ionize by the absorption of an additional photon. Two-photon resonances are narrow and allow efficient population transfer only for zero or small detunings. Therefore, the enhancement of He^+ production is restricted to near the 1s2s–1sns or 1s2s–1snd resonances, yielding the narrow peak series observed in the spectrum. These peaks series thus confirm that double detachment occurs by photodetachment and (2+1) REMPI of He(1s2s ^{3}S), as shown in Fig. 3.1.

The spectrum displayed in Fig. 3.7(a) shows Rydberg resonances spanning $n = 7$ to $n = 12$, corresponding to the wavelength range we could cover with the Coumarin 500 dye. Higher n-values of these Rydberg series have been studied in details by Wall *et al.* [212], up to $n = 115$, using a two-photon laser excitation and static field ionization scheme. On the low photon energy side, a continuous, slowly rising background is observed. It is attributed to the onset of the (1+1) REMPI of the 1s2p state through a one-photon resonance with the 1s3d state, located at $\lambda = 587.7$ nm (2.110 eV). Although we are still far detuned from this resonance, contribution of this (1+2)-photon process to the double photodetachment yield should be non-negligible compared to the (1+3)-photon process examined here. Complementary measurements and modeling are however required to confirm this.

The DPD spectrum simulated with the effective Hamiltonian model is shown in Fig. 3.8(a) and is similar to its experimental counterpart, although the amplitude of the peaks is not well reproduced by the model. Such a discrepancy is probably due to a difference between the idealized interaction volume, as used in the simulation, and the experimental one. A simulation run for a 68 μm laser waist (Fig. 3.9) is, for example, in much better quantitative agreement with experimental amplitudes. The chaotic nature of the laser pulses, generated from a multimode Nd:YAG laser, must also affect the multiphoton dynamics. This effect is however expected to be small, as demonstrated for the 2-photon ionization of O^- (see Sec. 2.5.4).

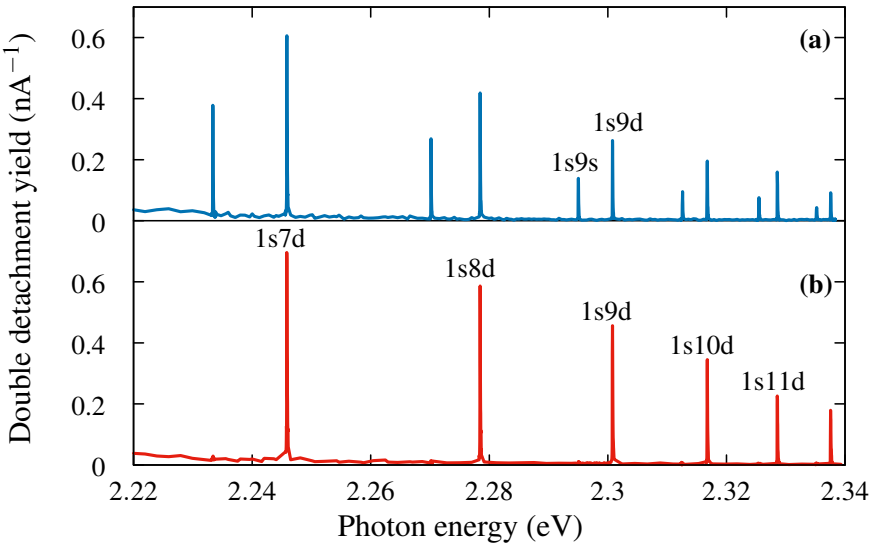

Figure 3.7: *Experimental double photodetachment spectrum as a function of the photon energy. Top graph (a): linear polarization. Bottom graph (b): circular polarization. Data shown is the number of He^+ ions produced by a 6 mJ laser pulse and for a He^- beam of 1 nA .*

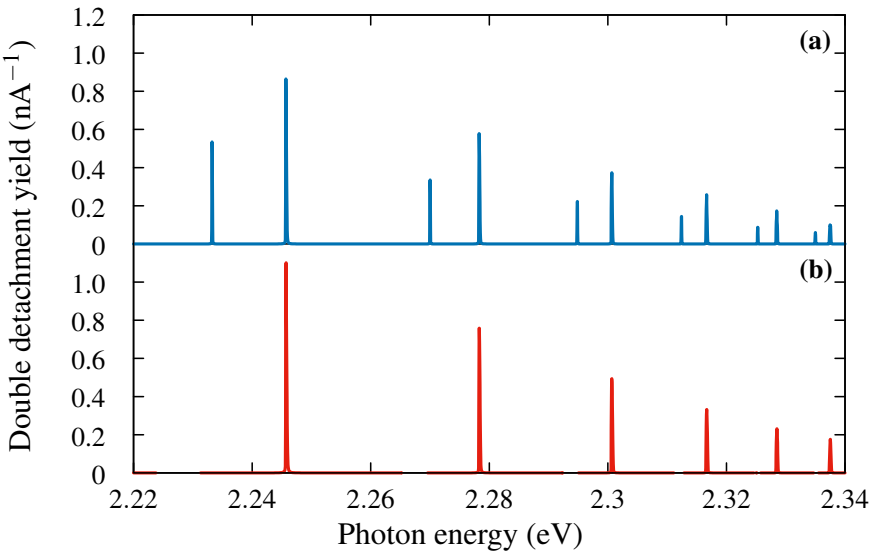

Figure 3.8: *Simulated double photodetachment spectrum as a function of the photon energy. Top graph (a): linear polarization. Bottom graph (b): circular polarization.*

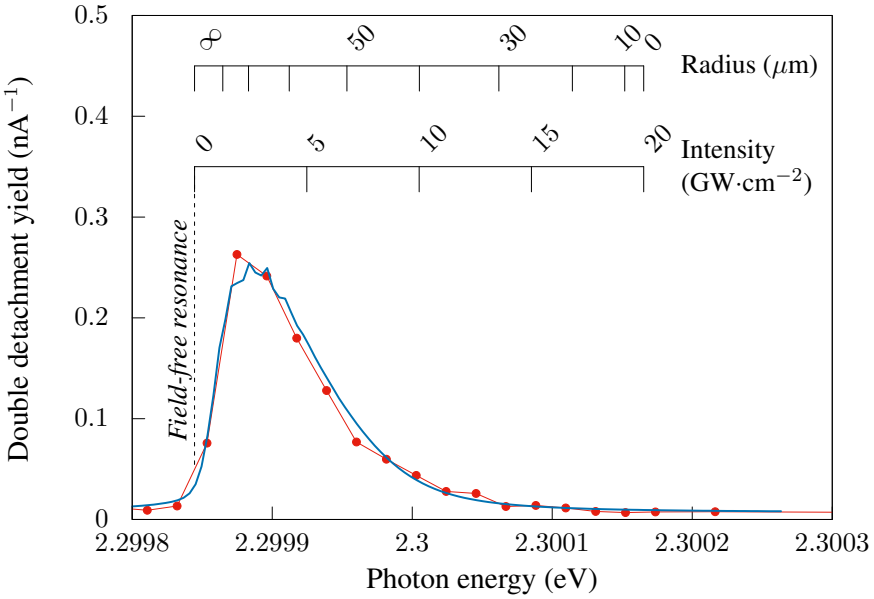

Figure 3.9: *Details of the 1s9d peak in the double photodetachment spectrum. Full circles: experiment, full line: simulation with a 68 μm laser waist. Data is for linear polarization and 6 mJ laser pulses. The vertical dotted line indicates the position of the field-free 1s2s-1s9d two-photon resonance. For larger photon energies, the 1s2s state is Stark shifted and resonance condition is met for a given laser intensity, as indicated by the intensity scale. The given intensity corresponds to a given radius with respect to the center of the laser profile, as indicated by the radius scale. This radius defines an effective interaction cylinder, within which production of He^+ can occur.*

The detailed profile of the peaks in the DPD spectrum, such as the one corresponding to the 1s2s-1s9d resonance shown in Fig. 3.9, provides additional information on the ionization dynamics of the transient neutral. Note that in this case simulation was performed for a 68 μm laser waist in order to match the width of the experimental peak. The size of the waist has not been measured for the present wavelength range and deviations from the 54 μm waist measured for range II are possible. The width of the peak is much larger than the laser bandwidth of 0.05 cm^{-1} (6.2×10^{-6} eV) and it shape is asymmetrical, with a pronounced spread towards higher photon energies. Mechanisms leading to this type of profile are threefold, and have been partly discussed by other authors [212]. We first note that the 1s2s state is blue-shifted by the AC Stark shift, which in turn depends on the intensity, while the Rydberg series remain essentially unperturbed. Therefore, even if the laser is blue-detuned

from the 1s2s-1s9d resonance, the increasing intensity experienced by the helium atom moving through the laser focus will *dynamically* bring it to resonance and population transfer still efficiently occurs. Furthermore, as the laser is further blue-detuned, the exact resonance condition is met at increasing intensities, until the value required exceeds the laser peak intensity. Assuming a Gaussian profile, the intensity at which resonance occurs corresponds to a specific radius with respect to the center of the profile. This radius combined with the transverse width of the ion beam define an effective interaction cylinder, within which production of He^+ can occur. The volume of this cylinder shrinks as detuning becomes larger, consequently decreasing the He^+ signal. Finally, close to a zero-field resonance, population transfer to the Rydberg state occurs early on as the atom crosses the laser focus. Therefore, the duration of the interaction between the Rydberg state and the laser field is long and the ionization probability high. Blue-detuning results in delayed population transfer, reduced interaction time and therefore reduced ionization probability, also resulting in a drop in the He^+ yield.

Turning to circular polarization, Fig. 3.7(a-b) provides a particularly illustrative example of dipolar selection rules. In the case of left circular polarization, selection rules for a two-photon transition give $\Delta M_L = +2$. Excitation from the 1s2s state ($M_L = 0$) to a Rydberg 1sns state ($M'_L = 0$) is therefore forbidden, and the 1sns peak in the He^+ spectrum disappears. The same argument applies in the case of right circular polarization, for which the two-photon selection rule is $\Delta M_L = -2$, hence leading to the same spectrum.

The evolution of double photodetachment yield as the polarization is tuned from linear to left circular is shown in Fig. 3.10. Measurements were performed both for the 1s2s – 1s9d and 1s2s – 1s9s resonances, corresponding to photon energies of 2.2999 eV and 2.2942 eV respectively, by stepwise rotation of the $\lambda/4$ plate while recording the corresponding He^+ signal. The effective Hamiltonian approach was used to simulate the experiment for the same photon energies, and the final results are scaled by 0.8 and 1.02 respectively in order to best fit the experimental values. We first note that the shape of the simulation curves follows the experimental data very well. The 1s9d peak amplitude increases as the polarization gets closer to circular, a fact that can be attributed to increasing coupling strength and ionization rate. For example, inspection of the value of the matrix element coupling the 1s2s state to the 1s9d state shows that, while the reduced matrix elements are identical, geometrical factors arising from the polarization are 1.22 times higher for circular polarization than for linear polarization – see, *e.g.* , Eqs. (3.3) and (3.25). In sharp contrast, the amplitude of the 1s9s peak drops to

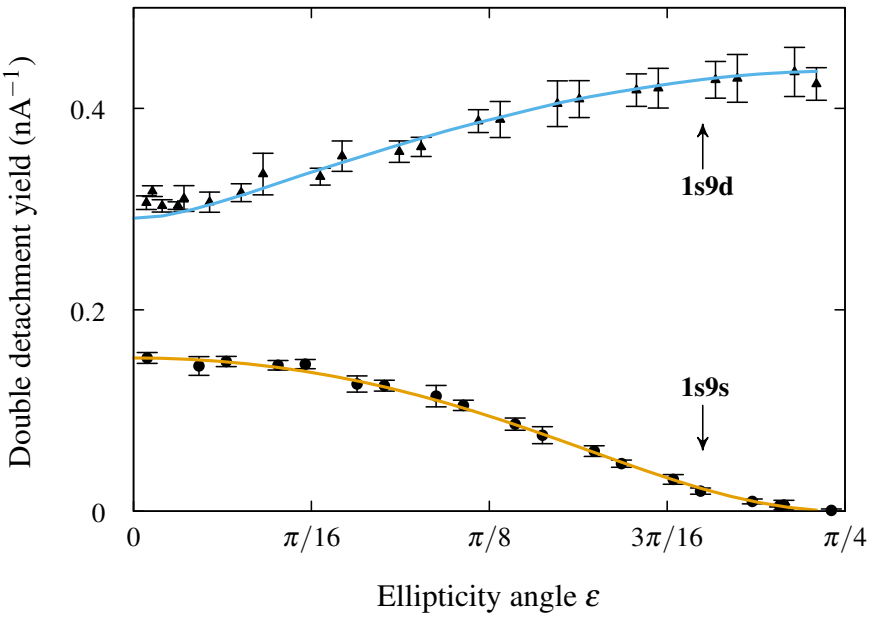

Figure 3.10: *Experimental and simulated double photodetachment yield as a function of the ellipticity angle. Triangles are experimental data for* $\lambda =$ 539.08 *nm and correspond to resonance with the Rydberg 1s9d state. Circles are experimental data for* $\lambda = 540.43$ *nm and correspond to resonance with the Rydberg 1s9s state. Both full lines are the result of simulations for the same wavelengths, and have been scaled by 0.8 and 1.02 for the 1s9d and 1s9s states respectively.*

zero as the polarization becomes circular, a direct result of the dipole selection rules.

3.6 Double detachment *via* He(1s2p ^{3}P^o)

The double photodetachment (DPD) of He^- has been studied in the wavelength range from 685 nm to 730 nm, where it is enhanced by resonances in the transient atom involving the 1s2p ^{3}P^o state. A first insight on the underlying intricate dynamics is provided by inspection of the dressed-states quasi-energies for a fixed intensity. The DPD spectra, involving time-dependent population transfers and shifts, are then presented and theory is confronted to experiment. This combination further provides detailed information on the dependence of the yields on the pulse energy and laser polarization. Finally, the possibility for non sequential DPD is investigated experimentally.

3.6.1 Multiphoton ionization within the dressed states picture

Diagonalizing the effective Hamiltonian gives a set of complex quasi-energies E of the form

$$E = E_0 + \Delta E - \mathrm{i}\frac{\Gamma}{2}, \tag{3.42}$$

where $E_0 + \Delta E$ is the Stark-shifted energy of the dressed atomic state and Γ its total ionization rate. In order to assess our choice of model space and to validate the associated computer code, we first performed a comparison of the quasi-energies obtained using the model with those obtained from *R*MF calculations. The agreement was satisfactory, indicating that the main physical properties of the ionization process are accounted for.

We now consider the field-dressed atomic states used for the modeling of the experiment[3]. They can be identified by plotting the real part of the quasi-energies as a function of the photon energy ω as in Figs. 3.11a and 3.11b, including the 1s2p ($M_L = \pm 1$) and ($M_L = 0$) states respectively. The dashed curves correspond to the field-free energy of the 1s2p state and of the 1s3s state shifted down by one photon energy while the full curves are the results of the EH calculation. For the case $M_L = \pm 1$ at an intensity of 3.6×10^{10} W/cm^2, the 1snp and 1snf Rydberg states can be populated by a two-photon transition from the initial 1s2p state, and are represented by the lines of slope -2ω. The value of n can be determined by extrapolating the lines to $\omega = 0$. The thick dot-dashed line indicates the 2-photon ionization threshold. The horizontal line is the energy of the initial dressed 1s2p $^3\mathrm{P}^\mathrm{o}(M_L{=}\pm1)$ state, Stark-shifted down compared to its field-free value. The Stark shift of the Rydberg states is extremely small, of the order of 5×10^{-5} a.u.

At resonance, *i.e.* when $E_{2\mathrm{p}} + 2\omega = E_{n\ell}$, the diabatic dressed-state energies intersect. The adiabatic energies exhibit avoided crossings whose distance of closest approach is proportional to the strength of the interaction between the states. The coupling of the initial state with the 1snf Rydberg states is stronger than with 1snp states. This implies that multiphoton ionization proceeds preferentially through the (2+1) REMPI scheme, with two-photon excitation to the 1snf states followed by one-photon ionization into the $\ell = 2$ and $\ell = 4$ continua. Branching ratios calculated using the *R*MF and QDT approaches indicate a propensity ($\sim 97\%$) for the photolectron to be ejected in the $\ell = 4$ channel.

[3]We consider in this subsection the case of linear polarization only. Quasi-energies would be different for elliptic or circular polarization.

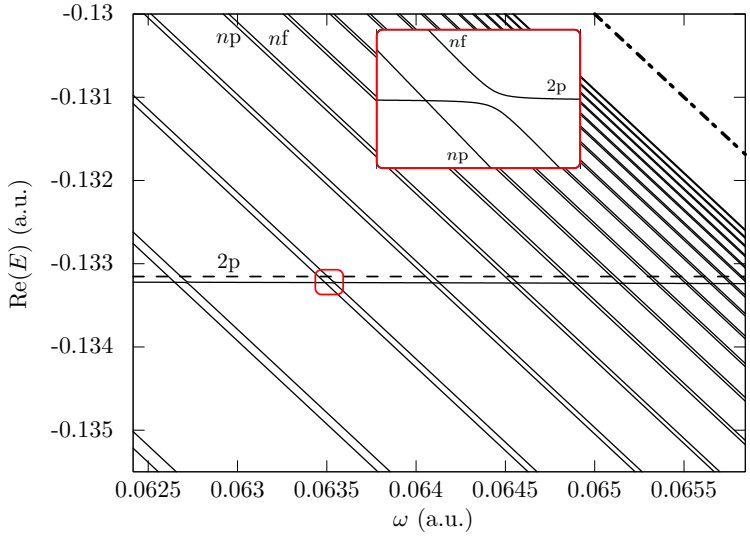

(a) $M_L = \pm 1$

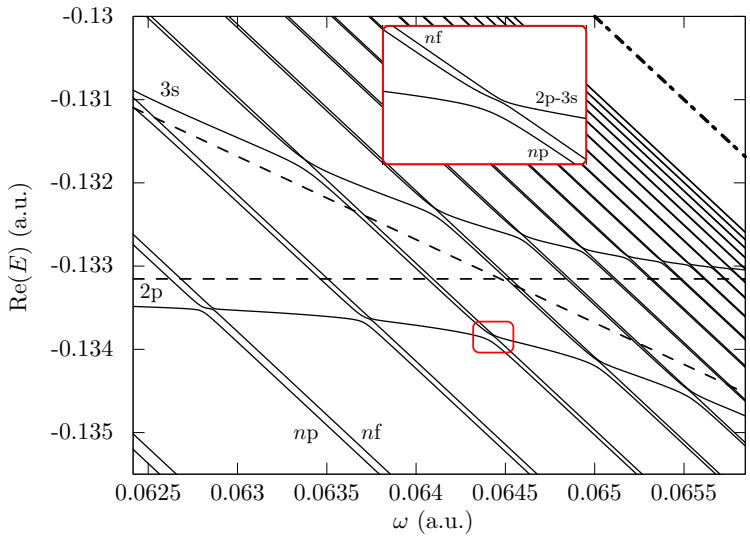

(b) $M_L = \pm 0$

Figure 3.11: *Real part of the EH quasi-energies as a function of the laser angular frequency at a fixed intensity of 3.6×10^{10} W/cm^2. Rydberg states from $n = 6$ to $n = 22$ are included. The horizontal dashed line corresponds to the field-free energy of the 1s2p state while the oblique dashed line corresponds to that of the 1s3s state shifted down by ω. The thick dot-dashed line in the upper right corner is the two-photon ionization threshold. The insert is a magnified view of the crossing highlighted in the small box.*

For the case $M_L = 0$, shown in Fig. 3.11b, the dressed-state energies exhibit a much richer structure. In addition to the initial state and the two Rydberg series, resonances with the 1s3s ^{3}S state are also present. The initial 1s2p ^{3}P^o(M_L=0) state interacts strongly with the 1s3s ^{3}S state resulting in a very large avoided crossing centred around $\omega_r = 0.06447$ a.u. and extending over a broad range of photon energy. As the 1s3s ^{3}S state is populated by absorption of one photon, its energy curve has a slope of $-\omega$ away from the crossing. The presence of this physical intermediate state implies that the ionization preferentially occurs following a (1+1+1) REMPI scheme, via the 1snp Rydberg states. Branching ratios obtained from our *R*MF and QDT calculations indicate a 30% probability for the photoelectron to be ejected in the $\ell = 0$ channel and a 70% probability to be in the $\ell = 2$ channel.

One further consequence of the strong interaction between the 1s2p and 1s3s states is that the Stark shift of the 1s2p (M_L=0) state is of opposite sign on either side of the resonance: below the resonance, the energy is shifted down, while above the resonance it is shifted up. A manifestation of this difference will be seen in the ionization spectra presented below.

The ionization rates, related to the imaginary part of the quasi-energies by (3.42), are plotted in Fig. 3.12a as a function of the photon energy ω for $M_L = \pm 1$. The plateaus correspond to the one-photon ionization rates of the Rydberg states while the non-resonant three-photon ionization rate of the 1s2p ^{3}P^o(M_L=$\pm$1) initial state is about three or four orders of magnitude smaller. In the region of two-photon resonances between the initial and the Rydberg states, the ionization rates cross over a range of ω whose width characterizes the interaction strength. The one-photon ionization rate of the 1snf is lower than that of 1snp due to the centrifugal barrier, but the two-photon 1s2p–1snf interaction is stronger than the 1s2p-1snp interaction.

Ionization rates for $M_L = 0$, shown in Fig. 3.12b, present plateaus corresponding to the Rydberg states, while the 1s2p ^{3}P^o(M_L=0) and 1s3s ^{3}S ionization rates are negligible on the scale of the figure. The presence of the 1s3s ^{3}S state again significantly enriches the picture: the number of resonances is increased and the strong one-photon interaction with the 1s2p ^{3}P^o(M_L=0) initial state broadens the range of ω over which the crossings occur. EH calculations show that the asymmetry of the crossings is due to two-photon couplings between Rydberg states via the continuum.

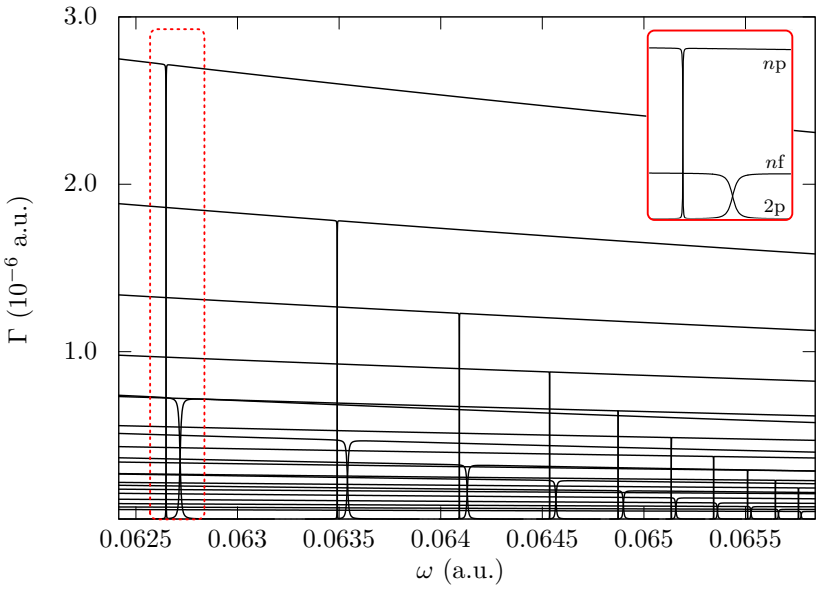

(a) $M_L = \pm 1$

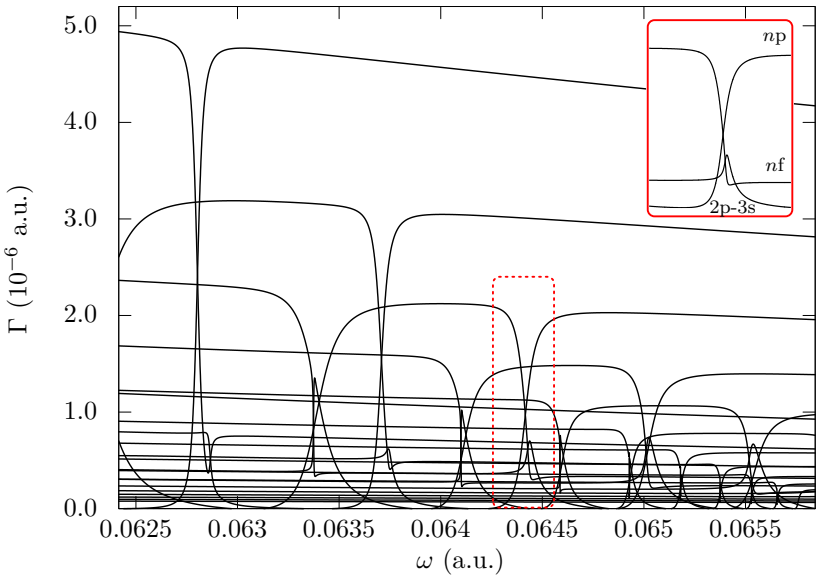

(b) $M_L = 0$

Figure 3.12: *Total ionization rates of the dressed states for $n = 7$ up to $n = 16$, as a function of the laser angular frequency at a fixed intensity of 3.6×10^{10} W/cm^2. The insert is a magnified view of the narrow region highlighted by the box.*

3.6.2 Experimental and modeling results

The dynamical counterpart of the time-independent results presented so far is obtained by propagating the wave function in time according to scheme (3.29). It is combined with R-Matrix results for the single photodetachment of He^- in Eq. (3.38) in order to obtain the double photodetachment yield. As an example, the simulated results computed for a pulse energy of 6 mJ and linear polarization are plotted in Fig. 3.14, while the corresponding experimental spectrum is shown in Fig. 3.13. In both spectra, a series of double peaks is visible: the peak at lower photon energy corresponds to photodetachment to the 1s2p state followed by a (1+1+1) REMPI process via the 1snp state, which is favourable for $M_L = 0$; the peak at higher photon energy also corresponds to photodetachment to the 1s2p state, followed in this case by a (2+1) REMPI process via the Rydberg 1snf state, favourable for $M_L = \pm 1$. It should be noted that the assignment of the peaks corresponds to their major contributors: it is of course possible to ionize for example via a 1snf Rydberg state for $M_L = 0$, albeit with a small probability.

Multiphoton ionization dynamics

As for the He(1s2s ^{3}S) case, the precise position of each resonance depends on the laser intensity which influences the Stark shift of the initial 1s2p ^{3}P^o and the intermediate 1s3s ^{3}S states, while that of the Rydberg states is very small. The peaks are asymmetric with the sharp rise corresponding to zero-field resonances between the 1s2p ^{3}P^o and Rydberg states. In this case, transfer of population occurs early in the propagation through the laser field, maximising the interaction time and the probability of ionization. Above the zero-field resonance and for $M_L = \pm 1$, the atom needs to experience a field strong enough to induce a downward Stark-shift to bring it into resonance with a Rydberg state. This effect will extend over a wider range of frequencies as the pulse energy increases. Since the laser beam profile is Gaussian, the Stark induced resonance will occur twice, during the onset and the falloff of the laser intensity experienced by the atom, whose population is transferred back to the initial state by adiabatic rapid passage [205]. The ionization yield is smaller since the interaction of the Rydberg state with the laser field is greatly reduced, explaining the tail of the peaks towards higher frequencies as a result of this dynamic blue-shift. For $M_L = 0$, the physics is more complicated due to the existence of the one-photon resonance with the 1s3s ^{3}S state at $\hbar\omega_r = 1.754379$ eV. As illustrated by the two-state model in section 3.3.2, for $\omega < \omega_r$, the Stark shift of the initial state leads to resonances with Rydberg states at higher pho-

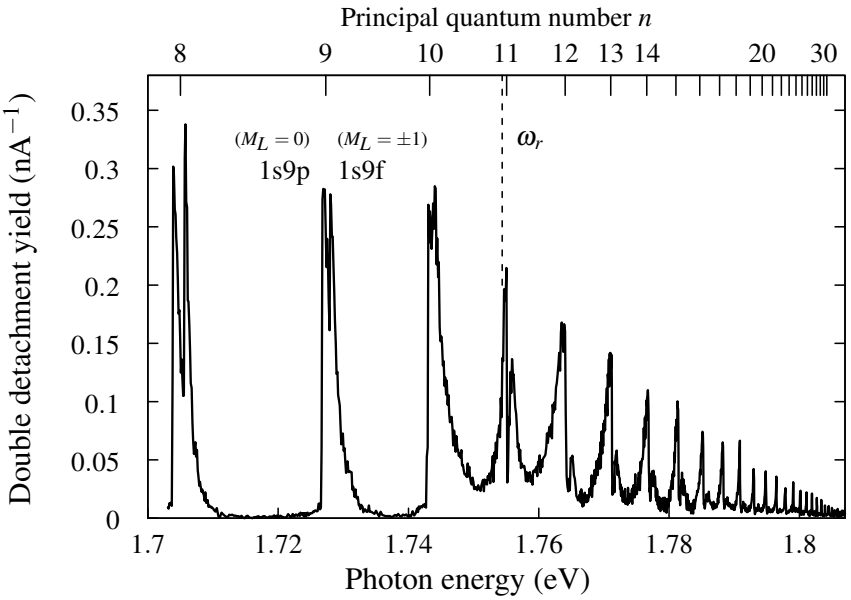

Figure 3.13: *Experimental double photodetachment spectrum for a laser pulse energy of 6 mJ and linear polarization. The vertical dashed line indicates the 1s2p-1s3s resonance.*

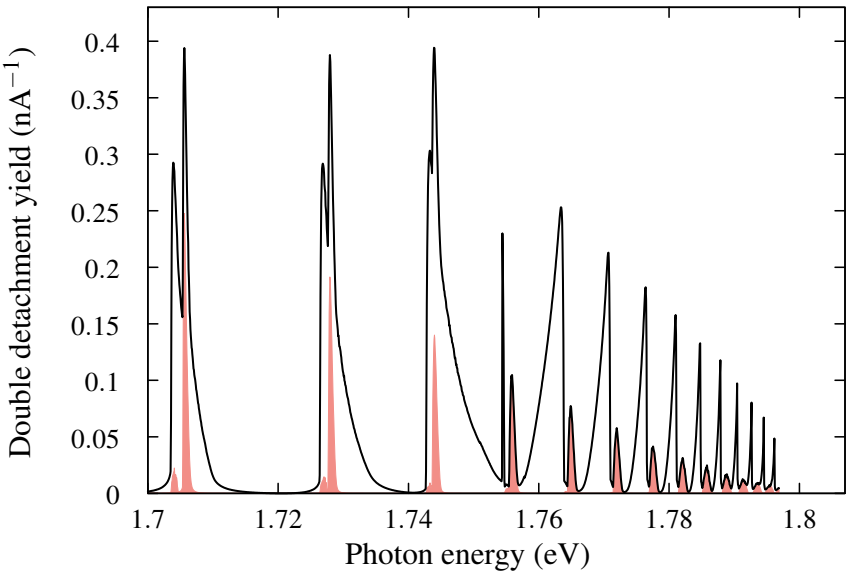

Figure 3.14: *Simulated double photodetachment spectrum for a laser pulse energy of 6 mJ and linear polarization. The shaded curve is the contribution from $M_L = \pm 1$ states and the full line is the weighted sum of the contributions from $M_L = 0$ and $M_L = \pm 1$ states.*

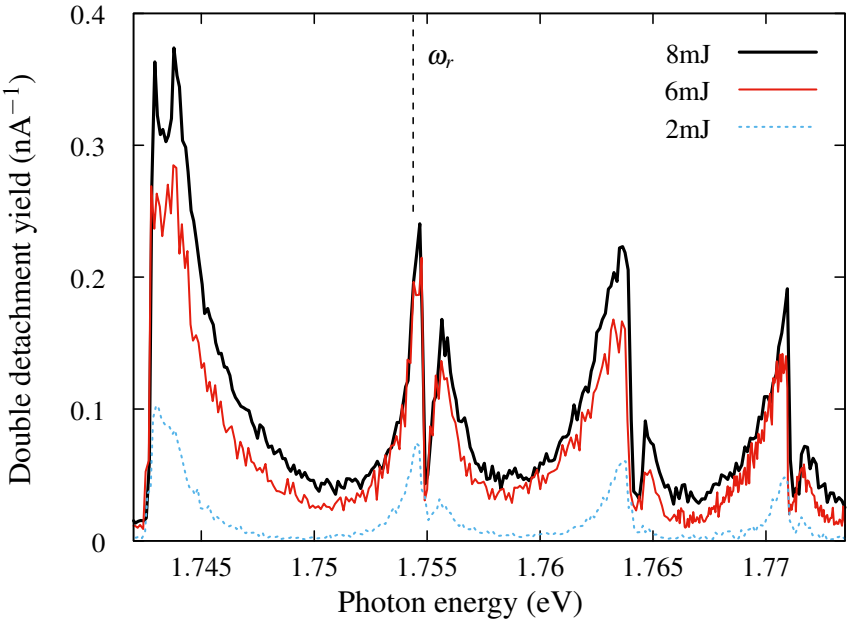

Figure 3.15: *Experimental double photodetachment spectra for 8, 6 and 2 mJ laser pulses and linear polarization. The vertical dashed line indicates the 1s2p-1s3s resonance.*

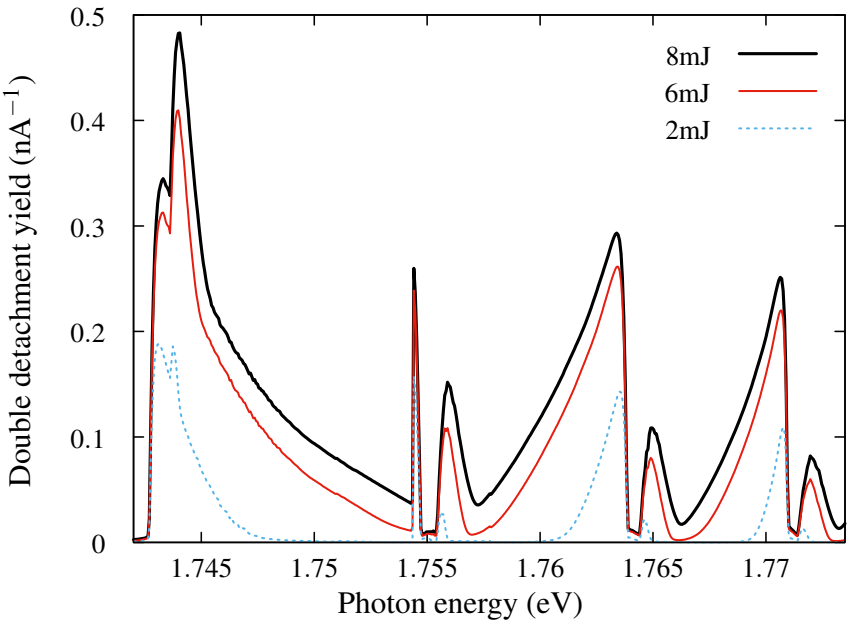

Figure 3.16: *Simulated double photodetachment spectra for 8, 6 and 2 mJ laser pulses and linear polarization.*

ton energies, while the inverse is true for $\omega > \omega_r$, leading to a dynamic red-shift. Hence the asymmetry of the peaks in the ionization yield is reversed as the 1s2p-1s3s resonance is crossed. The two successive one-photon transitions lead to more complex population dynamics, resulting in an ionization yield larger than for $M_L = \pm 1$. This is clear from the comparison between the total spectrum and the separate spectrum for $M_L = \pm 1$ presented in Fig. 3.14.

Although there is qualitative agreement between the simulated and experimental spectra presented in Figs. 3.13 and 3.14, small discrepancies exist in the width of the tails and the magnitudes of the yields, with the simulated 1snp peaks wider than the measurement and the 1snf peaks larger at low energy. This may be due to imprecisions in some couplings in our semi-perturbative EH model, for instance those involving the continuum which are not possible to validate *ab initio*. The multimode nature of the laser pulse may also alter the multiphoton dynamics. However, this effect must be small since, as demonstrated in Sec. 2.5.4, the duration of the transit of the ions through the laser pulse is shorter than intensity fluctuations due to mode beating. Furthermore, the heights of the measured peaks decrease rapidly with increasing ω, which is not reproduced to the same extent in our model. These discrepancies remain to be explained.

Figures 3.15 and 3.16 show the variation of the double detachment yield with respect to the pulse energy, which determines the peak laser intensity experienced by the ions and atoms. As one would expect, the amplitude of the ion signal increases with the pulse energy, a consequence of the increased ionization probability and interaction volume. The tail of the peaks is broadened since the Stark shift of the 1s2p initial state is larger. A thorough analysis of the pulse energy-dependence of the ion signal reveals no simple scaling, illustrating the complex interplay between the (1+1+1) REMPI and (2+1) REMPI mechanisms. We remark that the tails of the peaks in the simulation do not decay as rapidly as in the experiment, particularly for the highest pulse energy of 8 mJ. Their shape depends on the intensity of the field experienced by the atoms as they traverse the laser beam. A more accurate knowledge and control of the laser pulses would therefore be essential in order to improve the simulation.

The influence of polarization

The double photodetachment spectra for linear and circular polarizations are compared in Fig 3.17 and significant differences can be observed, especially on the high photon energy end. Let us investigate

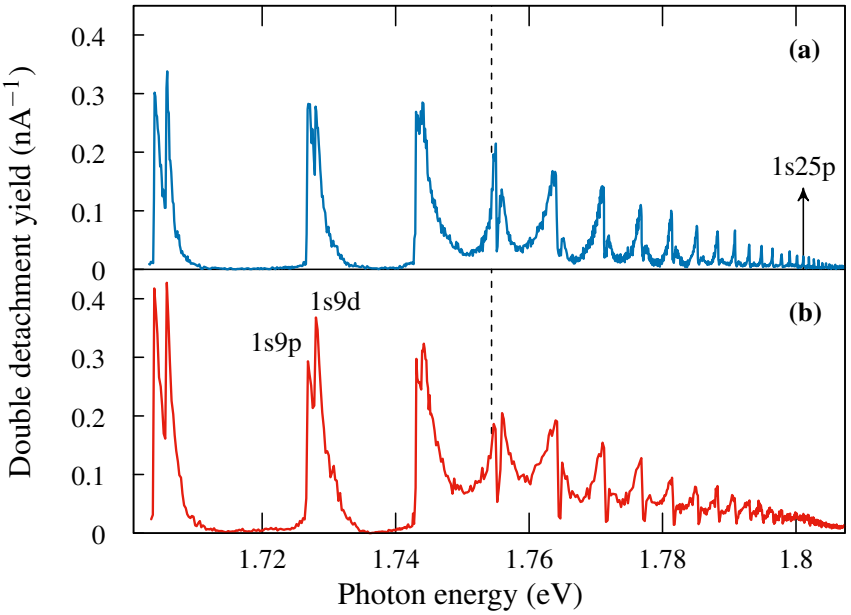

Figure 3.17: *Experimental double photodetachment spectra as a function of the photon energy. Top graph (a): linear polarization. Bottom graph (b): circular polarization. The vertical dashed lines indicate the position of the 1s2p-1s3s resonance. Resonances with Rydberg states are observed up to $n = 35$. The laser pulse energy is 6 mJ.*

how polarization affects double detachment dynamics, and in particular how it modifies the respective contributions of the various magnetic sublevels of the 1s2p state. The part of the spectrum corresponding to resonances with $n = 13$ states is shown in Fig. 3.18, along with the simulated contributions from the $M_L = 0, \pm 1$ magnetic sublevels. The most striking difference between linear and circular polarization is the major change of shape of the $M_L = 0$ and $M_L = -1$ contributions to the He^+ yield, which reverse. For linear polarization, selection rules allow the 1s2p (M_L=0) state to couple to the 1s3s state, which itself couples to the 1s13p state, thus yielding a broad, intense peak reminiscent of the strong 1s2p AC Stark shift and the strong enhancement of ionization by the (1+1+1) channel. In the case of left circular polarization, coupling to the 1s3s state becomes allowed for the $M_L = -1$ magnetic sublevel, and the contributions of the various magnetic sublevels change accordingly. Therefore, the loose attribution of the 1snp peaks to $M_L = 0$ and the 1snf peaks to $M_L = \pm 1$ for linear polarization changes to $M_L = -1$ and $M_L = 0, 1$ respectively for left circular polarization.

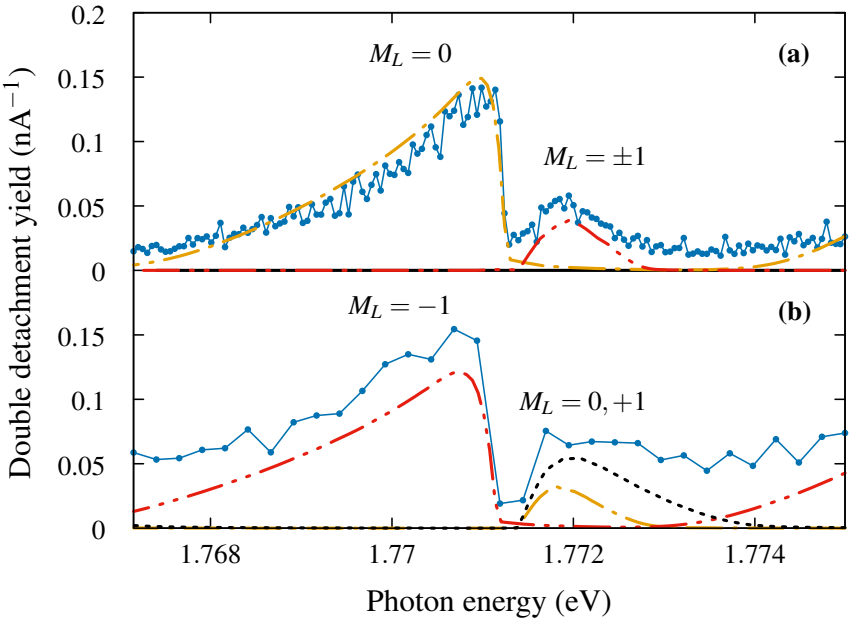

Figure 3.18: *Details of the double photodetachment spectrum around the 1s2p–1s13p (left peak) and 1s2p–1s13f (right peak) resonances. Top graph (a): linear polarization; bottom graph (b): circular polarization. Full circles: experimental data, dash-dot-dot line: simulated $M_L = -1$ contribution, dash-dot line: simulated $M_L = 0$ contribution, dotted line: simulated $M_L = +1$ contribution. For linear polarization, $M_L = +1$ and $M_L = -1$ contributions are identical therefore only twice the $M_L = -1$ contribution is shown. Simulated data are scaled by 0.7.*

Apart from the changes in the different M_L contributions, other differences in the shape of the peaks are readily observed in the DPD spectra, as is evident on the high photon energy side of Fig. 3.17 and in Fig. 3.18). Such differences arise from two different effects and differ for the 1snp and 1snf peaks. Let us consider first the 1snp peaks. The non resonant AC Stark shift of the initial state is smaller in the case of circular polarization, hence, since Rydberg series are unperturbed, the blue shift will be smaller and the peaks will spread less towards higher photon energies. However, the 1s2p state will experience significant red-shift above the 1s2p-1s3s resonance due to its interaction with the 1s3s state. The spread of the 1snp peak is therefore the result of a competition between the non-resonant and resonant AC Stark shifts, so that a smaller non-resonant contribution leads to an increased red-shift, and therefore an increased spread of the peak towards lower photon energies. All couplings being equal otherwise, the variation of the peak amplitude

between the linear and circular polarization, best seen in Fig. 3.18, is the result of the different initial populations of the M_L sublevels as produced by photodetachment. This effect is not observed to the same extent in the experimental spectrum.

Let us now consider the 1snf peak. For linear polarization, contributions from $M_L = -1$ and $M_L = +1$ are strictly equivalent. This is no longer true in the case of circular polarization, and the $M_L = +1$ sublevel gives the dominant contribution while the $M_L = 0$ one is very similar to that of the $M_L = \pm 1$ sublevels for linear polarization. Investigating changes in matrix elements due to modified geometrical factors shows that, compared to $M_L = \pm 1$ for linear polarization, the non-resonant AC Stark shift of the 1s2p state is identical for $M_L = 0$ and twice larger for $M_L = 1$. Matrix elements coupling the 1s2p states with $M_L = 0, 1$ to Rydberg 1snf states are also significantly larger for circular polarization, and so are the ionization widths of the 1snf states. Finally, the $M_L = 1$ sublevel is slightly more populated by photodetachment in circular polarization. Such increases explain why the 1snf peak becomes larger and significantly broadens when switching from linear to circular polarization.

Finally, the evolution of the double detachment yield as a function of the light polarization is shown in Fig. 3.19. The experimental yield was measured for a photon energy of 1.767 eV, chosen to probe the minimum between the 1s2p-1s12f and 1s2p-13p resonances, where the influence of the polarization is most prominent. Simulation is also performed at the minimum, located at slightly lower photon energy (1.766 eV). The double detachment signal is dominated by the 1s2p-1s13p resonance, and contributions of the various magnetic sublevels clearly evolve from dominant contribution of $M_L = 0$ to $M_L = -1$. The onset of contribution from $M_L = +1$ as the polarization becomes more circular is reminiscent of the broadening and increase in magnitude of the 1s2p–1snf peaks observed previously, with $n = 12$ here.

Sequential *vs.* non-sequential

The above treatment considers photodetachment and REMPI as two sequential events. Indeed, detachment is very efficient and occurs at low intensity, *i.e.* , early in the pulse. The onset of REMPI requires much higher intensities and occurs later, when detachment is fully saturated. Hence the two processes are, in good approximation, decoupled. Given the satisfactory agreement between the shape of the simulated and measured ion yields, this approximation appears reasonable. However, when the photon energy is tuned exactly at the 1s2p–1s3s resonance, popu-

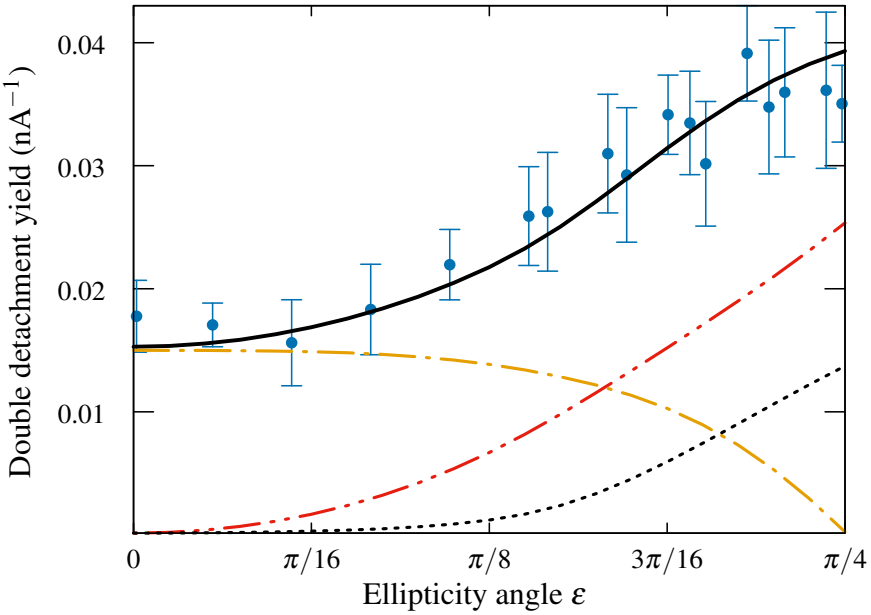

Figure 3.19: *Experimental and simulated double photodetachment yield as a function of the ellipticity angle. Full circles: experimental yield, full line: simulated yield, dash-dot-dot line: $M_L = -1$ contribution, dash-dot line: $M_L = 0$ contribution, dotted line: $M_L = +1$ contribution. The experimental yield is for a photon energy of 1.767 eV (701.72 nm) and the simulated one for 1.766 eV (702.05 nm). Simulated yields are scaled by 0.65 to match experimental values. The laser pulse energy is 6 mJ.*

lation transfer to the 1s3s state can occur very early in the pulse, at intensities comparable to those of photodetachment. The 1s3s state being resonantly coupled to the 1s11p state, population transfer to the Rydberg states can thus also occur early in the pulse and the sequential treatment may be doubtful in this specific case.

In order to assess the sequential nature of the double detachment process close the 1s2p–1s3s resonance, we have performed a two-laser experiment where helium atoms are first prepared in the 1s2p state by photodetachment by a CW laser, and subsequently ionized downstream by the second, pulsed dye laser used previously. The two laser beams are spatially separated, and we select those He^+ that come from detachment by the first laser and ionization by the second only.

The resulting double detachment spectrum is shown in Fig. 3.20 and compared against the one-laser spectrum, where detachment and ionization occur within the same laser pulse. Because production of

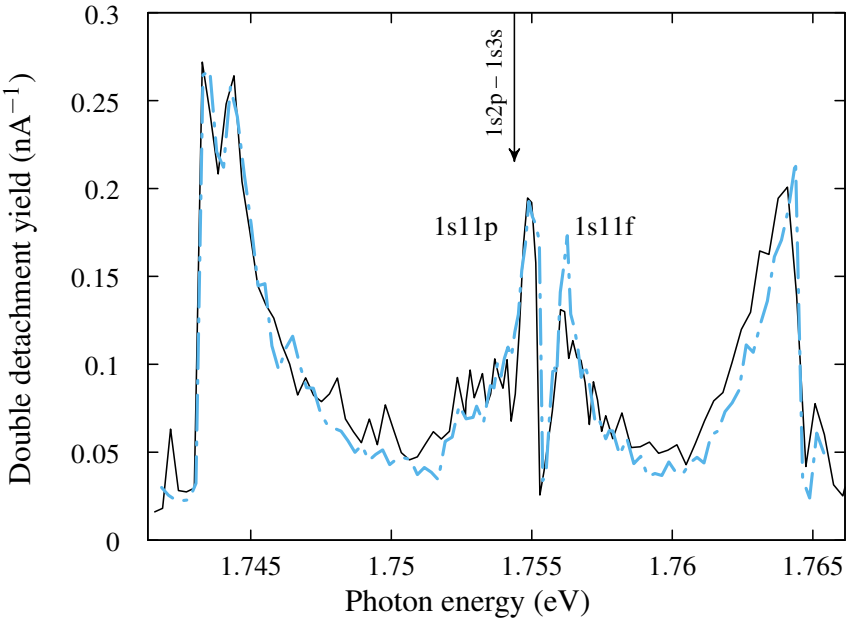

Figure 3.20: *Double photodetachment spectrum around the 1s2p–1s3s resonance. Dot-dashed line: two-color, sequential measurement, multiplied by 35; full line: one-color measurement. The vertical arrow indicates the exact position of the 1s2p–1s3s resonance. The laser pulse energy is 6 mJ.*

helium atoms is less efficient in the two-laser case, the corresponding spectrum was scaled to match the single-laser measurement. No stark difference is observed between the two spectra, suggesting that no strong non-sequential channels exist. In fact, this even suggests that the detachment and ionization steps are essentially independent events. The experiment was run for linear polarization and we have also observed that, whether the two laser polarizations are parallel or perpendicular, the same spectra are obtained within error bars.

3.7 Conclusion

The double photodetachment of He^- in moderately strong laser fields has been successfully studied in a joint experimental and theoretical investigation, which shed light on its underlying, intricate dynamics. The experiment relies on counting He^+ ions produced by few-mJ, nanosecond laser pulses in a fast He^- beam as a function of the laser wavelength and polarization. The theoretical work treats double detachment in two, sequential steps. The single detachment step is studied within

R-matrix theory and we calculated the partial cross sections to the various final atomic states and their magnetic sublevels for any polarization state. Subsequent resonance-enhanced ionization of the neutral atom is studied by means of EH models, designed to account for all possible polarizations. They allow lightweight calculations with which the experimental interaction volume can be faithfully reproduced. The validity of the effective hamiltonians have further been checked against *ab initio* R-Matrix Floquet calculations, with successful outcome.

The double detachment spectra show peak series attributed to resonances between the initial state of the transient atom and Rydberg series. In the wavelength range from 530 nm to 560 nm, the 1s2s state produced by photodetachment is coupled, *via* a two-photon transition, to Rydberg 1sns and 1snd states. In this case, we could show that double detachment proceeds through single detachment and (2+1) REMPI of the neutral. The profile of the resonance peaks in the DPD spectra was further related to the AC Stark shift of the initial state of the transient atom and the corresponding intensity dependence of the exact energy of the two-photon resonance. In the range from 685 nm to 730 nm, the 1s2p state of the atom is resonantly coupled by one photon to the 1s3s state and by two photons to the 1snp and 1snf Rydberg series. Double detachment proceeds in this case through single detachment and both (1+1+1) and (2+1) REMPI of the atom, and the respective weights of these channels strongly depend on the magnetic quantum numbers of the initial atomic state. The striking reversal of the asymmetry of the 1snp resonance peaks as the laser crosses the 1s2p-1s3s resonance is attributed to the strong 1s2p-1s3s mixing.

The influence of the laser polarization is manifest in the 1s2s case, where 1sns resonances disappear for circular polarization as a result of selection rules. Changes of the profile of the peaks in the double detachment spectrum induced by polarization can further be explained in terms of geometrical factors. In the 1s2p case, the magnetic quantum number M_L strongly influences double detachment and determines the ionization pathway in the neutral. Changing the polarization from linear to elliptic and circular substantially modifies the various M_L contributions, which could be computed with the theoretical model. Differences in the shape of the double detachment spectra are further explained by geometrical factors and the slight orientation of the atom produced by photodetachment. Finally, the sequential nature of double detachment was assessed by a two-laser experiment and no evidence was found of the presence of non-sequential channels.

Chapter 4

Electron impact ionization of He(1s2s ^{3}S) and He$^-$

4.1 State of the art

Helium is considered a benchmark for the study of electron scattering and, as such, has been the subject of much investigation. Although processes involving the ground state are now generally well understood, this is not always the case for the first excited state, He(1s2s ^{3}S). For the particular case of electron impact ionization, there has been only one experiment spanning a significant energy range, performed more than forty years ago [213] and whose results are in sharp disagreement with the most accurate calculations performed over the last twenty years [214–217]. The benchmark character of this problem has also motivated a large number of model calculations, ranging from Born-type to distorted wave [213, 214, 218–223], although the results vary widely in shape and magnitude. The difference of up to 60% in the total cross section between experiment and state-of-the-art calculations is not acceptable as metastable helium plays an important role in a wide range of environments, from plasma physics to Bose-Einstein condensates [20], and there has consequently been many calls for further experimental investigation [214, 215, 217, 221, 224, 225]. This discrepancy also raises uncertainties on theoretical values of the cross sections for higher-lying excited states, which are in great demand since no experimental cross sections are available.

Electron impact double ionization (EIDI) has been studied in some details for the helium ground state and is still the subject of a number of ongoing works. The total, partial and fully differential cross sections

have been determined experimentally and, for a small number of electron energies, theoretically, casting light on the mechanisms at play [226–231]. However, data concerning both the first excited state and the helium negative ion He$^-$ are non-existent. The absence of experimental results ensues from the difficulty to produce He(1s2s ^{3}S) and He$^-$ with sufficient density and purity. EIDI is also very challenging for theoretical methods, and in particular *ab initio* techniques, since they must tackle a four-body Coulomb scattering problem, leaving three electrons in the continuum. This fact explains why, for all but the simplest, two-electron systems in their ground state [231, 232], the determination of EIDI total cross sections is limited to experimental work and semi-empirical methods (see [233] and references therein).

Measuring the electron impact single and double ionization cross sections of metastable helium is challenging, which explains the absence of other measurements since the work of Dixon *et al.* [213]. Difficulties that must be addressed are twofold: first, the source of metastable helium must have a high purity while keeping sufficient brightness; second, the measurement of absolute cross section is very sensitive to experimental inaccuracies. Over the past few decades, the animated crossed beam technique and the corresponding experimental set-up were developed in the lab [79, 234] and have allowed accurate and absolute values of cross sections for electron-impact ionization of atoms and molecules to be measured. However, the first difficulty can only be tackled by designing a new source of pure metastable helium since no existing setup matches the present requirements.

The production of helium atoms in the 1s2s ^{3}S state is challenging since optical dipole excitation from the ground state is forbidden. Electron impact excitation of ground state helium is widely used, either in a gas discharge or using an electron gun [235, 236], but produces a beam of ground state helium containing minute fractions of singlet (1s2s ^{1}S) and triplet (1s2s ^{3}S) metastable atoms. Neutralization of fast He$^+$ ions onto alkali vapor produces fast atoms in the 1s^2 ^{1}S, 1s2s ^{1,3}S and 1s2p ^{1,3}P excited states with a population distribution that has been characterized for all alkali targets [235, 237–241]. While generally acceptable, such a distribution is inappropriate when turning to state-specific measurements. As an alternative, we propose in the following to use the photodetachment of He$^-$(1s2s2p ^{4}P^o), which leaves helium in the 1s2s ^{3}S state only provided that the photon energy is tuned below the 1s2p ^{3}P threshold, *i.e.* , below 1.1 eV. (see, *e.g.*, Xi and Froese Fischer [183]).

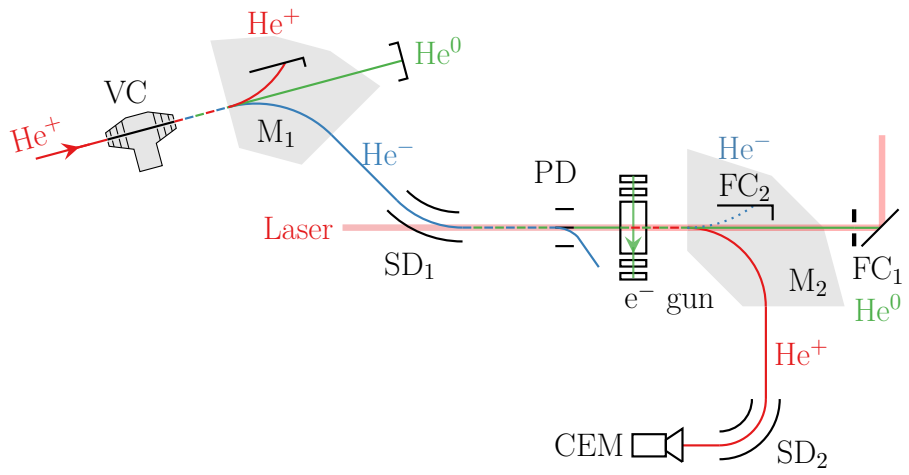

Figure 4.1: *Experimental setup. VC: sodium vapor cell; M_1: magnet mass selector; $SD_{1,2}$: spherical deflector; PD: planar deflector; M_2: magnetic analyzer; $FC_{1,2}$: Faraday cup; CEM: channel electron multiplier. Only the major parts of the apparatus are shown here, for a more detailed sketch of the electron impact apparatus (starting after M_1), see, e.g., [234].*

4.2 Experimental setup

4.2.1 Metastable helium source

The production of a fast beam of metastable helium atoms follows three steps, of which the two latter are represented in the sketch of the experimental setup in Fig. 4.1. First, He^+ ions are extracted from a duoplasmatron source fed with He gas and accelerated to 8 keV. Second, the He^+ beam is passed through a Na vapor cell where it is converted into He^- by double charge exchange with sodium atoms with an efficiency of the order of 1%. Downstream, a magnet selects the He^- component of the beam and injects it into the electron impact ionization setup. Although $He^-(1s2s2p\ ^4P)$ is metastable, the lifetimes of its $J = 1/2, 3/2$ and $5/2$ fine-structure components are sufficiently long (7.8 μs, 12.3 μs and 359.0 μs respectively [39]) to permit the use of conventional beam transport and detection techniques. In a third step, after passing through several deflectors, the anion beam interacts collinearly with the light from a CO_2 laser. Photodetachment occurs along this path (17.5 cm) and leaves helium atoms in the $1s2s\ ^3S$ state only.

The ion beam kinetic energy of $E = 8$ keV is chosen in order to maximize the ionization signal and results from considerations concerning (i) the electron impact ionization signal itself, (ii) the He^- beam current,

(iii) the He^- detachment efficiency and (iv) the He^+-He^- conversion efficiency. The ionization signal K is inversely proportional to the atoms' velocity ($E^{-1/2}$) and proportional to the current of metastable atoms. This current is in turn proportional to the detachment efficiency, which scales as $E^{-1/2}$ in the linear regime, and the anion current. The anion current itself scales as $E^{3/2}$ due to space-charge effects [242]. Therefore, the final signal loosely depends on the kinetic energy of the particles ($E^{1/2}$) and higher energies give in principle higher signals. Let us now consider the He^+-He^- conversion efficiency, which influences the available He^- current. The cross section for formation He^- by double charge exchange with alkali vapor depends on the kinetic energy of the incident He^+ ions. It presents a maximum around a few keV whose precise position for Na cannot be determined to better than between 6 keV and 10 keV since data for this atom are scarce and contradictory (see Hooper *et al.* [243] and references therein). The conversion efficiency measured by Hooper *et al.* in this range is around 1.5% and does not vary by more than 20%, but drops rapidly above it. Similar peak efficiencies have been measured for other alkali atoms such as Cs or Rb [244, 245]. Therefore, the maximum electron-impact ionization signal is reached for kinetic energies lying in the range of maximum He^+-He^- conversion efficiency and, in the same time, being sufficiently high so that the $E^{1/2}$ scaling factor is favorable. While no extensive tests were carried out to determine the optimal beam energy, the 8 keV value appears as a reasonable compromise between these various constraints.

We may further note that the He^+-He^- conversion efficiency also depends on the temperature of the sodium cell, which determines in turn the Na vapor thickness or line density. If too small, the probability of occurrence of two sequential collisions is low, and so is the efficiency. If too high, the probability that He^- ions are stripped in a third collision with Na atoms raises, thus lowering the conversion efficiency. The present experiment was run at low-temperature, so as to limit the cell temperature to below 350 °C and avoid both rapid depletion of the amount of liquid sodium in the oven and reduce sodium deposition on the electrodes of the source and ion optics.

Detachment of He^- is realized by interaction with the light beam from a CO_2 laser which generates 10 W of light with $\lambda = 10.6$ μm and an M^2 factor smaller than 1.2. It is loosely focused onto the atomic beam by the combination of a divergent ($f = -10$ cm) and a convergent ($f = 20$ cm) lens, at mid-distance between the exit of the spherical deflector SD_1 and the electron beam. The optics were chosen and placed so that the spot size (1.3 mm) is close to the atomic beam diameter (2 mm) and the Rayleigh range (10.4 cm) is large enough to maintain

sufficient intensity throughout the detachment region. The laser beam enters the vacuum chamber through an AR-coated Germanium window, reaches the atomic beam *via* a hole drilled in the spherical deflector SD_1 and leaves the vacuum chamber through another AR-coated ZnSe window in order to be collected by a powermeter.

After detachment, the metastable atoms fly straight through the collision region and analysis magnet (M_2) and are collected onto a Faraday cup (FC_1). Due to the collinear detachment arrangement, the laser beam still overlaps the atom beam. In order to simultaneously allow the laser beam to exit the vacuum chamber and measure the current of neutral atoms, the Faraday cup consists in a guard electrode and a polished Al surface oriented at 45° with respect to the direction of the incident beams. While the neutrals hit the Al surface, the laser beam is be reflected out of the vacuum chamber as the reflectivity of Aluminum is 95% for $\lambda = 10.6$ μm. The current of neutrals is determined by measuring, on the Al plate, the current generated by secondary electrons emitted upon atom impact and leaving the surface under the action of the electric field of the guard electrode, set to a high positive voltage. These two currents are linked by the proportionality constant γ, which stands for the average number of secondary electrons emitted per neutral impact. In order to determine γ, we have measured the He^- current I_- and the secondary electron current I_s for increasing laser powers. For this measurement, the planar deflector PD is switched off so that the anions reach the Farady cup FC_2 located inside the analysis magnet. The attenuation of the He^- beam due to photodetachment corresponds to the increase of the neutrals' current, therefore we have the following relation,

$$I_s(P) - I_s(0) = \gamma \left[I_-(0) - I_-(P) \right], \tag{4.1}$$

where $I_s(0)$ and $I_-(0)$ are the currents when the laser is switched off and $I_s(P)$ and $I_-(P)$ those for a given laser power P. However, one must also take into account the fact that the part of the secondary electron current due to neutrals produced by spontaneous detachment and collisions with the residual gas will decrease as the anion current is attenuated by the laser. Doing so, we obtain the equation

$$I_s(P) = \gamma \left[I_-(0) - I_-(P) \right] + \delta I_-(P), \tag{4.2}$$

where δ is defined as $I_s(0)/I_-(0)$. In practice, the coefficients γ and δ are determined by fitting the left hand side of the above equation to its right hand side for 7 laser powers. An example is shown in Fig. 4.2, for which we obtain $\gamma = 3.51$ and $\delta = 0.222$. We have repeated this procedure

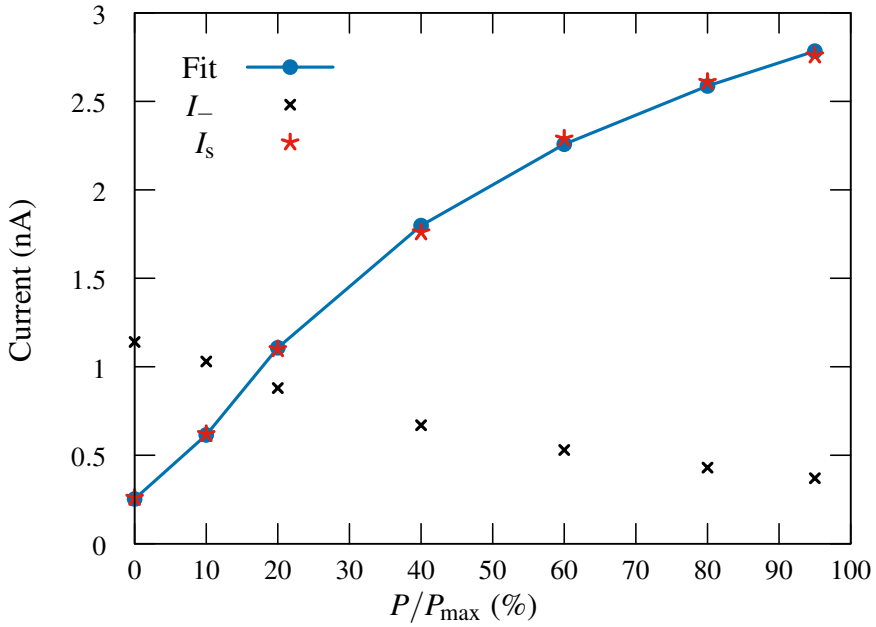

Figure 4.2: *Anion and secondary electron currents as a function of ratio between applied and maximum laser power. Crosses: anion current, stars: secondary electron current, full line: fit of* $I_s(P)$ *using Eq.* (4.2).

frequently throughout the several weeks of measurements, and found $\gamma = 3.44$ in average, with very little variation (3%).

In order to characterize the interaction between the ion and laser beams and further investigate the performances of the metastable atom source, we have measured the He$^-$ detachment efficiency for increasing overlap distances Z between the laser and the ions. To do so, a set of 3 deflectors spaced by known distances and placed along the beams path were used to vary Z. The first deflector is located right after the cylindrical deflector (SD_1), the second is shown in Fig. 4.1 as PD and the third is located after the electron gun. If no deflectors are switched on, the anion beam travels to the Faraday cup FC_2 and the overlap distance is maximal. Switching on one of the deflectors, *e.g.* PD, the anion beam is deflected out of the light path earlier and Z is significantly reduced (by 90 cm for PD). The current of metastable atoms is measured when each of these deflectors is individually turned on, and provided that the incoming He$^-$ current is known, the detachment efficiency $A(Z)$ is readily obtained. The measured values of $A(Z)$ are shown in Fig. 4.3.

Since $A(Z)$ is an average over the volume of interaction between the two beams, characterization is best performed by comparison with a

simple modeling of the detachment process. The detachment efficiency can be written, in its most general form, as

$$A(Z) = \iint_{-R}^{R} dx\, dy\, \rho(x,y) \left[1 - \exp\left(-\int_{z_0}^{Z} \frac{dz}{v}\sigma\phi(x,y,z)\right)\right], \qquad (4.3)$$

where v is the ions' velocity and σ the photodetachment cross section of 11.5×10^{-21} m^2 taken from Ramsbottom and Bell [182]. The anion and laser beams propagate along the z direction and start overlapping at a position z_0 corresponding, in the experiment, to the exit of the spherical deflector SD_1. The anion beam is collimated by two diaphragms ($R =$ 1 mm) before the interaction region, therefore its normalized profile ρ can be approximated by a uniform distribution over a disc of area πR^2,

$$\rho(x,y) = \frac{\sqrt{(R^2 - x^2)(R^2 - y^2)}}{\pi R^2}. \qquad (4.4)$$

Deviation of the photon flux ϕ from a Gaussian profile is given by its M^2 factor, and ϕ thus reads

$$\phi(x,y,z) = \frac{1}{\hbar\omega}\frac{2P_{\text{laser}}}{\pi w^2(z)} \mathrm{e}^{-2(x^2+y^2)/w^2(z)}, \qquad (4.5)$$

where the beam radius $w(z)$ is expressed in terms of the waist radius w_0 and the Rayleigh range z_R,

$$w(z) = w_0\sqrt{1 + \left(\frac{z}{z_R}\right)^2}, \qquad \text{with } z_R = \frac{\pi w_0^2}{M^2\lambda}. \qquad (4.6)$$

The M^2 factor is taken as 1.2, given by the manufacturer, the waist radius w_0 is defined by the lenses set and is slightly adjusted in the calculation to match experimental data, the laser power P_{laser} is chosen as 8 W in order to account for reflection and absorption by the entrance window and collimation by the hole in the spherical deflector SD_1. The integrals in Eq. (4.3) are computed numerically using the QUADPACK routines [210].

The measured and calculated detachment efficiencies are shown in Fig. 4.3. An overall good agreement is observed and suggests that the main properties of the overlap region are well reproduced by the model. The efficiency reaches $\sim 45\%$ after the deflector PD, which corresponds to the working conditions when measuring cross sections. This value is very high compared to common standards and can be explained by two factors. First, the photodetachment cross section of He^- is large,

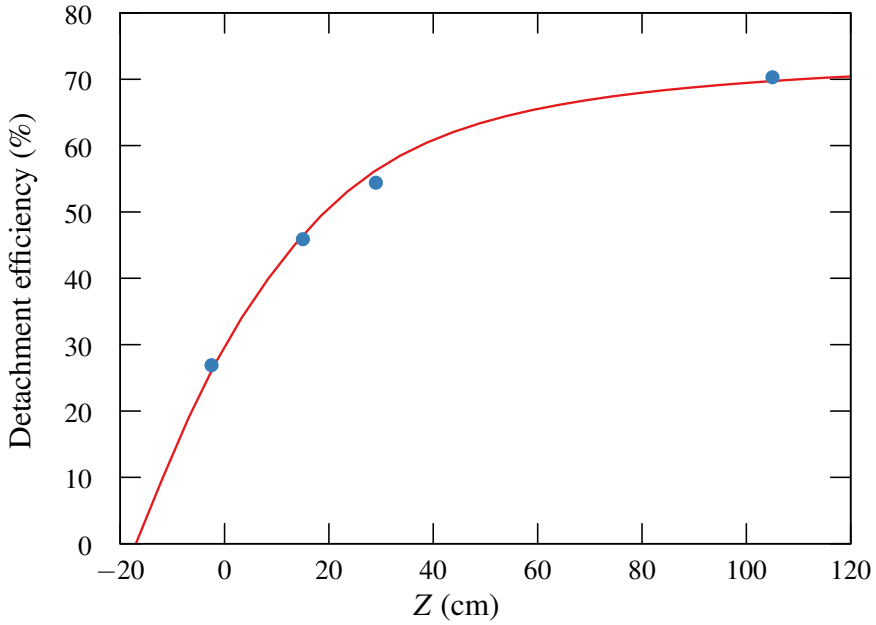

Figure 4.3: *Detachment efficiency as a function of the overlap distance Z, referenced to the laser focus. The circles are experimental data. The full line is the simulated efficiency for a laser power of 8 W and a waist radius of 0.825 mm.*

reaching 10^{-20} m^2 at the CO_2 laser wavelength [183]. Second, the photodetachment rate is inversely proportional to the photon energy which, for $\lambda = 10.6$ μm (0.117 eV), is 20 times lower than for visible light (500 nm, 2.48 eV). Therefore, all other quantities being equal, the detachment efficiency is strongly enhanced when using long-wavelength infrared radiation.

As a result of the high detachment efficiency and relatively intense He$^-$ beam, the present source is able to generate a bright, fast beam of metastable atoms. He$^-$ currents of 15 nA are routinely achieved in the collision region and yield currents of metastable helium, as measured in amperes, of 6 nA. This corresponds to neutral particle densities of 5×10^3 cm^{-3}. Such densities can certainly be increased by enhancing the detachment efficiency with a longer overlap distance, as seen in Fig. 4.3, a reduced ion beam velocity or a higher laser power. Interestingly, high power CO_2 lasers are commercially available for industrial applications and can easily deliver more than 100 W. On the ion side, high current He$^-$ sources have been developed for applications in particle accelerators and thermonuclear fusion devices and may certainly be used to further

increase densities [246].

Finally, we note that although free from other excited states, the metastable beam is contaminated by ground state atoms due to spontaneous detachment and stripping on residual gas. Spontaneous detachment occurs along the 17.5 cm-long interaction region, located 2 m after the Na vapor cell, and neutralizes 2.3%, 1.7% and 0.08% of the incoming anions initially in the $J = 1/2, 3/2$ and $5/2$ respectively. Neutralization of the incoming He^- ions thus occurs at the level of 1%, assuming that the fine structure states of He^- are statistically populated during the charge exchange process. The amount of neutralization by stripping collisions with the residual gas can be estimated from the electron impact ionization signal measured when the laser is switched off and using both the neutralization fraction due to spontaneous detachment and the known ionization cross section of ground state helium [247]. We determined that collisions with the background gas convert about 3.5% of the incoming anion beam into ground state helium. Therefore, in total, about 4.5% of the anion beam is neutralized into ground state helium.

4.2.2 Electron impact ionization setup

The atom source being now well characterized, we can turn to the electron impact ionization experiment. The absolute cross section is measured with the animated-crossed-beam technique (ACBT), originally developed for electron impact ionization by Defrance *et al.* [79, 122], which we used to determine photodetachment cross sections in Part 2. We recall that its main advantage lies in the fact that the form factor, related to the interaction volume, needs not be determined. The corresponding experimental setup has already been described in some length elsewhere (see [234] and references therein), thus only its major features will be outlined below.

As it passes through the collision region, the incoming metastable atom beam is intersected at right angle by the ribbon-shaped electron beam from an electron gun with an indirectly-heated cathode. The kinetic energy of the electrons is determined by the potential difference between the cathode and the biased interaction region. It is further corrected to account for a contact potential difference, determined by fitting the measured ionization cross section of Ne^+ at threshold. The energy spread of the electron beam is estimated to be 0.5 eV (FWHM). The ACBT relies on sweeping one of the beams across the other, therefore the electron beam is moved vertically across the atom beam in a linear see-saw motion by means of electrostatic deflection. The collision region is brought to a high positive voltage (1000 V) which allows to

separate the electron impact ionization signal from the background. Indeed, He^+ ions formed in this region will gain a kinetic energy of 1 keV, thus reaching $E = 9$ keV, while He^+ ions produced by collision with the residual gas up- and down-stream gain no energy ($E = 8$ keV). The 9 keV ions produced by electron impact are mass- and energy-selected by the analyzing magnet M_2, subsequently deflected by a 90° spherical deflector (SD_2) and counted with a channel electron multiplier (CEM).

During one sweep of the electron beam, the He^+ ions are counted and the electron beam current I_e and secondary electron current I_s, related to the current of metastable atoms by γ, are measured. The total number of He^+ ions K produced during the sweep is related to the cross section σ by

$$\sigma = \frac{v_e v_n}{(v_e^2 + v_n^2)^{1/2}} \frac{\gamma e^2}{I_s I_e} \frac{uK}{\eta}, \tag{4.7}$$

where v_e and v_n are the velocities of the electrons and atoms respectively, e is the elementary charge, u is the sweeping speed and η is the detection efficiency. The sweeping speed u of ~ 8 m/s is determined by measuring the travel time of the electron beam between two wires located above and below the atomic beam, and separated by a known distance. The detection efficiency for 9 keV He^+ ions is 0.95 ± 0.05, as estimated from the known detection efficiency for protons at 5 keV [136]. Sweeping of the electron beam is performed at 2×383 Hz and the final cross section is an average over measurements lasting from a few minutes to more than 1 hour.

Two corrections to Eq. (4.7) must be considered in order to account for spurious experimental effects. First, some anions are detached *inside* the spherical deflector SD_1, where the neutrals produced do not have the correct trajectory to reach the collision region. Using the model of the laser-atom overlap developed in the previous section, we have determined that this effect decreases γ by 3%. Second, electron impact ionization of ground state atoms contaminating the metastable beam will also contribute to the He^+ signal. By performing a measurement when the laser was switched off, we could determine that the ground state contribution amounts to less than 1% of the measured ionization yield.

Uncertainties arising from systematic effects are estimated as follows: the uncertainty of 1.5% on the sweeping speed, 0.5% on the kinematic factor $v_e v_n / \left(v_e^2 + v_n^2\right)^{1/2}$ and 1.5% on the electron current have been previously estimated [234] ; the uncertainty of 5% on the detection efficiency reflects the uncertainty on the estimate made from proton detection efficiency [136] ; the observed 3% standard deviation around the mean value

of γ gives a conservative estimate of its uncertainty; the uncertainty of 6% on the secondary electron current is obtained by comparison with a calibrated current source. The total systematics are thus 8.6%, as obtained by taking the quadrature sum of all uncertainties.

4.3 Ionization cross sections

4.3.1 Single ionization of metastable helium

The results for electron impact ionization of He(1s2s ^{3}S) are presented in Fig. 4.4 along with existing theories and experiment. Only one absolute measurement is available over a wide electron energy range, by Dixon *et al.* [213], and it lies much higher than the present results. In their experiment, a fast beam of metastable atoms was first formed by charge exchange between fast He^+ ions and cesium vapour and subsequently crossed perpendicularly by an electron beam. The cross section was determined under the assumption that, after charge exchange, 80% of the beam is in the 1s2s ^{3}S state while the remaining atoms are in the ground state. This assumption was later weakened by Reynaud *et al.* [237] and Neynaber and Magnuson [238] who showed that, for a 1 keV He^+ beam, the neutral beam emerging after charge exchange consists in 60.5% of He(1s2s ^{3}S), 23.5% of He(1s2s ^{1}S) and 16% of He($1s^2$ ^{1}S). We have therefore computed a rough estimate of the corresponding correction to the 4 keV data of Dixon *et al.* by using the 1 keV populations and the ionization cross section of He(1s2s ^{1}S) from Ralchenko *et al.* [216]. The correction is found to be small, the larger ionization cross section of He(1s2s ^{1}S) counterbalancing the reduced He(1s2s ^{3}S) fraction, and certainly cannot account for the large discrepancy observed with the present experiment. The origin of such a large difference remains unclear.

A handful of absolute experiments were performed (see [248] and references therein) prior to the experiment of Dixon *et al.* [213], however they are limited to electron energies ranging from the metastable ionization threshold (4.77 eV) to the ground-state ionization threshold (24.59 eV). Indeed, the thermal-energy beams used contained predominantly ground state atoms and therefore ionization of the small fraction of metastable atoms was masked by ground state ionization above 24.59 eV. The cross sections obtained vary greatly in shape and magnitude (see, for example, Long and Geballe [248]) and vastly differ from the present cross section.

Before turning to comparison with theory, we may stress that, in both the present experiment and that of Dixon *et al.* , the measured sig-

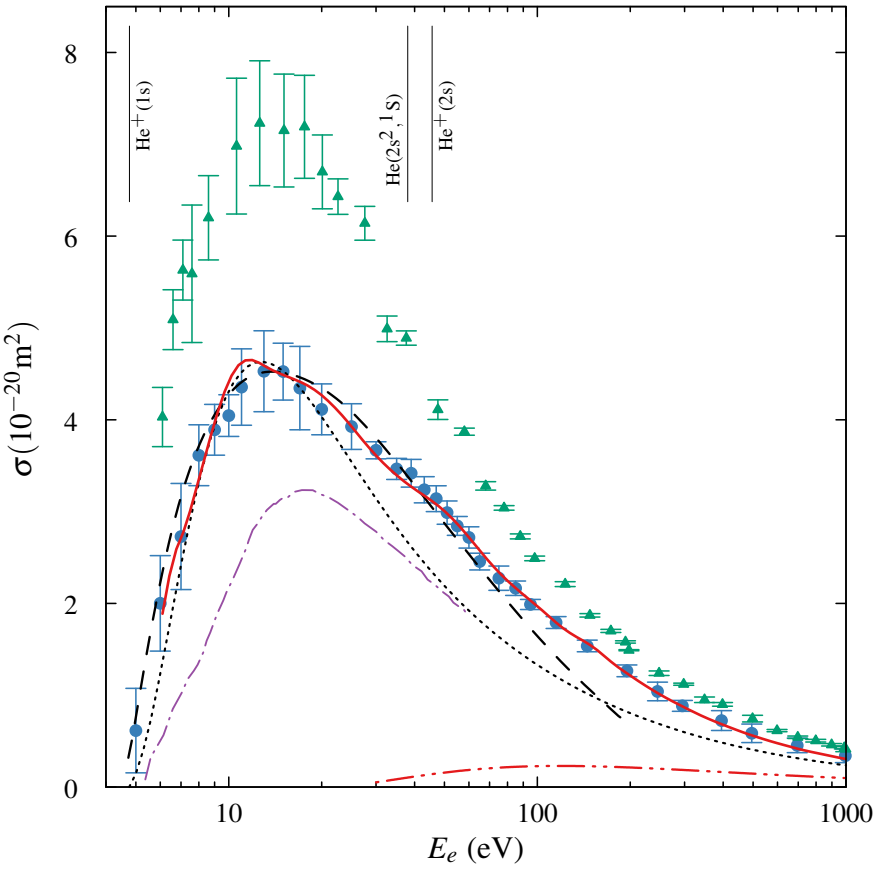

Figure 4.4: *Electron impact ionization cross section of He(1s2s ^3S). Full circles: present work; full triangles: absolute measurement of Dixon et al. [213]; dotted line: CCC calculation [216]; dashed line: TDCC calculation [214]; dash-dotted line: RMPS calculation [217]; full line: CCC and Born calculation [215]; dash-dot-dotted line: contribution of autoionization and ionization with excitation to the total cross section [215]. The vertical lines indicate the position of the various thresholds. The error bars are the 2σ statistical uncertainties.*

nal is the sum of three contributions: (i) ionization of the outer electron leaving the He^+ ion in its ground state; (ii) ionization of the inner electron leaving the He^+ ion in an excited state; (iii) excitation to doubly excited states of He and subsequent autoionization.

On the theoretical side, the electron impact ionization of He(1s2s ^{3}S) is a benchmark process that has been the object of a number of theoretical calculations of ever-increasing sophistication. Numerous examples of model calculations can be found in the literature and use, with increasing degree of sophistication, the semi-classical Deutsch-Märk formalism, a formula based on the Binary-Encounter-Bethe model, Born-type methods or the perturbative distorted-wave method [213, 214, 218–223]. A series of *ab-initio* calculations has also been performed in the recent years, the results of which are represented in Fig. 4.4. Several convergent-close-coupling (CCC) calculations were dedicated to computing the electron impact ionization cross section [215, 216, 224], and systematically fall more than a factor 1.5 below the experimental data of Dixon *et al.* [213]. In order to assess the validity of the CCC calculations, R-matrix method with pseudo state (RMPS) and time-dependent close-coupling (TDCC) calculations were also performed [214, 217]. The present measurement lies higher than the RMPS calculation of Bartschart [217], but matches the TDCC calculation of Colgan and Pindzola [214] up to electron energies of 100 eV and is in excellent agreement with the calculation of Fursa and Bray [215] over the whole energy range covered. Fursa and Bray performed a frozen-core CCC calculation which was smoothly scaled, in the range from 30 eV to 120 eV, by the ratio between multi-core and single-core Born calculations in order to account for ionization with excitation and excitation to doubly excited states of helium followed by autoionization, up to $n = 3$. Above 120 eV, the cross section is the one obtained from the multi-core Born calculation. The difference between the frozen-core calculation, comprising the CCC calculation matched, at higher energies, with frozen-core Born calculations, and the multi-core calculation is also shown in Fig. 4.4. It is apparent that the contribution of autoionization and ionization with excitation is non-negligible, and amounts to about 30% of the total cross section at an energy of 1000 eV. While ionization through doubly excited states is negligible for ground state atoms [249], the present measurement suggests along with [215] that it contributes to the ionization cross section for excited states. Surprisingly, the most recent frozen-core CCC calculation of Ralchenko *et al.* [216] deviates from the frozen-core CCC calculation of Fursa and Bray [215] at intermediate energies.

The high-energy behavior of the ionization cross section is best observed in the Bethe plot presented in Fig. 4.5. Again, agreement with

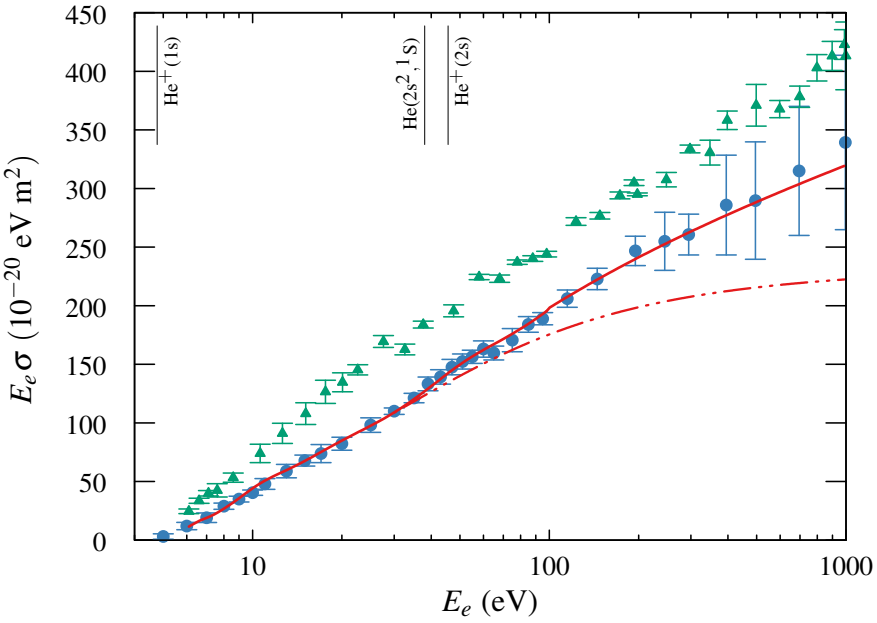

Figure 4.5: *Bethe plot of the electron impact ionization cross section of He(1s2s ^3S). Full circles: present work; full triangles: absolute measurement of Dixon et al. [213]; full line: CCC and Born calculation of Fursa and Bray [215]; dash-dot-dotted line: contribution of autoionization and ionization with excitation to the total cross section, as calculated by Fursa and Bray [215]. The vertical lines indicate the position of the various thresholds. The error bars are the 2σ statistical uncertainties.*

the calculation of Fursa an Bray is excellent [215]. The importance of the autoionization and ionization with excitation channels is evident at high energies, where the frozen-core Born calculation fails to reproduce the experimental asymptotic behavior. The shape of the cross section measured by Dixon *et al.* is similar to the present data but its magnitude is larger.

4.3.2 Double ionization of He$^-$

The cross section for the electron impact double ionization (EIDI) of He$^-$ is readily measured with the apparatus described above. It suffices to switch the CO_2 laser and deflector PD off and run the experiment while measuring the He$^-$ current on the Faraday cup FC_2 instead of the secondary electron current on FC_1. The present results are shown in Fig. 4.6, and no other experimental data or *ab initio* calculations are available for comparison. The magnitude of the cross section is

higher than for other light atomic anions [233], for which σ lies below 8×10^{-21} m^2. This may be expected since He^- is a weakly bound anion, with a double ionization potential of 4.84 eV, and two of its electrons reside in the outer shell (1s2s2p).

The dotted curve in Fig. 4.6 corresponds to the generic shape function for EIDI cross sections of negative ions, established by Rost and Pattard [250] and given by the formula

$$\sigma(E) = \sigma_M \left(\frac{E}{E_M} \right)^{\beta} \left(\frac{\beta + 1}{\beta \frac{E}{E_M} + 1} \right)^{\beta+1}, \tag{4.8}$$

where $E = E_e - I$ is the excess energy of the system measured from the double ionization threshold I, σ_M is maximum of the cross section, located at an energy E_M, and β is the Wannier exponent. The values of E_M and σ_M are determined from a fit of the cross section using the function of Ralchenko *et al.* [216]. The Wannier exponent determines the power law behavior of the cross section at threshold ($\sigma(E) \propto E^{\beta}$), as derived both classically and quantum mechanically, and its value depends on the final, fragmented state *only*. A value of $\beta = 2.83$ corresponds to the EIDI of a negative ion [251]. Equation (4.8) provides an *ad hoc* shape for the EIDI cross section which reduces to the Wannier law close to threshold and behaves as the classical $1/E$ asymptotic limit for high energies. It was first shown to match surprisingly well the ionization cross sections of a large number of atomic targets (H, He, C, N, O, Ar, Ne) by charged projectiles such as electrons, positrons, protons and antiprotons [252]. Subsequent work considered its application to the EIDI of negative ions and the experimental cross sections for H^-, O^- and C^- were, again, well accounted for [250]. The authors stressed that their formula can be used as a tool to determine the degree of importance of direct EIDI against indirect EIDI processes such as excitation to autoionizing states. Indeed, since Eq. (4.8) only accounts for direct EIDI, deviations from this universal shape such as those observed for C^- indicate the presence, and possibly prevalence, of indirect EIDI channels.

Departure from the analytical shape at intermediate energies, as seen in Fig. 4.6, may indicate the onset of indirect EIDI mechanisms. In the same energy region, a plateau can be observed in the Bethe plot shown in Fig. 4.7. Note that deviations from the analytical shape close to threshold may not be regarded as significant since, in this electron energy range, an accurate measurement is very difficult with the present setup. The mechanism underlying indirect EIDI is presently unknown, although we can note that departure from the direct EIDI shape is important in the energy region of triply excited states of He^- and doubly

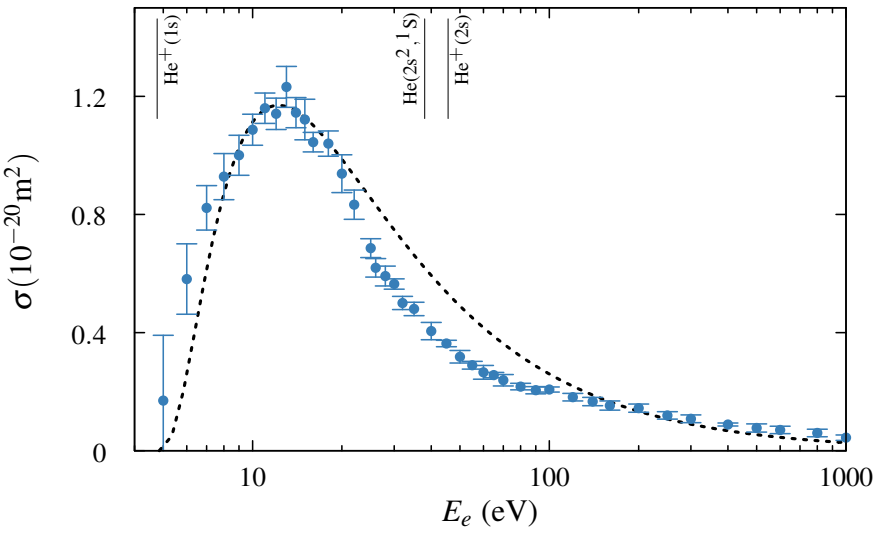

Figure 4.6: *Electron impact double ionization cross section of He$^-$(1s2s2p ^{4}P^o). Full circles: present work; dotted line: analytical formula of Rost and Pattard [250]. The error bars are the 2σ statistical uncertainties.*

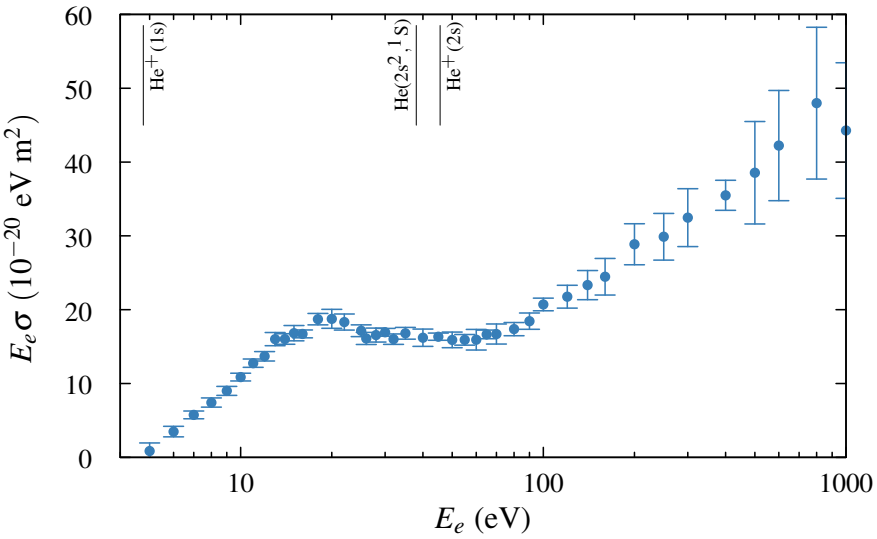

Figure 4.7: *Bethe plot of the electron impact double ionization cross section of He$^-$(1s2s2p ^{4}P^o). Full circles: present work. The error bars are the 2σ statistical uncertainties.*

excited states of He. The excitation-autoionization mechanisms responsible for the enhancement of the single ionization of the metastable atom may thus partly cause the suppression of the double ionization of He^-. Note however that the possible onset of indirect process lies below the energy of the first doubly excited state of He. It is interesting to note that experimental and theoretical works on the double photodetachment of He^- have evidenced the important role played by autoionizing triply excited states of He^- and doubly excited He states, provided that the photon energy is tuned between the $He^+(1s)$ and $He^+(2s)$ thresholds (38 eV – 44 eV) [157, 253–255]. While some channels lead to an enhancement of the He^+ production, a few others such as the detachment through the He(2s2p $^3P^o$) transient state have been shown to favor the production of neutral helium [253]. In regard of the quenching of He^+ production observed in the present data, such channels may also play a role in the double ionization by electron impact.

As a final remark, we note that the present cross section does not match those derived from semi-empirical formulas for EIDI such as that of Shevelko and Tawara [233, 256].

4.3.3 Double ionization of metastable helium

The electron impact double ionization cross section of He(1s2s ^{3}S), measured with the exact same setup as for single ionization but detecting He^{2+} ions instead, is shown in Fig. 4.8. It is compared to the cross section for the double ionization of He($1s^2$ ^{1}S) measured by Bahati *et al.* [226] and Shah *et al.* [257]. Surprisingly, the magnitude of the cross section for the metastable state is similar to that for the ground state, although it lies 19.6 eV above it. This violates the classical Thomson scaling law which states that cross sections scale as the inverse of the square of the ionization potential I_p. In the present case, the EIDI cross section of He(1s2s ^{3}S) should thus be 1.8 times larger than that of He($1s^2$ ^{1}S). The $1/I_p^2$ scaling law has been verified for a number of systems, and is used in most semi-empirical formulas describing EIDI cross sections [233, 258–260]. We have no clear explanation for the present deviation.

The EIDI cross sections of metastable and ground state helium further exhibit a similar high energy behavior, as seen in the Bethe plot presented in Fig. 4.9 where both cross sections reach a plateau. The plateau for He(1s2s ^{3}S) exhibits a slightly negative slope. As discussed by Bahati *et al.* [226], the sign of the plateau for He($1s^2$ ^{1}S) is unclear since, while the results of Shah *et al.* [257] show a slight, negative slope, other experimental results (not shown) find a plateau with a slight

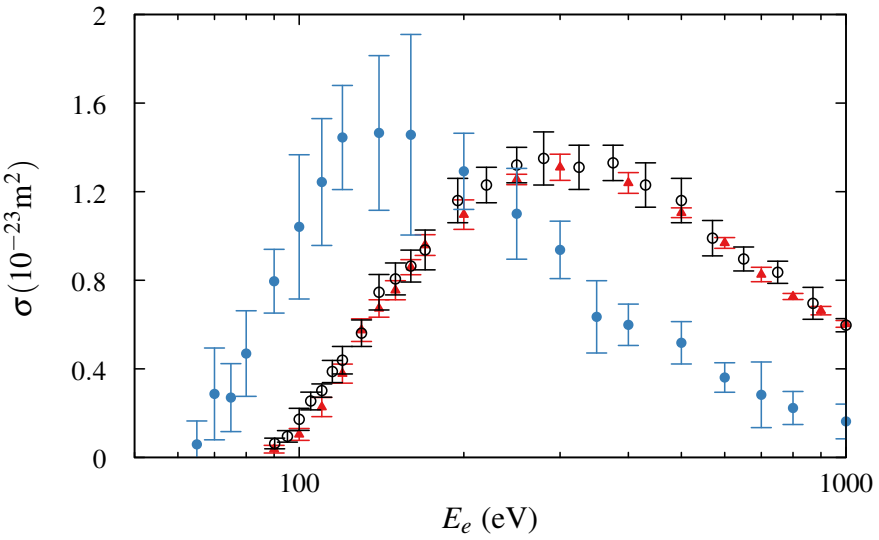

Figure 4.8: *Electron impact double ionization cross section of the ground and first excited states of helium. Full circles: present work for He(1s2s ^3S); full triangles: experiment of Bahati et al. for He(1s^2 ^1S) [226]; empty circles: experiment of Shah et al. for He(1s^2 ^1S) [257]. The error bars are the 2σ statistical uncertainties.*

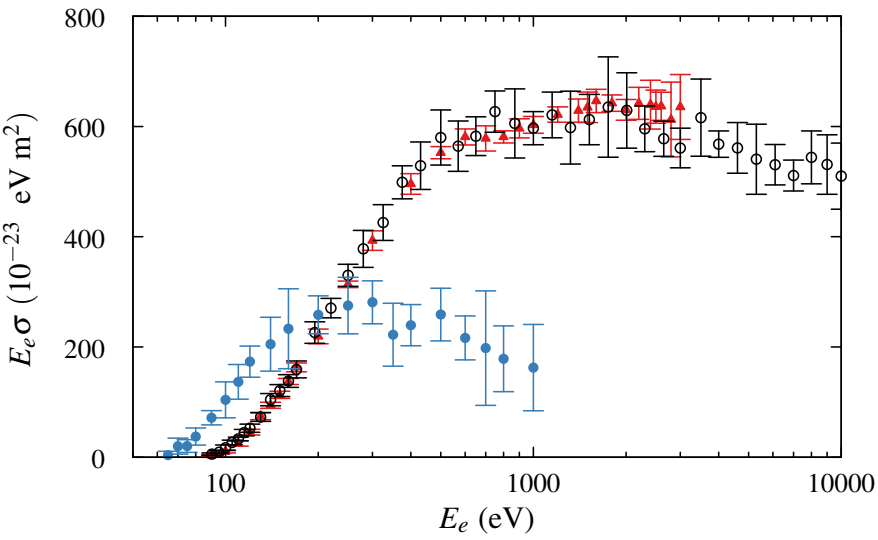

Figure 4.9: *Bethe plot of the electron impact double ionization cross section of the ground and first excited states of helium. Full circles: present work for He(1s2s ^3S); full triangles: experiment of Bahati et al. for He(1s^2 ^1S) [226]; empty circles: experiment of Shah et al. for He(1s^2 ^1S) [257]. The error bars are the 2σ statistical uncertainties.*

positive slope. The slope is related to the double photoionization cross section and must thus be, in theory, strictly positive [261].

Theoretical input concerning the physical mechanisms underlying EIDI is scarce in general, and limited to the work of Defrance *et al.* [262] in the present case. They calculated the EIDI cross section of He($1s^2\ ^1S$), He(1s2s ^{1,3}S) and of the corresponding isoelectronic ions up to carbon within the framework of a shake-off model and first Born approximation. The calculated cross sections for the ground state and metastable triplet state both lie below 5×10^{-24} m^2 and differ by more than a factor of 2, in stark contrast with the present results. The large deviation between theory and experiment suggests that shake-off is either not the dominant process in the present energy range or not properly estimated with this model because of, *e.g.* , limitations in the description of electron-electron correlations in the target atom.

Simple considerations concerning the behavior of the cross section with respect to the electron energy can provide further hints on a *tentative* ionization mechanism. Let us first note that the ionization cross section of H(2s) has a shape very similar to that of He(1s2s ^{3}S) when the latter is computed within the frozen-core approximation, *i.e.* , neglecting the influence of excitation and ionization of the 1s electron. Hence, correlations between the 1s and 2s electrons may not significantly affect the energy dependence of the ionization cross section of He(1s2s ^{3}S), as long as the 1s electron is a spectator. In a second step, we consider the double ionization process and assume that it proceeds through the successive knockout of the two electrons. This assumption is nothing but that of a two step 1 or two step 2 mechanism, both of which have been discussed for ground state helium [263]. We then suppose, following the above argument, that the two ionization events are uncorrelated. Within this simplistic picture, the double ionization cross section σ_{DI} may be thought as the product of the single ionization cross section $\sigma_{2\mathrm{s}}$ of H(2s)[1] with the single ionization cross section $\sigma_{1\mathrm{s}}$ of He^+(1s). Such a product is represented in Fig. 4.10 by the dash-dotted curve, which was scaled to the maximum of the experimental data. We first notice that agreement is surprisingly good for such a primitive model. On the low energy side, between threshold and ∼102 eV, the modeled cross section lies higher than experimental data. Such a discrepancy may be explained, if the 2s electron is ejected first, by the loss of an energy ΔE_e by the projectile during the first knockout step. The multiplication leading to σ_{DI} should then be $\sigma_{2\mathrm{s}}(E_e) \times \sigma_{1\mathrm{s}}(E_e - \Delta E_e)$, where E_e is the energy of the incident electron. For energies below 102 eV, this effect will cause $\sigma_{1\mathrm{s}}$

[1] or, similarly, that of He(1s2s ^{3}S) within the frozen-core approximation

to be smaller and, consequently, the EIDI cross section to be lower. As the energy of the incident electron increases, the loss ΔE_e amounts to a smaller fraction of the total energy and this effect becomes less important. We may also note that the present model can account, to some extent, for the similar amplitudes of the EIDI cross sections for ground and metastable helium. Indeed, it suffices to note that in both cases the bottleneck for double ionization is the ejection of the 1s electron evolving in the residual He^+ core, which is significantly more difficult than ejection of the first 1s or 2s electron. As a final word of caution, it is important to remind that such a model is crude, and while the agreement with the experimental cross section is interesting, it may very well be accidental.

As for the EIDI of He^-, the cross sections calculated from semi-empirical, analytical formulas do not reproduce well the measured one.

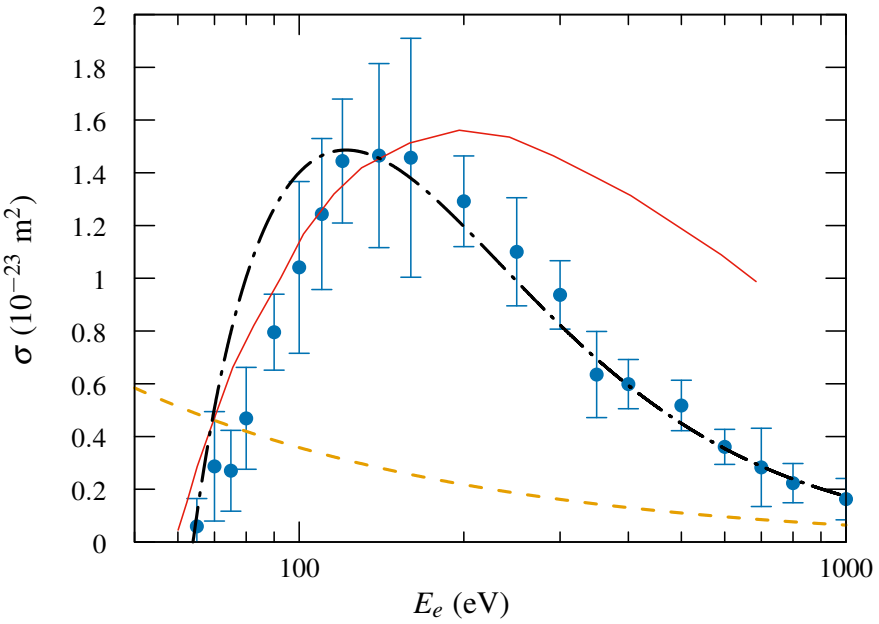

Figure 4.10: *Cross section from a tentative double knockout model for the electron impact double ionization of He(1s2s ^3S) as a function of the projectile energy (see text). Full circles: present work; dashed line: frozen-core CCC calculation for electron impact single ionization cross section of He(1s2s ^3S) [216], scaled by 3.1×10^3; full line: CCC calculation for the electron impact ionization of He$^+$(1s) [264], scaled by 27; dash-dotted line: cross section of a tentative "double knock-off" ionization mechanism. The error bars are the 2σ statistical uncertainties.*

4.4 Conclusion

In an effort to measure the electron impact ionization cross section of metastable helium, a novel source capable of producing an intense, fast and pure beam of He(1s2s ^{3}S) atoms was designed and built. It is based on the photodetachment of a He^- beam, which leaves helium in its 1s2s ^{3}S state only. Excellent production efficiencies are reached and can in principle be scaled up for applications requiring larger yields and densities. It may also pave the way to measurements of other quantities, such as the photoionization cross section of He(1s2s ^{3}S).

The cross section for single ionization by electron impact was measured using the animated-crossed-beam technique and the corresponding apparatus, developed over the past decades in the laboratory. The present results are in excellent agreement with the calculation of Fursa and Bray [215] and lie much lower than previous experimental data [213]. They resolve a long-lasting discrepancy and support the validity *ab initio* methods for the 1st excited state of helium. The present work also confirms the role of doubly excited states and suggest that they should be included in future accurate reference data [216]. In view of the increased importance of such states compared to their negligible role in ground state ionization, comparisons between the present data and fully *ab initio* multi-core calculations would be interesing, as was already performed for ground state helium [247].

Cross sections for the double ionization of He^- and He(1s2s ^{3}S) have also been measured for the first time. The former is high compared to common values and shows evidence of indirect double ionization mechanisms at intermediate electron energies. The latter is surprisingly low, matching in amplitude the cross section of ground state helium. A tentative mechanism was proposed based on crude considerations concerning the energy behavior of the double ionization cross section.

Chapter 5

Conclusion & perspectives

5.1 Conclusion

The work presented in this thesis explored different facets of the photoionization and electron impact ionization of negative ions and atoms. We first investigated the simplest form of photodetachment in much details: the one-photon detachment, in the perturbative regime, of the light atomic anions of hydrogen and oxygen. To do so, the animated-crossed-beam technique was developed for laser-ion interactions, including its extension to the multiphoton regime, and provided with absolute total cross sections that do *not* rely on modeling the overlap region between the laser and ion beams. A first benchmark measurement was carried out to determine the absolute total photodetachment cross section of H^-, falling in excellent agreement with compelling theoretical results. Photodetachment of O^- was later studied, within the same framework, both using CW and pulsed lasers. The good mutual agreement confirmed the validity of the ACBT for pulsed laser systems. Combining together the animated-crossed-beam technique, the velocity map imaging technique applied to photoelectron spectroscopy and a broadband tunable OPO laser, we were able to determine the total, partial and differential cross sections in a absolute manner and over an unprecedented range of photon energies (1.48 eV – 5.5 eV). These quantities give altogether a complete picture of the photodetachment of O^- from threshold to the ultraviolet region. Overall, good agreement with previous works is obtained for asymmetry parameters β and branching ratios. However, discrepancies are observed for the total cross section and prompts for further experiments to be carried out. Our results fall in fair agreement below the $O(^1D)$ threshold with a recent R-Matrix Floquet calculation. The

two-photon generalized cross section was also measured at the Nd:YAG laser frequency and, in combination with the same *R*MF calculation, a long-lasting discrepancy was resolved.

The second part was dedicated to the 4-photon double detachment of He^-, which is a non-perturbative, highly non-linear process. The intricate photon-induced dynamics could be disentangled only by combining experiment with both theoretical methods, namely *R*-Matrix and *R*-Matrix Floquet theory, and an accurate time-dependent modeling of the experiment by means of an effective Hamiltonian model. We could show that double detachment proceeds through the one-photon detachment of He^- followed by the resonance-enhanced multiphoton ionization of the transient atomic states 1s2s ^{3}S or 1s2p ^{3}P^o, depending on the photon energy. Series of Rydberg states, along with the 1s3s ^{3}S state, could be identified as the major source for resonance-enhancement, which was further found to be M_L-dependent. We considered explicitly the influence of the laser peak intensity and polarization and showed that it modifies coupling strengths, AC Stark shifts and dipole selection rules, thus altering double detachment dynamics. The second, ionization step was found not to depend strongly on the first, single detachment step. Double detachment thus proved a valuable tool for producing atoms in states that are difficult to reach with other, more conventional methods, and then study multiphoton dynamics *in situ*.

This observation naturally brings us to the third part of the work presented above, dedicated the electron impact single and double ionization of metastable helium and He^-. Such a difficult, state-selective experiment prompted the development of a source of fast metastable helium atoms with high purity that did not exist in the literature. It is based on the photodetachment of He^- by a CO_2 laser, which produces helium in its 1s2s ^{3}S state only, and does so with a very large efficiency ($\geq 40\%$). With this source, we could reach the high level of purity (95% 1s2s ^{3}S – 5% ground state) and reasonably large fluxes (6 nA) required for electron impact ionization measurements. We then explored a long lasting discrepancy concerning the absolute, total cross section for electron impact single ionization of metastable helium, which we could solve. Absolute double ionization cross sections for metastable helium and the helium negative ion were also recorded for the first time to our knowledge. Tentative explanations on their shape and anomalous features was given.

5.2 Perspectives

From a practical perspective, several improvements to the experimental setups described above would enhance the quality and ease of measurements. Developing a better magnetic shield for the velocity map imaging spectrometer would most certainly result in better energy resolutions, allowing to separate for example different photodetachment channels that cannot be resolved at the moment. Merging together the ACBT and VMI setups would result in faster cross section measurements, eventually allowing "one-shot" experiments where all total, partial and differential cross sections could be determined together. Finally, developing a reliable and accurate technique to determine *in situ* the absolute detection efficiency of channel electron multipliers would help reduce uncertainties on absolute measurements.

The measurement of all quantities governing the photodetachment of O^- on a broad photon energy range further paves the way to systematic studies of the photodetachment of anions of interest. An obvious target is H^-, for which we measured the total cross section only from 1.165 eV to 1.77 eV. Since it is a system of choice for testing theoretical methods, providing benchmark values is certainly desirable for photon energies above 2.2 eV, where no experimental data are available. In this respect, the OPO light source makes a measurement from threshold (0.755 eV) to 5.5 eV possible. Furthermore, the measurement of partial cross sections is not required since the 1s state of hydrogen is the only final state energetically allowed and, since photodetachment consists in detachment of an s-electron, the asymmetry parameter is expected to be constant and equal to 2. Photodetachment for higher photon energies can be envisioned using synchrotron light sources and one could go up to the resonance series converging to the $n = 2$ and $n = 3$ states of neutral hydrogen [36]. Angular distributions of photoelectrons in these channels are subject to rapid variations and are poorly studied [47].

Beyond studying the photodetachment of H^-, investigating the photodetachment of other anions such as C^-, Si^- or Na^- is a perspective for future work. C^- bears some interest in astrophysics and its total photodetachment section is only poorly known. In particular, available experimental total cross sections are put on an absolute scale using the absolute cross section for O^- measured by Smith and Branscomb *et al.* [80, 98], with which we did not find agreement. The photodetachment of Si^- is similar to that of C^- and quite eventful, one of its main feature being a broad shape resonance around 5 eV where the total cross section falls down to a near-zero value [265]. Only the total cross section has been measured in the vicinity of the resonance, and neither partial

nor differential data are available. Experimental data away from that region are also non existent. Therefore, a complete measurement is much needed to better understand this anion. The experimental procedure presented above is not limited to studying atomic anions, and its application to molecular anions is in principle quite straightforward. The first molecule one could envision to study is the hydroxyl anion OH^- which is important for, *e.g.* , interstellar chemistry. It is probably the anion for which the most detailed cross section studies exist (see [73] and references therein), and would be in this respect a necessary step in applying the ACBT+VMI+OPO procedure to molecular systems.

Multiphoton single detachment is another field of investigation that we only superficially considered. With the proposed multiphoton extension of the animated-crossed-beam technique, systematic studies are feasible. The largest concern in this perspective is the need for tunable, high-energy pulsed lasers in the infrared in order for the photon energy to be well below the detachment threshold. The spectral distribution of such lasers must be, if not well-controlled, at least well-characterized, since photon statistics effects become more important as the number of photons absorbed increases. One could investigate predictions made by Gribakin and Kuchiev on the properties and energy-behavior of multiphoton detachment cross sections [121, 154]. First of all their analytical formula for generalized total cross sections for n-photon detachment is expected to become more accurate for higher n. This allegation could be verified by studying the two, three and four photodetachment of the series O^-, F^-, Cl^-, for which experimental data exist but may be unreliable [266]. Second, Gribakin and Kuchiev gave closed formulas for the angular distributions of photoelectrons emitted upon multiphoton detachment. Such distributions have been measured only for the multiphoton detachment of a few anions such as F^- and I^- [267, 268], and other species or higher photon numbers could be investigated with our VMI spectrometer. The influence of laser polarization on these cross sections is also largely unexplored.

The double detachment of He^- in moderately strong laser fields was studied above, and by comparing theory and experiment we could investigate its underlying dynamics in details. This work may thus lay ground for studying the double detachment of He^- in very intense fields, as obtained with high-energy femtosecond lasers. The present understanding of sequential dynamics could help, for example, disentangling possible non-sequential processes occurring in the strong-field regime. Another perspective of future work could include investigating the photoelectron distributions following double detachment. The preliminary work we performed has shown that they depart from the description in terms of

asymmetry parameters due to the presence of intermediate resonances. Photoelectron spectroscopy may also serve, when combined with two-color experimental schemes, as a way to investigate multiphoton dynamics within the detachment continuum.

Finally, the development of a source of metastable helium atoms with high purity makes possible detailed studies of , *e.g.* , its photophysical properties. Experimental data are indeed scarce for this system due to the aforementioned production difficulties. Targets include, for example, the full cross sections set for single photoionization of He^*. The study of the chemical reactivity of He^* can also be envisioned, motivated by the importance of Penning ionization in cold plasma environments. Finally, the present source of metastable helium atoms paves the way to the production atoms in higher-lying states by resonant excitation. With such a scheme, the electron impact ionization cross section of excited states of helium belonging to the triplet manifold could be measured. Such data could serve, as for that of He(1s2s ^{3}S), as a benchmark for theoretical methods. The production of metastable atom beams is certainly not limited to helium, and we performed some preliminary work on the production of a O(^{1}D) beam. Once the source is operational, a measurement of electron impact ionization cross section of metastable oxygen could be envisioned since such data is demanded by the planetary science community.

Chapter A

Effective Hamiltonian theory

The effective Hamiltonian (EH) method, also called "Essential states method" by some authors [200], can be used to treat in a semi- perturbative manner resonance-enhanced multiphoton ionization (REMPI). It considers explicitly, *i.e.* in a non- perturbative way, the quasi-resonant bound states involved in the REMPI process. Other (off-resonance) bound states and continuum states are treated with perturbation theory up to any desired order. While extensive literature is available on EH theory and its wide range of applications, we feel that its derivation for the specific case of REMPI lacks a detailed, unified presentation. For more general information on EH theory, the reader may consider reading the comprehensive topical reviews by Killingbeck and Jolicard [202, 203].

The EH derivation presented below is based on the wave-operator method of Durand [204] and, while other derivation techniques exist, we believe it is the one providing the most intuitive and trouble-free approach. We also borrow from the deep insights found in Baker's article about the physical significance of EH for REMPI [201].

Atomic units are used throughout this appendix.

A.1 Preliminary Definitions

We consider an atom, prepared in a well-defined quantum state, in the presence of a laser field of angular frequency ω. The exact time-dependent Hamiltonian $H(t)$ of the system can be expressed as:

$$H(t) = H_A + H_F + V(t).$$

H_A is the Hamiltonian of the isolated atom, H_F that of the laser field and $V(t)$ is the time-dependent atom-field interaction. Merging H_A and H_F into H_0, the "free" Hamiltonian, we obtain :

$$H(t) = H_0 + V(t). \tag{A.1}$$

We denote by $|a\rangle |m\rangle = |a, m\rangle$ the discrete eigenstates of the free Hamiltonian H_0. $|a\rangle$ is a discrete eigenstate of the atomic Hamiltonian and $|m\rangle$ an eigenstate of the laser field Hamiltonian. The discrete eigenvalue spectrum of H_0 is given by

$$H_0 |a, m\rangle = (\mathcal{E}_a - m\omega) |a, m\rangle , \tag{A.2}$$

where $\mathcal{E}_a$ is the energy of the atomic state. The ionization continuum states are designated as $|\varepsilon, m\rangle$ where ε is the photoelectron energy. The continuum eigenvalue spectrum of H_0 is thus

$$H_0 |\varepsilon, m\rangle = (\varepsilon - m\omega) |\varepsilon, m\rangle . \tag{A.3}$$

The integer m can be chosen as the number of absorbed photons. We further make the following assumptions:

i. The system is well into the multiphoton regime and tunnel ionization can be neglected.

ii. The rotating-wave approximation (RWA) holds.

iii. The following closure relation holds,

$$\sum_m |m\rangle \langle m| \left(\int de\, |e\rangle \langle e| + \sum_a |a\rangle \langle a| \right) = 1.$$

A.2 Hilbert space partitioning

Let us start from the time-independent Schrödinger equation,

$$H |\psi\rangle = E |\psi\rangle .$$

The first, essential step is to partition the Hilbert space spanned by a complete set of basis vectors, which is given in our case by the eigenvectors of the free Hamiltonian H_0. Let us call $\mathscr{P}$ a small subspace of the Hilbert space, spanned by some of these basis vectors. This is the space "of interest", or *model* space. The rest of the basis vectors is grouped into the orthogonal complement of $\mathscr{P}$, denoted $\mathscr{Q}$ and called the *outer*

space. The Feshbach projection operators associated with these two subspaces are respectively P and Q, with $P + Q = 1$ given by the closure relation. They can be expressed in terms of the basis vectors as:

$$P = \sum_{i \in \mathscr{P}} |p_i\rangle \langle p_i| , \tag{A.4}$$

and

$$Q = \sum\!\!\!\!\!\!\int_{j \in \mathscr{Q}} |q_j\rangle \langle q_j| . \tag{A.5}$$

The vectors $|p_i\rangle$ are a given set of discrete states $|a, n\rangle$. The vectors $|q_j\rangle$ are both discrete and continuum states, *i.e.* $|a', n\rangle$ and $|\varepsilon, n\rangle$, orthogonal to the $|p_i\rangle$ vectors. The integral-sum symbol thus denotes a sum over all outer space bound states and an integral over all continuum states. We also refer to the dimensions of the $\mathscr{P}$ and $\mathscr{Q}$ spaces as:

$$N(\mathscr{P}) = \text{card}(\mathscr{P}), \qquad N(\mathscr{Q}) = \text{card}(\mathscr{Q}).$$

The goal of building an effective Hamiltonian is to replace the *infinite* set of coupled equations contained in the Schrödinger equation by a small, *finite-size* set of such equations which *preserves* a given number $N(\mathscr{P})$ of eigenvalues of the exact Hamiltonian. Figures A.1 and A.2 represent this "folding" procedure which drastically reduces the size of the Hamiltonian matrix while preserving the desired eigenvalues. In mathematical terms, the effective Hamiltonian thus obeys the equation,

$$H_{\text{eff}} |\psi_p\rangle = E |\psi_p\rangle ,$$

where we defined the model space wave function $|\psi_p\rangle = P |\psi\rangle$.

A.3 Wave operator method

For the effective Hamiltonian approach to be relevant, there must exist a non trivial transformation operation leading from the exact to the effective Hamiltonian. The most general transformation is given by the following canonical equation,

$$W H_{\text{eff}} = H W, \tag{A.6}$$

where W is unknown. We shall define it as the *wave operator*. The so-called intermediate normalization of the wave operator is verified in the present case (see Durand [204]), hence:

$$PW = P. \tag{A.7}$$

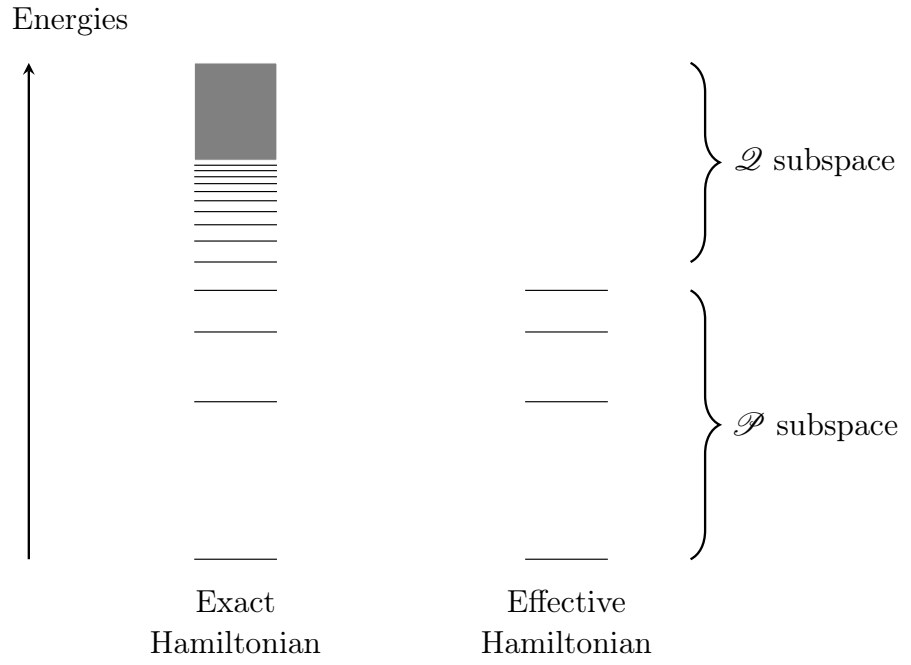

Figure A.1: *Hilbert spaces of the exact and effective Hamiltonians. They share the same energies in the subspace* $\mathscr{P}$

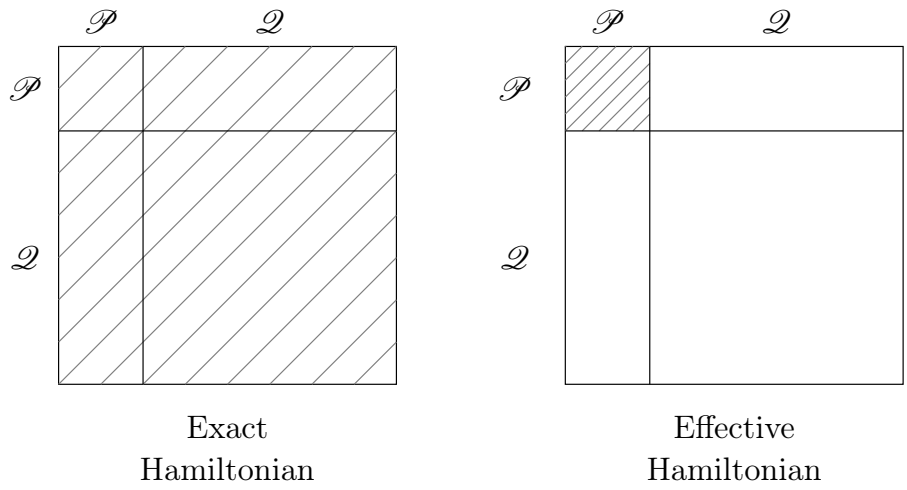

Figure A.2: *Matrix representation of the exact and effective Hamiltonians. The hatched lines represent the non-zero parts of the matrices*

Multiplying Eq. (A.6) by P on the left and using the intermediate normalization property, we obtain

$$PH_{\text{eff}} = PHW, \tag{A.8}$$

where H_{eff} acts only on the $\mathscr{P}$ subspace, thus $PH_{\text{eff}} = H_{\text{eff}}$. Replacing in Eq. (A.6) yields the generalized Bloch equation,

$$HW = WPHW. \tag{A.9}$$

We recall that the exact Hamiltonian can be separated in a free part and an interaction part,

$$H = H_0 + V,$$

where H_0 is real and diagonal hence H_0 commutes with P and $PH_0Q = 0$. Replacing in (A.9) and multiplying by P on the right yields

$$\begin{aligned} WPVWP - VWP &= H_0WP - WPH_0WP \\ &= H_0WP - WPH_0(P+Q)WP, \\ &= H_0WP - WPH_0P, \\ &= H_0WP - WH_0P, \\ &= [H_0, W]P, \end{aligned} \tag{A.10}$$

which gives a set of $N(\mathscr{P})$ coupled equations. For each of these equations, we multiply by Q on the left,

$$\begin{aligned} Q\left(WPVW - VW\right)|p_i\rangle\langle p_i| &= Q\left(H_0W - WH_0\right)|p_i\rangle\langle p_i| \\ &= Q\left(H_0 - E_i\right)W|p_i\rangle\langle p_i|. \end{aligned}$$

Notice the use of $E_i = \mathcal{E}_i - m\omega$, as defined in Eq. (A.2), to denote the energies of the eigenvectors of H_0 belonging to the $\mathscr{P}$ subspace.

In order to obtain an expression for the wave operator, we wish to multiply the above equation by $(H_0 - E_i)^{-1}$ and use the fact that Q commutes with H_0 to isolate QW. However, at least one eigenvalue of H_0 is to equal E_i. In order to avoid divergence we instead multiply by $(H_0 - E_i - \mathrm{i}\beta)^{-1}$, where β is real and nonzero, and then take the limit $\beta \to 0$. We also recast the set of $N(\mathscr{P})$ coupled equations in its compact form, based on projection operators. It leads to the final expression for the (reduced[1]) wave operator,

$$QWP \underset{\beta\to 0}{=} \sum_{i\in\mathscr{P}} \frac{Q}{E_i - H_0 + \mathrm{i}\beta}\left(VW - WPVW\right)|p_i\rangle\langle p_i|. \tag{A.11}$$

[1]In the literature the operator QW is sometimes called the *reduced* wave operator [203, 269]

In the following developments, equations are always to be taken in the limit $\beta \to 0$. It is useful to recall Green's operator spectral representation,

$$\frac{Q}{E_i - H_0 + \mathrm{i}\beta} = \sum_{j \in \mathscr{Q}} \frac{|q_j\rangle \langle q_j|}{E_i - E_j + \mathrm{i}\beta}.$$

Now, the wave operator can be found recursively from Eq. (A.11). Let us write it as a (perturbative) expansion,

$$W = W^{(0)} + W^{(1)} + W^{(2)} + \ldots \tag{A.12}$$

An obvious choice for $W^{(0)}$ is the P operator. Indeed, in this case the effective Hamiltonian is simply the exact Hamiltonian truncated to the $\mathscr{P}$ subspace and all states from the outer space are neglected. Higher-order terms in W will progressively add contributions from those states lying in the $\mathscr{Q}$ space, which act as *perturbers*. To see that, we start by replacing W by P on the right hand side of Eq. (A.11) to obtain $QW^{(1)}P$,

$$QW^{(1)}P = \sum_{i \in \mathscr{P}} \frac{Q}{E_i - H_0 + \mathrm{i}\beta} V |p_i\rangle \langle p_i| . \tag{A.13}$$

In a similar fashion, one can replace W by $P + W^{(1)}$ on the right hand side of Eq. (A.11) to obtain $QW^{(2)}P$ and keep terms only up to the second order in V,

$$\begin{aligned} QW^{(2)}P = &\sum_{i \in \mathscr{P}} \frac{Q}{E_i - H_0 + \mathrm{i}\beta} V \frac{Q}{E_i - H_0 + \mathrm{i}\beta} V |p_i\rangle \langle p_i| \\ &- \sum_{i \in \mathscr{P}} \sum_{j \in \mathscr{P}} \frac{Q}{(E_i - H_0 + \mathrm{i}\beta)(E_j - H_0 + \mathrm{i}\beta)} V |p_j\rangle \langle p_j| V |p_i\rangle \langle p_i| . \end{aligned} \tag{A.14}$$

This procedure can be, of course, repeated until the desired perturbation order is reached.

Finally, we can use the above equations for the wave operator to write an expression for the effective Hamiltonian H_{eff}. To do so, let us start from Eq. (A.8),

$$\begin{aligned} PH_{\mathrm{eff}}P = H_{\mathrm{eff}} &= PHWP \\ &= P(H_0 + V)WP \\ &= PH_0WP + PV(Q + P)WP \\ &= PH_0P + PVP + PVQWP. \end{aligned}$$

Replacing QW by $Q(W^{(0)} + W^{(1)})$, where $W^{(1)}$ is taken as the right hand side of Eq. (A.13), one obtains the EH valid up to the 2$^{\text{nd}}$ order in V,

$$H_{\text{eff}} \underset{\beta\to 0^+}{=} PH_0P + PVP + PV\sum_{i\in\mathscr{P}} \frac{Q}{E_i - H_0 + \mathrm{i}\beta} V \left|p_i\right\rangle \left\langle p_i\right| , \quad \text{(A.15)}$$

where we recalled that all expressions must be taken in the limit $\beta \to 0$. Similarly, replacing QW by $Q(W^{(0)} + W^{(1)} + W^{(2)})$ gives the EH valid up to the 3$^{\text{rd}}$ order in V, and so on.

To summarize, we have found the expression for an effective, finite-size Hamiltonian acting onto a subspace $\mathscr{P}$ of the Hilbert space and whose aim is to model the action of the exact Hamiltonian on the complete Hilbert space. In other words, we reduced a infinite set of coupled equation to a small set of such equations. Note that no assumption has been made concerning the hermicity of H_{eff}, which may thus be either hermitian or non-hermitian.

A.4 Time-dependent Schrödinger equation

The case of a stationary effective Hamiltonian, derived from the time-independent Schrödinger equation, was considered above. However, REMPI processes are intrinsically dynamical. It is thus necessary to write a few words on the time-dependence of H_{eff}. The time-dependent Schrödinger equation for the exact Hamiltonian reads

$$\mathrm{i}\frac{\partial}{\partial t}\left|\psi(t)\right\rangle = H(t)\left|\psi(t)\right\rangle .$$

In the usual separation $H = H_0 + V$, the free Hamiltonian H_0 is time-independent. Time-dependence of the Hamiltonian is contained within the interaction term $V(t)$ and the same is true of the effective Hamiltonian. One may then naively write, using Eq. (A.15), that

$$H_{\text{eff}}(t) = PH_0P + PV(t)P + PV(t)\sum_{i\in\mathscr{P}} \frac{Q}{E_i - H_0 + \mathrm{i}\beta} V(t) \left|p_i\right\rangle \left\langle p_i\right| . \quad \text{(A.16)}$$

This is correct up to the 2nd order in W ($W^{(0)}$+$W^{(1)}$), but not for higher orders. Indeed, derivation of the wave operator and effective Hamiltonian from the time-dependent Schrödinger equation slightly differs from the time-independent case. In the former case, Eq. (A.10) becomes

$$W(t,0)PV(t)W(t,0)P - VW(t,0)P = [H_0, W(t,0)]P + \mathrm{i}\frac{\partial W(t,0)}{\partial t}P, \quad \text{(A.17)}$$

as demonstrated by, *e.g.* , Jolicard and Killingbeck [203]. The wave operator $W(t,0)$ now depends on the time t elapsed since the interaction has been switched on at a remote time $t = 0$. The difference with the time-independent case lies in the appearance of the time-derivative of the wave operator on the right hand side. One can demonstrate that it yields an additional term containing the time derivative of the interaction operator V in the expression of $W^{(n)}$ with $n \geq 2$ (see Faisal [270]). The work presented in the main body of the thesis used effective Hamiltonians derived from an expansion of the wave operator up to $n = 1$, for which the expression (A.16) is correct.

A.5 Effective Hamiltonian sub-operators

Let us now focus on the significance of the different operators included in the definition of the effective Hamiltonian up to to the 2nd order ($m \leq 1$), given by Eq. (A.15). The first term on the right hand side, PH_0P, contains obviously the energies of the states belonging to the model space. The term PVP represents one-photon couplings between these states. The third term represents two-photon couplings *via* states of the outer space. Using the spectral representation of Green's operator, it becomes

$$V\frac{Q}{E_i - H_0 + \mathrm{i}\beta}V = \int de \frac{V\left|e\right\rangle\left\langle e\right|V}{E_i - e + \mathrm{i}\beta} + \sum_j \frac{V\left|j\right\rangle\left\langle j\right|V}{E_i - E_j + \mathrm{i}\beta}, \qquad \text{(A.18)}$$

where we now separate contributions from the *bound* and *continuum* states belonging to the $\mathscr{Q}$ subspace, denoted $|j\rangle$ and $|e\rangle$ respectively. The summation $\sum_{i\in\mathscr{P}}$ is omitted for brevity.

Let us now recall the mathematical relation [205]

$$\lim_{\beta\to 0^{\pm}} \int \mathrm{d}x \frac{1}{x + \mathrm{i}\beta} = \mathcal{P}\int \frac{1}{x} \mp \mathrm{i}\pi \int \mathrm{d}x \delta(x),$$

where $\mathcal{P}$ denotes principal value integration and $\delta(x)$ is Dirac's delta function. Equation (A.18) thus becomes

$$\lim_{\beta\to 0^{\pm}} V\frac{Q}{E_i - H_0 + \mathrm{i}\beta}V = \Omega \mp \mathrm{i}\frac{\Gamma}{2} + S. \qquad \text{(A.19)}$$

Γ is a real positive value representing an ionization rate. In order for the norm of the model space wave function to decrease upon ionization, we must of course choose the term $-\mathrm{i}\Gamma/2$, and thus the limit $\beta \to 0^+$. This limit can also be related, in the context of scattering theory, to boundary conditions on the continuum wave function [201].

The matrix elements for Ω, Γ and S are given by

$$\Omega_{ab} = \mathcal{P}\int de \frac{\langle b|V|e\rangle \langle e|V|a\rangle}{E_a - e}, \tag{A.20}$$

$$\Gamma_{ab} = 2\pi \times \langle b|V|e\rangle \langle e|V|a\rangle \Big|_{e=E_a}, \tag{A.21}$$

$$S_{ab} = \sum_{j\in\mathcal{Q}} \frac{\langle b|V|q_j\rangle \langle q_j|V|a\rangle}{E_a - E_j}, \tag{A.22}$$

and, in the particular case $a = b$, they represent (i) the AC Stark shift of the state $|a\rangle$ due to its interaction with the continuum, (ii) the ionization width of $|a\rangle$, (iii) the AC Stark shift of $|a\rangle$ due to non-resonant bound states. The corresponding effective Hamiltonian reads

$$H_{\text{eff}} = PH_0P + PVP + P\left(\Omega - \mathrm{i}\frac{\Gamma}{2} + S\right)P, \tag{A.23}$$

which is the expression we used in the main body of the thesis. We immediately notice that the operator $\mathrm{i}\Gamma/2$ will introduce imaginary numbers in both the diagonal and non-diagonal elements of the effective Hamiltonian matrix, which is therefore *non hermitian*. The non-hermicity of H_{eff} is a consequence of the elimination of the continuum states from the model space.

Chapter B

Velocity map imaging lens

A picture of the VMI lens is shown in Fig. B.1 and its detailed drawing in Fig. B.2. The electrodes shown by the solid lines are made of non-magnetic stainless steel and are 1 mm thick. They are spaced by distances, referenced to the middle of each electrode, that were optimized by León *et al.* [135]. The repeller (lowest, hatched electrode) is made of ARCAP non-magnetic alloy. A series of PEEK insulators are placed between the electrodes (not shown). They are traversed by a threaded rod (dash dot line) which is screwed on both ends. Two aluminum plates (blue dotted lines) are placed below the lens and their bottom is covered with μ-metal. Two μ-metal cylinders surround the lens and rest on these plates.

Figure B.1: *Picture the VMI lens.*

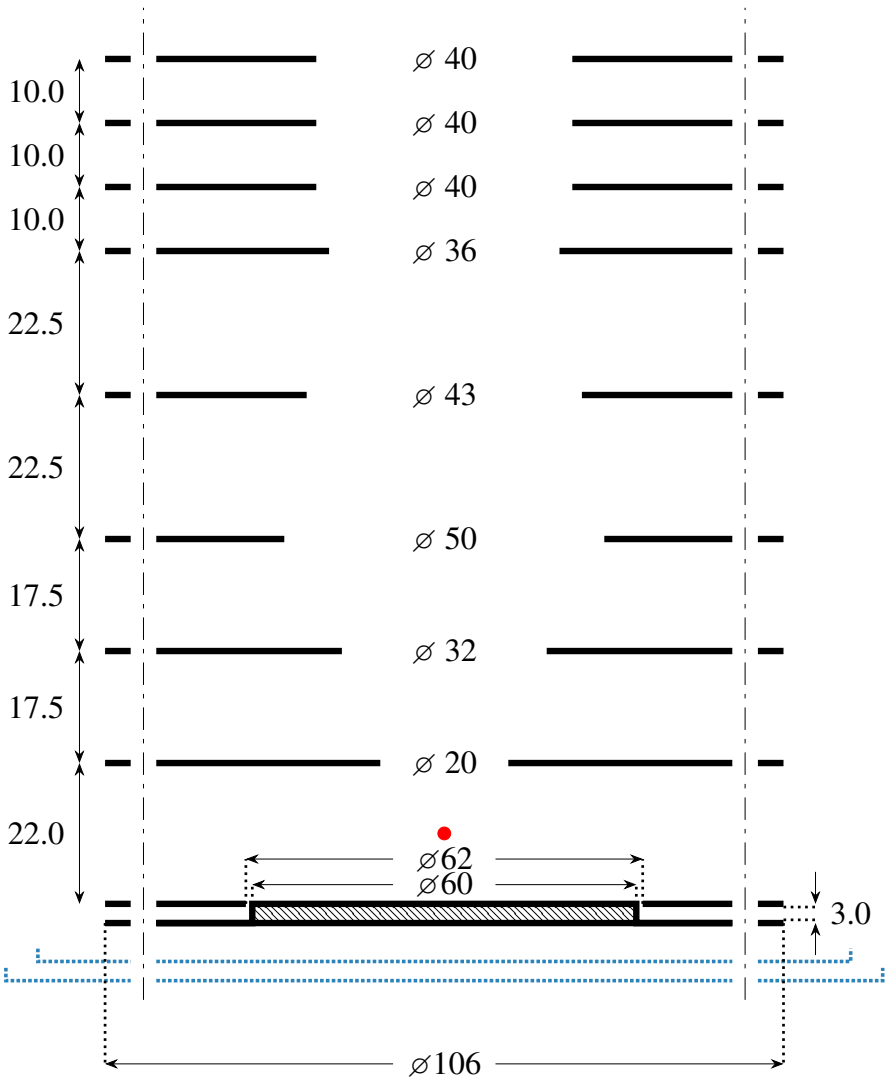

Figure B.2: *Detailed drawing of the VMI electrostatic lens (see text). All dimensions are in mm. The red dot indicates where the laser and ion beams intersect.*

References

[1] R. Wildt, Astrophys. J. **90**, 611 (1939).

[2] A. R. P. Rau, J. Astrophys. Astron. **17**, 113 (1996).

[3] H. Kreckel, H. Bruhns, M. Cizek, S. C. O. Glover, K. A. Miller, X. Urbain, and D. W. Savin, Science **329**, 69 (2010).

[4] M. C. McCarthy, C. A. Gottlieb, H. Gupta, and P. Thaddeus, Astrophys. J. **652**, L141 (2006).

[5] J. Wisemberg and G. Kockarts, J. Geophys. Res. Sp. Phys. **85**, 4642 (1980).

[6] D. J. Pegg, Rep. Prog. Phys. **67**, 857 (2004).

[7] A. J. Coates, F. J. Crary, G. R. Lewis, D. T. Young, J. H. Waite, and J. C. Sittler, Geophys. Res. Lett. **34**, 6 (2007).

[8] V. Vuitton, P. Lavvas, R. V. Yelle, M. Galand, A. Wellbrock, G. R. Lewis, A. J. Coates, and J. E. Wahlund, Planet. Space Sci. **57**, 1558 (2009).

[9] T. E. Cravens, I. P. Robertson, S. A. Ledvina, D. Mitchell, S. M. Krimigis, and J. H. Waite, Geophys. Res. Lett. **35**, L03103 (2008).

[10] J. Bishop and R. Link, Geophys. Res. Lett. **20**, 1027 (1993).

[11] L. S. Waldrop, R. B. Kerr, S. A. González, M. P. Sulzer, J. Noto, and F. Kamalabadi, J. Geophys. Res. Sp. Phys. **110**, 1 (2005).

[12] S. Falcinelli, F. Pirani, and F. Vecchiocattivi, Atmosphere **6**, 299 (2015).

[13] S. S. Hodgman, R. G. Dall, L. J. Byron, K. G. H. Baldwin, S. J. Buckman, and A. G. Truscott, Phys. Rev. Lett. **103**, 053002 (2009).

[14] A. V. Phelps, Phys. Rev. **99**, 1307 (1955).

[15] K. Niemi, J. Waskoenig, N. Sadeghi, T. Gans, and D. O'Connell, Plasma Sources Sci. Technol. **20**, 055005 (2011).

[16] E. Stoffels, I. E. Kieft, R. E. J. Sladek, L. J. M. van den Bedem, E. P. van der Laan, and M. Steinbuch, Plasma Sources Sci. Technol. **15**, S169 (2006).

[17] G. Fridman, M. Peddinghaus, M. Balasubramanian, H. Ayan, A. Fridman, A. Gutsol, and A. Brooks, Plasma Chem. Plasma Process. **26**, 425 (2006).

[18] H. Morgner, in *Adv. At. Mol. Opt. Phys.*, Vol. 42 (2000) pp. 387–488.

[19] A. Pratt, M. Kurahashi, X. Sun, D. Gilks, and Y. Yamauchi, Phys. Rev. B **85**, 180409 (2012).

[20] K. Baldwin, Contemp. Phys. **46**, 105 (2005).

[21] S. Nowak, T. Pfau, and J. Mlynek, Appl. Phys. B Laser Opt. **63**, 203 (1996).

[22] S. J. H. Petra, L. Feenstra, W. Hogervorst, and W. Vassen, Appl. Phys. B Lasers Opt. **78**, 133 (2004).

[23] E. Stamate and M. Draghici, J. Appl. Phys. **111**, 083303 (2012).

[24] R. Hemsworth, H. Decamps, J. Graceffa, B. Schunke, M. Tanaka, M. Dremel, A. Tanga, H. De Esch, F. Geli, J. Milnes, T. Inoue, D. Marcuzzi, P. Sonato, and P. Zaccaria, Nucl. Fusion **49**, 045006 (2009).

[25] M. Kovari and B. Crowley, Fusion Eng. Des. **85**, 745 (2010).

[26] A. P. O'Connor, F. Grussie, H. Bruhns, N. de Ruette, T. P. Koenning, K. A. Miller, D. W. Savin, J. Stützel, X. Urbain, and H. Kreckel, Rev. Sci. Instrum. **86**, 113306 (2015).

[27] G. Serianni, P. Agostinetti, M. Agostini, V. Antoni, D. Aprile, C. Baltador, M. Barbisan, M. Brombin, M. Cavenago, G. Chitarin, M. D. Palma, R. Delogu, F. Fellin, N. Fonnesu, N. Marconato, R. Pasqualotto, A. Pimazzoni, E. Sartori, S. Spagnolo,

M. Spolaore, P. Veltri, B. Zaniol, and M. Zaupa, New J. Phys. **19**, 045003 (2017).

[28] R. McAdams, Rev. Sci. Instrum. **85**, 02B319 (2014).

[29] A. Donné, A. Costley, R. Barnsley, H. Bindslev, R. Boivin, G. Conway, R. Fisher, R. Giannella, H. Hartfuss, M. von Hellermann, E. Hodgson, L. Ingesson, K. Itami, D. Johnson, Y. Kawano, T. Kondoh, A. Krasilnikov, Y. Kusama, A. Litnovsky, P. Lotte, P. Nielsen, T. Nishitani, F. Orsitto, B. Peterson, G. Razdobarin, J. Sanchez, M. Sasao, T. Sugie, G. Vayakis, V. Voitsenya, K. Vukolov, C. Walker, K. Young, and the ITPA Topical Group on Diagnostics, Nucl. Fusion **47**, S337 (2007).

[30] S. Menhart, M. Proschek, H. Falter, H. Anderson, H. Summers, A. Staebler, P. Franzen, H. Meister, J. Schweinzer, T. T. C. Jones, S. Cox, N. Hawkes, F. Aumayr, and H. P. Winter, J. Nucl. Mater. **293**, 673 (2001).

[31] J. M. Munoz Burgos, O. Schmitz, S. D. Loch, and C. P. Ballance, Phys. Plasmas **19**, 012501 (2012).

[32] T. Barbui, M. Krychowiak, R. König, O. Schmitz, J. M. Munoz Burgos, B. Schweer, and A. Terra, Rev. Sci. Instrum. **87**, 11E554 (2016).

[33] B. Schweer, M. Brix, and M. Lehnen, J. Nucl. Mater. **266**, 673 (1999).

[34] V. K. Ivanov, Radiat. Phys. Chem. **70**, 345 (2004).

[35] T. Andersen, H. K. Haugen, and H. Hotop, J. Phys. Chem. Ref. Data **28**, 1511 (1999).

[36] T. Andersen, Phys. Rep. **394**, 157 (2004).

[37] S. J. Buckman and C. W. Clark, Rev. Mod. Phys. **66**, 539 (1994).

[38] P. Kristensen, U. V. Pedersen, V. V. Petrunin, T. Andersen, and K. T. Chung, Phys. Rev. A **55**, 978 (1997).

[39] P. Reinhed, A. Orbán, J. Werner, S. Rosén, R. D. Thomas, I. Kashperka, H. A. B. Johansson, D. Misra, L. Brännholm, M. Björkhage, H. Cederquist, and H. T. Schmidt, Phys. Rev. Lett. **103**, 213002 (2009).

[40] R. C. Bilodeau and H. K. Haugen, Phys. Rev. Lett. **85**, 534 (2000).

[41] C. W. Walter, N. D. Gibson, C. M. Janczak, K. A. Starr, A. P. Snedden, R. L. Field III, and P. Andersson, Phys. Rev. A **76**, 052702 (2007).

[42] C. W. Walter, N. D. Gibson, D. J. Matyas, C. Crocker, K. A. Dungan, B. R. Matola, and J. Rohlén, Phys. Rev. Lett. **113**, 063001 (2014).

[43] A. Pais, Rev. Mod. Phys. **51**, 863 (1979).

[44] E. P. Wigner, Phys. Rev. **73**, 1002 (1948).

[45] T. F. O'Malley, L. Spruch, and L. Rosenberg, J. Math. Phys. **2**, 491 (1961).

[46] S. Watanabe and C. H. Greene, Phys. Rev. A **22**, 158 (1980).

[47] M. Venuti and P. Decleva, J. Phys. B At. Mol. Opt. Phys. **30**, 4839 (1997).

[48] M. Yan, H. R. Sadeghpour, and A. Dalgarno, Astrophys. J. **496**, 1044 (1998).

[49] L. M. Branscomb, D. S. Burch, S. J. Smith, and S. Geltman, Phys. Rev. **111**, 504 (1958).

[50] T. J. Millar, C. Walsh, and T. A. Field, Chem. Rev. **117**, 1765 (2017).

[51] P. G. Burke, *R-Matrix Theory of Atomic Collisions*, Springer Series on Atomic, Optical, and Plasma Physics, Vol. 61 (Springer, Berlin, Heidelberg, 2011).

[52] A. F. Starace, in *Corpuscles and Radiation in Matter I / Korpuskeln und Strahlung in Materie I*, Vol. 31, edited by W. Mehlhorn (1982) pp. 1–121.

[53] A. R. Edmonds, *Angular Momentum in Quantum Mechanics* (Princeton University Press, London, 1996).

[54] J. M. Blatt and L. C. Biedenharn, Rev. Mod. Phys. **24**, 258 (1952).

[55] A. Starace, in *Springer Handbook of Atomic, Molecular, and Optical Physics*, edited by G. Drake (Springer, New York, 2006) pp. 379–390.

[56] H. Bethe, in *Quantentheorie*, edited by H. Bethe, F. Hund, N. F. Mott, W. Pauli, A. Rubinowicz, G. Wentzel, and A. Smekal (Springer, Berlin, Heidelberg, 1933).

[57] J. Cooper and R. N. Zare, J. Chem. Phys. **48**, 942 (1968).

[58] L.-S. Wang, C.-F. Ding, X.-B. Wang, and S. E. Barlow, Rev. Sci. Instrum. **70**, 1957 (1999).

[59] D. Hanstorp, C. Bengtsson, and D. J. Larson, Phys. Rev. A **40**, 670 (1989).

[60] H. T. Schmidt, R. D. Thomas, M. Gatchell, S. Rosén, P. Reinhed, P. Löfgren, L. Brännholm, M. Blom, M. Björkhage, E. Bäckström, J. D. Alexander, S. Leontein, D. Hanstorp, H. Zettergren, L. Liljeby, A. Källberg, A. Simonsson, F. Hellberg, S. Mannervik, M. Larsson, W. D. Geppert, K. G. Rensfelt, H. Danared, A. Paál, M. Masuda, P. Halldén, G. Andler, M. H. Stockett, T. Chen, G. Källersjö, J. Weimer, K. Hansen, H. Hartman, and H. Cederquist, Rev. Sci. Instrum. **84**, 055115 (2013).

[61] E. Bäckström, D. Hanstorp, O. M. Hole, M. Kaminska, R. F. Nascimento, M. Blom, M. Björkhage, A. Källberg, P. Löfgren, P. Reinhed, S. Rosén, A. Simonsson, R. D. Thomas, S. Mannervik, H. T. Schmidt, and H. Cederquist, Phys. Rev. Lett. **114**, 1 (2015).

[62] R. Von Hahn, A. Becker, F. Berg, K. Blaum, C. Breitenfeldt, H. Fadil, F. Fellenberger, M. Froese, S. George, J. Göck, M. Grieser, F. Grussie, E. A. Guerin, O. Heber, P. Herwig, J. Karthein, C. Krantz, H. Kreckel, M. Lange, F. Laux, S. Lohmann, S. Menk, C. Meyer, P. M. Mishra, O. Novotný, A. P. O'Connor, D. A. Orlov, M. L. Rappaport, R. Repnow, S. Saurabh, S. Schippers, C. D. Schröter, D. Schwalm, L. Schweikhard, T. Sieber, A. Shornikov, K. Spruck, S. Sunil Kumar, J. Ullrich, X. Urbain, S. Vogel, P. Wilhelm, A. Wolf, and D. Zajfman, Rev. Sci. Instrum. **87**, 1 (2016).

[63] A. P. O'Connor, A. Becker, K. Blaum, C. Breitenfeldt, S. George, J. Göck, M. Grieser, F. Grussie, E. A. Guerin, R. Von Hahn, U. Hechtfischer, P. Herwig, J. Karthein, C. Krantz, H. Kreckel, S. Lohmann, C. Meyer, P. M. Mishra, O. Novotný, R. Repnow, S. Saurabh, D. Schwalm, K. Spruck, S. Sunil Kumar, S. Vogel, and A. Wolf, Phys. Rev. Lett. **116**, 1 (2016).

[64] L. H. Andersen, O. Heber, and D. Zajfman, J. Phys. B At. Mol. Opt. Phys. **37**, R57 (2004).

[65] R. Wester, J. Phys. B At. Mol. Opt. Phys. **42**, 154001 (2009).

[66] U. V. Pedersen, M. Hyde, S. P. Møller, and T. Andersen, Phys. Rev. A **64**, 012503 (2001).

[67] S. J. Smith and L. M. Branscomb, Rev. Sci. Instrum. **31**, 733 (1960).

[68] W. C. Lineberger and B. W. Woodward, Phys. Rev. Lett. **25**, 424 (1970).

[69] C. Valli, C. Blondel, and C. Delsart, Phys. Rev. A **59**, 3809 (1999).

[70] A. Osterwalder, M. J. Nee, J. Zhou, and D. M. Neumark, J. Chem. Phys. **121**, 6317 (2004).

[71] P. Balling, C. Brink, T. Andersen, and H. K. Haugen, J. Phys. B At. Mol. Opt. Phys. **25**, L565 (1992).

[72] M. Vandevraye, P. Babilotte, C. Drag, and C. Blondel, Phys. Rev. A **90**, 13411 (2014).

[73] P. Hlavenka, R. Otto, S. Trippel, J. Mikosch, M. Weidemüller, and R. Wester, J. Chem. Phys. **130**, 061105 (2009).

[74] V. V. Petrunin, J. D. Voldstad, P. Balling, P. Kristensen, T. Andersen, and H. K. Haugen, Phys. Rev. Lett. **75**, 1911 (1995).

[75] I. Y. Kiyan, U. Berzinsh, D. Hanstorp, and D. J. Pegg, Phys. Rev. Lett. **81**, 2874 (1998).

[76] J. L. Hall and M. W. Siegel, J. Chem. Phys. **48**, 943 (1968).

[77] F. Breyer, P. Frey, and H. Hotop, Zeitschrift für Phys. A **286**, 133 (1978).

[78] S. J. Cavanagh, S. T. Gibson, M. N. Gale, C. J. Dedman, E. H. Roberts, and B. R. Lewis, Phys. Rev. A **76**, 052708 (2007).

[79] P. Defrance, W. Claeys, A. Cornet, and G. Poulaert, J. Phys. B At. Mol. Phys. **14**, 111 (1981).

[80] L. M. Branscomb, S. J. Smith, and G. Tisone, J. Chem. Phys. **43**, 2906 (1965).

[81] P. Defrance, F. Brouillard, W. Claeys, and G. V. Wassenhove, J. Phys. B At. Mol. Phys. **14**, 103 (1981).

[82] J. Ullrich, R. Moshammer, A. Dorn, R. Dörner, L. P. H. Schmidt, and H. Schmidt-B cking, Rep. Prog. Phys. **66**, 1463 (2003).

[83] D. R. Bates and H. S. W. Massey, Mon. Not. R. Astron. Soc. **106**, 432 (1946).

[84] S. Chandrasekhar, Astrophys. J. **102**, 395 (1945).

[85] A. G. Abrashkevich and M. Shapiro, Phys. Rev. A **50**, 1205 (1994).

[86] A. L. Stewart, J. Phys. B At. Mol. Phys. **11**, 3851 (1978).

[87] A. W. Wishart, Mon. Not. R. Astron. Soc. **187**, 59P (1979).

[88] H. P. Saha, Phys. Rev. A **38**, 4546 (1988).

[89] J. T. Broad and W. P. Reinhardt, Phys. Rev. A **14**, 2159 (1976).

[90] M. P. Ajmera and K. T. Chung, Phys. Rev. A **12**, 475 (1975).

[91] A. S. Kheifets and I. Bray, Phys. Rev. A **58**, 4501 (1998).

[92] M. Masili and A. F. Starace, Phys. Rev. A **62**, 33403 (2000).

[93] A. M. Frolov, J. Phys. B At. Mol. Opt. Phys. **37**, 853 (2004).

[94] T. N. Chang and X. Tang, Phys. Rev. A **44**, 232 (1991).

[95] C.-H. Park, A. F. Starace, J. Tan, and C.-D. Lin, Phys. Rev. A **33**, 1000 (1986).

[96] M. G. J. Fink and P. Zoller, J. Phys. B At. Mol. Phys. **18**, L373 (1985).

[97] L. M. Branscomb and S. J. Smith, Phys. Rev. **98**, 1028 (1955).

[98] S. J. Smith and D. S. Burch, Phys. Rev. **116**, 1125 (1959).

[99] H.-P. Popp and S. Kruse, J. Quant. Spectrosc. Radiat. Transf. **16**, 683 (1976).

[100] M. Bacal and G. W. Hamilton, Phys. Rev. Lett. **42**, 1538 (1979).

[101] M. Nishiura, M. Sasao, and M. Bacal, J. Appl. Phys. **83**, 2944 (1998).

[102] M. Dörr, J. Purvis, M. Terao-Dunseath, P. G. Burke, C. J. Joachain, and C. J. Noble, J. Phys. B At. Mol. Opt. Phys. **28**, 4481 (1995).

[103] L. C. Lee and G. P. Smith, J. Chem. Phys. **70**, 1727 (1979).

[104] M. L. Seman and L. M. Branscomb, Phys. Rev. **125**, 1602 (1962).

[105] G. Haeffler, D. Hanstorp, I. Y. Kiyan, U. Ljungblad, H. H. Andersen, and T. Andersen, J. Phys. B At. Mol. Opt. Phys. **29**, 3017 (1996).

[106] P. Kristensen, H. H. Andersen, P. Balling, L. D. Steele, and T. Andersen, Phys. Rev. A **52**, 2847 (1995).

[107] D. S. Burch, S. J. Smith, and L. M. Branscomb, Phys. Rev. **112**, 171 (1958).

[108] O. Zatsarinny and K. Bartschat, Phys. Rev. A **73**, 022714 (2006).

[109] E. J. Robinson and S. Geltman, Phys. Rev. **153**, 4 (1967).

[110] W. Jian-Hua, Y. Jian-Min, and V. K. Lan, Chinese Phys. **12**, 1390 (2003).

[111] C. M. Oana and A. I. Krylov, J. Chem. Phys. **131**, 124114 (2009).

[112] C. Domesle, B. Jordon-Thaden, L. Lammich, M. Förstel, U. Hergenhahn, A. Wolf, and H. B. Pedersen, Phys. Rev. A **82**, 033402 (2010).

[113] J. W. Cooper and J. B. Martin, Phys. Rev. **126**, 1482 (1962).

[114] W. R. Garrett and H. T. Jackson, Phys. Rev. **153**, 28 (1967).

[115] R. L. Chase and H. P. Kelly, Phys. Rev. A **6**, 2150 (1972).

[116] D. Hanstorp, C. Bengtsson, and D. J. Larson, Phys. Rev. A **40**, 670 (1989).

[117] M. Génévriez, X. Urbain, A. Dochain, A. Cyr, K. M. Dunseath, and M. Terao-Dunseath, Phys. Rev. A **94**, 023407 (2016).

[118] S. J. Cavanagh, S. T. Gibson, and B. R. Lewis, J. Phys. Conf. Ser. **194**, 022026 (2009).

[119] S. J. Cavanagh, S. T. Gibson, and B. R. Lewis, J. Phys. Conf. Ser. **212**, 012034 (2010).

[120] H. Stapelfeldt, C. Brink, and H. K. Haugen, J. Phys. B At. Mol. Opt. Phys. **24**, L437 (1991).

[121] G. F. Gribakin and M. Y. Kuchiev, Phys. Rev. A **55**, 3760 (1997).

[122] F. Brouillard and P. Defrance, Phys. Scr. **1983**, 68 (1983).

[123] J. J. Blangé, X. Urbain, H. Rudolph, H. A. Dijkerman, H. C. W. Beijerinck, and H. G. M. Heideman, J. Phys. B At. Mol. Opt. Phys. **29**, 2763 (1996).

[124] R. N. Bracewell, *The Fourier transform and its applications*, 3rd ed. (McGraw Hill, Boston, 2000) p. 616.

[125] R. D. Guenther, *Modern Optics* (Wiley, 1990) p. 720.

[126] D. H. Parker and A. T. J. B. Eppink, in *Imaging in Molecular Dynamics*, edited by B. Whitaker (Cambridge University Press, 2003) Chap. 2, p. 267.

[127] C. L. Lawson and R. J. Hanson, *Solving least squares problems* (SIAM, 1995) p. 351.

[128] E. Jones, T. Oliphant, and P. Peterson, "SciPy: Open source scientific tools for Python," (2001).

[129] A. N. Tikhonov and V. Y. Arsenin, *Solutions of ill-posed problems* (Wiley, New York, 1977) p. 258.

[130] P. C. Hansen, SIAM Rev. **34**, 561 (1992).

[131] D. W. Chandler and P. L. Houston, J. Chem. Phys. **87**, 1445 (1987).

[132] A. T. J. B. Eppink and D. H. Parker, Rev. Sci. Instrum. **68**, 3477 (1997).

[133] B. Dick, Phys. Chem. Chem. Phys. **16**, 570 (2014).

[134] V. Dribinski, A. Ossadtchi, V. A. Mandelshtam, and H. Reisler, Rev. Sci. Instrum. **73**, 2634 (2002).

[135] I. León, Z. Yang, H.-T. Liu, and L.-S. Wang, Rev. Sci. Instrum. **85**, 083106 (2014).

[136] A. Naji, K. Olamba, J. P. Chenu, S. Szücs, M. Chibisov, and F. Brouillard, J. Phys. B At. Mol. Opt. Phys. **31**, 2961 (1998).

[137] P. Lambropoulos, Adv. At. Mol. Opt. Phys. **12**, 87 (1976).

[138] C. Lecompte, G. Mainfray, C. Manus, and F. Sanchez, Phys. Rev. A **11**, 1009 (1975).

[139] L. Mandel and E. Wolf, Rev. Mod. Phys. **37**, 231 (1965).

[140] X. Urbain, D. Bech, J.-P. Van Roy, M. Géléoc, S. J. Weber, A. Huetz, and Y. J. Picard, Rev. Sci. Instrum. **86**, 023305 (2015).

[141] C. J. Johnson, B. B. Shen, B. L. J. Poad, and R. E. Continetti, Rev. Sci. Instrum. **82**, 105105 (2011).

[142] B. F. Parsons, S. M. Sheehan, K. E. Kautzman, T. A. Yen, and D. M. Neumark, J. Chem. Phys. **125**, 244301 (2006).

[143] B. N. Taylor and C. N. Kuyatt, NIST tech. note. **1297** (1994).

[144] R. J. W. Henry, Phys. Rev. **162**, 56 (1967).

[145] G. Miecznik and C. H. Greene, Phys. Rev. A **53**, 3247 (1996).

[146] Y. Liu and C. Ning, J. Chem. Phys. **143**, 144310 (2015).

[147] D. M. Neumark, K. R. Lykke, T. Andersen, and W. C. Lineberger, Phys. Rev. A **32**, 1890 (1985).

[148] T. Suzuki and T. Kasuya, Phys. Rev. A **36**, 2129 (1987).

[149] C. Blondel, C. Delsart, C. Valli, S. Yiou, M. R. Godefroid, and S. Van Eck, Phys. Rev. A **64**, 052504 (2001).

[150] A. Kramida, Yu. Ralchenko, J. Reader, and NIST ASD Team, NIST Atomic Spectra Database (ver. 5.4), [Online]. Available: `http://physics.nist.gov/asd` [2017, July 04]. National Institute of Standards and Technology, Gaithersburg, MD. (2016).

[151] A. R. P. Rau and U. Fano, Phys. Rev. A **4**, 1751 (1971).

[152] C. Pan and A. F. Starace, Phys. Rev. A **47**, 295 (1993).

[153] DLMF, "*NIST Digital Library of Mathematical Functions*," http://dlmf.nist.gov/, Release 1.0.15 of 2017-06-01, f. W. J. Olver, A. B. Olde Daalhuis, D. W. Lozier, B. I. Schneider, R. F. Boisvert, C. W. Clark, B. R. Miller and B. V. Saunders, eds.

[154] G. F. Gribakin and M. Y. Kuchiev, J. Phys. B At. Mol. Opt. Phys. **30**, L657 (1997).

[155] A. Aguilar, J. S. Thompson, D. Calabrese, A. M. Covington, C. Cisneros, V. T. Davis, M. S. Gulley, M. Halka, D. Hanstorp, J. Sandström, B. M. McLaughlin, and D. J. Pegg, Phys. Rev. A **69**, 022711 (2004).

[156] V. T. Davis, A. Aguilar, A. M. Covington, J. S. Thompson, D. Calabrese, C. Cisneros, M. S. Gulley, M. Halka, D. Hanstorp, J. Sandström, B. M. McLaughlin, G. F. Gribakin, and D. J. Pegg, J. Phys. B At. Mol. Opt. Phys. **38**, 2579 (2005).

[157] N. Berrah, J. D. Bozek, G. Turri, G. Akerman, B. Rude, H.-L. Zhou, and S. T. Manson, Phys. Rev. Lett. **88**, 093001 (2002).

[158] H. Stapelfeldt and H. K. Haugen, Phys. Rev. Lett. **69**, 2638 (1992).

[159] H. Stapelfeldt, P. Kristensen, U. Ljungblad, T. Andersen, and H. K. Haugen, Phys. Rev. A **50**, 1618 (1994).

[160] V. V. Petrunin, M. H. Jacobsen, L. B. Madsen, S. A. Aseyev, and T. Andersen, Phys. Rev. Lett. **90**, 013002 (2003).

[161] A. E. Klinkmüller, G. Haeffler, D. Hanstorp, I. Y. Kiyan, U. Berzinsh, C. W. Ingram, D. J. Pegg, and J. R. Peterson, Phys. Rev. A **56**, 2788 (1997).

[162] A. E. Klinkmüller, G. Haeffler, D. Hanstorp, I. Y. Kiyan, U. Berzinsh, and D. J. Pegg, J. Phys. B At. Mol. Opt. Phys. **31**, 2549 (1998).

[163] J. B. Greenwood, G. F. Collins, J. Pedregosa-Gutierrez, J. McKenna, A. Murphy, and J. T. Costello, J. Phys. B At. Mol. Opt. Phys. **36**, L235 (2003).

[164] J. Pedregosa-Gutierrez, P. A. Orr, J. B. Greenwood, A. Murphy, J. T. Costello, K. Zrost, T. Ergler, R. Moshammer, and J. Ullrich, Phys. Rev. Lett. **93**, 223001 (2004).

[165] B. Bergues, Y. Ni, H. Helm, and I. Y. Kiyan, Phys. Rev. Lett. **95**, 263002 (2005).

[166] H. W. van der Hart, Phys. Rev. A **74**, 053406 (2006).

[167] B. Bergues and I. Y. Kiyan, Phys. Rev. Lett. **100**, 143004 (2008).

[168] A. Gazibegović-Busuladžić, D. B. Milošević, W. Becker, B. Bergues, H. Hultgren, and I. Y. Kiyan, Phys. Rev. Lett. **104**, 103004 (2010).

[169] J. A. R. Samson, Z. X. He, L. Yin, and G. N. Haddad, J. Phys. B At. Mol. Opt. Phys. **27**, 887 (1994).

[170] R. F. Stebbings, F. B. Dunning, F. K. Tittel, and R. D. Rundel, Phys. Rev. Lett. **30**, 815 (1973).

[171] A. Burgess and M. J. Seaton, Mon. Not. R. Astron. Soc. **120**, 121 (1960).

[172] V. Jacobs, Phys. Rev. A **4**, 939 (1971).

[173] M. Gisselbrecht, D. Descamps, and C. Lyngå, Phys. Rev. Lett. **82**, 4607 (1999).

[174] T. N. Chang and M. Zhen, Phys. Rev. A **47** (1993).

[175] T. N. Chang and T. K. Fang, Phys. Rev. A **52** (1995).

[176] F. Dunning and R. Stebbings, Phys. Rev. Lett. **32**, 1286 (1974).

[177] L. A. Lompre, G. Mainfray, B. Mathieu, G. Watel, M. Aymar, and M. Crance, J. Phys. B At. Mol. Phys. **13**, 1799 (1980).

[178] H. Haberland, M. Oschwald, and J. T. Broad, J. Phys. B At. Mol. Phys. **20**, 3367 (1987).

[179] M. Madine and H. van der Hart, J. Phys. B At. Mol. Opt. Phys. **38**, 3963 (2005).

[180] M. Madine and H. van der Hart, J. Phys. B At. Mol. Opt. Phys. **39**, 4049 (2006).

[181] H. D. Zeman, Rev. Sci. Instrum. **48**, 1079 (1977).

[182] C. A. Ramsbottom and K. L. Bell, J. Phys. B At. Mol. Opt. Phys. **32**, 1315 (1999).

[183] J. Xi and C. Froese Fischer, Phys. Rev. A **53**, 3169 (1996).

[184] C. W. Walter, J. A. Seifert, and J. R. Peterson, Phys. Rev. A **50**, 2257 (1994).

[185] J. R. Peterson, Y. K. Bae, and D. L. Huestis, Phys. Rev. Lett. **55**, 692 (1985).

[186] P. A. Závodszky, L. Sarkadi, L. Víkor, and J. Pálinkás, Phys. Rev. A **50**, R899 (1994).

[187] M. Bylicki, J. Phys. B At. Mol. Opt. Phys. **30**, 189 (1997).

[188] D.-S. Kim, H.-L. Zhou, and S. T. Manson, Phys. Rev. A **55**, 414 (1997).

[189] C. A. Nicolaides and T. Mercouris, J. Phys. B At. Mol. Opt. Phys. **29**, 1151 (1996).

[190] D. J. Pegg, J. S. Thompson, J. Dellwo, R. N. Compton, and G. D. Alton, Phys. Rev. Lett. **64**, 278 (1990).

[191] A. M. Tumaikin and V. I. Yudin, Sov. Phys. JETP **71**, 43 (1990).

[192] A. V. Taichenachev, A. M. Tumaikin, V. I. Yudin, and G. Nienhuis, Phys. Rev. A **69**, 033410 (2004).

[193] "UK APAP (Atomic Processes for Astrophysical Plasmas) network," http://www.apap-network.org/.

[194] A. Hibbert, Comput. Phys. Commun. **9**, 141 (1975).

[195] K. M. Dunseath and M. Terao-Dunseath, J. Phys. B At. Mol. Opt. Phys. **46**, 235201 (2013).

[196] G. Drake, ed., *Springer Handbook of Atomic, Molecular, and Optical Physics*, Vol. 1 (Springer New York, New York, NY, 2006).

[197] A. V. Bunge and C. F. Bunge, Phys. Rev. A **30**, 2179 (1984).

[198] P. G. Burke, P. Francken, and C. J. Joachain, J. Phys. B At. Mol. Opt. Phys. **24**, 761 (1991).

[199] M. Dörr, M. Terao-Dunseath, J. Purvis, C. J. Noble, P. G. Burke, and C. J. Joachain, J. Phys. B At. Mol. Opt. Phys. **25**, 2809 (1992).

[200] C. J. Joachain, N. J. Kylstra, and R. M. Potvliege, *Atoms in Intense Laser Fields* (Cambridge University Press, Cambridge, 2011).

[201] H. C. Baker, Phys. Rev. A **30**, 773 (1984).

[202] J. P. Killingbeck and G. Jolicard, J. Phys. A. Math. Gen. **36**, R105 (2003).

[203] G. Jolicard and J. P. Killingbeck, J. Phys. A. Math. Gen. **36**, R411 (2003).

[204] P. Durand, Phys. Rev. A **28**, 3184 (1983).

[205] B. W. Shore, *The Theory of Coherent Atomic Excitation, Vol. 2, Multilevel Atoms and Incoherence* (Wiley, New York, 1990).

[206] K. M. Dunseath, J.-M. Launay, M. Terao-Dunseath, and L. Mouret, J. Phys. B At. Mol. Opt. Phys. **35**, 313 (2002).

[207] M. J. Seaton, Rep. Prog. Phys. **46** (1983).

[208] A. R. Barnett, Comput. Phys. Commun. **27** (1982).

[209] C. J. Noble, Comput. Phys. Commun. **159**, 55 (2004).

[210] R. Piessens, E. de Doncker-Kapenga, C. W. Überhuber, and D. K. Kahaner, *Quadpack*, Springer Series in Computational Mathematics, Vol. 1 (Springer Berlin Heidelberg, Berlin, Heidelberg, 1983).

[211] R. B. Sidje, ACM Trans. Math. Softw. **24**, 130 (1998).

[212] T. E. Wall, D. B. Cassidy, and S. D. Hogan, Phys. Rev. A **90**, 053430 (2014).

[213] A. J. Dixon, M. F. A. Harrison, and A. C. H. Smith, J. Phys. B At. Mol. Phys. **9**, 2617 (1976).

[214] J. Colgan and M. S. Pindzola, Phys. Rev. A **66**, 062707 (2002).

[215] D. V. Fursa and I. Bray, J. Phys. B At. Mol. Opt. Phys. **36**, 1663 (2003).

[216] Y. Ralchenko, R. K. Janev, T. Kato, D. V. Fursa, I. Bray, and F. J. de Heer, At. Data Nucl. Data Tables **94**, 603 (2008).

[217] K. Bartschat, J. Phys. B At. Mol. Opt. Phys. **35**, L527 (2002).

[218] D. Ton-That, M. R. Flannery, and S. T. Manson, J. Phys. B At. Mol. Phys. **10**, 621 (1977).

[219] I. L. Beigman, L. A. Vainshtein, M. Brix, A. Pospieszczyk, I. Bray, D. V. Fursa, and Y. V. Ralchenko, At. Data Nucl. Data Tables **74**, 123 (2000).

[220] J. S. Briggs and Y. K. Kim, Phys. Rev. A **3**, 1342 (1971).

[221] M. A. Ali and P. M. Stone, Int. J. Mass Spectrom. **271**, 51 (2008).

[222] H. Deutsch, K. Becker, S. Matt, and T. D. Märk, J. Phys. B At. Mol. Opt. Phys. **32**, 4249 (1999).

[223] I. R. Taylor, A. E. Kingston, and K. L. Bell, J. Phys. B At. Mol. Phys. **12**, 3093 (1979).

[224] D. V. Fursa and I. Bray, J. Phys. B At. Mol. Opt. Phys. **30**, 757 (1997).

[225] I. Bray, D. V. Fursa, A. S. Kheifets, and A. T. Stelbovics, J. Phys. B At. Mol. Opt. Phys. **35**, 201 (2002).

[226] E. Bahati, H. Cherkani-Hassani, P. Defrance, J. J. Jureta, T. Kereselidze, Z. Machavariani, and I. Noselidze, J. Phys. B At. Mol. Opt. Phys. **38**, 1261 (2005).

[227] A. Dorn, A. Kheifets, C. D. Schröter, B. Najjari, C. Höhr, R. Moshammer, and J. Ullrich, Phys. Rev. Lett. **86**, 3755 (2001).

[228] J. Berakdar, A. Lahmam-Bennani, and C. Dal Cappello, Phys. Rep. **374**, 91 (2003).

[229] X. Ren, A. Dorn, and J. Ullrich, Phys. Rev. Lett. **101**, 1 (2008).

[230] M. S. Pindzola, S. Abdel-Naby, J. Colgan, and A. Dorn, J. Phys. B At. Mol. Opt. Phys. **45**, 215208 (2012).

[231] M. S. Pindzola, F. Robicheaux, J. P. Colgan, M. C. Witthoeft, and J. A. Ludlow, Phys. Rev. A **70**, 032705 (2004).

[232] M. S. Pindzola, F. Robicheaux, and J. Colgan, J. Phys. B At. Mol. Opt. Phys. **39**, L127 (2006).

[233] C. Bélenger, P. Defrance, E. Salzborn, V. P. Shevelko, H. Tawara, and D. B. Uskov, J. Phys. B At. Mol. Opt. Phys. **30**, 2667 (1997).

[234] J. Lecointre, D. S. Belic, H. Cherkani-Hassani, J. J. Jureta, and P. Defrance, J. Phys. B At. Mol. Opt. Phys. **39**, 3275 (2006).

[235] T. J. Gay, in *Atomic, Molecular, and Optical Physics: Atoms and Molecules*, Vol. 29, Part B, edited by F. Dunning and R. G. Hulet (Academic Press, 1996) Chap. 6, pp. 95–114.

[236] T. Halfmann, J. Koensgen, and K. Bergmann, Meas. Sci. Technol. **11**, 1510 (2000).

[237] C. Reynaud, J. Pommier, V. N. Tuan, and M. Barat, Phys. Rev. Lett. **43**, 579 (1979).

[238] R. H. Neynaber and G. D. Magnuson, J. Chem. Phys. **65**, 5239 (1976).

[239] V. Sidis, C. Kubach, and J. Pommier, Phys. Rev. A **23**, 119 (1981).

[240] T. Hecht, H. Winter, and R. W. McCullough, Rev. Sci. Instrum. **68**, 2693 (1997).

[241] A. Dinklage, T. Lokajczyk, and H. J. Kunze, J. Phys. B At. Mol. Opt. Phys. **29**, 1655 (1996).

[242] M. Reiser, ed., *Theory and Design of Charged Particle Beams* (Wiley-VCH Verlag GmbH, Weinheim, Germany, 1994).

[243] E. B. Hooper, P. A. Pincosy, P. Poulsen, C. F. Burrell, L. R. Grisham, and D. E. Post, Rev. Sci. Instrum. **51**, 1066 (1980).

[244] M. Tanaka, Y. Takahashi, T. Shimoda, T. Furukawa, M. Yosoi, K. Takahisa, N. Shimakura, and S. Yasui, Nulc. Instrum. Meth. A **568**, 543 (2006).

[245] B. L. Donnally and G. Thoeming, Phys. Rev. **159**, 87 (1967).

[246] N. Tanaka, M. Sasao, K. Terai, A. Okamoto, S. Kitajima, H. Yamaoka, and M. Wada, Rev. Sci. Instrum. **83**, 3 (2012).

[247] I. Bray and D. V. Fursa, J. Phys. B At. Mol. Opt. Phys. **44**, 061001 (2011).

[248] D. R. Long and R. Geballe, Phys. Rev. A **1**, 260 (1970).

[249] D. V. Fursa and I. Bray, Phys. Rev. A **52**, 1279 (1995).

[250] J.-M. Rost and T. Pattard, J. Phys. B At. Mol. Opt. Phys. **32**, L457 (1999).

[251] H. Klar and W. Schlecht, J. Phys. B At. Mol. Phys. **9**, 1699 (1976).

[252] J.-M. Rost and T. Pattard, Phys. Rev. A **55**, R5 (1997).

[253] J. L. Sanz-Vicario, E. Lindroth, and N. Brandefelt, Phys. Rev. A **66**, 052713 (2002).

[254] O. Zatsarinny, T. W. Gorczyca, and C. F. Fischer, J. Phys. B At. Mol. Opt. Phys. **35**, 4161 (2002).

[255] R. C. Bilodeau, J. D. Bozek, A. Aguilar, G. D. Ackerman, G. Turri, and N. Berrah, Phys. Rev. Lett. **93**, 193001 (2004).

[256] V. P. Shevelko and H. Tawara, J. Phys. B At. Mol. Opt. Phys. **28**, L589 (1995).

[257] M. B. Shah, D. S. Elliott, P. McCallion, and H. B. Gilbody, J. Phys. B At. Mol. Opt. Phys. **21**, 2751 (1988).

[258] M. Zambra, D. Belic, P. Defrance, and D. J. Yu, J. Phys. B At. Mol. Opt. Phys. **27**, 2383 (1994).

[259] K. Aichele, U. Hartenfeller, D. Hathiramani, G. Hofmann, V. Schäfer, M. Steidl, M. Stenke, E. Salzborn, T. Pattard, and J. M. Rost, J. Phys. B At. Mol. Opt. Phys. **31**, 2369 (1998).

[260] V. A. Bernshtam, Y. V. Ralchenko, and Y. Maron, J. Phys. B At. Mol. Opt. Phys. **33**, 5025 (2000).

[261] F. W. Byron and C. J. Joachain, Phys. Rev. **164**, 1 (1967).

[262] P. Defrance, T. M. Kereselidze, I. L. Noselidze, and M. F. Tzulukidze, unpublished .

[263] A. Dorn, R. Moshammer, C. D. Schröter, T. J. M. Zouros, W. Schmitt, H. Kollmus, R. Mann, and J. Ullrich, Phys. Rev. Lett. **82**, 2496 (1999).

[264] I. Bray, I. E. McCarthy, J. Wigley, and A. T. Stelbovics, J. Phys. B At. Mol. Opt. Phys. **26**, L831 (1993).

[265] G. F. Gribakin, A. A. Gribakina, B. V. Gul'tsev, and V. K. Ivanov, J. Phys. B At. Mol. Opt. Phys. **25**, 1757 (1992).

[266] C. Blondel and R. Trainham, J. Opt. Soc. Am. B **6**, 1774 (1989).

[267] I. Kiyan and H. Helm, Phys. Rev. Lett. **90**, 183001 (2003).

[268] C. Blondel and C. Delsart, Nulc. Instrum. Meth. B **79**, 156 (1993).

[269] P. Durand and I. Paidarová, Int. J. Quantum Chem. **58**, 341 (1998).

[270] F. H. M. Faisal, *Theory of Multiphoton Processes* (Springer US, Boston, MA, 1987).

Acronyms

*R***MF** *R*-Matrix Floquet. 19, 20, 57, 70, 72, 74, 75, 84, 89, 92, 93, 110, 112, 123, 147, 148

ACBT animated-crossed-beam technique. 18, 19, 24, 26–29, 34, 50, 59, 69, 74, 75, 133, 145, 147, 149, 150

AR anti-reflection. 41, 45, 48, 129

ASDEX axially symmetric divertor experiment. 4

CEM channel electron multiplier. 41, 42, 44–46, 50, 134

CI configuration interaction. 57

COBRA correlation between brightness and amplitude. 49

CW continuous wave. 41, 44, 55, 56, 59, 83, 147

DEMO DEMOnstration Power Plant. 4

DPD double photodetachment. 77–79, 81, 83, 84, 105–109, 114–119, 121–123

DVR discrete variable representation. 20

EH effective Hamiltonian. 19, 20, 84, 93, 94, 98, 105, 110, 112, 117, 123, 153, 155, 159

EIDI electron impact double ionization. 125, 126, 138, 139, 141, 143, 144

ITER international thermonuclear experimental reactor. 3, 4

JET joint european torus. 4

MCP multi-channel plates. 46, 49, 82, 83, 102

MEVELER maximum entropy velocity Legendre reconstruction. 38, 39

MPI multiphoton ionization. 79, 84, 89, 93

OPO optical parametric oscillator. 44, 48, 55–59, 147, 149, 150

PSD position sensitive detector. 34–36, 39, 47

QDT Quantum Defect theory. 20, 96, 110, 112

REMPI resonance-enhanced multiphoton ionization. 80, 81, 83, 94, 102, 105, 110, 112, 114, 117, 120, 123, 148, 153, 159

TEM00 transverse electromagnetic mode 00. 30–32, 41, 59, 100

TEXTOR tokamak experiment for technology oriented research. 5

VMI velocity map imaging. 18, 20, 34–36, 38, 40, 46–49, 64, 75, 147, 149, 150, 163, 164